REPORT DOCUMENTATION PAGE

Public reporting burden for this collection of information is estimated to average 1 hour per response, including the time for reviewing instructions, searching existing data sources, gathering and maintaining the data needed, and completing and reviewing the collection of information. Send comments regarding this burden estimate or any other aspect of this collection of information, including suggestions for reducing this burden, to Washington Headquarters Services, Directorate for Information Operations and Reports, 1215 Jefferson Davis Highway, Suite 1204, Arlington, VA 22202-4302, and to the Office of Management and Budget, Paperwork Reduction Project (0704-0188), Washington, DC 20503.

1. AGENCY USE ONLY (Leave blank)	2. REPORT DATE 17 May 96	3. REPORT TYPE AND DATES COVERED Final Technical 1 Apr 95 –31 Mar 96

4. TITLE AND SUBTITLE

Centrifuge Modeling of NAPLs (Preliminary title)

Centrifuge Modeling of Flow Processes (Final)

5. FUNDING NUMBERS

F49620 - 95-1-0283

6. AUTHOR(S)
Michael Chipley
Dobroslav Znidarcic

7. PERFORMING ORGANIZATION NAME(S) AND ADDRESS(ES)

The Regents of the University of Colorado
Campus Box 19
Boulder, CO 80309-0019

AFOSR-TR-96

0389

9. SPONSORING / MONITORING AGENCY NAME(S) AND ADDRESS(ES)

AFOSR/NA
110 Duncan Ave Suite B115 Bldg 410
Bolling AFB, DC 20332-001

NA

10. SPONSORING / MONITORING AGENCY REPORT NUMBER

95-1-0283

11. SUPPLEMENTARY NOTES

12a. DISTRIBUTION / AVAILABILITY STATEMENT

Approved for public release,
distribution unlimited

12b. DISTRIBUTION CODE

13. ABSTRACT (Maximum 200 words)

The research investigated the use of a geotechnical centrifuge to model nonaqueous phase liquids (NPALs) flowing through a porous media. Experiments modeled saturated and unsaturated flow through homogeneous and heterogeneous sands, smooth parallel plates, and rough rock fissures. The research validated the use of the centrifuge to model flow processes, however, there are limitations and restrictions on the nature and type of problems which can beinvestigated.

19960726 089

14. SUBJECT TERMS

NUMBER OF PAGES 280

16. PRICE CODE

17. SECURITY CLASSIFICATION OF REPORT Unclassified	18. SECURITY CLASSIFICATION OF THIS PAGE Unclassified	19. SECURITY CLASSIFICATION OF ABSTRACT Unclassified	20. LIMITATION OF ABSTRACT

DTIC QUALITY INSPECTED 1

DISCLAIMER NOTICE
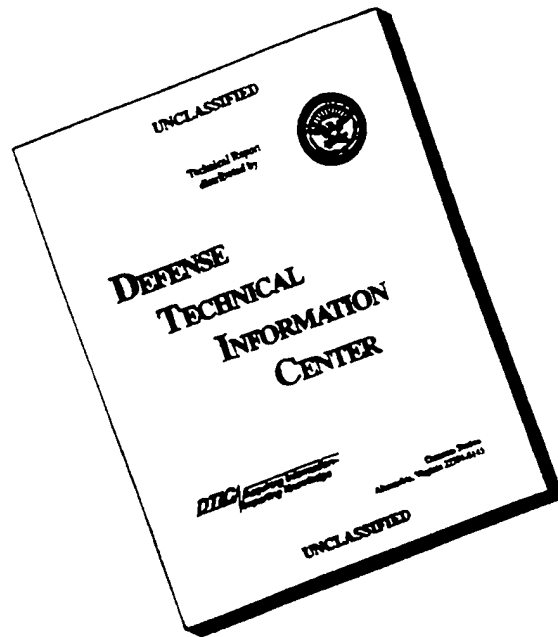
Centrifuge Modeling of Flow Processes

by

Michael TY Chipley

and

Dobroslav Znidarcic

Report prepared for:
AFOSR/NA
110 Duncan Ave Suite B115 Bldg 410
Bolling AFB, DC 20332-001

Depart,ment of Civil, Environmental and Architectural
Engineering
University of Colorado, Boulder, CO 80309-0428

May 1996

This report is identical in its content to the Ph.D. Dissertation by Michael TY Chipley:

Centrifuge Modeling of Flow Processes

Submitted to the Faculty of the Graduate School of the University of Colorado in partial fulfillment of the requirement for the degree of Doctor of Philosophy in 1996

TABLE OF CONTENTS

Chapter		Page

LIST OF FIGURES

Figure	Page

xv

LIST OF TABLES

CHAPTER 1

INTRODUCTION

1.1 - Objective

In the last five years, the centrifuge has gained in popularity as a research tool to model environmental problems. Centrifuge models can theoretically duplicate, in a time period of hours to days, the flow and transport problems which, at the prototype scale, can span several years. Experimental confirmation for most scaling laws that relate the model to prototype for flow processes has yet to be accomplished. Many of the very basic physical forces controlling flow and entrapment at normal gravity levels are not well understood, and the increased gravity levels in the centrifuge may or may not properly duplicate these forces.

The objective of this research is to prove the viability of using the centrifuge to model environmental contaminant flow problems, and to establish the appropriateness and limitations of the models. The fundamental question is, "Can the centrifuge be used to model, realistically, multiphase flow problems in porous media such as soils and rock fissures?"

1.2 - Scope of this study

To validate the use of the centrifuge as a research tool, this experimental program covered an extensive range in the properties of the porous medium and pore fluid. To do

this, both saturated and unsaturated flow processes were modeled. The porous media consisted of three different types of sands and several rock fissure apertures, with hydraulic conductivities ranging from 0.00036 cm/s to 145 cm/s. Test fluids were water, a lighter than water nonaqueous phase liquid (LNAPL) known as Soltrol 220, and a variable viscosity fluid called Metolose. The density of the fluids ranged from 0.809 to 1.00 g/cm^3. The viscosities of the fluids ranged from 1 to 30 centistokes. Denser than water nonaqueous phase liquids (DNAPLs) were not used in this research, but were simulated by reversing the order of the water and Soltrol 220 (i.e., water is a denser fluid than Soltrol).

The first goal of the experimental program is to verify the scaling laws for flow processes. Single-phase flow experiments were used to determine the scaling relationship for the hydraulic conductivity for homogeneous sands, layered sands, and fissures, and verified the range of the Reynolds number over which laminar flow occurred. Multiphase flow experiments were conducted to explore one-dimensional drainage of homogeneous sands, layered sands, and fissures. The experiments were used to validate the scaling relationships for the hydraulic conductivity and time.

The second goal is to determine the effect of the arm radius of the centrifuge on the scaling relationships. This was accomplished by constructing large scale 1g prototype models and conducting unsaturated flow experiments at normal gravity. The centrifuge models were scaled replicas of the 1g prototype models and of each other, commonly referred to as the modeling of models technique, and tests were conducted at various g-levels in the small and large centrifuges. Each centrifuge test was compared to the 1g

2

prototype and to each other. A theoretical derivation indicates that for true modeling of models, the centrifuge arm radius must be changed.

The third goal is to validate the concept of a "critical velocity" and stability criteria when both water and NAPL phases are present. The "critical velocity" and stability criteria indicate whether a porous medium will display sharp front or viscous fingering behavior. The order of fluids was chosen using the stability criteria of the "critical velocity" such that sharp front behavior was always ensured, or that viscous fingering would occur. Sharp front and viscous fingering behavior were explored using unsaturated sands and fissures. With the unsaturated fissure experiments, an actual rock surface was used to determine the effect of the aperture distribution on the degree of entrapment. In the centrifuge, the experiments used a lighter fluid overlying a heavier fluid (always stable) and a heavier fluid overlying a lighter fluid (possibly stable). These experiments verified the stability criteria and validated the capability of the centrifuge to address qualitatively this type of problem.

The experimental program was designed to validate the scaling laws and concepts in a particular order. The saturated flow experiments were designed to validate the scaling of the hydraulic conductivity for a single fluid using a wide range of porous media. The unsaturated flow experiments were designed to validate the scaling of the hydraulic conductivity and time using a single wetting fluid. All tests can be related through the use of the hydraulic conductivity and viscosity ratio. Having verified that Soltrol flowed no differently than water as a single-phase fluid, the two fluids were combined to explore the multiphase flow problems.

3

This chapter concludes with a short description of the thesis layout. Chapter 2 is a short literature review of research relevant to this study. Chapter 3 explains the theoretical background of flow processes, entrapment, and centrifuge modeling. Rather than separate chapters based on saturated or multiphase flow, the following chapters are separated and grouped according to the porous medium used. Chapters 4 through 6 explore saturated and multiphase flow in sands. Chapters 7 and 8 explore saturated and multiphase flow in fissures. Chapter 9 describes some geochemical observations made over the course of the research. Finally, Chapter 10 presents the conclusions and recommendations.

CHAPTER 2

LITERATURE REVIEW

2.1 - Overview

The literature review is presented in two parts: fluid flow and entrapment of NAPLs at normal gravity levels, and centrifuge modeling of flow problems. The review of fluid flow emphasizes the physics of flow and entrapment of NAPLs using a variety of porous media. Fluid flow through soils is described using Darcy's law, a topic thoroughly explored in most geotechnical or groundwater texts. A topic not usually covered in most texts is Darcy's law in fissure flow, therefore, a few select references are presented. The centrifuge modeling review presented herein covers the theoretical derivations and experimental investigations that have been developed to date. Because centrifuge modeling of environmental problems is still in its infancy, there are very few published papers. Many of the early papers have highlighted the difficulty in obtaining repeatable results, and described experimental problems. Several papers present only the numerical data and do not attempt to analyze the data. Only two papers attempt to validate the theoretical scaling laws. The remaining papers assume the scaling laws to be valid and present model results scaled to prototype performance using the theoretical scaling laws.

The literature review is not meant to be all encompassing, but rather a highlight of the concepts needed to design a comprehensive modeling program. The review is presented in a chronological order.

2.2 - NAPL flow and entrapment

Fluid flow and entrapment can occur in a wide range of materials, from large fractures to fine grained soils. The petroleum industry has examined extensively the interaction of porous media and NAPLs with regards to recovering the maximum NAPL fraction for economic gain. The residual NAPL fraction remaining was assumed to be immobile and not recoverable. Only within the last 20 years have NAPLs been explored with an emphasis on the identification and remediation problem from an environmental viewpoint and, in particular, the removal of the residual fraction that remains entrapped.

The physics governing flow and entrapment of NAPLs in a porous medium have been approached by researchers in several different fields: petroleum engineers, physicists, soil scientists, environmental and geotechnical engineers. The petroleum industry has used the "critical velocity" criteria as a means to determine the maximum pumping rate for an oil reservoir before viscous fingering occurs. If viscous fingering occurred, the amount of oil which could be economically extracted decreased. For this research, the "critical velocity" and stability criteria are of major importance. As will be developed in later chapters, only sharp front behavior can be modeled in the centrifuge. Viscous fingering behavior is by definition instable, and in the centrifuge, these instabilities are magnified.

Chuoke et al. (1959) used Hele-Shaw cells to show how the velocity of the fluid front could be used to control the formation of fingers. If a slow velocity was maintained, the fluid front remained sharp. At higher velocities, however, the front became unstable and fingers formed. A "critical velocity" was based upon the ratio of the viscosity and

6

relative permeabilities for each phase. The ratio is defined as the mobility ratio of the two fluids.

The displacement of the residual nonwetting fluid from a porous medium was examined by Larson et al. (1981) using percolation theory. They found that the initial distribution of the nonwetting fluid controlled residual saturation. A continuous phase behaved differently than disconnected blobs, and the blobs were functions of the pore geometry and topology. If the "critical velocity" was exceeded, viscous fingers and ganglia formed. Once ganglia formed, it was almost impossible to remove the entrapped ganglia.

The mechanics of entrapment was explored by Morrow and Songkran (1981). They examined the role of viscous and buoyancy forces on the nonwetting phase entrapment and found that entrapment could be related to the Capillary and Bond numbers. The Capillary number is a function of the displacing fluid velocity, and the degree of entrapment is sensitive to the Capillary number.

The mechanism for entrapment was explored by Kia (1988) using a uniform spherical porous medium. He found that the residual saturation was a function of contact angle, porosity, and particle size and that the variation in residual saturation was strongly dependent upon the pore geometry. The residual saturation can occur as pendular rings, connecting bridges, or ganglia. The value of the residual saturation was constant only when the entrapped fluid existed as pendular rings and small connecting bridges.

The effects of NAPL flowing through a residually water saturated vadose zone was studied by Reible and Illangasekare (1989). Infiltration of an immiscible phase

7

displayed essentially sharp front behavior. The mobility of contaminants was found to be a strong function of the physical form of the NAPL, the porous media, and the chemical properties.

Determination of the relative permeabilities for the wetting and nonwetting phases was done by Carpaneto (1989). He found that the shape of the meniscus was a function of the flow rate. This indicated that the capillary pressure was not a static but rather a dynamic quantity. Below the "critical velocity", the meniscus was concave towards the displacing fluid and completely forced the displaced fluid out of the pore space. Above the "critical velocity", the meniscus was concave outward from the displacing fluid and viscous fingers could form.

Armbruster (1990) examined the study and transport of NAPLs in groundwater. He used both homogeneous and heterogeneous sand packings with a surface spill of the NAPL migrating downward through the unsaturated zone to the water table. He was able to observe both sharp front and diffusive drainage front behavior.

Experiments using Hele-Shaw cells are conceptually small scale fissures with a uniform aperture. The tests only measure the fluid velocity to determine the effect of the velocity on finger formation. A more quantitative method is to determine the hydraulic conductivity of the cell by measuring the head loss which occurs over the length of the cell, and by measuring the aperture distribution. The hydraulic conductivity of a uniform aperture is theoretically given by the "cubic law". Fryberger (1990) undertook an extensive investigation of large scale fissure flow in laminar flow conditions to validate the "cubic law". He used large concrete slabs with a variety of surface roughness

8

conditions, varied the waviness of the slabs, and used various in-plane tortuosities. He found the cubic law to be valid for laminar flow through parallel plates. The effects of waviness and tortuosity could be accounted for by modifications of the basic cubic law. Water was the only test fluid.

Moreno et al. (1990) explored model fractures with variable apertures generated by statistical methods. They found that the fluid flow rate was constant in time but varied along the face of the fracture, indicating that the fluid flowed in preferential channels. Regions of small aperture had negligible or very small flows.

Glass et al. (1991) performed experiments to determine the effects of gravity and density with regards to gravity-driven wetting front instabilities. They examined the viscous fingering behavior and developed stability criteria to predict the onset of fingering.

Zimmerman et al. (1991) used lubrication theory to study the permeability of rough-walled fractures. They reduced the Navier-Stokes equation that governs fluid flow to a more tractable form of the Reynolds equation. They found that for lubrication theory to be valid, the fracture walls must be smooth over lengths on the order of one standard deviation of the aperture. The "cubic law" could be easily modified to account for the rough walls and surface variations.

A closed-form analytical solution for fissure flow was developed by Amadei and Illangasekare (1992) for non-homogeneous and anisotropic rock joints. This method allows two-dimensional analysis of flow problems where the grain shape and aperture are allowed to vary in space. The variations induce preferential flow channels which can be

shown as velocity vectors to visualize the flow.

Campbell (1993) performed two-dimensional experiments using NAPL and heterogeneous sands. He found that the relative differences between the materials dictated behavior. The degree of heterogeneity dominated the NAPL flow patterns, but LNAPLs displayed sharp front infiltration, while DNAPLs always formed fingers.

Held (1993) used dense nonaqueous phase liquids (DNAPLs) to investigate the fingering phenomena. He found that trichloroethene (TCE) and tetrachloroethane (TCA) displayed fingering behavior under all circumstances, but no set relationships could be determined for the rate of the finger growth or the final pore saturation distribution. Dibutylphthalate (DBP) displayed both sharp front and fingering behavior and the imposed flow rate and boundary conditions seemed to dictate fingering.

Fairbanks (1994) examined the role of layered sands and entrapment. Depending upon the order of layering, different levels of entrapment could be observed. The entrapment was related to the pore geometry and entry pressure of the porous media. The experiments were one-dimensional drainage and displayed essentially sharp front behavior behind the drainage front.

The evaluation of the sharp front behavior was accomplished by Walser (1994). The NAPL front was tracked as it infiltrated downward through homogeneous sand columns and layered sand columns. Material discontinuities were found to cause entrapment and the capillary pressure was found to be a dynamic and not a static quantity, similar to the results of Carpaneto.

2.3 - Centrifuge modeling

While many questions remain to be answered for NAPL flow, the basic relationships between density, viscosity, and the types of porous media are fairly well understood. Entrapment and removal of the entrapped fraction are still the most difficult and complex problem, in part because it is a microscopic process (pore scale) which is usually related to macroscopic measurements (saturation, pressures, etc.). Experimental investigations of entrapment using a real porous medium can require extensive time periods. Numerical models of entrapment provide very quick results, but typically use an idealized porous medium. The centrifuge can bridge the gap between the normal gravity experiments and the numerical models.

The centrifuge uses a real porous medium in the experimental investigation, and the experiment can be completed in a very short time. Experiments that are physically too large or require a long time period to test can be easily scaled down to fit into the centrifuge. The centrifuge models are then physical models that are duplicates of the prototype and the scaling relationships are used to predict the prototype performance from the model data. In addition, from the model data, the input parameters required by the numerical models can be determined. The centrifuge experimental results can be compared to the numerical model results and provide a means to validate the numerical models.

The use of a centrifuge to model flow problems is first mentioned by Pokrovski and Fyodorov in 1936 (in Goodings, 1985). At that time, the centrifuge was used primarily to examine geotechnical problems involving slope stability in river channels and

11

rock beams in tunnels. The derivations of scaling laws for fluid flow were developed for seepage and consolidation with regard to slope stability. Muskat (1937) investigated high velocity flow in sand and lead shot using dimensional analysis. Many years elapsed before new research into fluid flow problems occurred. Laut (1975) considered the scaling laws for laminar seepage through a small soil model when the model is subjected to an increase in self-weight by a factor of N on a geotechnical centrifuge, but did not perform any experimental investigations. In the 1980's and early 1990's, several papers were published specifically addressing fluid flow problems using dimensional analysis and similarity of forces techniques.

Cargill and Ko (1983) used dimensional analysis to derive centrifuge scaling laws for transient water flow in embankment dams. They compared the limitations of available analytical solutions and full-scale modeling to the benefits of centrifuge modeling. They built a scale model of an embankment dam and tracked the phreatic surface as it changed due to changes in the headwater elevation. They concluded that centrifuge modeling is a technique which implicitly considers all of the variables of the flow problem and can properly simulate prototype behavior by using the applicable scaling laws.

Croce et al. (1984) used similarity of forces to derive centrifuge scaling laws for consolidation. They examined the consolidation behavior of several clays in various drainage configurations. They concluded that the centrifuge time required is extremely short compared to field consolidation tests. The effects of boundary conditions can be experimentally reproduced with ease and experimental measurements can be performed with sufficient accuracy and without sophisticated equipment. The scaling relationships

12

derived using similarity of forces were in agreement with scaling relationships derived using dimensional analysis.

Tan and Scott (1985) examined the theoretical contradictions of differing time scales for diffusion and dynamic time problems. They were exploring liquefication produced by static or dynamic cyclic stresses. These problems involve relative particle-fluid motion and are difficult to properly scale. They concluded that there is only one time scale but that the other parameters must be scaled so that the equations are made similar. Coriolis effects must also be considered.

A comprehensive review of modeling relationships was presented by Goodings (1985). She examined the scaling laws for saturated steady state and transient laminar and turbulent groundwater flow, unsaturated groundwater, surface flow and erosion. She concluded that grain size must be properly scaled. Changes in other properties, such as soil strength or soil density, are not acceptable if the model is to be related to the prototype.

Pollutant transport processes were examined by Arulanandan et al. (1986). They used dimensional analysis to obtain the scaling laws for advection, dispersion, adsorption, and degradation that control the pollutant transport processes in groundwater. They concluded that the scaling laws are valid for adsorption and advection, but for coarse-grained soils where the Peclet number is greater than one, the dispersion process cannot be directly scaled from model to prototype.

Ibrahim (1990) modeled two-phase unsaturated flow using water and air. He found that the suction-saturation behavior was essentially properly modeled and that the

time factor appeared to be N^2. He performed modeling of models using a very fine sand and Bonny silt at 30g and 60g, but did not perform a 1g prototype test.

Goforth et al. (1991) used the governing differential equations to derive the centrifuge scaling laws for saturated and unsaturated flow. They used a fine sand and a fine sand-clay mixture to verify the scaling laws for intrinsic permeabilities. Goforth et al. concluded that the scaling laws were in excellent agreement, but that the centrifuge offered no advantage over 1g tests for saturated flow. They also found the upper limit of laminar flow to have a Reynolds number of 0.2, an order of magnitude lower than predicted by Bear (1972).

Multiphase flow in porous media was first explored by Illangasekare et al. (1991). They performed a ponding experiment using Soltrol percolating down through a sand. They concluded that the centrifuge is a feasible modeling technique for studying processes of immiscible fluid flow through soils. The centrifuge allows the use of reduced scale models and reduces the required testing time by N^2.

The use of the centrifuge for modeling contaminant transport in partially saturated soils was evaluated by Cooke and Mitchell (1991). They concluded that modeling of contaminant transport in partially saturated soils in a centrifuge can be combined with numerical models to provide a detailed understanding of the phenomenon.

Goodings (1994) examined the fluid flow transition from laminar to turbulent flow to obtain an upper limit on the Reynolds number. She used sand, copper shot, and glass marbles to give different effective grain sizes and plotted the friction factor (similar to the Moody friction factor) versus the Reynolds number. She concluded that the upper limit

14

for laminar flow was between 3 and 10, as predicted by Bear (1972).

The scaling for immiscible multiphase flow in porous media was theoretically derived by Peterson and Cooke (1994). Their derivations and analysis of the Bond and Capillary numbers showed that similitude between model and prototype cannot be achieved. They concluded that the centrifuge causes a divergence of phenomena between the model and the prototype, and that the centrifuge is not a suitable tool for modeling of immiscible multiphase flows, or any other two-phase water and LNPAL displacement.

Cooke (1994) also developed techniques using the centrifuge to estimate the unsaturated flow parameters by measuring the cumulative outflow under gravity drainage. The method allows estimation of the soil suction, moisture content, and hydraulic conductivity.

A simulated 2000 liters of LNAPL spilled onto a medium sand was performed by Mitchell and Stratton (1994). They collected the oil saturation data, but did not perform an analysis or try to interpret the data. They provide the complete data set for numerical model validation purposes.

Villar and Merrifield (1994) explored the effects of dispersion and adsorption of radioactive tracers by using Geiger tubes imbedded into the soil. They have developed techniques using radiotracers to study pollutant migration.

2.4 - Summary

The literature review has examined immiscible phase flow and entrapment, and the use of the centrifuge in modeling flow problems. The governing equations of multiphase

15

flow are derived assuming that fluid flow is laminar and has a Reynolds number less than 1. The crucial issue in modeling flow problems in the centrifuge is the validity of Darcy's law. The centrifuge experiments to date have been inconclusive on determining the largest Reynolds number for which Darcy's law is still valid. Single-phase flow experiments will be used to validate Darcy's law by determining the scaling relationship of the hydraulic conductivity and finding the largest Reynolds number for which laminar flow occurs.

For multiphase flow, laminar flow is still required, but Darcy's law is applied to each phase. In addition to the Reynolds number, the Capillary and Bond numbers may be of importance. The concept of the "critical velocity" and stability criteria will be used to design multiphase experiments that ensure sharp front behavior and prevent viscous fingering. As will be seen in Chapter 3, only multiphase flow problems displaying sharp front behavior are appropriate for centrifuge modeling.

CHAPTER 3

THEORETICAL BACKGROUND

3.1 - Introduction

The use of the centrifuge to model flow problems involving organic contaminants requires an understanding of the basic physics of flow and entrapment. Entire texts are devoted to the presentation of the fundamentals of flow processes and entrapment of immiscible fluids in porous media (Bear, 1972; Corey, 1986). Only a few areas of particular relevance to this work are presented in this chapter, with an emphasis on how the higher g-level in the centrifuge will affect the parameters of interest.

3.2 - Governing equations of fluid flow

The law of conservation of mass requires the flow of a fluid entering a porous medium minus the flow exiting to be equal to the net storage of the elemental volume element. An elemental control volume is shown in Figure 3-1.
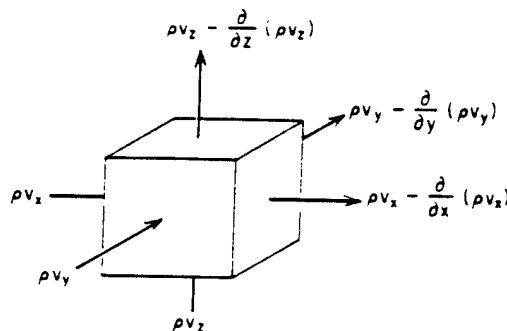
Figure 3-1. Control volume for porous media (from Freeze and Cherry, 1979)

In mathematical form:

$$\left[-\frac{\partial(\rho v_x)}{\partial x}-\frac{\partial(\rho v_y)}{\partial y}-\frac{\partial(\rho v_z)}{\partial z}\right]dxdydz = \frac{\partial m}{\partial t} \tag{3.1}$$

where:

ρ = the density of the fluid

v_i = the velocity of the fluid in the i direction

m = the mass of fluid per unit volume

The right hand side can be expanded using the chain rule

$$\frac{\partial m}{\partial t} = \frac{\phi S \partial \rho}{\partial t}+\frac{\phi \rho \partial S}{\partial t}+\frac{S \rho \partial \phi}{\partial t} \tag{3.2}$$

where:

ϕ = porosity

ρ = the density of the fluid (M/L^3)

S = the saturation (dimensionless)

For most contaminant problems encountered in the subsurface, the change in density is minimal and flow occurs mainly in sands or gravel which have negligible change in porosity (consolidation). Therefore, Equation (3.1) can be simplified to:

$$-\frac{\partial \rho v_x}{\partial x}-\frac{\partial \rho v_y}{\partial y}-\frac{\partial \rho v_z}{\partial z} = \frac{\rho \phi \partial S}{\partial t} \tag{3.3}$$

Darcy's law is expressed as:

$$v = -K\frac{dh}{dl} \tag{3.4}$$

18

where:

K = hydraulic conductivity (L/T)

h = total head (L)

l = length over which differential head occurs (L)

In Darcy's law, the hydraulic conductivity K is dependent upon the porous medium and fluid properties and is given as:

$$K = \frac{k\rho g}{\mu}$$ (3.5)

where:

k = intrinsic permeability, a function of the porous medium only (L^2)

ρ = the fluid density (M/L^3)

μ = dynamic viscosity, a function of the fluid only (M/LT)

g = gravitational constant (L/T^2)

Substituting Equation (3.4) into Equation (3.3) and dividing by ρ gives:

$$\frac{\partial}{\partial x}(K_x \frac{\partial h}{\partial x}) + \frac{\partial}{\partial y}(K_y \frac{\partial h}{\partial y}) + \frac{\partial}{\partial z}(K_z \frac{\partial h}{\partial z}) = \frac{\phi \partial S}{\partial t}$$ (3.6)

The governing equation is valid for saturated and unsaturated flow, and for all porous media with a single fluid. It is important to note that the "type" of porous medium is reflected only in the intrinsic permeability; a rock fissure can be considered to have an "effective intrinsic permeability" based upon the aperture and roughness of the fissure surfaces (i.e., a very high porosity). The "type" of fluid is described entirely by the density and viscosity terms. The hydraulic conductivity describes the interaction of the porous

19

media and fluid.

When Equation (3.6) is solved assuming a constant hydraulic conductivity and by setting the righthand side equal to zero (saturated flow), the Laplace equation is obtained as:

$$\frac{\partial^2 h}{\partial x^2} + \frac{\partial^2 h}{\partial y^2} + \frac{\partial h^2}{\partial z^2} = 0 \tag{3.7}$$

Saturated flow can be completely described by two parameters: the hydraulic conductivity and the Darcy velocity. If Equation (3.6) is solved using a variable hydraulic conductivity, and the righthand side is not equal to zero (transient single-phase unsaturated flow), the Richards equation is obtained as given by:

$$\frac{\partial}{\partial x}[K(h)\frac{\partial h}{\partial x}] + \frac{\partial}{\partial y}[K(h)\frac{\partial h}{\partial y}] + \frac{\partial}{\partial z}[K(h)\frac{\partial h}{\partial z}] = \frac{\partial \theta}{\partial t} \tag{3.8}$$

The Richards equation assumes the air phase is free to flow to the atmosphere, but unlike saturated flow, the hydraulic conductivity is now a function of the head and adds an additional complexity. The change of the Darcy velocity and hydraulic conductivity with respect to time must be given to fully describe unsaturated flow.

In the analysis of Equation (3.8), it is often assumed the porous medium is homogeneous and isotropic and that only a single fluid is present. Hydraulic conductivity, however, can also be anisotropic or vary in time due to chemical and physical changes in the porous media (i.e., consolidation), or more than one fluid may be present. For the purpose of this research, the type of fluid is of primary importance as the objective is to

20

understand organic contaminant flow in the subsurface. Therefore, changes in porous medium properties will not be permitted, and only the type of fluid will be varied.

To model an environmental problem properly, the domain of interest must be thoroughly understood and a systematic investigation must examine each variable that impacts the physics of the problem. The following section examines typical contaminant problems which are potential centrifuge modeling experiments and the variables of interest.

3.3 - Organic contaminants in the subsurface

Once an organic contaminant enters a soil or water body, the problem becomes one of multiphase flow. Multiphase flow modeling involves modeling systems where more than one continuous fluid phase is present (i.e., an organic contaminant NAPL and air, NAPL and water, or NAPL, air and water). Modeling a multiphase problem requires an understanding of the chemical, physical, and biological processes involved and the interactions between the various fluid phases and the porous media under a flow potential. The flow potential of a fluid is a function of extensive properties and physical factors (i.e., porosity, viscosity, grain size, and density) and intensive properties (i.e., pressure, relative permeabilities, flow rate, capillary heads, surface forces, and saturation). A separate phase immiscible fluid will have a flow potential different from that of miscible phase and water or that of pure water.

NAPLs are usually considered immiscible and most NAPLs are less dense than water, with the exception of bitumens and chlorinated solvents. NAPLs denser than

21

water are commonly referred to as dense nonaqueous phase liquids (DNAPL) and NAPLs lighter than water are light nonaqueous phase liquids (LNAPL).

The subsurface flow of an organic contaminant can occur in two regimes, the unsaturated and the saturated zones. The initial release of a NAPL usually occurs in the unsaturated zone due to leaks in underground storage tanks (UST), leaks in piping networks and valves, and accidental spills or discharges. The NAPL will tend to migrate downward occupying pore space and displacing air from the pores as it flows. In the unsaturated zone, water is usually present only in small quantities often referred to as residual saturation. This water is assumed immobile and tightly bound to the soil grains. As the NAPL migrates downward, the NAPL fills the remaining pore space to full saturation. As drainage proceeds, the NAPL vacates the pore space and goes to residual saturation. Water and NAPL can remain in the pore space as pendular rings, isolated blobs, or interconnected ganglia, all of which can be considered entrapped fluid. Typical LNAPL and DNAPL penetrations into a soil matrix and water table are shown in Figures 3-2 and 3-3. In the unsaturated zone, there are four components: the soil grains, the air phase, the nonaqueous phase, and the water phase, as shown in Figure 3-4. In the saturated zone, the system reduces to a three-phase problem, as shown in Figure 3-5.
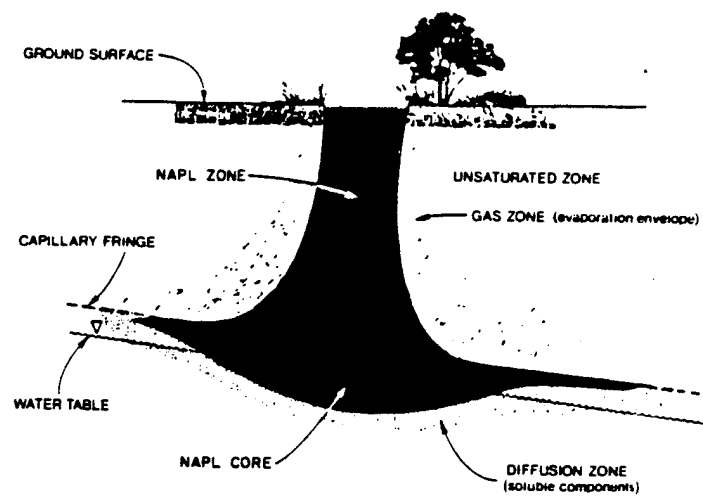
Figure 3-2. LNAPL migration (from Abriola and Pinder, 1986)
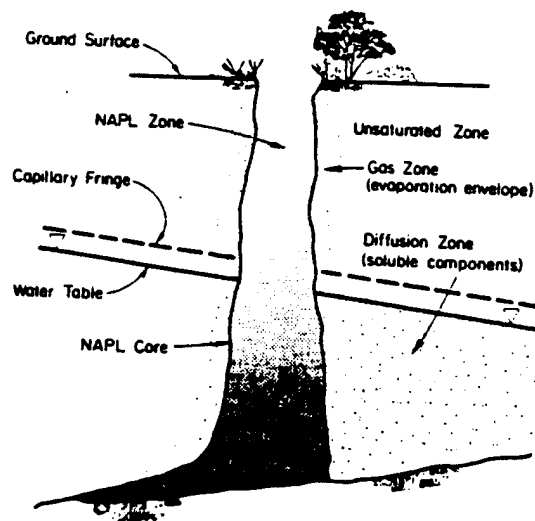
Figure 3-3. DNAPL migration (from Abriola and Pinder, 1986)

23
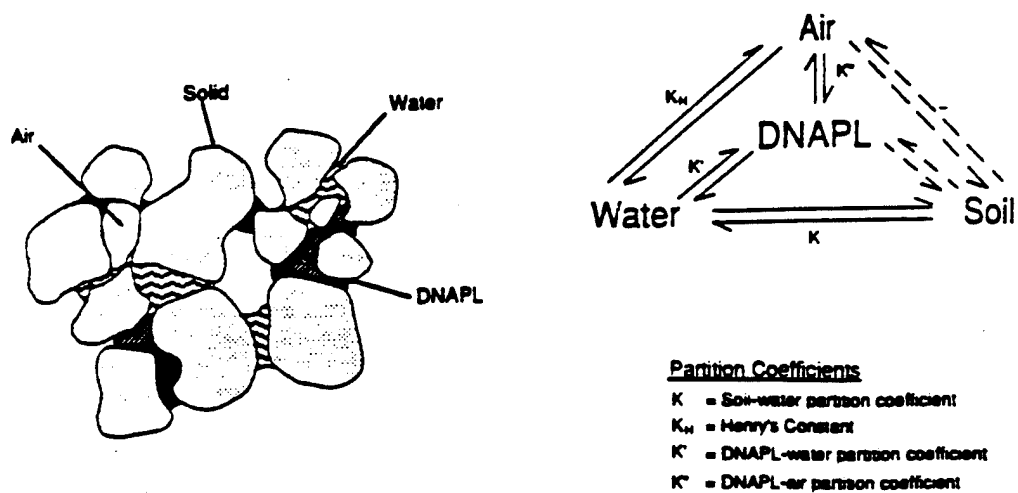
Figure 3-4. Four phases in the unsaturated zone
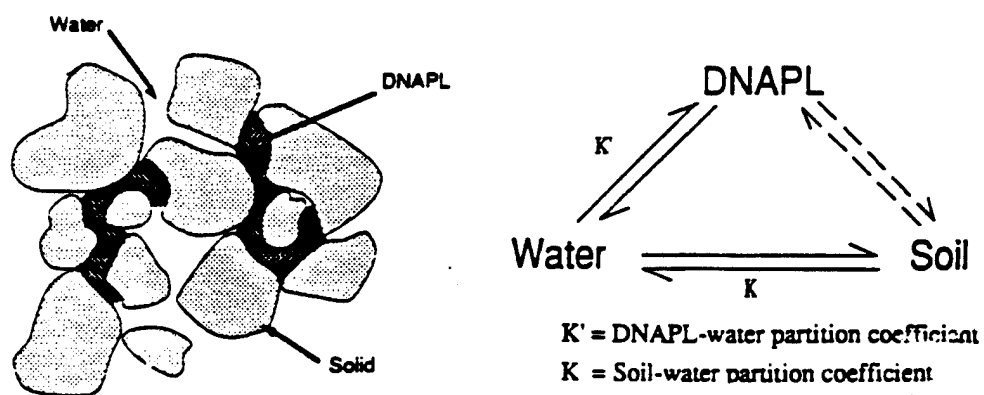
Figure 3-5. Three phases in the saturated zone

For most flow problems, the soil phase is usually assumed incompressible and stationary and is therefore neglected; however, it should be realized that the soil phase is not always incompressible or stationary, especially with regard to problems involving marine, lake, or river sediments.

Research indicates that the hydrocarbon molecules attach to organic matter (i.e., humic matter) bound to the porous media. The organic matter comes from the degradation of living tissue (plants, animals, microbes), which usually occurs in the upper layers of the soil profile. If organic matter is above approximately 1 % by weight, it will dominate the sorption process.

The process of the NAPL binding to the aquifer media is one form of partitioning. The partitioning of NAPLs is a function of the porous media, porosity, density, and percentage of organic carbon. The organic carbon in the soil matrix is the predominant absorption site that will capture the NAPL molecules. The approach most often used to determine the partitioning of oil to the soil is to correlate the fraction of organic carbon present in the soil to the octanol-water partition coefficient for the oil. Within aquifers, there is very little organic matter, no sunlight, no aeration, and few microorganisms capable of degrading NAPLs and partitioning is not thought to be an important process. Several chemical reactions, however, can take place depending upon the pH of the water, dissolved ions, microbial degradation, and oxidation/reduction reactions.

In general, a hydrocarbon can migrate through the air and water, partition to the porous media, and undergo several degradation processes such as microbial, photolytic, and chemical conversion. LNAPLs will tend to remain in the upper saturated zone and

"float" at the interface of the water saturated and unsaturated zones and usually have a horizontal gradient of flow in relation to the water table gradient. Variations in the groundwater level due to weather and seasonal variations can cause the LNAPLs to rise and fall with the fluctuating water table. Over time, the LNAPL can become entrapped in the porous media below the water table and can no longer be flushed out, causing significant quantities of LNAPLs to remain below the water table. DNAPLs tend to have vertical flow paths and are not affected by the groundwater gradient to the same extent as an LNAPL. DNAPLs tend to sink through the groundwater to the lowest impermeable layer and may even migrate in paths opposite to those of the groundwater gradient.

The entrapment of NAPLs in the subsurface is then a problem of interest to both geoenvironmental and petroleum engineers, albeit with different motives. The centrifuge has been used for many years in the petroleum industry to determine fluid extraction flow parameters and is well suited to examining one-dimensional flow problems. The test involves placing a rock core from an oil bearing stratum and spinning the sample to residual saturation. Various surfactants and fluids are used to flood the core to try to recover a higher percentage of the residual NAPL. The equipment and methodology used in the petroleum industry, however, are not suitable for use in modeling environmental problems, especially with regard to the boundary conditions. The analysis methods and techniques used in the petroleum industry can provide insight into ways to properly model environmental problems. The following section examines the physics of entrapment in greater detail.

3.4 - Organic phase entrapment

There are several characteristics of the fluid and porous media which are normally used to determine the fate and transport of a NAPL:

1. Density

2. Viscosity

3. Solubility

4. Vapor pressure

5. Volatility

6. Interfacial tension

7. Wettability

8. Capillary pressure

9. Pore size distribution

10. Initial moisture content

11. Groundwater flow velocity

12. Residual saturation

13. Relative permeability

Each of the above characteristics can have a significant impact upon the distribution and migration of the NAPL. In particular, the fluid interfaces within the porous media tend to dominate flow behavior. In the pore space, an interface exists between the two fluids across which a pressure difference occurs. This is defined as the capillary pressure, as shown in Figure 3-6.
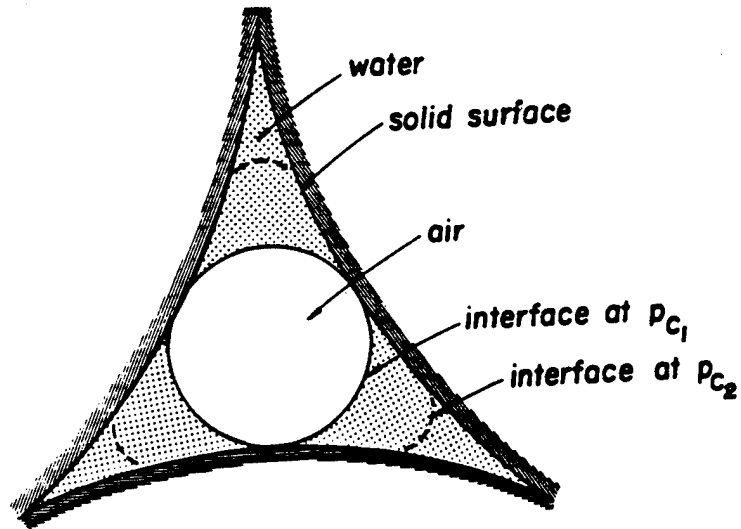
Figure 3-6. Cross section of pore space (from Corey, 1986)

During the immiscible phase flow, the soil grains have a preference for which fluid will be in intimate contact with the surface; this fluid is designated as the wetting fluid. The fluid that is excluded from contact is designated as the nonwetting fluid, schematically shown in Figure 3-7.
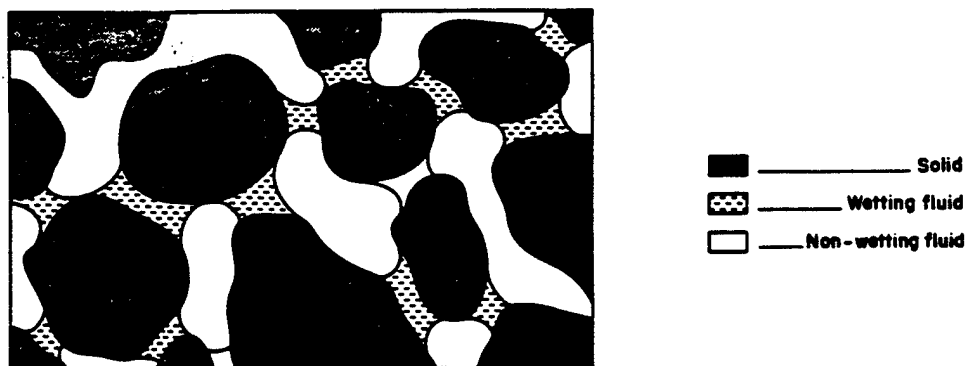
Figure 3-7. Pore scale (from Baviere, 1991)

For systems in which water is involved, water is normally the wetting fluid. In the case of water and NAPLs, the NAPL is the nonwetting fluid. Where the two immiscible fluids meet an interface exists where the pressures and densities are discontinuous. The interfacial force across the interface is a function of the two fluids, temperature, and other dissolved agents, as shown in Figure 3-8.
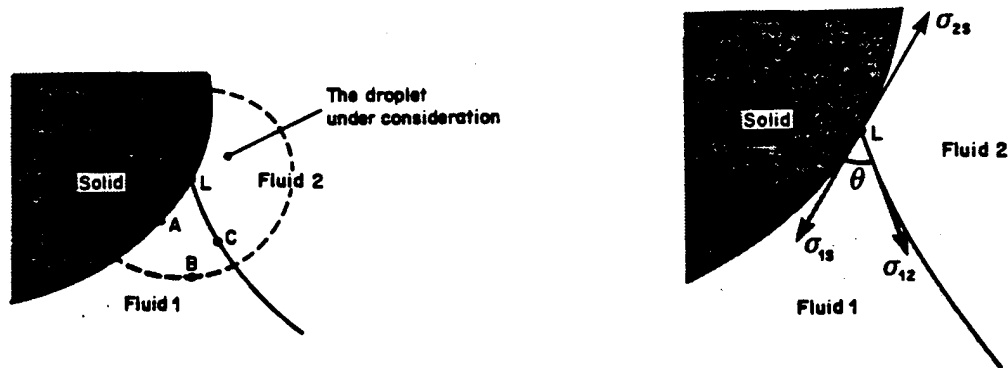
Figure 3-8. Surface tension (from Baviere, 1991)

In a static system, the capillary pressure across the interface is given as:

$$p_c = \sigma\left(\frac{1}{r_1} + \frac{1}{r_2}\right) \tag{3.9}$$

where:

σ = interfacial surface tension (M/T^2)

r = radius (L)

This static capillary equation is assumed to remain approximately valid for fluid that is flowing due to the capillary forces being much greater than the viscous forces. In

a flowing system, the water will try to displace the NAPL by forcing it into other pores, as shown in Figure 3-9.
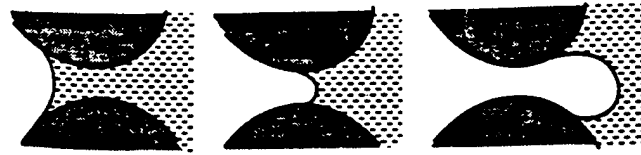
Figure 3-9. NAPL displacement (from Baviere, 1991)

The NAPL will remain in the largest pores surrounded by water. The NAPL may still flow inside the pores, but along the way droplets may encounter some channels narrower than their width. To enter the channels, the curvature of the droplet must decrease, as shown in Figure 3-10.
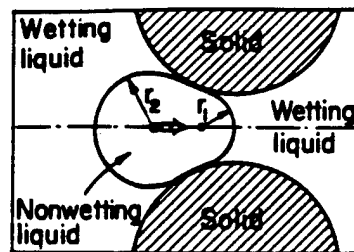
Figure 3-10. Curvature decrease (from Bear, 1972)

For the droplet to flow across the channel, the pressure in the NAPL phase must be higher than the pressure in the water phase. A simplified model of a porous media like Figure 3-10 is shown in Figure 3-11.

30

Cross-section A   Longitudinal section
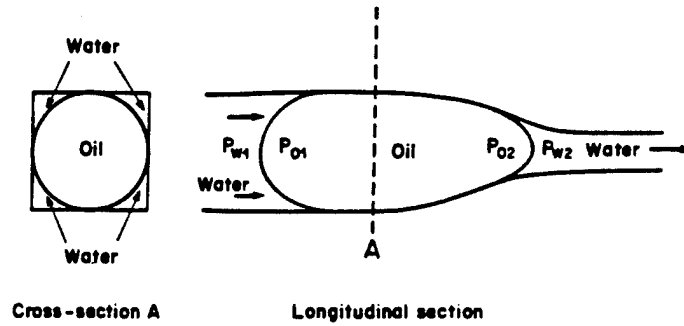
Figure 3-11. Pore pressures (from Baviere, 1991)

Water will occupy the part of the tube along the edges of the square cross section and the NAPL will occupy the center channel. The NAPL droplet cannot flow unless P_{01} > P_{02} or:

$$P_{w1}-P_{w2} > \sigma[(\frac{1}{r_1}+\frac{1}{r_2})_2-(\frac{1}{r_1}+\frac{1}{r_2})_1]$$ (3.10)

If the pressure drop in the flowing water phase is small, the NAPL phase is unable to penetrate into the narrower part of the tube. At this point the remaining fluid has become entrapped. The amount of entrapped fluid is a function of the contact angle of the fluid and soil, the porosity, and the soil grain size. The entrapped fluid can remain in single isolated pores or in several interconnected pores, often called ganglia. In essence, two major forces are competing to force the fluids to move; the buoyant forces try to force a fluid out of a pore, and capillary forces try to retain the fluid in the pore.

Entrapment in a porous medium has been related to the Capillary number and the Bond number, the ratios of the capillary to viscous forces and the ratio of the buoyant to

31

viscous forces, respectively, and are given as:

$$Ca = \frac{\mu V}{\sigma} \tag{3.11}$$

$$Bo = \frac{\Delta \rho g R^2}{\sigma} \tag{3.12}$$

where:

V = the velocity of the displacing fluid front (L/T)

R = the characteristic pore size, normally the d_{10} particle size (L)

σ = the liquid-liquid interfacial tension (M/T^2)

Whereas the Capillary and Bond numbers are used most often with regard to fully saturated cores, for environmental problems flow and entrapment can occur in both the saturated and unsaturated zones. For environmental modeling, the Capillary and Bond numbers must be applicable for both regimes. Modeling the saturated and unsaturated zones, however, requires vastly different assumptions and analysis techniques, and will be examined in more detail in the following paragraphs.

A NAPL spill on the ground surface will percolate downwards through the unsaturated zone. Any water present in the unsaturated zone pores is usually at a value near residual saturation but the pore space begins to fill with water close to the groundwater table. As the NAPL is percolating downwards, there is an infiltration front and a drainage front. The infiltration front tends to remain relatively sharp and the drainage front tends to be diffused and not well defined. Within the pore space, the capillary forces can trap the fluids in three different configurations: as pendular rings or bridges, as shown in Figure 3-12, or as several filled and connected pores (i.e., ganglia).

32
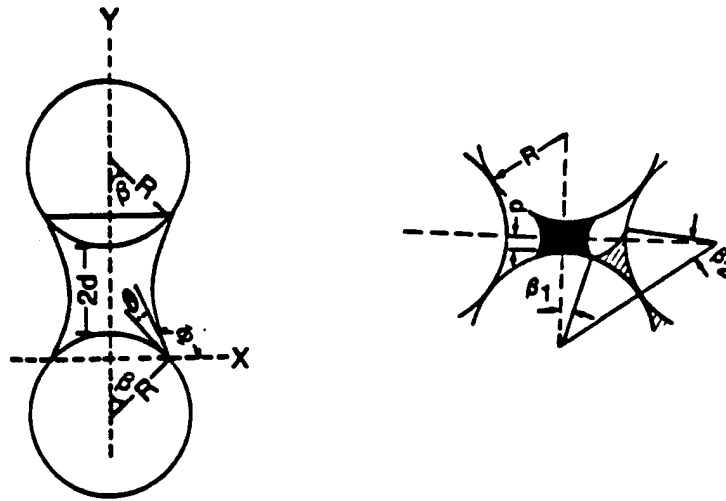
Figure 3-12. Entrapped fluid (from Kia, 1988)

At the water table elevation the porous media will be fully saturated. Extending above the water table is the capillary fringe where water is held by suction. There is a region where the soil is fully suction saturated and above this region the pore space is unsaturated. The capillary suction saturation curve is used to represent the degree of saturation with capillary head, as shown in Figure 3-13.

Two limiting curves exist for a soil: one a drainage curve, and the second a wetting curve. In general, the two curves are not the same, and the wetting curve is not well defined at the end point near the maximum saturation, as seen in Figure 3-15. The two curves belong to an infinite family of curves which can be obtained by starting at any given saturation, and either increasing or decreasing the saturation. This relationship is commonly referred to as hysteresis. All of the curves, in theory, will be bound by the wetting and drainage curves. Normally, the drainage curve is used to obtain an analytical

33

expression which can be used in other equations. The most common expressions used are those given by Brooks and Corey (1966), and van Genuchten (1980).
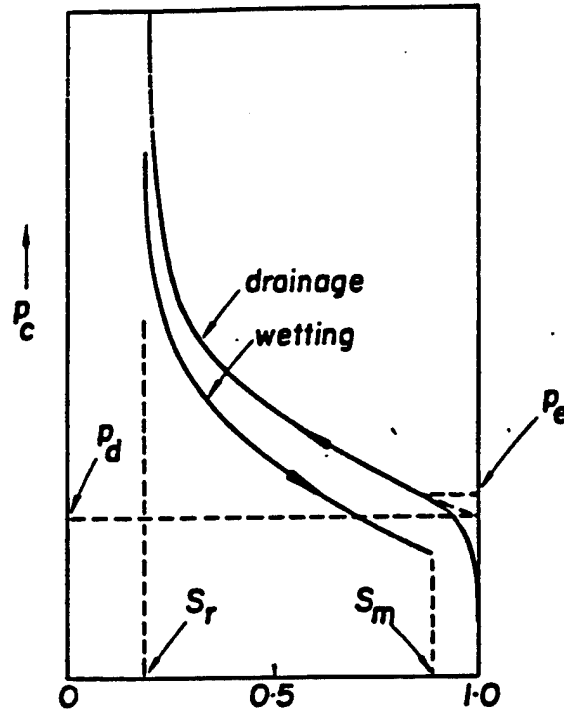
Figure 3-13. Suction-saturation curve (from Corey, 1986)

The entrapped fluids have an effect on hydraulic conductivity. In a system that is initially at full NAPL saturation, then drained to residual NAPL saturation, the effective porosity is reduced by the entrapped NAPL. Water flowing through this system will experience an effective hydraulic conductivity less than that for zero NAPL entrapment and is shown using relative permeability versus saturation curves as shown in Figure 3-14.
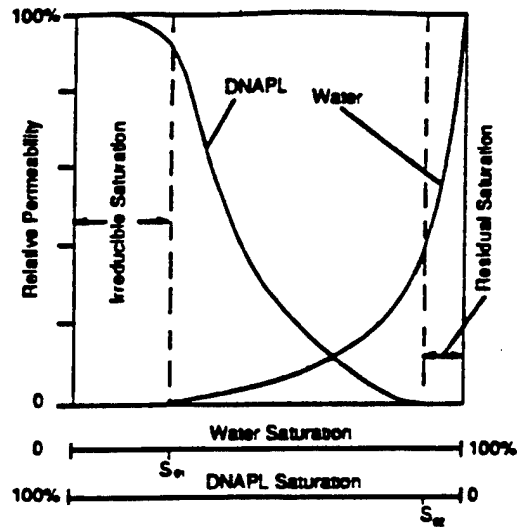
Figure 3-14. Typical relative permeability curves

Larson et al. (1981) found that the relative permeabilities are a function of the Capillary number when there are sufficiently large pressure gradients. If the Capillary number is less than about 10^{-6}, relative permeabilities are independent of pressure gradients, total volummetric flow rate, and interfacial tension, and the relative permeabilities approach limiting values of saturation, as shown in Figure 3-15.
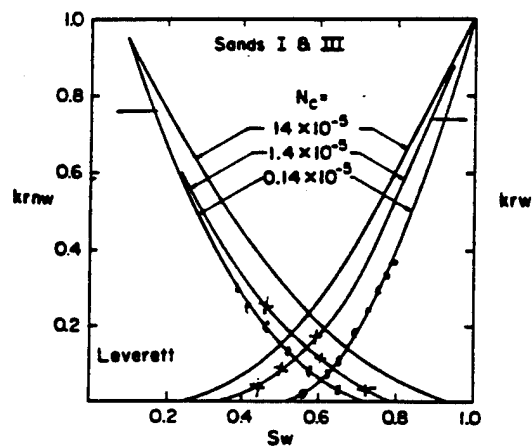
Figure 3-15. Relative permeability as function of N_c (from Larson et al., 1981)

35

In the case where the DNAPL is moving into an aquifer, the mixing of the two phases will cause a reduction in the water's relative permeability, which then increases as the DNAPL is depleted. LNAPLs have previously been thought of as riding on top of the water table surface, however, new evidence points to a mixing zone where the LNAPL and water are intermixed.

As shown in the previous paragraphs, the organic phase can become entrapped within both the saturated and unsaturated zones due to capillary forces. In the unsaturated zone, if there is no water present, the retention of an organic phase should be similar to the retention of water according to the Richards equation. In the saturated zone at normal gravity level, there are several variables determining entrapment: the Capillary number, the Bond number, the change in relative permeabilities, pore geometry, and wetting fluid-soil interactions. Morrow and Songkran (1981) used Soltrol (LNAPL) as the wetting fluid and air as the nonwetting fluid to examine the retention of the organic phase as a function of the Capillary and Bond numbers, as shown in Figure 3-16.
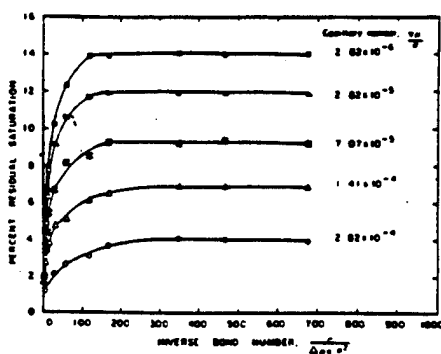
Figure 3-16. Soltrol retention (from Morrow and Songkran, 1981)

36

Morrow and Songkran (1981) proposed that the interaction mechanisms could be related to the imbibition pressure and imposed gravity field, as shown by Figure 3-17.
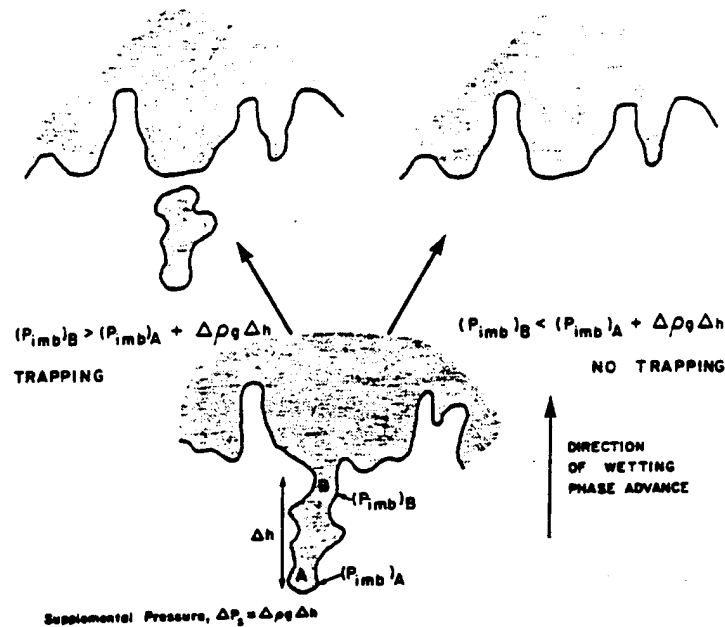
Figure 3-17. Entrapment mechanism (from Morrow and Songkran, 1981)

If the imposed pressure at the tip was always less than the imbibition pressure plus the gradient pressure, then sharp front behavior would be observed and the displacing fluid would occupy all of the pore space. However, if the imposed pressure at the tip was greater than the imbibition pressure plus the gradient, then entrapment would occur. The entrapment could remain as single pores or ganglia.

Several approaches to modeling one phase of fluid displacing another fluid can be taken. The Buckley-Leverett equation (1942) for saturated flow is often employed when the driving force causing flow is large, viscosities are comparable, and density differences

37

are small. The model was originally developed for porous media which is oil saturated and subjected to water flooding. The interface moves as a sharp front until breakthrough of the water phase occurs. Preferential flow then occurs through the channels where water has broken through and oil becomes entrapped within the porous media. For most problems, however, a true sharp front does not exist. The small variations in the pores cause the front to be perturbed about some mean value which is related to the velocity of the front, as shown in Figure 3-18 .
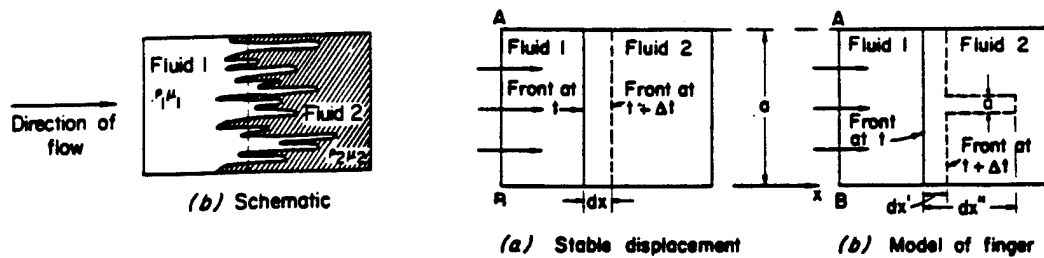
Figure 3-18. Sharp front behavior (from Bear, 1972)

As the front velocity increases, the fluids can become unstable causing fingers to form, as shown in Figure 3-19. The effects of the fingering phenomenon can be related to the mobility ratio:

$$M = \frac{\lambda_w}{\lambda_{nw}} = \frac{k_w \mu_{nw}}{k_{nw} \mu_w} \tag{3.13}$$

where:

k = relative permeability for each phase (L^2)

μ = dynamic viscosity (M/T^2)

38
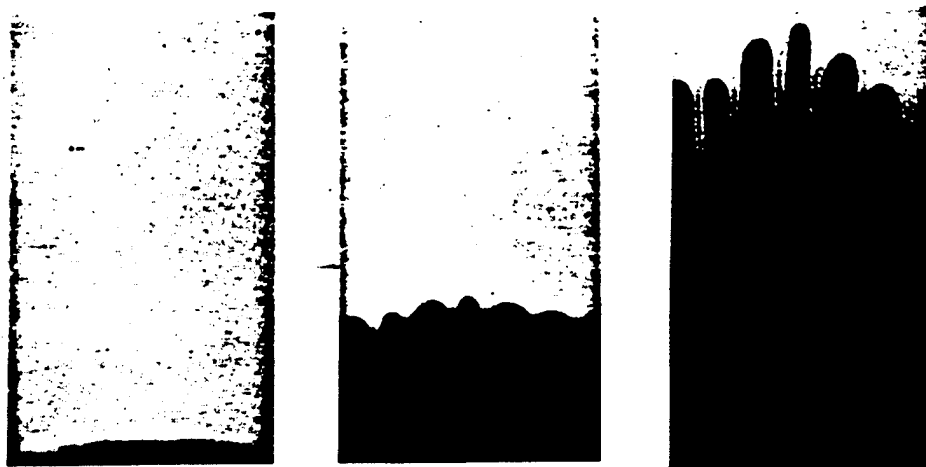
Figure 3-19. Finger formation (from Chuoke et al., 1959)

If the water mobility λ_w is greater than the NAPL mobility λ_{nw}, the flow becomes easier in the regions where the NAPL has been replaced by the more mobile water. The fluid velocity will tend to increase in these areas so that any initial irregularities in the displacement pattern are amplified. If the water mobility λ_w is less than the NAPL mobility λ_{nw}, then the irregularities in the displacement pattern will tend to be reduced.

When the density difference is large enough, gravity forces can be used to prevent fingering. If the displacing fluid has a density less than the NAPL and the displacement is in the downward vertical direction, the gravity forces tend to reduce the growth of any fingers of the displacing fluid. If the flow is in the upward vertical direction and the density of the displacing fluid is greater than the NAPL, then gravity forces will tend to

prevent finger growth. It has been shown that viscous fingering can be eliminated when the flow rate is less than some critical value. For a vertical displacement of a horizontal front, the mobility ratio can be used to derive a critical velocity given as:

$$v_c = \frac{g(\rho_w - \rho_{nw})}{(\frac{\mu_w}{k_w}) - (\frac{\mu_{nw}}{k_{nw}})}$$

(3.14)

The critical velocity and mobility ratio can then be used to evaluate potential instability of the front. Let V_D be the velocity at the tip of the finger and V_F be the velocity of the front then:

$$V_D - V_F = -\frac{k_1}{\phi \mu_1}[(\phi V_F(\frac{\mu_1}{k_1} - \frac{\mu_2}{k_2}) + g(\rho_1 - \rho_2)] = (M-1)(V_F - V_C)$$

(3.15)

Let $V_F > 0$ be vertically upward flow, then the following criteria can be found:

- If $\mu_2/k_2 < \mu_1/k_1$ (i.e., M <1) and $\rho_1 > \rho_2$; $V_C < 0$ and always, $V_D - V_F < 0$, the front is stable.

- If $\mu_2/k_2 < \mu_1/k_1$ (i.e., M < 1) and $\rho_1 < \rho_2$; always $V_C > 0$, but there are two possibilities: if $V_F > V_C$ the front is stable; if $V_F < V_C$ the front is unstable.

- If $\mu_2/k_2 > \mu_1/k_1$ (i.e., M > 1) and $\rho_1 > \rho_2$; the displacement is stable if $V_F < V_C$ unstable if $V_F > V_C$.

- If $\mu_2/k_2 > \mu_1/k_1$ (i.e., M > 1) and $\rho_1 < \rho_2$; we cannot have if $V_F < V_C$ because $V_C < 0$, and the front is always unstable.

These criteria can be used to develop an experiment such that sharp front behavior

40

is always produced and ganglia formation is prevented. In a fully water saturated sand column undergoing one-dimensional downward drainage; the drainage front is always stable since the lighter air is above the water. If another fluid such as Soltrol replaces the air, the front still remains sharp and stable. If the order of the fluids is reversed, however, the front may become unstable. In an air saturated column being infiltrated by Soltrol, Illangasekare et al. (1991) showed that the front remained sharp and stable; the viscosity of the Soltrol acted to stabilize the front. When the column is infiltrated by water or a low viscosity DNAPL, Held (1993) showed that the front was always unstable and fingers developed. The same column saturated with Soltrol and with water infiltrated will become unstable only if the critical velocity is reached.

Recent research by Carpaneto (1989) and Walser (1994) has shown that the critical velocity can be related to the shape of the meniscus formed at the interface of the two fluids, as shown in Figure 3-20. In case a, fluid 1 is the wetting phase, in case b, fluid 1 is the nonwetting phase.
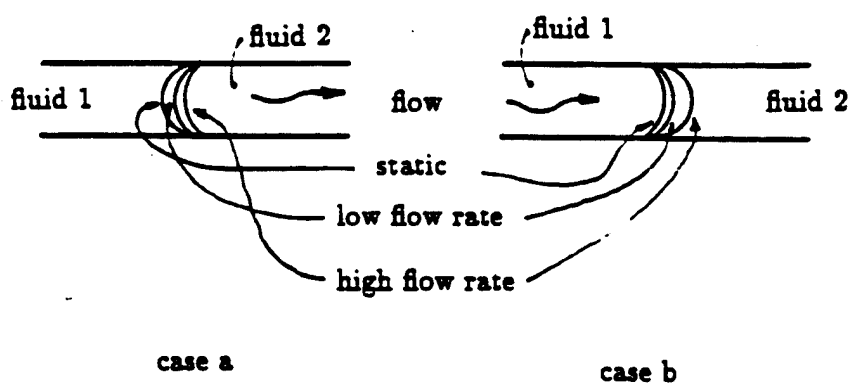
Figure 3-20. Meniscus shape as a function of flow rate (from Carpaneto, 1989)

41

The shape of the meniscus and, therefore, the capillary pressure is a function of the front velocity. Carpaneto (1989) found this to be the case when using the flow pump technique to measure suction saturation curves for multiphase flow. Carpaneto (1989) used automatic transmission fluid as the NAPL and observed that for vertical infiltration experiments, the front remained sharp and horizontal (no fingering) and that the effective capillary pressure was dependent upon the wettability characteristics of the water-oil-soil system and the imposed flow rate. Carpaneto (1989) was able to produce fingering behavior in both medium and fine sands at high flow rates, indirectly confirming the critical velocity concept. Campbell (1993) performed two-dimensional experiments using Soltrol and found that heterogeneities dominate the flow of NAPLs in a porous medium. The experiments indicated that it was not the individual material characteristics which mattered, but rather the relative differences between them.

The results of Carpaneto (1989) and Campbell (1993) were further validated by Walser (1994). In one- and two-dimensional experiments using homogeneous and layered sands, Walser (1994) found that the use of static capillary pressure distributions did not adequately predict residual saturations and entrapment of Soltrol. The two-dimensional experiments showed that vertical downward flow was essentially one-dimensional with little lateral spreading. Walser (1994) concluded that the experimentally found high saturations could not be explained under the assumption of static capillary pressure distribution, but required using steady state flow of very small flow rates. This indicated that the capillary pressure remains constant at some low value causing the unsaturated hydraulic conductivity to remain at a minimum fixed value. The macro-scale retention

was thus controlled by dynamic processes, and not static, as previously thought.

3.5 - Flow processes and entrapment in the centrifuge

In the previous sections, the governing equations for fluid flow and entrapment at normal Earth gravity were explored. The equations contain a gravity variable which will be used to transform the equations for a multi-g environment. In the centrifuge, a small scale model experiences the same stress field as a prototype would in a normal 1g gravity environment when the gravity-induced stresses are properly simulated. For an N-th scale model, a gravity field N times stronger than the prototype must be used.

The proper modeling of a prototype structure in a centrifuge depends on several well-known scaling relationships. Table 3-1 lists the commonly cited scaling relationships.

The scaling laws are conversion factors relating characteristics of the model to the prototype, usually derived using the Buckingham theorem (dimensional analysis), similarity of forces, or from the governing differential equations. When it is necessary to perform tests on a model to obtain information about prototype performance, the rules of similitude must be applied.

For physical models, three types of similarity need to be satisfied: geometric, kinematic, and dynamic. Geometric similarity is generally the easiest to satisfy and basically requires the model (subscript m) to be an exact scaled replica of the prototype (subscript p). The kinematic and dynamic similarity criteria are not unique and depend upon the problem of interest and will be addressed in subsequent chapters.

Table 3-1. Scaling relations (from Ko, 1988)

Quantity	Prototype	Model
Length	N	1
Area	N^2	1
Volume	N^3	1
Velocity	1	1
Acceleration	1	N
Mass	N^3	1
Force	N^2	1
Energy	N^3	1
Stress	1	1
Strain	1	1
Mass density	1	1
Energy density	1	1
Time (dynamic)	N	1
Time (diffusion)	N^2	1
Time (creep)	1	1
Frequency	1	N

For geometric similarity the following equations can be obtained:

Length: $N = \dfrac{l_p}{l_m}$ (3.16)

Area: $N^2 = \dfrac{l_p^2}{l_m^2}$ (3.17)

Volume: $N^3 = \dfrac{l_p^3}{l_m^3}$ (3.18)

where l is the length. The same soil will be used in the model as in the prototype, therefore, the following relationships can be derived:

Porosity: $\dfrac{\phi_p}{\phi_m} = \dfrac{\dfrac{V_{vp}}{V_{tp}}}{\dfrac{V_{vm}}{V_{tm}}} = \dfrac{N^3}{N^3} = 1$ (3.19)

Volummetric water content: $\dfrac{\theta_p}{\theta_m} = \dfrac{\dfrac{V_{wp}}{V_{sp}}}{\dfrac{V_{wm}}{V_{sm}}} = \dfrac{N^3}{N^3} = 1$ (3.20)

Saturation: $\dfrac{S_p}{S_m} = \dfrac{\dfrac{V_{wp}}{V_{vp}}}{\dfrac{V_{Wm}}{V_{vm}}} = \dfrac{N^3}{N^3} = 1$ (3.21)

where V is the volume and is valid for saturated and unsaturated flow and any porous media.

CHAPTER 4

SATURATED FLOW PROCESSES IN SANDS

4.1 - Objective and theory

The objective of the saturated flow through sands experiments is to verify the scaling relationship for the hydraulic conductivity and to find the upper limit of the Reynolds number for laminar flow.

The upper limit of the Reynolds number is of significance since Darcy's law is valid for laminar flow only and the theoretical scaling relationships are derived using this law. The Reynolds number is a criterion used to distinguish laminar from turbulent flow. For pipes, the critical R_e is about 2100 and the characteristic length l is the diameter of the pipe. In a porous medium, the d_{10} or d_{50} grain size is commonly used as the characteristic length. Bear (1972) states that, "for practically all cases, Darcy's law is valid as long as the Reynolds number based on average grain size does not exceed some value between 1 and 10" (pg 126).

Determining the maximum Reynolds number for laminar flow is a crucial issue for modeling flow problems in the centrifuge. As will be shown in the following section, the Reynolds number in a centrifuge model will be different from that of the prototype. However, if the flow is always laminar, then Darcy's law applies, and equality of the Reynolds number is not required. Figure 4-1 shows the relationship between the Reynolds number and the Fanning friction factor for porous media and delineates the

46

transition zone from laminar to turbulent flow. As long as the friction factor is a linear

function of the Reynolds number, the flow is laminar.
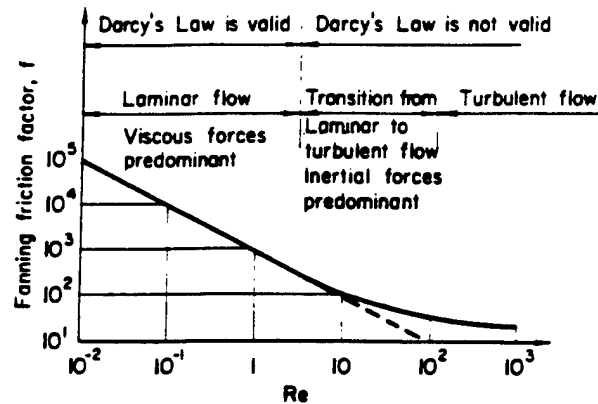
Figure 4-1. Schematic classification of flow through porous media (from Bear, 1972)

The Fanning friction factor used in Figure 4-1 is similar to the Moody friction

factor for pipe flow. The Fanning friction factor is given as:

$$f = \frac{2gdhR}{lv^2}$$

(4.1)

where:

g = acceleration (L/T^2)

dh = head loss (L)

R = hydraulic radius (L)

L = length (L)

v = velocity (L/T)

In the centrifuge, the velocity of the flow and hence the Reynolds number will be

47

increased compared to the prototype. The equations governing saturated fluid flow through a porous medium in a centrifuge has been theoretically derived by several researchers, but only three experimental investigations have been published to date. The first, by Cargill and Ko (1983) measured the outflow and pore pressures through a model of an embankment dam undergoing transient rise and fall of the headwaters. They used four different fine grained soils made from a mixture of sand and silts. They performed modified modeling of models tests using the same model for each g-level (N), and then scaled each model to the next g-level. Their results for the scaling of the flow rate and hydraulic conductivity ranged from 0.9N to 1.8N as opposed to the theoretical value of N, as seen in Table 4-1. Cargill and Ko (1983) did not evaluate the Reynolds numbers for their experiments but implicitly assumed laminar flow in all of the experiments.

Table 4-1. Results of Cargill and Ko (1983), Flow Rate and Permeability Scale Factors

Acceleration ratio, N	Original soil	Coarse soil	Same d_{10} soil	Same C_u soil	Theoretical value
1.5	1/1.1N	1/1.1N	1/1.1N	1/0.9N	1/N
2.0	1/1.3N	1/1.8N	1/1.2N	1/N	1/N
1.33	1/1.2N	1/1.4N	1/1.2N	1/1.1N	1/N

The second experiment by Goforth et al. (1991) was designed to specifically determine the scaling of the hydraulic conductivity. They used a fine grained silica sand with a d_{50} of 0.2 mm mixed with kaolinite in a falling head test. They found excellent agreement between the 1g and centrifuge experiments for the hydraulic conductivity, as shown in Figure 4-2, but they reported an upper limit Reynolds number for laminar flow of 0.2, an order of magnitude lower than that predicted by Bear (1972). They did not provide the data or include the Reynolds number calculation.

a. Comparison of centrifuge and   b. Comparison of permeability at
   1g bench tests   19.3 and 24.4 g's
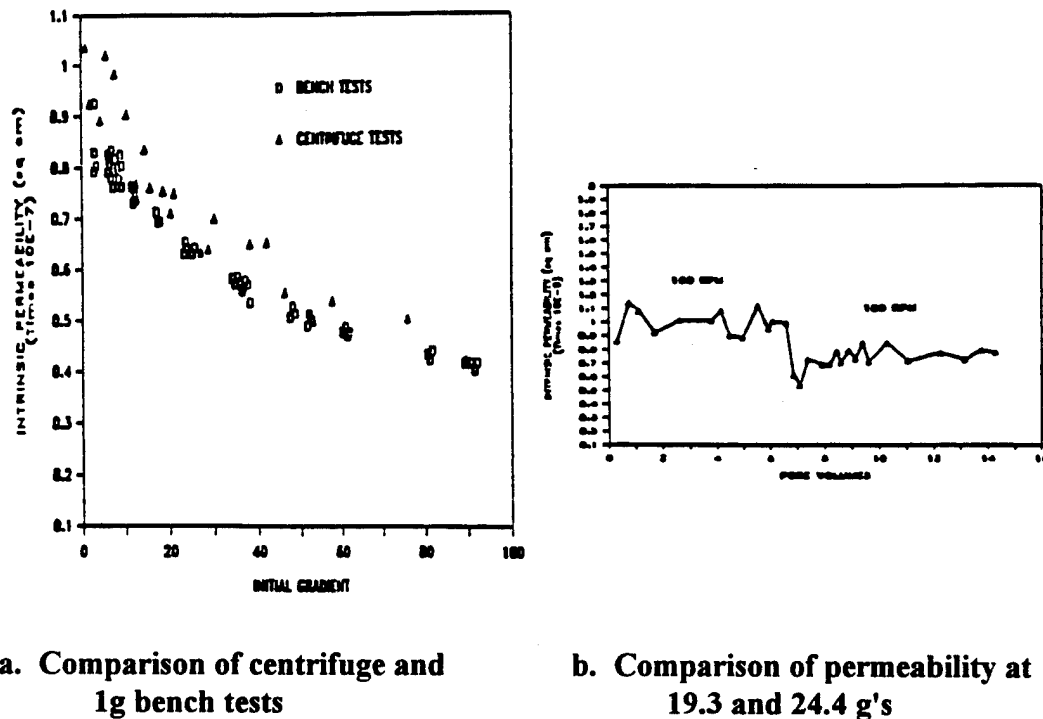
Figure 4-2. Goforth et al. (1991) saturated flow experimental results

Goodings (1994) looked at the fundamental issue of the Reynolds number. She used three uniformly graded materials: #30/#40 Ottawa sand with a d_{50} of 0.5 mm, copper

49

shot, and glass marbles and plotted the Reynolds number versus a friction factor. The

friction factor is given as:

$$F_f = \frac{iDgn^2}{v^2}$$

(4.2)

where:

i = gradient

D = grain size

g = gravity

n = porosity

v = velocity

In Figure 4-3, the plot of her data for all materials clearly shows the transition

from the laminar flow regime to the turbulent regime above a Reynolds number of 3 for

the Ottawa sand.
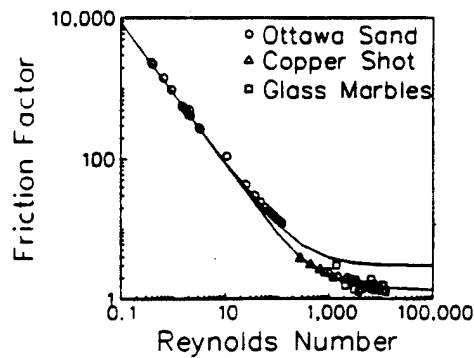
Figure 4-3. Goodings (1994) experimental results

Goodings (1994) used water as the test fluid and concluded that the scaling law

for the hydraulic conductivity was valid and the upper limit of the Reynolds number for the Ottawa sand was between 3 and 11.

4.2 - Saturated flow processes in the centrifuge

For saturated flow, the Laplace equation (3.7) is satisfied, which implies that Darcy's law (Equation 3.4) is valid. Within Darcy's law the hydraulic conductivity term is a function of the gravity, as seen by Equation (3.5). Saturated flow must still meet the geometric, kinematic, and dynamic criteria, as presented in Section 3.6, and by using the same porous media for all experiments, the geometric criteria for the porosity (Equation 3.19) is met. The kinematic and dynamic criteria must now be derived.

An analysis of the governing equations for fluid flow has been presented by Cargill and Ko (1983) using the Buckingham's π-theorem. Buckingham's π-theorem states that if an equation is dimensionally homogeneous or does not depend on a particular system of units, then it can be reduced to a relationship among a complete set of dimensionless groupings or π terms. For a complete similarity between a model and the prototype, the corresponding π terms must be equal. For kinematic similarity, the motion relationships in the model and prototype must be proportional. The total quantity of flow through a cylindrical soil sample in one-dimensional flow is affected by the mass density of the fluid, the difference in potentials measured in head ΔH at the top and bottom of the sample, the length of the column l, the area of the column A, the viscosity of the fluid, μ, the gravitational acceleration g, and the permeability of the soil k. Expressing the flow rate q as a function of the variables gives:

$$q = f(\rho, \Delta H, l, A, \mu, g, k)$$

There is an equation of the form:

$$f'(q, \rho, \Delta H, l, A, \mu, g, k) = 0$$

The flow rate in the model is related to the flow rate in the prototype by one of the following:

$$q_p = \frac{\rho_m l_m k_p^{0.5} \mu_p \Delta H_p}{\rho_p l_p k_m^{0.5} \mu_m \Delta H_m} q_M \qquad (4.3)$$

which for constant ρ, μ, and k can be simplified to:

$$q_p = \frac{l_m \Delta H_p}{l_p \Delta H_m} q_m \qquad (4.4)$$

which implies that if the flow rate is mainly dependent upon the ratio of $\Delta H/l$, then the flow rate in the model is the same as the flow rate in the prototype. If the flow rate is mainly dependent upon the cross-sectional area, the following grouping is found:

$$q_p = \frac{\rho_m k_m^{0.5} A_p \mu_p}{\rho_p k_p^{0.5} A_m \mu_m} = \frac{A_p}{A_m} q_m = N^2 q_m \qquad (4.5)$$

which states that the flow rate in the prototype will be N^2 times that measured in the model. If the flow rate is mainly dependent upon the gravity level, the following grouping is found:

$$q_p = \frac{k_p^2 g_p \rho_p \mu_m}{k_m^2 g_m \rho_m \mu_p} q_m = \frac{g_p}{g_m} = \frac{q_m}{N} \qquad (4.6)$$

which states that the flow rate in the model should be N times that of the prototype.

The hydraulic conductivity K is assumed to be dependent upon the intrinsic permeability of the soil k, velocity of the fluid flow v, mass density of the fluid ρ, viscosity of the fluid μ, and the acceleration g. The hydraulic conductivity of the soil can also be expressed in π terms:

$$K = f(v, g, k, \mu, \rho)$$

or

$$f(K, v, g, k, \mu, \rho) = 0$$

Cargill and Ko (1983) found that the hydraulic conductivity could be expressed as:

$$K_p = \frac{g_p k_p \rho_p \mu_m}{g_m k_m \rho_m \mu_p} K_m = \frac{K_m}{N} \qquad (4.7)$$

which for centrifuge testing of the same materials states that the hydraulic conductivity of the model should effectively be N times greater than that of the prototype.

Similarly, assuming that the velocity is dependent upon the hydraulic conductivity, a grouping of:

$$v = f(g, k, \mu, \rho, dh/dl)$$

and since dh/dl is already dimensionless:

$$f(v, g, k, \mu, \rho) = 0$$

and similar to K:

53

$$v_p = \frac{g_p k_p \rho_p \mu_m}{g_m k_m \rho_m \mu_p} v_m = \frac{v_m}{N} \qquad (4.8)$$

which for centrifuge testing of the same materials states that the velocity of the model should effectively be N times greater than that of the prototype. One might have guessed the model velocity should be N times greater than the prototype since the velocity is a function of the hydraulic conductivity, but the non-dimensional analysis for the velocity and hydraulic conductivity independently confirms the relationship. There are, then, several possible scaling factors, and the appropriate scaling for the flow rate, hydraulic conductivity, and velocity must be determined from the experimental data.

For dynamic similarity, the forces acting on the element must have the same ratios, and only those forces which impact the problem need to be modeled (Croce et al., 1984). Forces relevant to saturated steady state flow are:

F_W - forces due to weight

F_p - forces due to pressure

F_V - forces due to viscosity

F_σ - forces due to surface tension

F_I - inertial forces

F_S - seepage forces

As with kinematic similarity, for the complete similarity between the model and prototype, the corresponding π terms must be equal:

$$\pi_p = \pi_m \qquad (4.9)$$

$$\pi_p = \pi_m \qquad (4.9)$$

Dynamic similarity requires those forces which have a significant bearing on the problem to have constant ratios such that:

$$\frac{F_{Wp}}{F_{Wm}} = \frac{F_{Pp}}{F_{Pm}} = \frac{F_{Vp}}{F_{Vm}} = \frac{F_{Tp}}{F_{Tm}} = \frac{F_{Ip}}{F_{Im}} = \frac{F_{Sp}}{F_{Sm}} \qquad (4.10)$$

A key grouping in fluid flow is the Reynolds number where that number is a ratio of the inertial force to the viscous force. The Reynolds number at 1g is:

$$R_e = \frac{vl\rho}{\mu} \qquad (4.11)$$

where:

R_e = a dimensionless number

v = the average interstitial velocity (L/T)

l = the characteristic length (L)

ρ = the fluid density (M/L^3)

μ = the dynamic viscosity (M/LT)

In centrifuge modeling, the Reynolds number is usually expressed as the dimensionless ratio:

$$R_e = \frac{F_{Ip}}{F_{Vp}} = \frac{F_{Im}}{F_{Vm}} \qquad (4.12)$$

Since the Reynolds number is a function of the fluid velocity, a centrifuge model and the prototype will not have the same Reynolds number. However, as long as the

Reynolds number is less than 1, laminar flow occurs, Darcy's law is valid, and the model and the prototype do not require equality of the Reynolds number. The Reynolds number constrains the maximum g-level for which a porous medium can be used for laminar flow. Rearranging Equation (4.11), substituting Equation (4.8) for the velocity, and solving for the maximum g-level using #70 sand and water gives:

$$N_{max} = \frac{Rev}{Kid_{10}} = \frac{(1)(0.01)}{(0.0116)(1)(0.02)} = 43g's \tag{4.13}$$

Using Equation (4.13) with the same gradient and R_e, for #30 sand gives a maximum N of 3.8 and for a clay a maximum N of around 10^{11}. For coarse materials, the gradient should be restricted for testing at higher g-levels. For the #30 sand tested at 100 g's, the maximum gradient for which laminar flow is ensured is 0.38. While this may seem restrictive, it should be noted that in many geotechnical problems, the gradients are well below 1. Because the gradient in the centrifuge models is the same as in the prototype, the stated limit is not very restrictive. The use of prototype materials in the model and the gradient must be carefully selected, however, to ensure the applicability of the scaling laws.

A method to ensure independent confirmation of the experimental results is to use different porous media and fluid combinations to vary the hydraulic conductivity and viscosity and then compare the experimental results to theoretical results. For homogeneous sands, the intrinsic permeability k is a function of the soil medium only. The intrinsic permeability k can be related to the hydraulic conductivity by:

$$k = \frac{K\mu}{\rho g} \qquad (4.14)$$

where:

k = the intrinsic permeability (L^2)

K = the hydraulic conductivity (L/T)

μ = the dynamic viscosity (M/LT)

ρ = the density (M/L^3)

g = gravity (L/T^2)

Tests using the same sand but different fluids can then be compared using:

$$\frac{K_w}{K_{oil}} = \frac{\mu_{oil}\rho_w}{\mu_w\rho_{oil}} = \frac{\nu_{oil}}{\nu_w} \qquad (4.15)$$

Layered sand systems can also be examined by converting the heterogeneous layered system into an equivalent homogeneous layer using:

$$K_z = \frac{L}{\dfrac{L_1}{K_1} + \dfrac{L_2}{K_2} + .. + \dfrac{L_n}{K_n}} \qquad (4.16)$$

A significant advantage of the centrifuge for flow problems is the time factor. Using Equation (3.15) and Equation (4.5), a time ratio can be found as:

57

$$\text{Time:} \quad \frac{t_p}{t_m} = \frac{\dfrac{l_p}{q_p}}{\dfrac{l_m}{q_m}} = \frac{\dfrac{l_m N}{q_m}}{\dfrac{l_m}{q_m}} = N^2 \qquad (4.17)$$

The time ratio of Equation (4.17) compares with the diffusion time ratio of table 3-1. There are actually three possible time ratios, and all three ratios may have some impact on the problem of interest. For flow problems where seepage is the dominant process, Equation (4.17) has been found to be the correct time ratio (Cargill and Ko, 1983).

This feature makes the centrifuge very attractive for modeling contaminant-type problems. For example, a pollutant introduced into a groundwater aquifer can require several months to obtain the concentration breakthrough curve at field-scale distances. Using a centrifuge, an Nth scale model of the aquifer can be accelerated to a g-level N, and the transport process will be accelerated by N^2. As an example, a 1/50th scale model spun to 50 g's for one day which will simulate the prototype behavior of:

$$t_p = \frac{(1 day)(50)^2}{(365 days/year)} = 6.85 \ years \qquad (4.18)$$

This shows the applicability of the centrifuge to physically model long-term problems in a short period of time.

There are then several variations of the saturated flow equations using different homogeneous sands, layered sands, and different fluids which should be related to the

imposed g-level. For one-dimensional saturated flow, measurement of the flow rate and the head loss will provide the required data to verify the scaling laws.

4.3 - Modified constant head test

There are two common methods used to measure hydraulic conductivity K: the constant head test and the falling head test. Figure 4-4 shows the two types of tests. Goforth et al. (1991) conducted hydraulic conductivity experiments using the centrifuge with a falling head test and experienced difficulty obtaining accurate results due to the sloshing of the fluid within the reservoir. To avoid the problems experienced by Goforth et al., the constant head test was selected for this research and the centrifuge and associated equipment were modified.
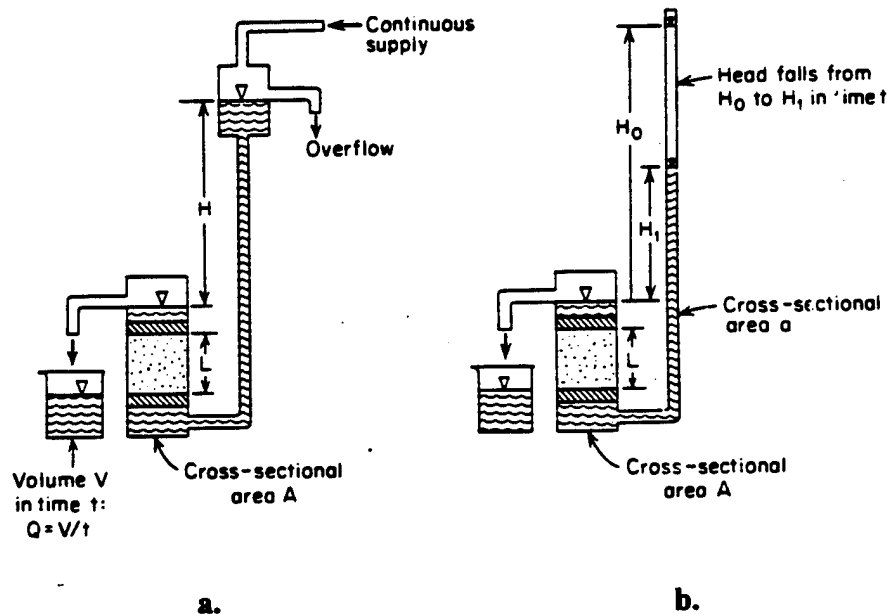
Figure 4-4. (a) Constant head and (b) falling head permeameters (from Freeze and Cherry, after Todd 1959)

The flow equation for a constant head test is given as:

$$K = \frac{QL}{AH}$$ (4.19)

where:

K = the hydraulic conductivity (L/T)

Q = the steady volummetric flow rate (L^3/T)

L = the length of the column (L)

A = the cross sectional area (L^2)

H = the constant-head differential (L)

In the centrifuge, pressure transducers will be used to measure the steady volummetric flow rate and the head differential. Equation (4.19) will be used to calculate the hydraulic conductivity for the saturated flow experiments.

4.4 - Experimental materials

There are constraints imposed on the selection of the materials based upon the size of the model samples, ability of the pressure transducer membranes to measure heads, toxicity of the organic contaminant, and measurement of the parameters of interest such as flow rates and pore pressures. The materials used for this experimental program have been standard laboratory materials for the past several years and are well categorized. Table 4-2 is a compilation of various laboratory sand characteristics; over the last five years the sand supplier has changed as well as the sand compositions. Figure 4-5 are the gradation curves for the standard laboratory sands. Figures 4-6 and 4-7 are the suction

saturation and relative permeability curves for the #30 and #70 sands.

Table 4-2. Hydraulic conductivity data

Sand	K (cm/s)	d_{50} (mm)	From
#8	1.2	1.5	Lab
#16	0.8		Ramsey (1992)
#16	0.43	0.88	Lab
#30		0.35	Walser (1994])
#30	0.145	0.49	Lab
#30	0.122	0.41	Mapa (1994)
#70		0.19	Held (1991)
#70	0.024	0.20	Lab
#70		0.185	Held (1993)
#70	0.017		Walser (1994)
#70	0.00997	0.18	Mapa (1994)
#125	0.007	0.10	Held (1991)
#125		0.103	Held (1993)
#125	0.00984		Walser (1994)
#F75	0.005		Stadler (1994)
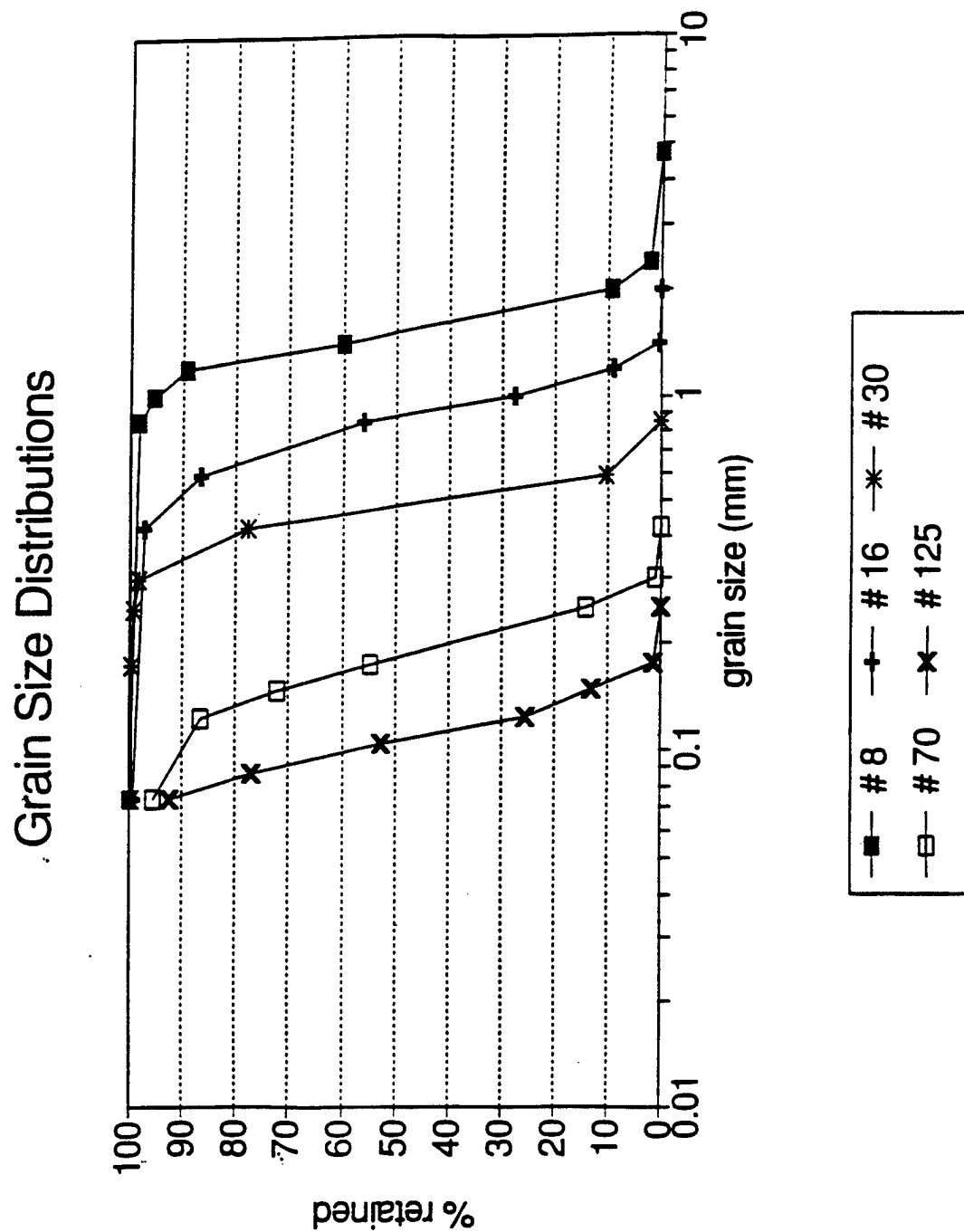
Figure 4-5. Gradation curves

62
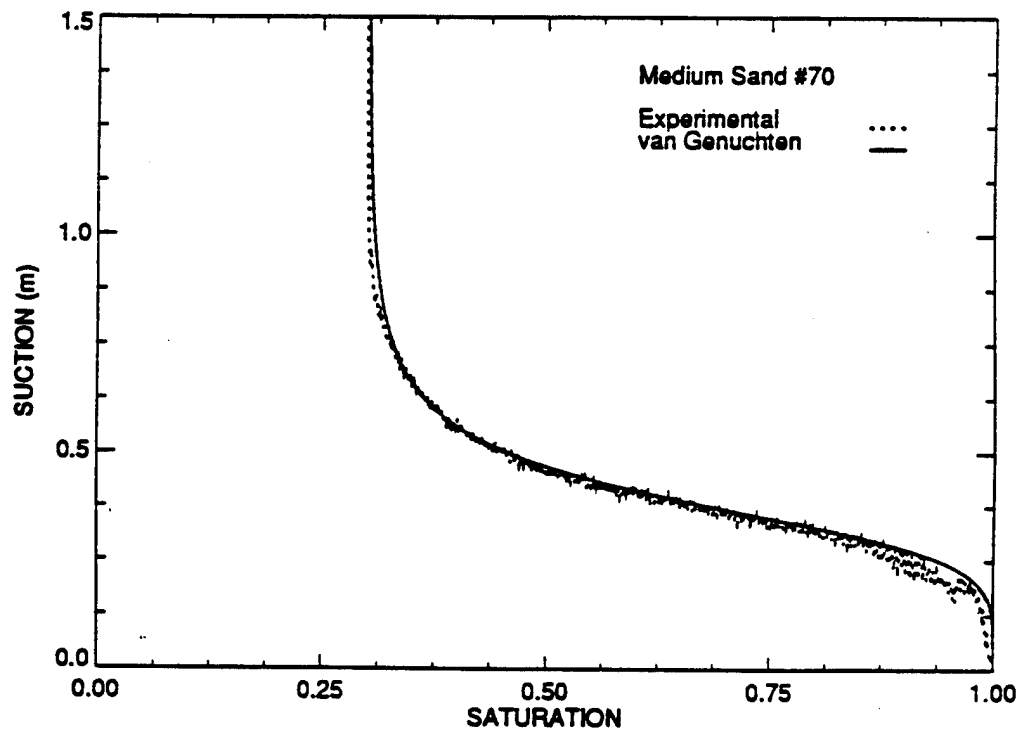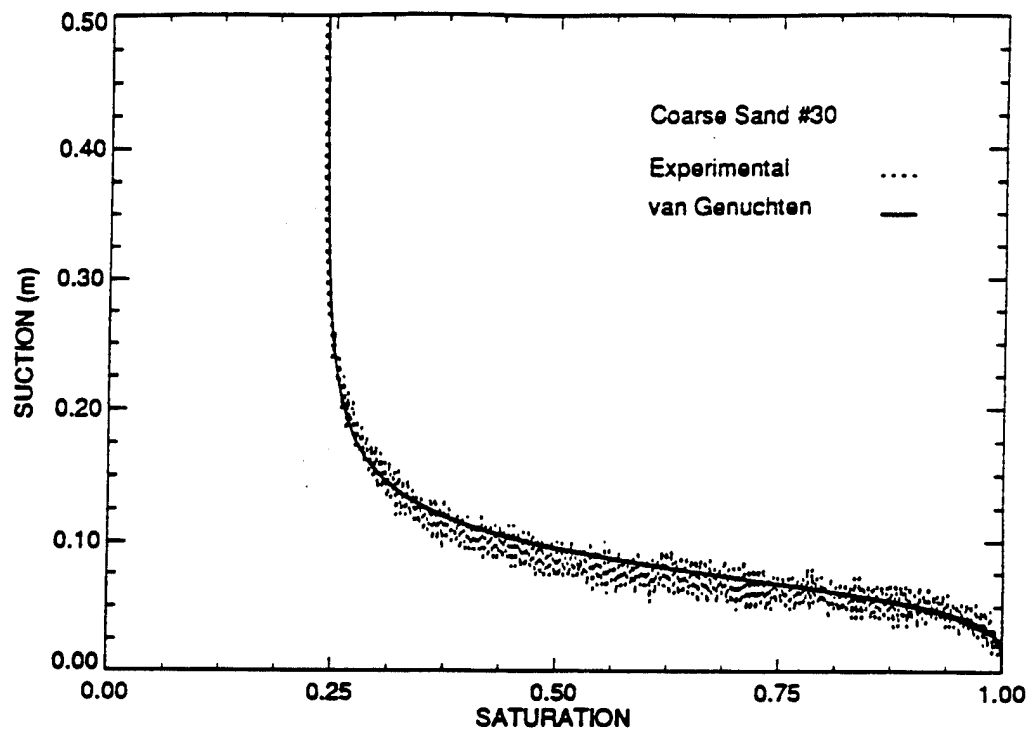
Figure 4-6. Suction-saturation curves for #30 and #70 sand (from Manna, 1991)

63
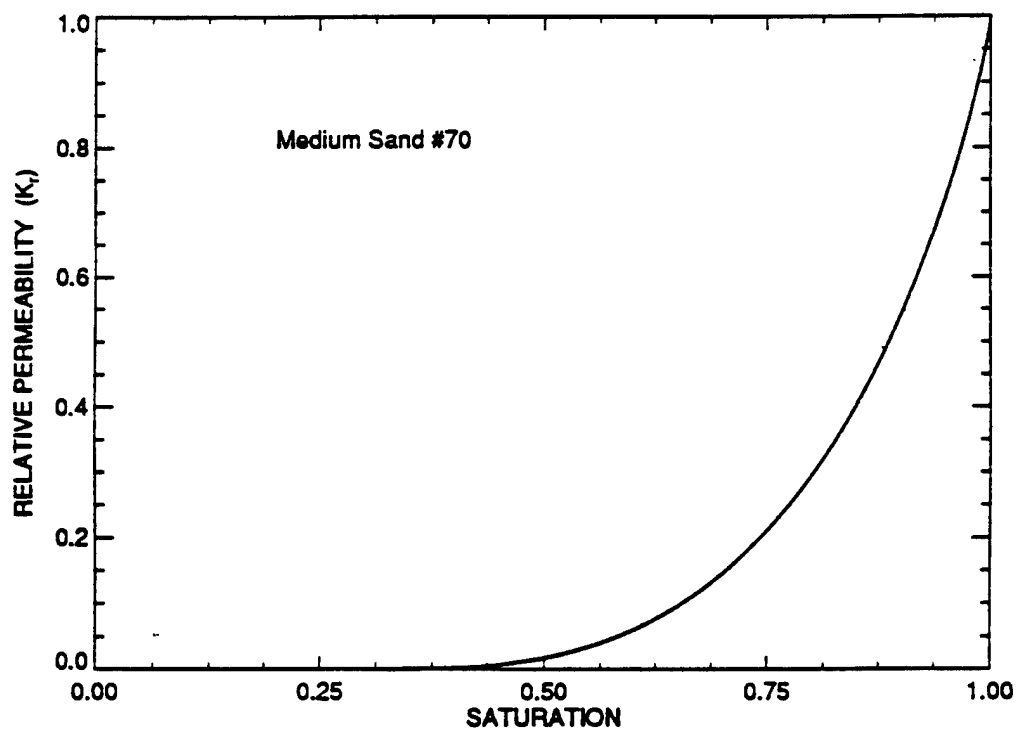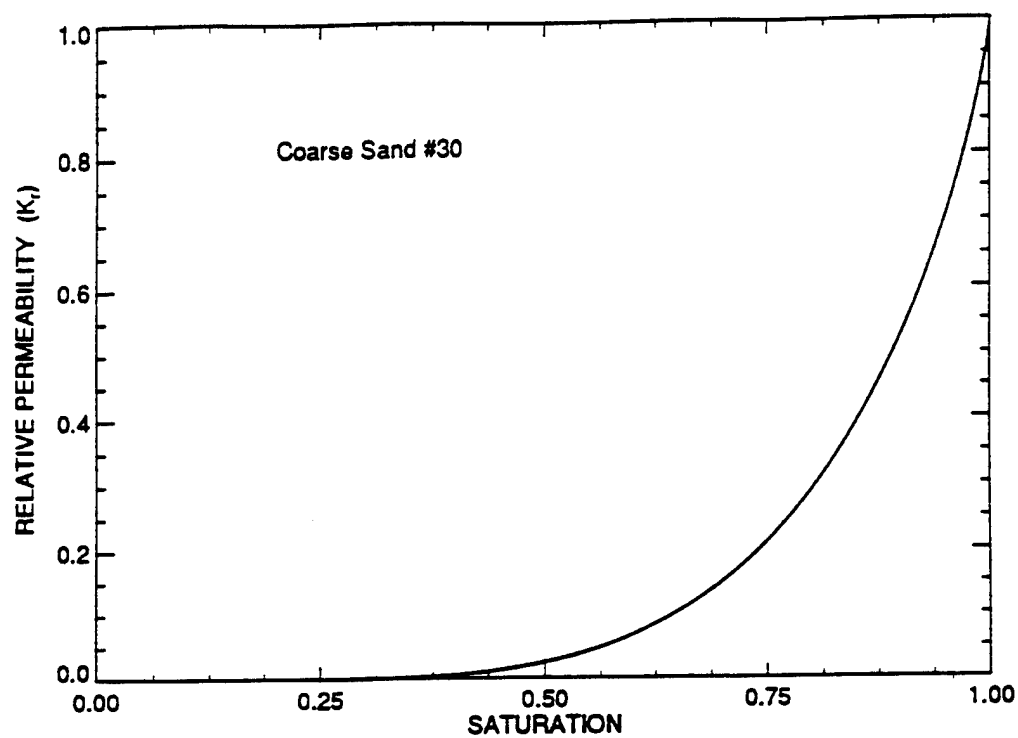
Figure 4-7. Relative permeability curves for #30 and #70 sand (from Manna , 1991)

Due to the volatility and hazardous nature of fuel oils and solvents, selecting an organic fluid for an experimental program that will exhibit the desired characteristics of most fuels or solvents without being volatile or toxic is desirable. A solvent manufactured by Phillips Petroleum Company, called Soltrol 220, will be used in this experimental program. Maximum exposure times and toxicity data are provided in the manufacturer's Material Data Safety Sheet (MSDS) for Soltrol, located in the Porous Media lab. Soltrol is an isoparaffinic solvent comprised of C13 through C17 hydrocarbons. The material properties are listed in Table 4-3.

Table 4-3. Soltrol physical data (from Phillips Petroleum Company)

Appearance: Colorless liquid

Odor: Mild

Vapor pressure: 0.004 psia (0.2 mm Hg) at 77°F

Vapor Density (Air = 1): >1

Solubility in water: Negligible

Specific gravity (Water =1): 0.809 at 60/60°F (15°C)

Percent Volatile by volume: 100

Evaporation rate (Butyl Acetate = 1): <1

Kinematic viscosity: 6.12 centistokes

Surface tension: 27 dynes/cm

Automate Red Dye (1-iodoheptane), manufactured by Morton International is often added to the Soltrol to make viewing the Soltrol-water interface easier. The dye does not affect any of the properties of the Soltrol (i.e., density, interfacial tension, and viscosity). Unlike water, the viscosity of Soltrol is highly temperature dependent. For systems where water and Soltrol are present, the viscosity ratio is also temperature dependent, as shown in Figure 4-8.
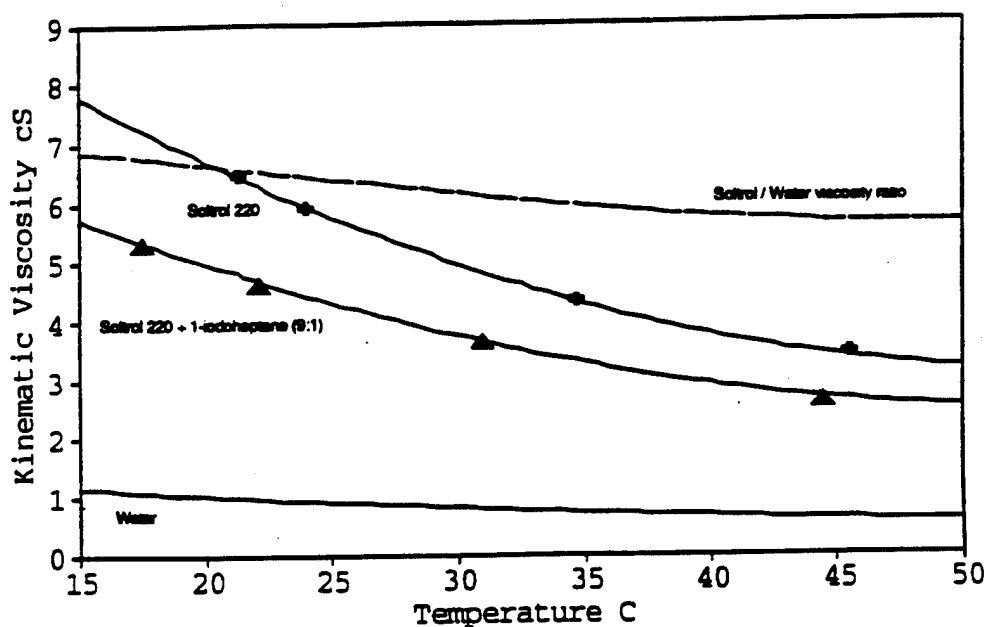
Figure 4-8. Kinematic viscosity of Soltrol vs temperature (from EPA, 1994)

4.5 - Centrifuge set-up

The permeameter cell (flexible or rigid wall) was placed on the centrifuge basket and the cell connected to the multi-channel data acquisition system (MDAS), constant head source, and high pressure air line (flexible only). From the constant head source, the

system was configured to force the fluid to flow from the bottom to the top of the sample. Figure 4-9 is a schematic of the constant head source and soil sample in-flight.
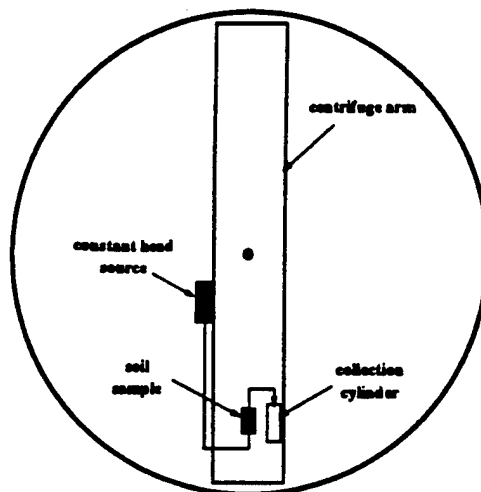
Figure 4-9. Schematic of constant head source and soil sample

Figures 4-10 and 4-11 are schematics of the flexible wall permeameter on the centrifuge basket. For the flexible wall permeameter, a constant confinement cell pressure of 30 psi of air was kept on the sample. The sand samples were compacted in three layers using a 500 g weight dropped twenty times from a one centimeter height for each layer. The head measurement ports were the standard ports located at the top and bottom porous stones and connected to the Validyne pressure transducer.
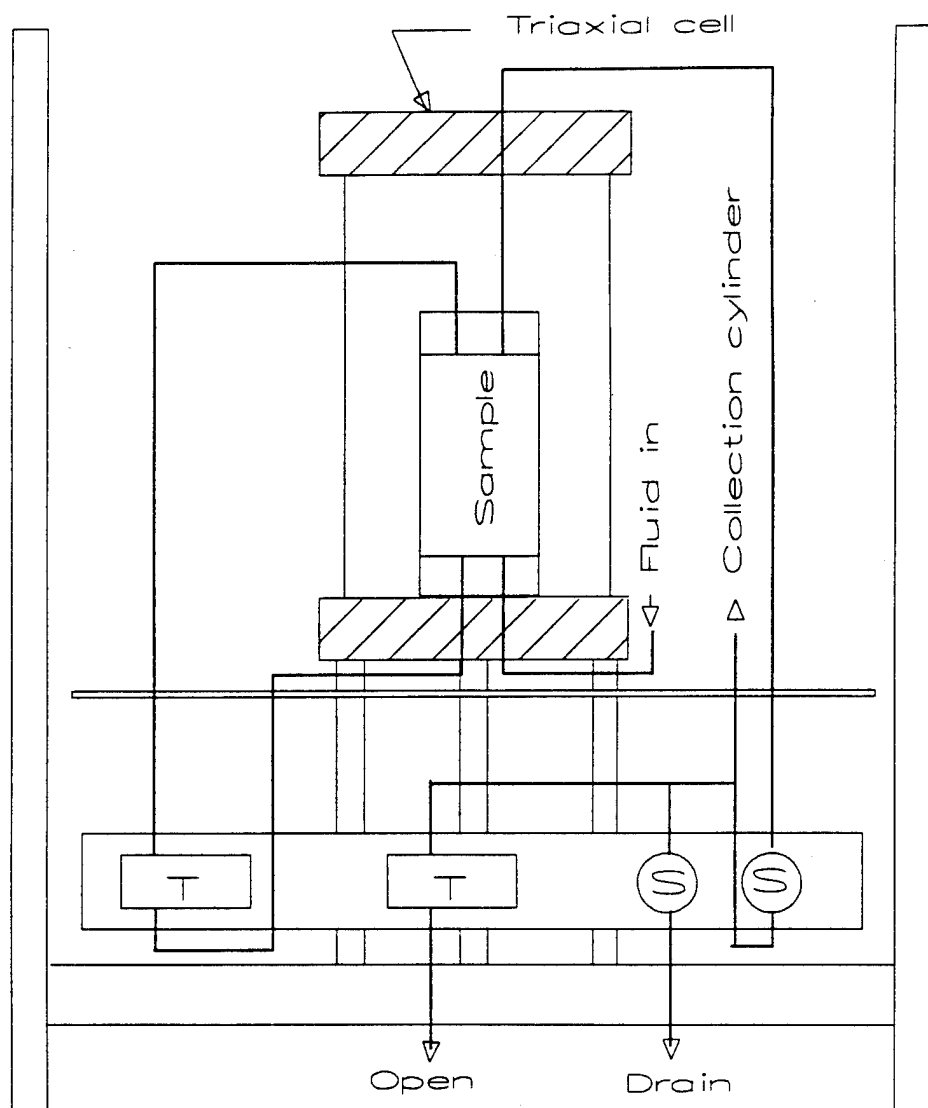
Figure 4-10. Flexible wall permeameter, front view

68
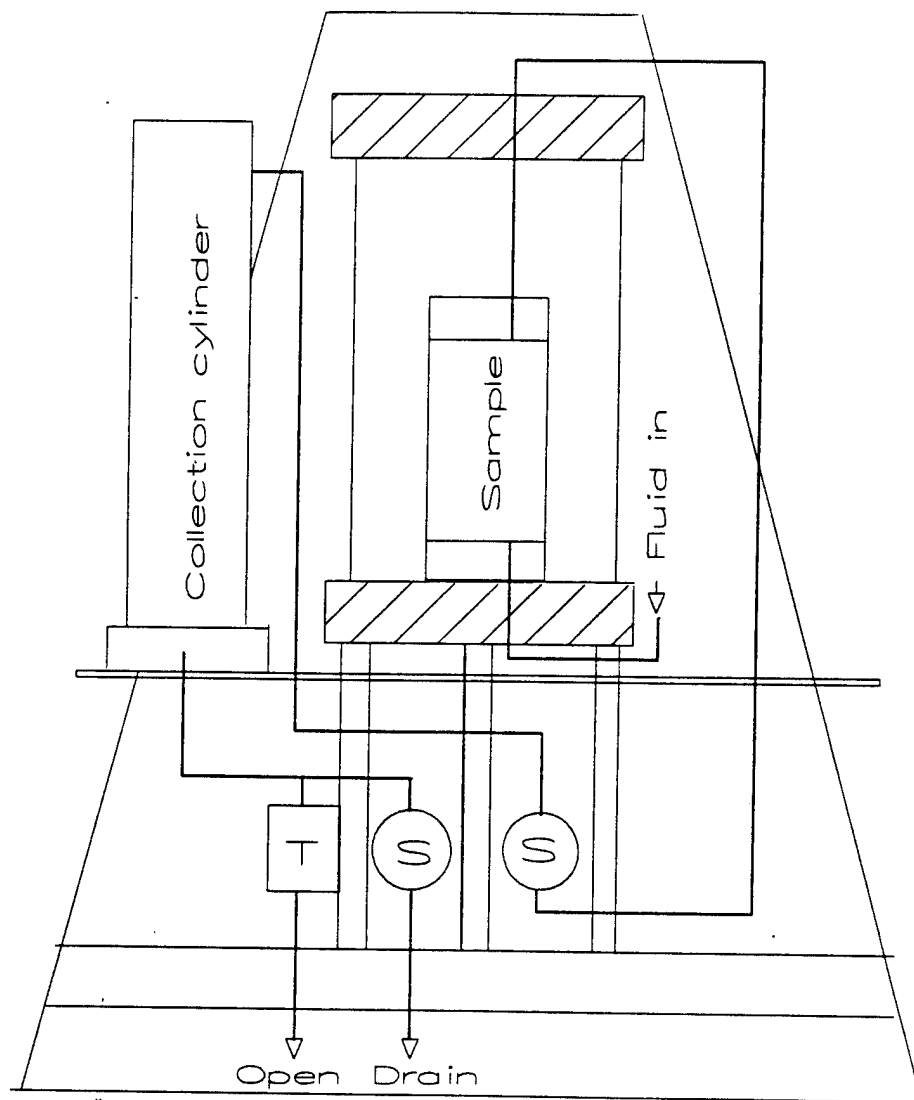
Figure 4-11. Flexible wall permeameter, side view

Figure 4-12 shows the rigid wall permeameter on the centrifuge basket. The plexiglass column had a 4" outside diameter (OD) and was 1/4" thick, with three 1/4" steel rods connecting the top and bottom aluminum end caps. Head measurement ports were located on the sides and connected to the Validyne pressure transducer.
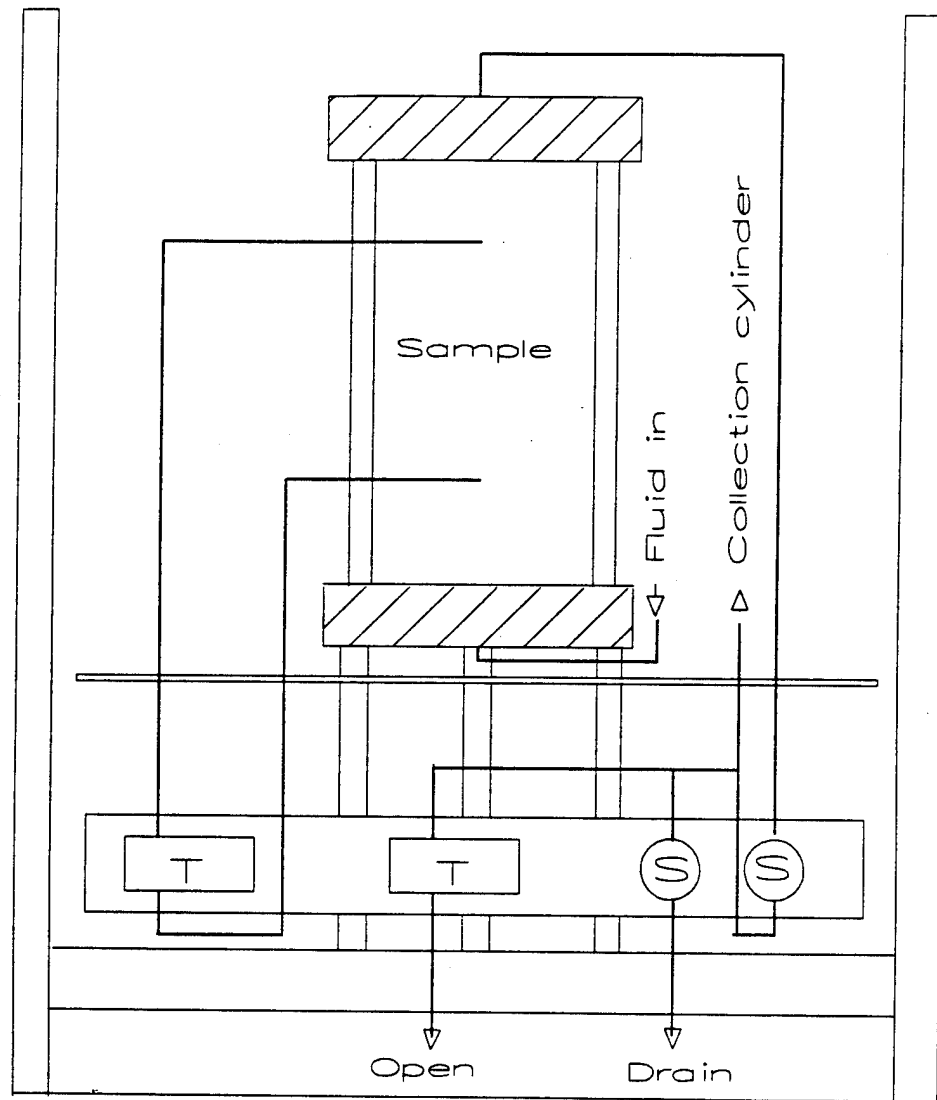
Figure 4-12. Rigid wall permeameter

To run the experiment, the centrifuge was brought to the appropriate RPM. The MDAS was zero referenced and the data collection started. The MDAS ran for 30 seconds without flow to ensure a reliable zero reference was obtained. After 30 seconds, the solenoid valve controlling the flow was opened. Most tests for water were run for 300 seconds; at higher g-levels, they did not require as long a time period. For Soltrol and Metolose, because of their higher viscosities, longer times were required. The MDAS data files were then imported into a Quattro Pro spreadsheet where the data manipulation was performed. Flow rate and head across the sample were plotted, as shown in Figure 4-13.
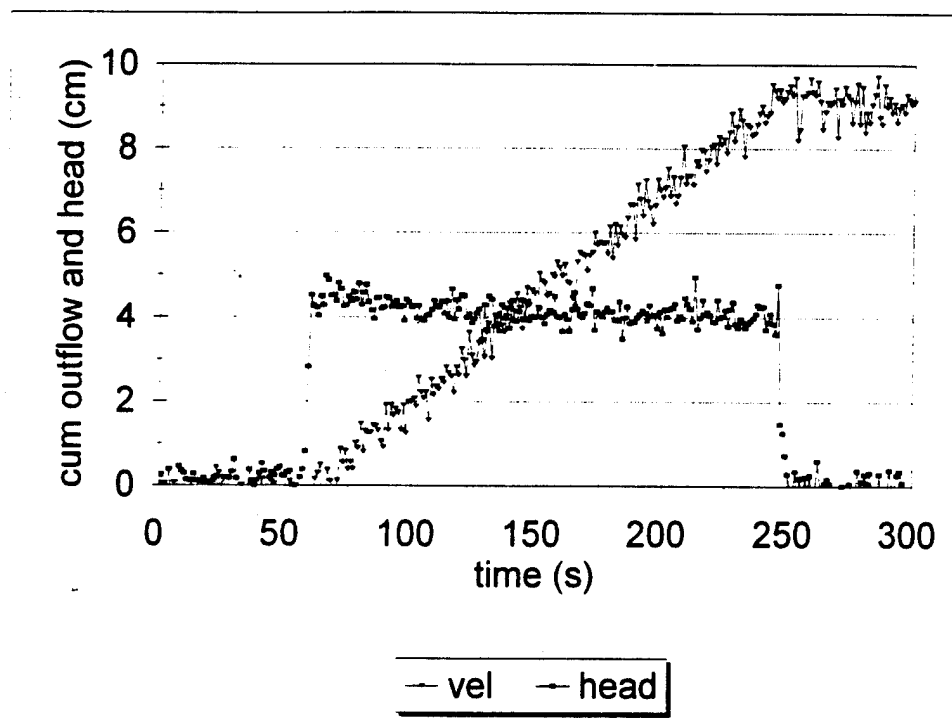
Figure 4-13. Typical velocity and head measurement

The initial portion shows the zero reference, and at the instant the solenoid valve is opened, the instantaneous jump occurs in the head measurement and flow begins. The flow and head data points show the normal noise, but the trend is very linear. The velocity is calculated using the cumulative outflow versus time with linear regression. Since the test is really a falling head test, the head curve displays a slight downward trend. The middle portion of the curve is averaged to give a head differential value. Values for the measured velocity and head were used to calculate the hydraulic conductivity, Darcy velocities, and Reynolds numbers.

4.6 - Head loss distribution through the system

To ensure the head loss measured through the sands controls the flow, the head loss distribution through the system of tubing, valves, and manifolds was measured. Head loss in a system varies depending upon the roughness of the tubing, number of sharp corners or edges, number of 90 degree bends, etc. To limit head losses through these areas, sharp corners were rounded and a total of only three 90 degree bends were used. Four pieces of tubing were required for connections and each length was kept to a minimum; the longest piece of tubing was 12 cm long.

The constant head source supplying the fluids was a plastic bottle which reduced to a standard Swagelock fitting at the top. Plastic tubing went from the Swagelock fitting directly to the inlet manifold. The outlet manifold tubing connected directly to the constant head collection cylinder. Since the highest heads were at the inlet manifold side, the highest percentage of head loss is expected to occur near the entrance.

To determine the head loss distribution, a manometer board was used to measure the fluid heights at several system locations: 1) at the supply constant head source, 2) in front of the inlet manifold, 3) behind the inlet manifold, 4) in front of the outlet manifold, 5) behind the outlet manifold, and 6) at the exit constant head source. Two types of tests were run: one test with the constant head source connected to the plastic bottle in-line and one test with the constant head source connected directly to the inlet manifold. The tests measured head loss through the bottle and the system. The 1g tests were run with the head source connected to the plastic bottle in-line while the centrifuge tests were run using the plastic bottle as the constant head source. Figure 4-14 is the head loss distribution in the system for the #F75 sand with the head source connected to the bottle. Figure 4-15 is the head loss distribution in the sand with the head source connected directly to the inlet manifold.

Similar results were obtained for the #30 and #70 sands. As expected the majority of the head loss occurred through the inlet manifold and sand sample. Higher head losses occur in the inlet manifold, but the majority of the head loss still occurred in the inlet manifold and the sand sample. Overall, between 40 and 60 percent of the available head is used getting the water to the sand, and 30 to 50 percent head loss occurred across the sand, with minor head losses in the rest of the system.
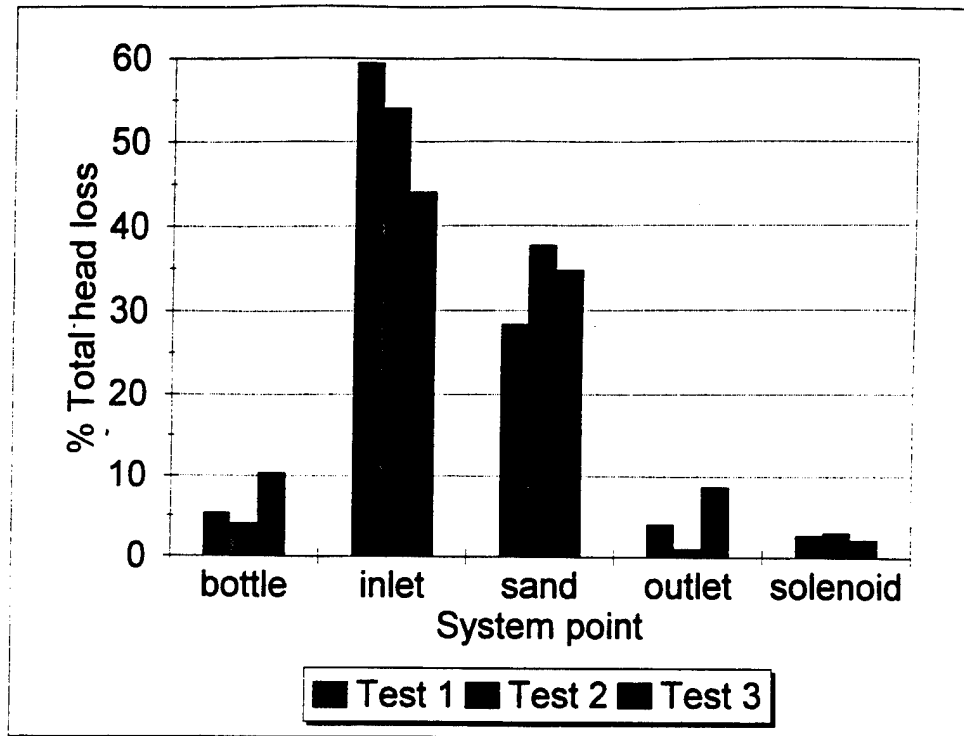
Figure 4-14. Head loss distribution in #F75 sand with bottle in-line
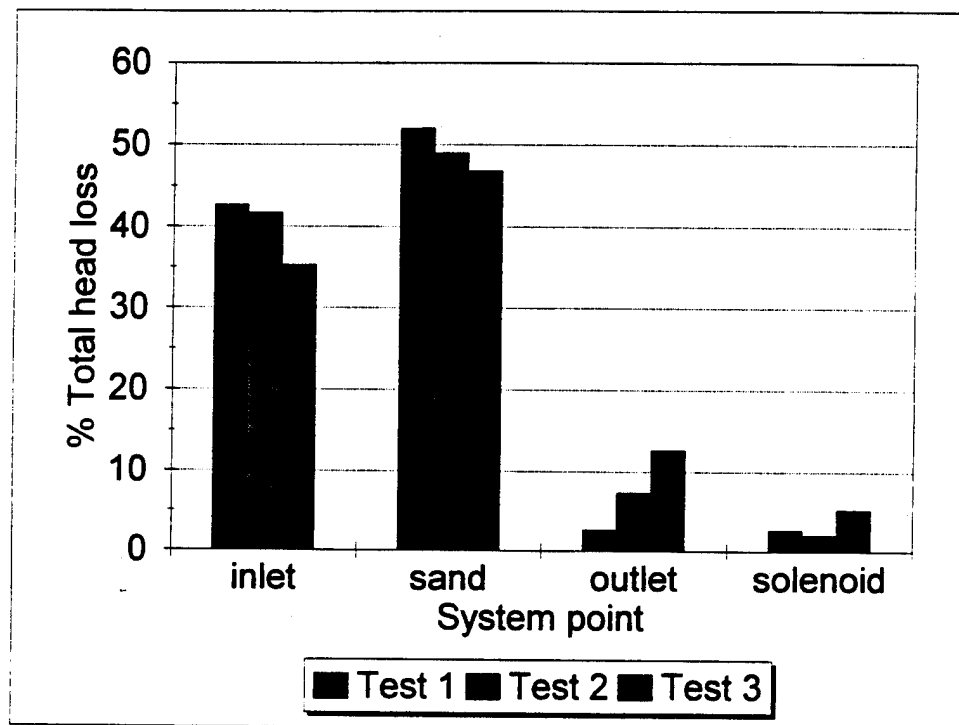
Figure 4-15. Head loss distribution in #F75 sand with direct connection

74

4.7 - Viscosity and density

Viscosity and density are independent of gravity and therefore should be independent of any imposed centrifuge gravity levels. The density can be shown to be a constant by use of the transducer calibration factors. Figures 4-16 and 4-17 show the master transducer calibration curves for water and Soltrol. The pressure transducers measure the deflection of a membrane due to a pressure difference. For the collection cylinder transducers, one pressure port is connected to the bottom of the collection cylinder and the opposite port is open to the atmosphere. Therefore, for any given level of fluid and g-level, the output voltage is only dependent upon the density of the fluid. The calibration constants for each membrane then relate the densities by:

$$\frac{C38_{water}}{C38_{Soltrol}} = \frac{84.67}{104.63} = 0.809 \tag{4.20}$$

and

$$\frac{C44_{water}}{C44_{Soltrol}} = \frac{230.98}{289.91} = 0.797 \tag{4.21}$$

which compare to the value of 0.809 from Table 4-3. The #44 transducer membrane is much stiffer than the #38 transducer membrane and therefore not as sensitive at low g-levels as the #38. The kinematic viscosity is dependent upon the density, and the hydraulic conductivity is dependent on the viscosity. Therefore the viscosity and hydraulic conductivity ratio of Equation (4.15) can be used to validate that the viscosity remains constant. All tests were performed at 18° C plus or minus 1° C.
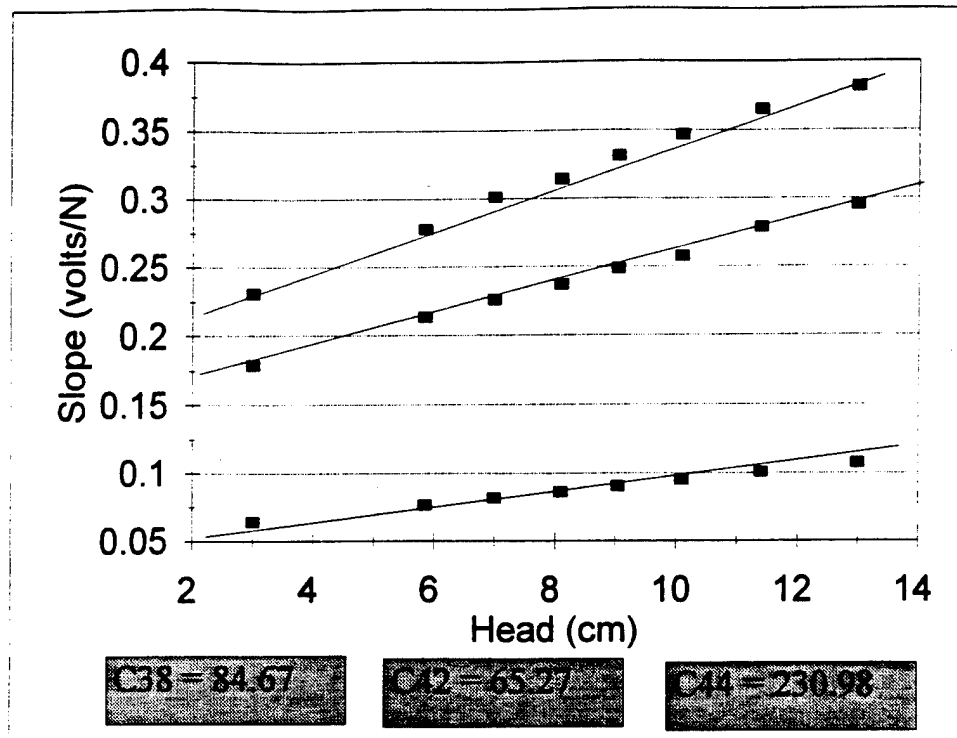
Figure 4-16. Master calibration for water
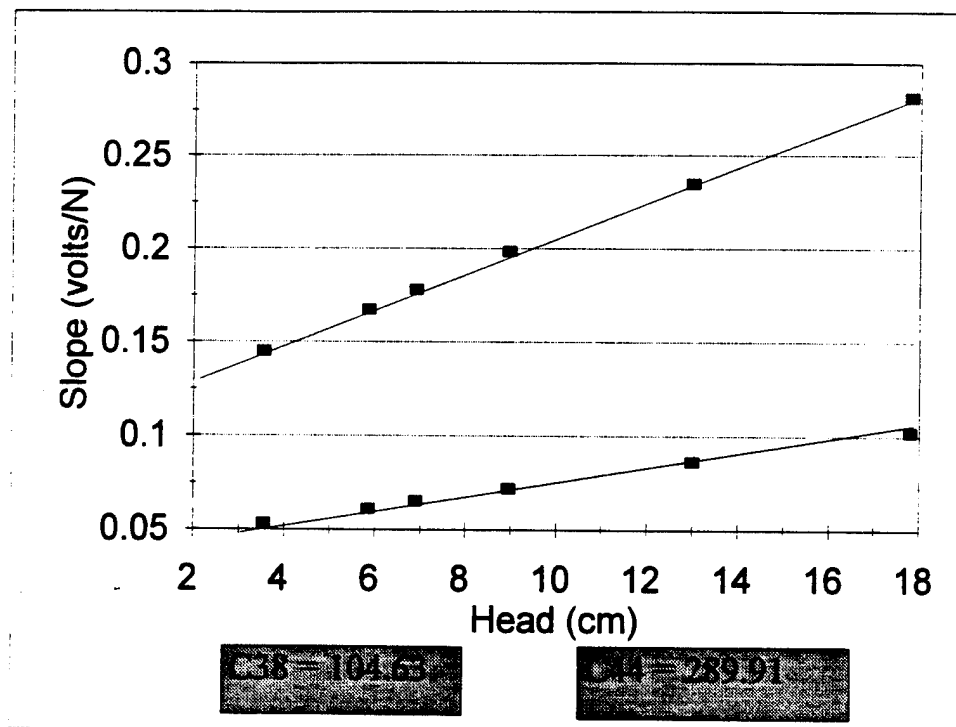
Figure 4-17. Master calibration for Soltrol

4.8 - Experimental results for #30 sand

Figure 4-18 shows the relationship between the hydraulic conductivity and the g-level (N) for water and #30 sand in the flexible wall permeameter. Figure 4-19 shows the relationship between the hydraulic conductivity versus the g-level (N) for Soltrol and #30 sand in the flexible wall permeameter. As expected, the data show a very strong linear relationship. The slope of the line of 0.131 cm/sec for water and #30 sand is seen to be very close to the reported values of the hydraulic conductivity value of 0.122 cm/sec (Mapa, 1994) in Table 4-2. Using Equation (4.11) and an estimated porosity of 0.4, a d_{50} of 0.049 cm, the Reynolds numbers for 1g and #30 sand gives:

$$Re = \frac{vd_{50}\rho}{\mu} = \frac{(\frac{0.07155}{0.4})(0.049)(1)}{0.01002} = 0.875 \tag{4.22}$$

and for the 20g tests and #30 sand gives:

$$Re = \frac{vd_{50}\rho}{\mu} = \frac{(\frac{0.25452}{0.4})(0.049)(1)}{0.01002} = 3.11 \tag{4.23}$$

The #30 sand is very similar to the sands used by Goforth et al. (1991) and Goodings (1994). The Reynolds numbers achieved in this experiment are significantly higher than Goforth et al.'s (1991) but confirm those of Goodings (1994). At 20g's, the data points lie on the regression line, indicating that laminar flow is still occurring. This test involved several samples but the data scatter is minimal, indicating sample preparation, saturation and measurements were well controlled.
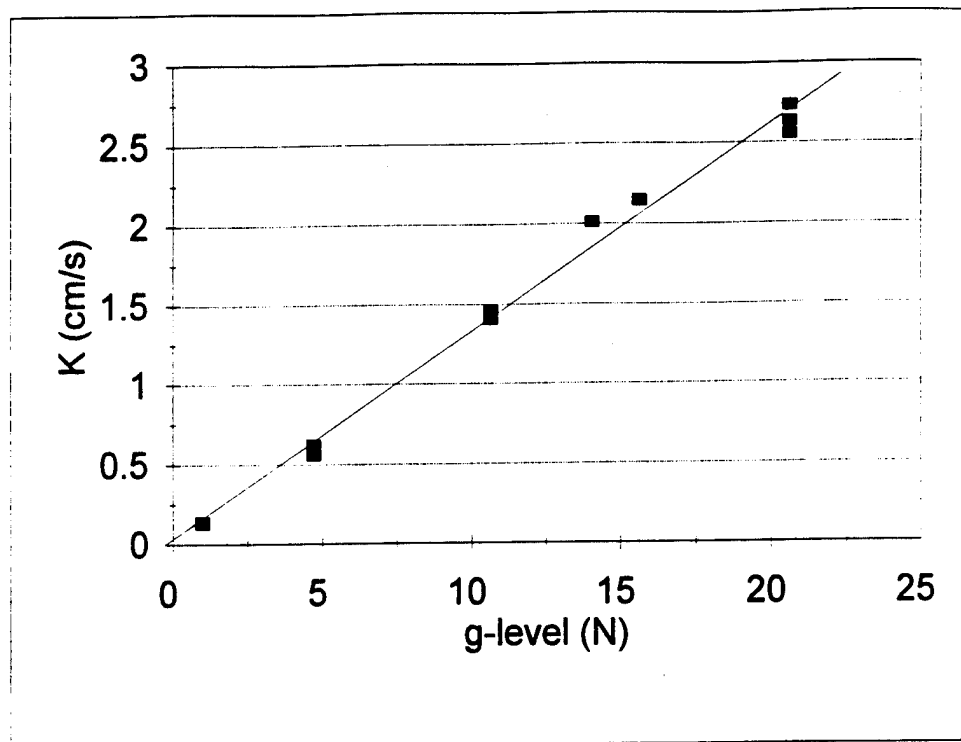
Figure 4-18. Hydraulic conductivity vs g-level (N) for water and #30 sand
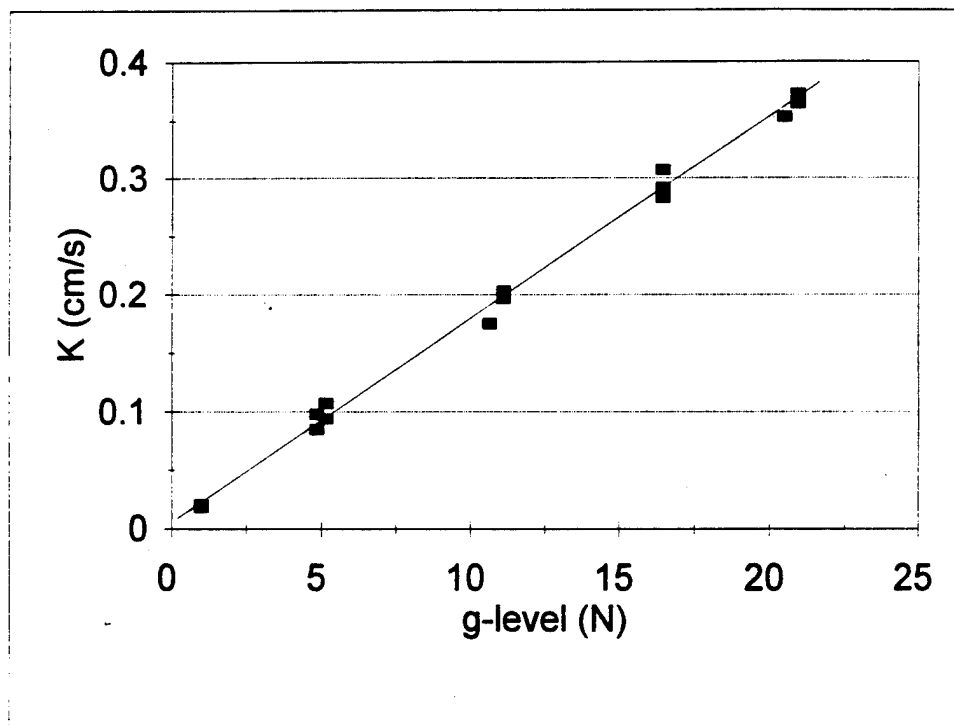
Figure 4-19. Hydraulic conductivity vs g-level (N) for Soltrol and #30 sand

78

For Soltrol and #30 sand, the hydraulic conductivity of 0.0173 cm/sec can be compared to water by using the hydraulic conductivity ratio as given by Equation (4.15) and substituting the values for K from the experimental data:

$$\frac{v_{oil}}{v_w} = \frac{K_w}{K_{oil}} = \frac{0.131}{0.0173} = 7.57 \ cs \qquad (4.24)$$

compared to Figure 4-8 which indicates the viscosity ratio of the two fluids is approximately 7.0 cs.

4.9 - Experimental results for #70 sand

Figure 4-20 shows the relationship between the hydraulic conductivity and the g-level (N) for water and #70 sand in the flexible wall permeameter. Figure 4-21 is the plot of hydraulic conductivity versus the g-level (N) for Soltrol and #70 sand in the flexible wall permeameter. The slope of the line of 0.0116 cm/sec for water and #70 sand is seen to be very close to the reported hydraulic conductivity (Mapa, 1994) value of 0.00997 cm/sec from Table 4-2. Using Equation (4.11) and an estimated porosity of 0.45, a d_{50} of 0.0185 cm, the Reynolds numbers for 1g and #70 sand gives:

$$Re = \frac{v d_{50} \rho}{\mu} = \frac{(\frac{0.01656}{0.45})(0.0185)(1)}{0.01002} = 0.0679 \qquad (4.25)$$

and for the 30g test and #70 sand gives:

$$Re = \frac{vd_{50}\rho}{\mu} = \frac{(\frac{0.09445}{0.45})(0.0185)(1)}{0.01002} = 0.388 \qquad (4.26)$$

For Soltrol and #70 sand, the hydraulic conductivity of 0.0156 cm/sec can be compared to the viscosity ratio of 7.0 cs obtained from Figure 4-8 by substituting the values for K from the experimental data into Equation (4.15):

$$\frac{v_{oil}}{v_w} = \frac{K_w}{K_{oil}} = \frac{0.1043}{0.01392} = 7.493 \ cs \qquad (4.27)$$

This test involved several samples and the data scatter is significant, indicating sample preparation, saturation and measurements were not as well controlled as the #30 sand. In particular, obtaining complete saturation was very difficult.
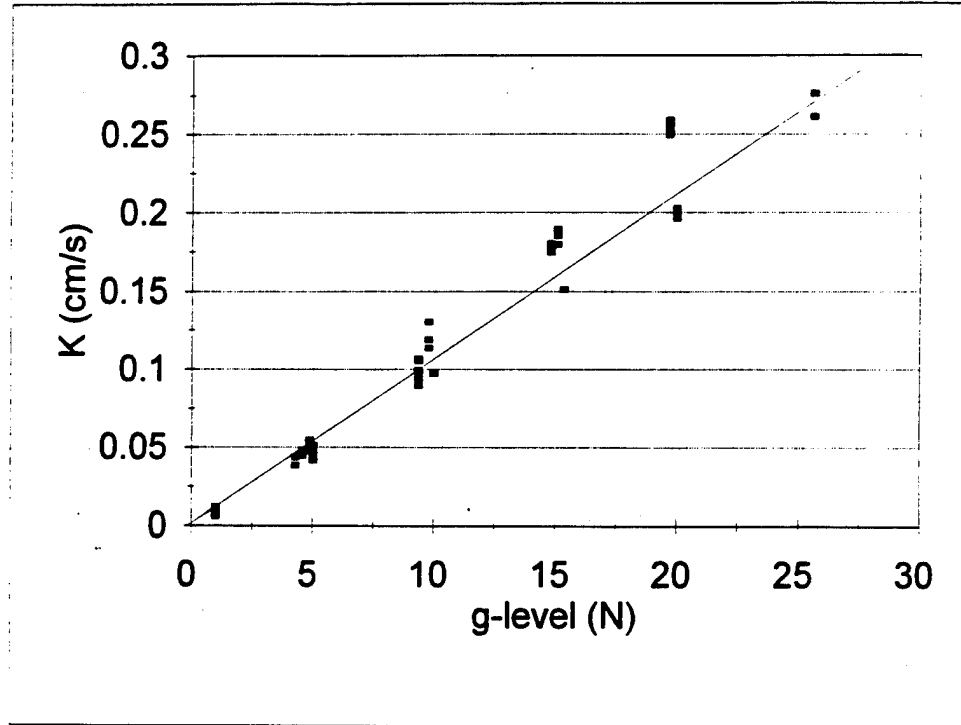
Figure 4-20. Hydraulic conductivity vs g-level (N) for water and #70 sand
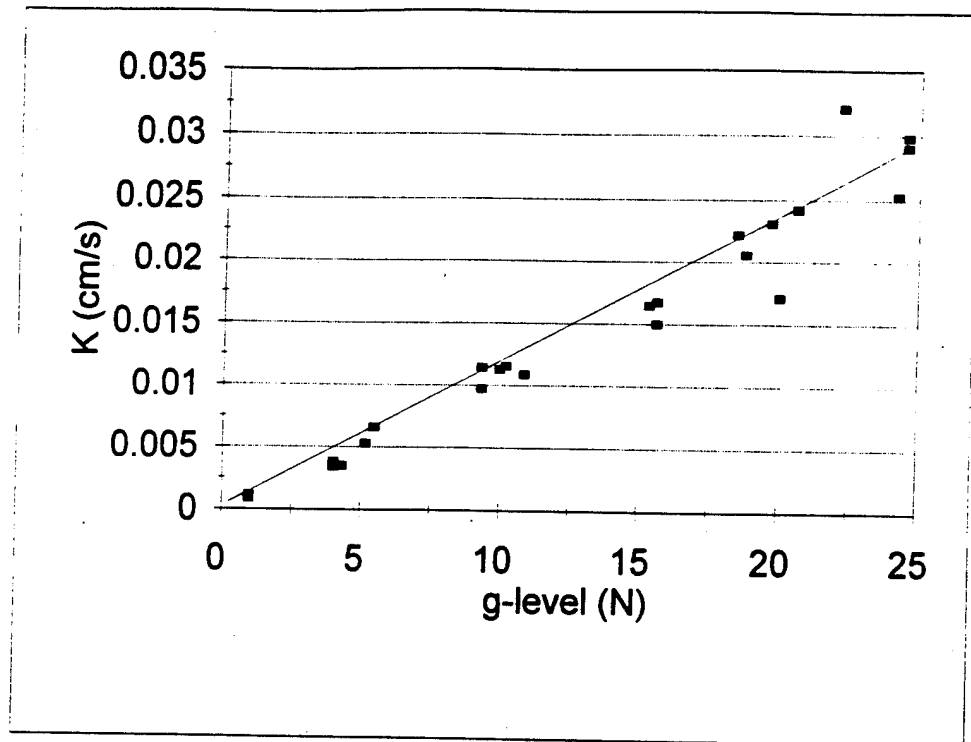
Figure 4-21. Hydraulic conductivity vs g-level (N) for Soltrol and #70 sand

4.10 - Experimental results for #F75 sand

Figure 4-22 shows the relationship between the hydraulic conductivity and the g-level (N) for water and #F75 sand in the rigid wall permeameter. Figure 4-23 shows the relationship between the hydraulic conductivity and the g-level (N) for Metolose and #F75 sand in the rigid wall permeameter. The slope of the line of 0.0155 cm/sec for water and #F75 sand is significantly different from that obtained by Stadler of 0.005cm/s, however, it matches the 1g tests of 0.016 cm/s. The slope of the line for the Metolose tests is 0.000479 cm/s. Comparing the hydraulic conductivities by substituting the values for K from the experimental data into Equation (4.15):

$$\frac{v_{met}}{v_w} = \frac{K_w}{K_{met}} = \frac{0.0155}{0.000479} = 32.4 \ cs \qquad (4.28)$$

The Metolose was nominally rated at 25 cs, but had sat for a long time. Viscosity tests on the Metolose yielded a viscosity of 30.7 cs, but even this value changed when evaporation occurred. The Metolose was so viscous that saturating the sample was impossible and air bubbles were visible at the plexiglass surface. Under even slight disturbance, the Metolose will form bubbles and "froth". From Figure 3-23, relative permeability curves, assuming the system was only 90% saturated, the hydraulic conductivity at 100% saturation would increase almost 30% and give a viscosity of 29.1 cs, certainly within the accuracy of the measurements.
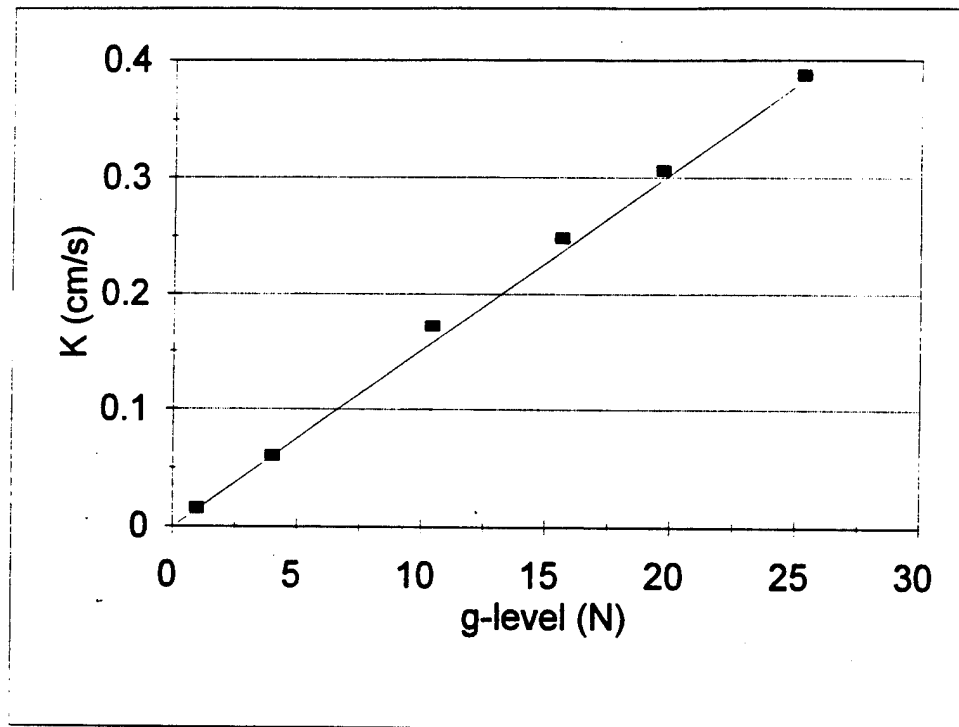
Figure 4-22. Hydraulic conductivity vs g-level (N) for water and #F75 sand
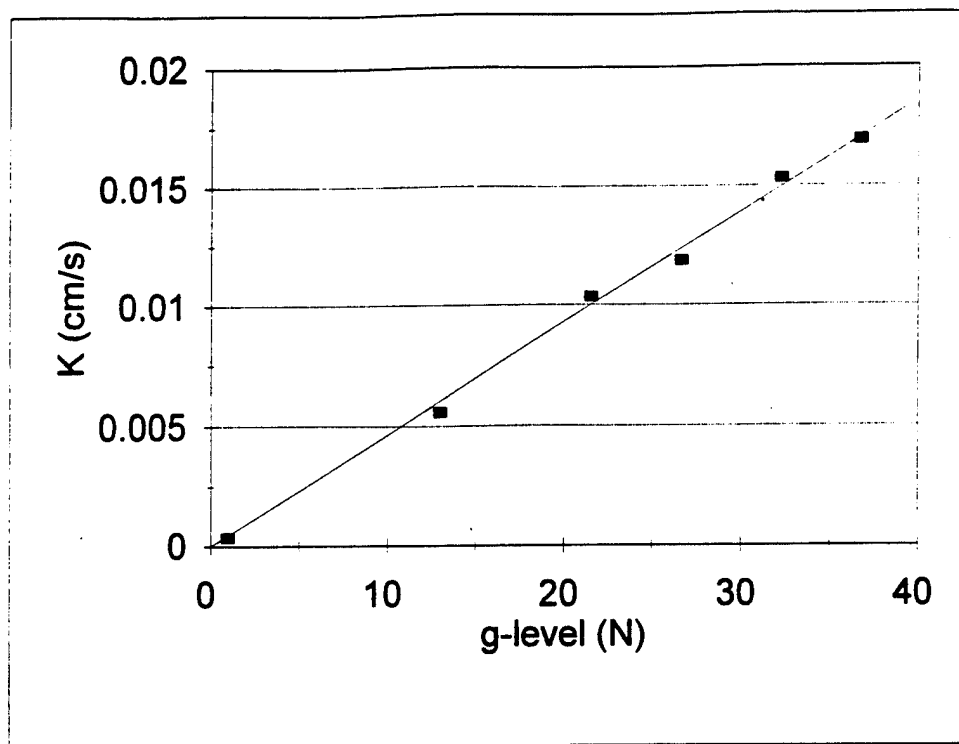
Figure 4-23. Hydraulic conductivity vs g-level (N) for Metolose and #F75 sand

4.11 - Experimental results for #30 and #70 layered sands

Figure 4-24 shows the relationship between the hydraulic conductivity and the g-level (N) for water and layered sands using the rigid wall permeameter. The #70 sand used for this experiment was supplied by a new manufacturer and has a slightly higher saturated hydraulic conductivity (0.02 cm/s). The theoretical effective hydraulic conductivity can be found using Equation (4.16) as:

$$K_z = \frac{17.2}{\frac{(3)(3.0)}{0.02} + \frac{(2)(3.0)}{0.131} + \frac{(1)(1.2)}{0.131} + \frac{(1)(1.0)}{0.131}} = 0.0195 \ cm/s \tag{4.29}$$

which is in excellent agreement with the measured value of 0.0188 cm/s.
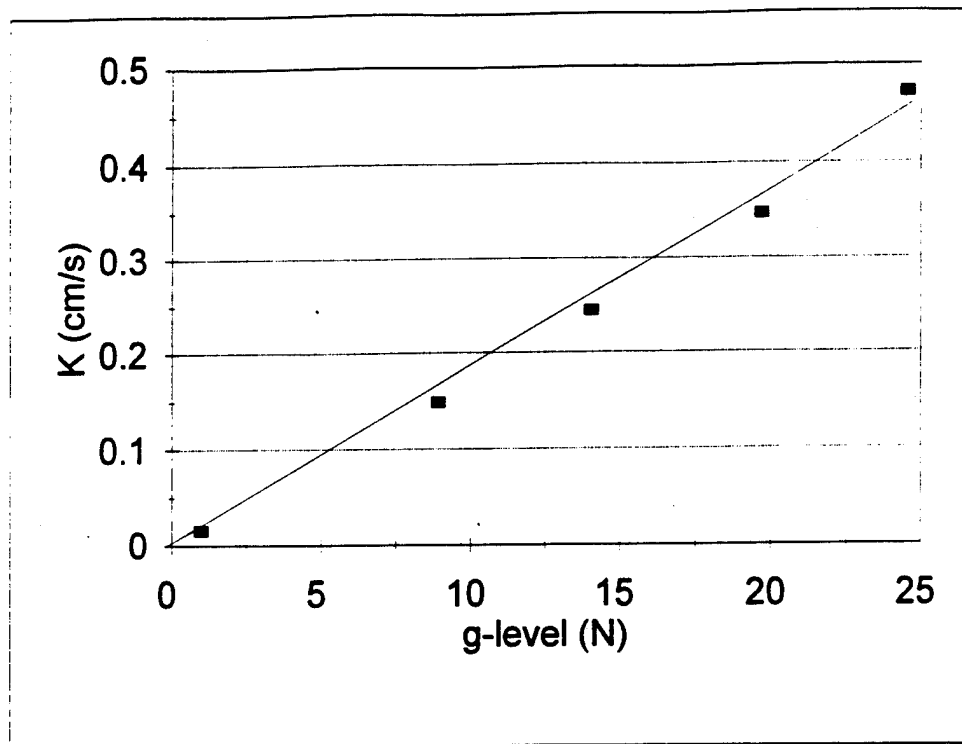
Figure 4-24. Hydraulic conductivity vs g-level (N) for water and layered sands

4.12 - Summary of results

The saturated flow experiments were designed to validate the scaling of the hydraulic conductivity using several types of porous media and different fluids. The experimental test program was designed as a step process, validating a specific concept, before proceeding to the next. The first concept which had to be validated was the gravity independence of the density and viscosity of the pore fluid. The density independence was accomplished using the pressure transducer master calibration curves. The viscosity independence was shown by comparing the hydraulic conductivity of each sand using a different pore fluid. The viscosity and hydraulic conductivity ratio for #30 and #70 homogeneous sands validated the scaling of the hydraulic conductivity. The

84

layered sands and #F75 mixed gradation sand tests were designed to validate the scaling

of the hydraulic conductivity for heterogeneous systems. Table 4-4 is a summary of the

saturated sands experimental tests.

Table 4-4. Summary of saturated sand tests

Test	Fluid	K1g (cm/s)	KNg (cm/s)	Re
#30 sand	water	0.133	0.131	3.11
#30 sand	Soltrol	0.0201	0.0173	0.239
#70 sand	water	0.0114	0.0116	0.388
#70 sand	Soltrol	0.00113	0.00156	0.021
#F75 sand	water	0.016	0.0155	1.073
#F75 sand	Metolose	0.00036	0.00048	0.00101
#30/#70/#30	water	0.0195	0.0188	1.003

The saturated sands results can be compared to the results obtained by Goodings

(1994) by using Equation (4.2). Figure 4-25 is a plot of the friction factor versus

Reynolds number for the water tests, similar to Figure 4-3 presented by Goodings (1994).

The plot clearly shows the sands remain within the laminar flow condition. The layered

sands link the range of the #30 and #70.
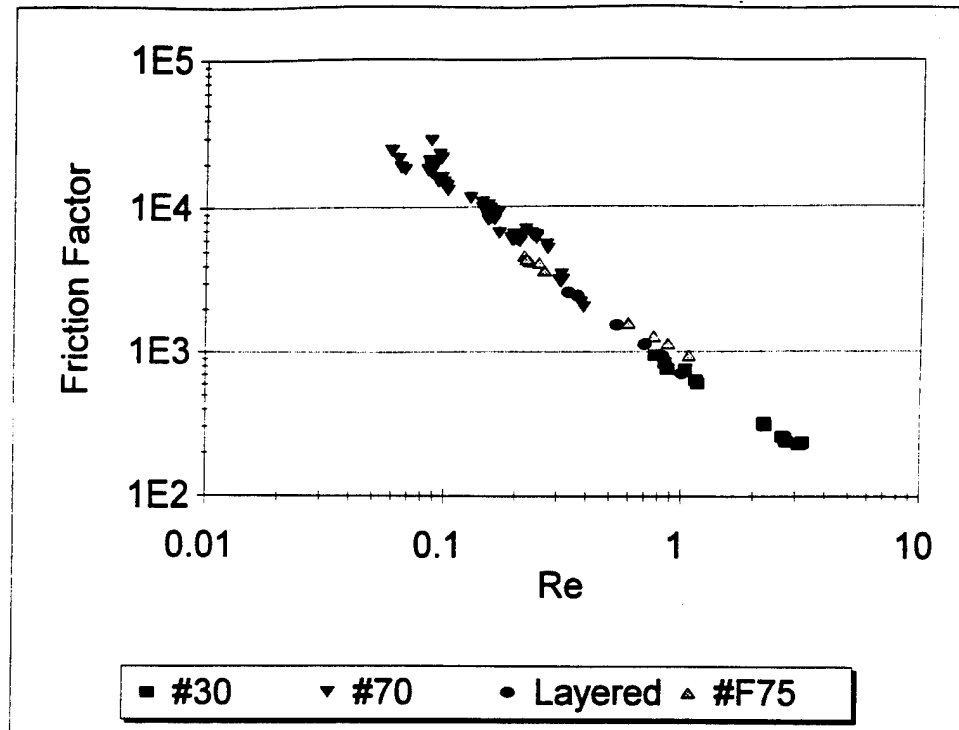
Figure 4-25. Friction factor versus Reynolds number

4.13 - Analysis and discussion of results

The experimental results for saturated flow verify the validity of the scaling relationship for the hydraulic conductivity as:

$$K_m = NK_p \qquad \text{(hydraulic conductivity)}$$

The Reynolds numbers for all sands are in agreement with the predictions of Bear (1972). For the #30 coarse sand, the maximum Reynolds number of 3.11 is in excellent agreement with that of Goodings (1994) for the #30/#40 Ottawa sand. From the data, the upper limit of the Reynolds number is not apparent, however, this test apparatus could be modified and used to explore the Reynolds number transition from laminar to turbulent

flow. Even under laminar flow conditions, it would be expected that within any centrifuge soil sample, some of the pore space would be experiencing turbulent flow due to tortuosity. This effect would cause higher head losses, and tend to reduce the hydraulic conductivity. The turbulent flow would be masked by the overall trend, however, and minor deviations would not be expected to invalidate the scaling law for most cases.

The type of permeameter (flexible or rigid wall) did not have an appreciable effect upon the overall trend, however, there was more data scatter with the flexible type. The flexible wall permeameter tests were the first tests performed and the data scatter using the flexible wall permeameter was caused more by inexperience and learning how to perform tests in the centrifuge than by an inherent defect. A review of the experimental assumptions and procedure can account for the data scatter. Basic assumptions for the experiments were:

1. The soil sample would be 100% saturated, and

2. The variation in the stress field would be minimal.

Assumption #1, the soil sample would be 100% saturated, turned out to be fairly accurate. Normal 1g hydraulic conductivity tests are run using back pressure on the sample to ensure saturation, and the B test is run to determine whether full saturation has been reached. The centrifuge tests did not use back pressure, however even small deviations in the saturation should provide reasonable results to prove the linear relationships. During the 1g test, the samples were not fully saturated, especially using the flexible wall permeameter. The tubing connecting to the porous stones was the standard small diameter tubing used for triaxial tests. In the rigid wall permeameter, the

tubing was a larger diameter. Air bubbles in the sample could not be seen within the flexible wall permeameter due to the solid aluminum outer cell, but the rigid wall permeameter sample was easily seen. Air bubbles were also visible in the plastic tubing as they came out of the sample.

Large air bubbles coming out of the sample could be visibly verified as they would cause a blip on the head curve. To determine when the sample was close to being saturated, the data acquisition system was used to monitor the head across the sample. As the sample was saturating, the head curve was not in a flat horizontal line, but rather, kept increasing in a gradual arc up to the steady state horizontal line, as shown in Figure 4-26.
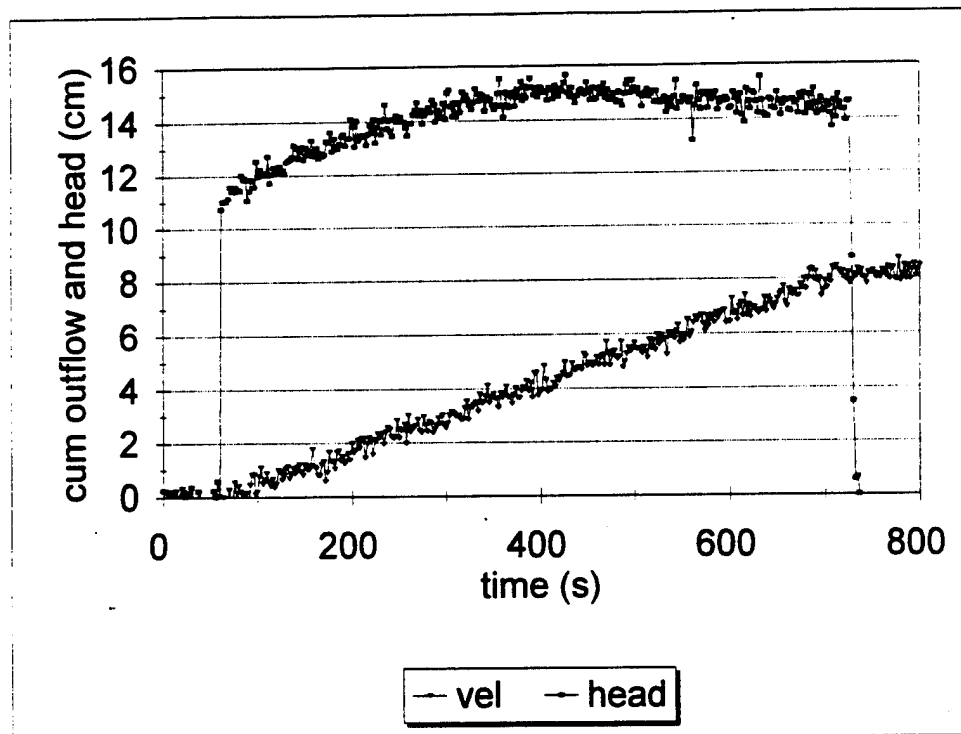
Figure 4-26. Unsaturated flow

The Soltrol and Metolose were very difficult to get to saturate the soil sample, and a 90% saturation was probably the highest obtained. Any movement or shaking of the system would cause the fluids to "froth" and create bubbles, even if sand was rained through the fluid to ensure 100% saturation. For the small centrifuge, while the system was in-flight, there was a slight vibration due to imbalance of the arm caused by the redistribution of the fluid. This problem can only be eliminated by incorporating compensation fluid tanks like those on the large centrifuge. This slight vibration may be enough to cause "frothing" and settlement of the sample while in-flight.

Assumption #2, the variation in the stress field would be minimal, proved to be more significant than was first thought. The variation in the stress field at low g-levels was not as critical as at higher g-levels. At higher g-levels, the high g-field would cause air to become entrapped or prevent the equipment, especially the solenoid valves, from operating properly. In addition, the RPM gauge had a limit of plus or minus 2 RPM, so at low g-levels higher relative fluctuations in N would be expected. At higher levels, N would be expected to be relatively constant. However, the calibration constants were very large at low g-levels and the data points multiplication by the large calibration constants contributed to data scatter.

The experimental procedure also incorporated some error. The measurement ability of the various transducer membranes is a tradeoff between accuracy at low levels for the ability to measure at higher g-levels. The measurement ability of the membranes was in most cases the limiting factor as to the ability to measure the flow rate and head across the sample at increasing g-levels. As the g-level is increased, stiffer membranes

must be used, however, these stiffer membranes do not measure the lower g-levels as accurately as more flexible membranes.

Even with the limitations of the equipment and the various combinations of experimental apparatus, the data points remained closely spaced. Overall, the assumptions and procedures proved to be reasonable in that a result of plus or minus 10% of the reported and theoretical values of the hydraulic conductivity and viscosity ratios were obtained.

The saturated flow experiments have verified the scaling relationship for the hydraulic conductivity. The relationship is valid for medium and coarse homogeneous sands, mixed gradation sands, and layered sands. The saturated hydraulic conductivity of coarser materials will be further explored in Chapter 7, Saturated fissure flow. As part of the hydraulic conductivity experiments, the viscosity and density were found to remain constant and are independent of g-level. Having verified the scaling relationship for the hydraulic conductivity, the scaling of time can now be examined. Chapter 5 will determine the time relationship using unsaturated flow experiments and the modeling of models technique.

CHAPTER 5

TWO-PHASE UNSATURATED FLOW THROUGH SAND

5.1 - Objective and theory

The objective of the two-phase unsaturated flow through sands experiments is to verify the scaling relationships for the hydraulic conductivity and time. The centrifuge offers several theoretical advantages in studying unsaturated flow due to the reduction in the time scale as shown by Equation (4.17).

The equations governing two-phase (air and water) unsaturated flow undergoing vertical drainage are based on Equation (3.8), commonly referred to as the Richards equation. As shown by Equation (3.8), the hydraulic conductivity is no longer a constant but is a function of the head and degree of saturation. For vertical drainage problems at 1g, unsaturated flow experiments can require extended periods of time to measure the parameters of interest. As shown in Chapter 4, in the centrifuge, the increased gravity field causes an increase in the soil Darcy velocity of N times that of the prototype. In addition, the unsaturated hydraulic conductivity in the centrifuge should be N times that of the prototype. However, the increased gravity field also affects the capillary forces and consequently the unsaturated hydraulic conductivity may not properly model prototype conditions.

To date, three experimental investigations have been published evaluating unsaturated flow scaling laws. The first attempt to model unsaturated flow was by

Goforth et al. (1991) as shown in Figure 5-1.
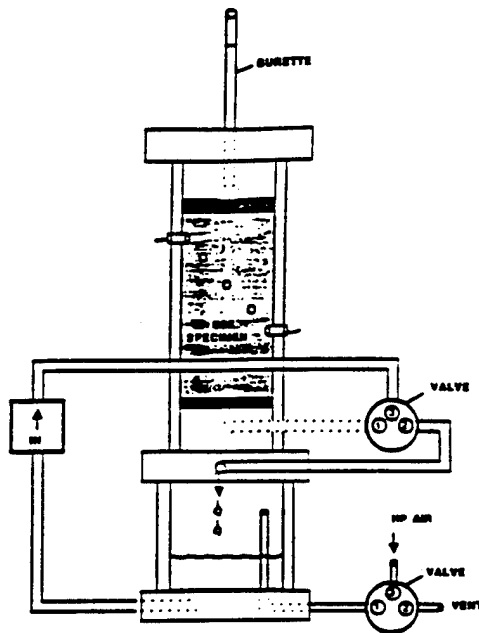
Figure 5-1. Unsaturated flow set-up (from Goforth et al., 1991)

They used a fine grained silica sand with a d_{50} of 0.2 mm mixed with kaolinite that was fully saturated and then allowed to drain. They were unsuccessful in obtaining repeatable results and were unable to verify the scaling relationships.

Cooke and Mitchell (1991) evaluated contaminant transport in partially saturated soils. They used a fine grained soil undergoing vertical drainage and performed two modeling of models tests. They did not perform a 1g prototype, but simulated the 1g prototype using an explicit finite difference code. Their centrifuge tests and numerically predicted outflow curves and moisture content distributions are shown in Figure 5-2. While the results showed reasonably good agreement using theoretical scaling laws, the

researchers did not specifically calculate the exponents. They concluded that the centrifuge was a valid tool for modeling transport problems.
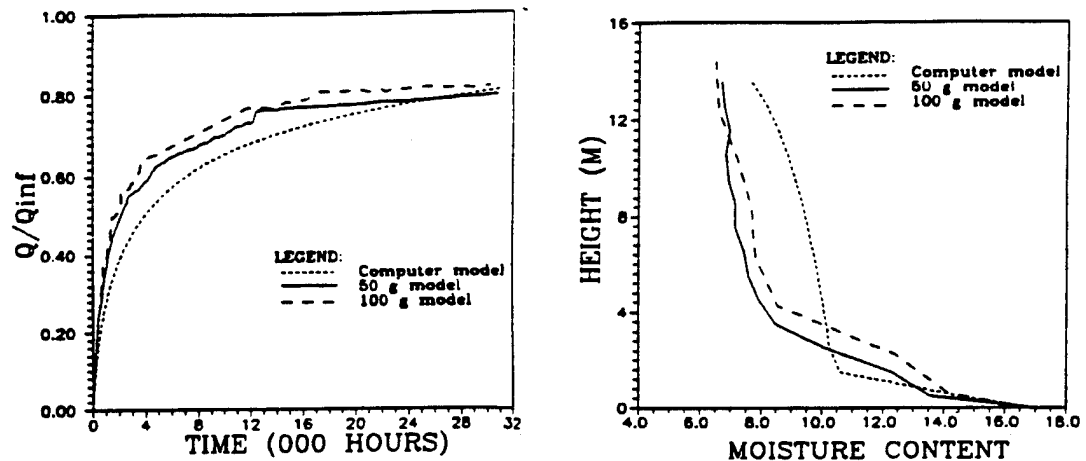
Figure 5-2. Unsaturated flow results (from Cooke and Mitchell, 1991)

Cooke (1994) examined use of the centrifuge to obtain the inverse solution for unsaturated flow parameters by measuring the cumulative outflow of an initially saturated column under gravity drainage. He used two different fine grained silty sands and let the soils drain for a predetermined time so that complete drainage occurred. The soil samples were then sectioned to determine water contents and the inverse parameters were estimated using a computer code. His results of the centrifuge tests and the parameter estimates are shown in Figure 5-3. Cooke (1994) did not perform prototype or modeling of models tests or calculate exponents to match the cumulative outflow curves.
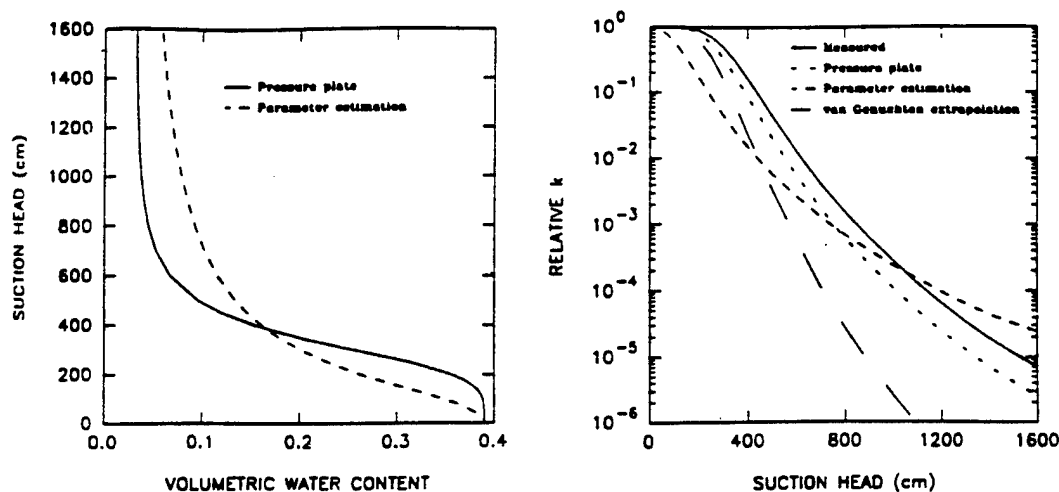
Figure 5-3. Unsaturated flow parameters (from Cooke, 1994)

All three previous experiments showed large data scatter but essentially showed the drainage behavior in the centrifuge was similar to that at 1g. None of the tests were designed to specifically determine the scaling exponents for the hydraulic conductivity or time. All tests used water and air as the test fluids.

Peterson and Cooke (1994) explored the use of NAPLs in the centrifuge and presented a theoretical argument based on the kinematics similarity criteria, concluding that "the centrifuge is not a suitable tool for the modeling of immiscible multiphase or any two phase water-LNAPL displacement" (page 392). They have pointed out a potentially serious problem in attempting to model environmental contaminant problems in the centrifuge. The researchers suggested that if the centrifuge model does not replicate prototype behavior, then there is little value in performing the experiments. To test their hypothesis, the drainage of water and NAPL in an open atmosphere must first be explored

94

to determine scaling exponents for the hydraulic conductivity and time, then both fluids can be combined to evaluate the water-LNPAL behavior. The following discussion explores one dimensional column water-air and LNAPL-air drainage in more detail.

For unsaturated flow, the size of the centrifuge models must be scaled in length. The geometric similarity criteria are met by using the same porous media for all tests such that the porosity, volummetric water content, and saturation criteria of Equations (3.19), (3.20), and (3.21) are met.

Multiphase flow is assumed to be characterized by the Capillary and Bond numbers and they must be examined for kinematic and dynamic similarity. In the centrifuge, the scaling of the Bond and Capillary numbers by Peterson and Cooke (1994) are in agreement with those of Arlunandan et al. (1991). Arlunandan et al. (1991) used the Buckingham π theory, as presented in Chapter 4, to find:

$$Ca_m = NCa_p \tag{5.1}$$

$$Bo_m = NBo_p \tag{5.2}$$

Using Figure 3-16, Peterson and Cooke (1994) concluded that at elevated g-levels the increase in the velocity and g-level causes a reduction in the residual saturation indicating that the altered properties in the model will not duplicate prototype behavior. Similar to the displacement model of Morrow and Songkran (1981), they proposed that the entrapment mechanism would look like Figure 5-4.

V LNAPL

A

P_c^B P_c^A

B

Δh

$\Delta \rho \, g \, \Delta h$

f_R

Mobilised

$P_c^A - P_c^B$

Proportion of ganglia mobilised by
supplementary pressure in prototype.

f_R

Mobilised

$P_c^A - P_c^B$

Proportion of ganglia mobilised by
supplementary pressure in model.
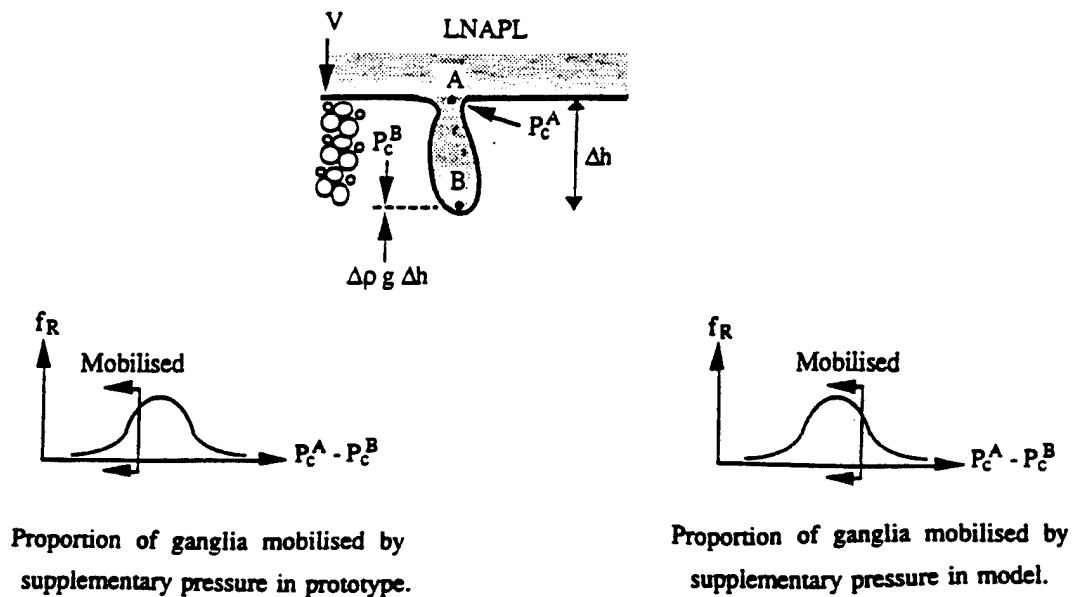
Figure 5-4. Entrapment scaling (from Peterson and Cooke, 1994)

Peterson and Cooke (1994) argue that the ganglia formed in a centrifuge model
do not have the same distribution as a 1g prototype. Their analysis is correct in situations
where ganglia form, however, it does not invalidate centrifuge modeling of all multiphase
flow problems. As shown in Section 3.3, depending upon the mobility ratio and direction
of flow, the formation of ganglia can be prevented. If the formation of ganglia can be
controlled such that sharp front behavior is induced, then, similar to the argument that
similarity of the Reynolds number is not required for laminar flow, the Capillary and Bond
numbers may not require similarity under certain conditions for multiphase flow.
However, the restrictions on the Reynolds number for laminar flow are still applicable.
The critical issue is determining the effects that the flow rate of the displacing fluid have
upon the redistribution of the two fluids.

96

As an example, consider one-dimensional drainage of a water-saturated column. As the water drains, an essentially sharp drainage front appears as the pore spaces desaturate. Only the region close above the bubbling pressure on the suction-saturation curve will have ganglia formation. In the case of the #70 sand, this region is from 20 to 30 cm above the static water table. Compared to the overall length of a 200 cm column, the fluid drained or retained within this region is a fraction of the total, and the effects of any ganglia are negligible. If the air phase is now replaced with an NAPL, sharp front behavior will still be exhibited, and behind the drainage front the sand will come to residual saturation with both a water and NAPL phase. However, since one fluid will be preferentially wetting, the wetting fluid will remain almost entirely as the residual fluid, and only the area where ganglia can form will there be significant amounts of both fluids. If this region is small compared to the overall drainage, then the effects of the ganglia can once again be neglected.

Reversing the order of the fluids so that the water is now above the NAPL, based on the critical velocity criteria of Section 3.4, if the critical velocity is exceeded, the denser water will form preferential flow channels. The remaining NAPL is entrapped as ganglia which cannot move into the pore space occupied by the water. Even at 1g, the ganglia formation is completely random and unpredictable. In the centrifuge, the ganglia scaled lengths will be different and they will not have the same distribution as in the prototype.

It should be pointed out that the preceding explanation is based upon arguments at the pore scale. In modeling of the multiphase flow problem, physical or numerical,

the porous medium is treated as a continuum and the macroscopic properties are of interest: flow rates, cumulative outflow, pore pressures, etc. Thus, the comparison of these quantities between the model and the prototype is the ultimate test of the validity of the centrifuge modeling technique for studying multiphase flow problems.

5.2 - Unsaturated flow processes in the centrifuge

The unsaturated flow test program investigated homogeneous and layered sand packings undergoing gravity drainage using both water and Soltrol as the wetting fluids and air as the nonwetting fluid. Unsaturated flow is a multiphase problem in that at least two phases (liquid and gas) are flowing simultaneously, but the air is assumed to be free to flow to the surrounding atmosphere and the problem becomes a single phase unsaturated flow problem. In contrast to saturated flow unsaturated flow is more complex due to suction-saturation behavior, boundary conditions, viscosity ratio, density ratio, etc. which must be measured or accounted for.

To model unsaturated flow in the centrifuge, the scaling laws relating the model performance to the prototype performance must be derived and validated and the fundamental physics involved must be properly duplicated. Modeling unsaturated flow in sands was accomplished using the modeling of models approach. The concept of comparing results of two physical experiments at two different gravity levels to validate the scaling relations is called "modeling of models" (Ko, 1988), and is illustrated in Figure 5-5. By comparing the results of these experiments, the scaling relations can be verified and the results extrapolated to the "real" prototype at 1g.
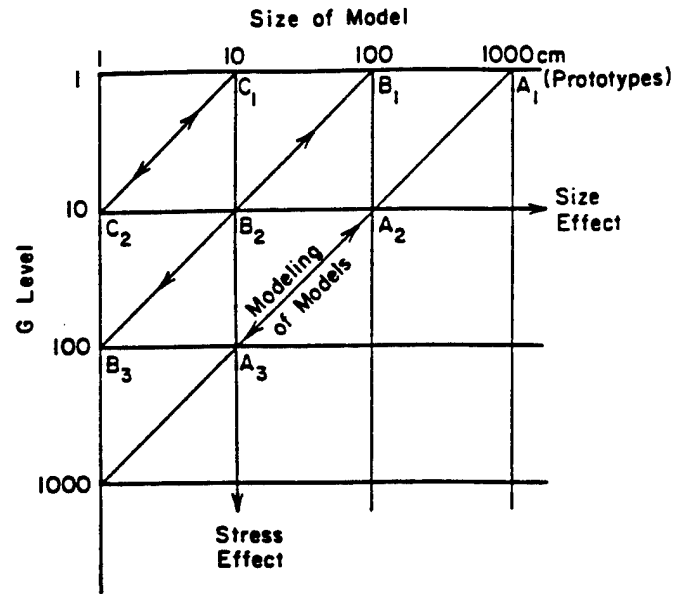
Figure 5-5. Principle of Modeling of Models (from Ko, 1988)

For the centrifuge experiments, the same porous media and liquids are used for each model, but under different gravity levels and the flow in the centrifuge models must then be scaled to prototype through the use of scale factors similar to those for saturated flow. Using the modeling of models criteria, the centrifuge models will be reduced in size according to:

$$L_m = \frac{L_p}{N} \qquad\qquad (5.3)$$

A fully saturated column using a single fluid will drain in the vertical direction according to the classic Richards equation:

$$\frac{\partial}{\partial z}[K(h_p)\frac{\partial}{\partial z}(h_p+1)] = \phi\frac{\partial S}{\partial t}$$ (5.4)

and the centrifuge models will predict prototype behavior if the moisture content (effective saturation) distributions with time are the same. While the Richards equation has been extensively used to model drainage problems, there is considerable evidence that the boundary conditions used can have a large impact on the solution.

There are several methods to non-dimensionalize the Richards equation depending upon the choice of scale factors. Corey (1990) non-dimensionalizes the equations by starting with Darcy's law for each phase:

$$q_{wi} = \frac{k_w}{\mu_w}(-\frac{\partial p_w}{\partial x_i}+\rho_w g_i)$$ (5.5)

$$q_{nwi} = \frac{k_{nw}}{\mu_{nw}}(-\frac{\partial p_{nw}}{\partial x_i}+\rho_{nw} g_i)$$ (5.6)

From continuity:

$$\phi\frac{\partial S}{\partial t} = \frac{\partial q_{nwi}}{\partial x_i}$$ (5.7)

$$-\phi\frac{\partial S}{\partial t} = \frac{\partial q_{wi}}{\partial x_i}$$ (5.8)

From the definition of capillary pressure:

$$\frac{\partial p_c}{\partial x_i} = \frac{\partial p_{nw}}{\partial x_i}-\frac{\partial p_w}{\partial x_i}$$ (5.9)

100

Substituting Equations (5.5) and (5.6) into Equation (5.9) and rearranging:

$$\frac{\partial p_c}{\partial x_i} = (\frac{q_{wi}\mu_w}{k_w} - \frac{q_{nwi}\mu_{nw}}{k_{nw}}) - (\Delta\rho g_i) \qquad (5.10)$$

$$q_{wi} = \frac{k_w}{\mu_w}(\frac{\partial p_c}{\partial x_i} + \Delta\rho g_i) + q_{nwi}(\frac{\mu_{nw}k_w}{\mu_w k_{nw}}) \qquad (5.11)$$

Substitution of Equation (5.11) into Equation (5.8) and rearrangement yields the governing equation for 1g two-phase flow as:

$$\phi\frac{\partial S}{\partial t} = \frac{\partial}{\partial x_i}[\frac{k_w}{\mu_w}(\frac{\partial p_c}{\partial x_i} + \Delta\rho g_i)] - \frac{\partial}{\partial x_i}[q_{nwi}(\frac{\mu_{nw}k_w}{\mu_w k_{nw}})] \qquad (5.12)$$

A similar equation can be developed for the centrifuge (Corey, 1990). The gravity field in the centrifuge is dependent upon the distance from the center shaft. The distance is comprised of a fixed length from the shaft to the top of the sample (r), and a variable length of the column itself, (x) :

$$N = \omega^2(r+x) = \omega^2 r(1+\frac{x}{r}) \qquad (5.13)$$

The differential flow equation can be expressed as:

$$\phi\frac{\partial S}{\partial t} = \frac{\partial}{\partial x_i}[\frac{k_w}{\mu_w}(\frac{\partial p_c}{\partial x_i} + \Delta\rho\omega^2 r_i)] - \frac{\partial}{\partial x_i}[q_{nwi}(\frac{\mu_{nw}k_w}{\mu_w k_{nw}})] \qquad (5.14)$$

Using Corey's (1990) method for scaling such that the governing equation

101

becomes dimensionless, the variables to be scaled are k_w, k_{nw}, P_c, q_{nw}, x, and t. The variable S is already dimensionless. Assume the model will be reduced in size such that:

$$k_{wp} = k_s\, k_{wm} \tag{5.15a}$$

$$k_{nwp} = k_s\, k_{nwm} \tag{5.15b}$$

$$p_{cp} = p_{cs}\, p_{cm} \tag{5.15c}$$

$$q_{nwp} = q_s\, q_{nwm} \tag{5.15d}$$

$$x_p = x_s\, x_m \tag{5.15e}$$

$$t_p = t_s\, t_m \tag{5.15f}$$

Substituting the above equations into Equation (5.14):

$$\left[\frac{x_s^2 \mu_w}{k_p p_{cs} t_s}\right]\phi\frac{\partial S}{\partial t_m} = \frac{\partial}{\partial x_m}\left[k_{wm}\left(\frac{\partial p_{cm}}{\partial x_m}+\frac{\Delta\rho\omega^2 r x_s}{p_{cs}}(1+\frac{x_s x_m}{r})\right)\right]-\left[\frac{q_s x_s \mu_w}{k_p p_{cs}}\right]\left[\frac{\partial}{\partial x_m}(q_{nwp}\frac{\mu_{nw}k_{wp}}{\mu_w k_{nwp}})\right]$$

$$\tag{5.16}$$

choose the scale factor:

$$x_s = \frac{p_{cs}}{\Delta\rho\omega^2 r} \tag{5.17}$$

Substituting Equation (5.17) into Equation (5.16) and rearranging yields:

$$\left[\frac{\phi p_{cs}\mu_w}{k_s(\Delta\rho\omega^2 r)^2 t_s}\right]\frac{\partial S}{\partial t_m} = \frac{\partial}{\partial x_m}\left[k_{wm}\left(\frac{\partial p_{cm}}{\partial x_m}+1+\frac{p_{cs}x_m}{\Delta\rho\omega^2 r^2}\right)\right]-\left[\frac{q_s\mu_w}{k_s\Delta\rho\omega^2 r_p}\right]\left[\frac{\partial}{\partial x_m}(q_{nwp}\frac{\mu_{nw}k_{wp}}{\mu_w k_{nwp}})\right]$$

$$\tag{5.18}$$

choose the scale factors:

102

$$q_s = \frac{k_s \Delta\rho\omega^2 r}{\mu_w} \qquad (5.19)$$

$$t_s = \frac{\phi p_{cs}\mu_w}{k_s(\Delta\rho\omega^2 r)^2} \qquad (5.20)$$

Substituting Equations (5.19) and (5.20) into Equation (5.18) and rearranging yields the governing dimensionless equation for two-phase flow in the centrifuge:

$$\frac{\partial S}{\partial t_m} = \frac{\partial}{\partial x_m}[k_{wm}(\frac{\partial p_{cm}}{\partial x_m}+1+\frac{p_{cs}x_m}{\Delta\rho(\omega r)^2})] - \frac{\partial}{\partial x_m}[\frac{q_{nwm}\mu_{nw}k_{wm}}{\mu_w k_{nwm}}] \qquad (5.21)$$

Length and time ratios can be found as:

$$\text{Length:} \quad \frac{(x_s)_m}{(x_s)_p} = \frac{(\dfrac{p_{cs}}{\Delta\rho\omega^2 R})_m}{(\dfrac{p_{cs}}{\Delta\rho\omega^2 R})_p} = \frac{1}{N} \qquad (5.22)$$

$$\text{Time:} \quad \frac{(t_s)_m}{(t_s)_p} = \frac{(\dfrac{\phi p_{cs}\mu}{k_o\Delta\rho^2(\omega^2 R)^2})_m}{(\dfrac{\phi p_{cs}\mu}{k_o\Delta\rho^2(\omega^2 R)^2})_p} = \frac{1}{N^2} \qquad (5.23)$$

From the length ratios, Equation (5.22), Corey (1990) concludes that true modeling of models requires that the radius of the centrifuge arm must be changed. To test this requirement, a set of experiments was performed on both the small and large

centrifuge. In addition, for the small centrifuge, the small arm radius induces a 11% vertical gravity variation over the 20 cm model column. Since the drainage of the column is related to the capillary forces, the vertical variation in the g-level implies that the unsaturated hydraulic conductivity will also vary. The magnitude of the effect on the time ratio for a varying $K(\theta)$ with g-level plus the effects of a constant radius arm are unknown.

The length ratio used by Corey (1990) is very similar to other ratios commonly used in the petroleum industry, but is not in a convenient form for centrifuge analysis. Therefore, an alternate transformation using different scale factors can be obtained by using Equation (5.4) and choosing scale factors:

$$h_{pp} = h_o h_{pm} \tag{5.24a}$$

$$K(h_p)_p = K_o K(h_p)_m \tag{5.24b}$$

$$z_p = z_o z_m \tag{5.24c}$$

$$t_p = t_o t_m \tag{5.24d}$$

Substitute the above equations into Equation (3.8):

$$\phi \frac{\partial S}{\partial t_o t_m} = \frac{\partial}{\partial z_o z_m}[K_o K(h_p)_m \frac{\partial}{\partial z_o z_m}(h_o h_{pm})+1)] \tag{5.25}$$

Rearranging Equation (5.25) gives:

$$\phi \frac{\partial S}{t_o \partial t_m} = \frac{\partial}{z_o \partial z_m}[K_o K(h_p)_m \frac{h_o}{z_o} \frac{\partial}{\partial z_m}(h_{pm}+\frac{1}{h_o})] \tag{5.26}$$

104

to obtain coefficients of unity, $h_o = z_o$ and a prudent choice for h_o would relate to some common length factor at all g-levels that can be physically measured. An easily measured point on the suction-saturation curve is the air entry head where the sample begins to desaturate. Therefore, choose:

$$h_o = h_e \tag{5.27}$$

and let:

$$K_o = K_{max} = NK_{max1g} \tag{5.28}$$

Substitute equations (5.27) and (5.28) into Equation (5.26):

$$\frac{\phi}{t_o}\frac{\partial S}{\partial t_m} = \frac{K_{max}}{h_e}\frac{\partial}{\partial z_m}[K(h_p)_m\frac{\partial}{\partial z_m}(h_{pm}+\frac{1}{h_e})] \tag{5.29}$$

Equating coefficients to unity:

$$t_o = \frac{\phi h_e}{K_{max}} \tag{5.30}$$

Substituting Equation (5.30) into Equation (5.29) gives:

$$\frac{\partial S}{\partial t_m} = \frac{\partial}{\partial z_m}[K(h_p)_m\frac{\partial}{\partial z_m}(h_{pm}+\frac{1}{h_e})] \tag{5.31}$$

The length and time ratios are then:

Length:
$$\frac{z_m}{z_p} = \frac{h_{em}}{h_{ep}} = \frac{(\frac{h_{ep}}{N})}{h_{ep}} = \frac{1}{N} \tag{5.32}$$

$$\text{Time:} \quad \frac{t_m}{t_p} = \frac{\dfrac{\phi h_{em}}{K_{max}}}{\dfrac{\phi h_{ep}}{K_{max}}} = \frac{1}{(N)(N)} = \frac{1}{N^2} \tag{5.33}$$

which yields the same relationships derived using dimensional analysis and Corey's (1990) transformation. In addition, the scale factors now have a physical meaning and can be physically measured after a drainage test has occurred by measuring the height of the capillary fringe.

5.3 - Centrifuge set-up

The basic rigid wall permeameter apparatus used for the saturated flow experiments was modified for the unsaturated flow test program. To maintain controlled boundary conditions for the drainage experiments, the bottom of the sand column drained into an artificial fluid level container with an overflow outlet. Between the bottom of the sample column and the artificial fluid level was a gate valve. When flow started, the fluid from the sample flowed through the overflow outlet and drained into the collection cylinder. The addition of the artificial fluid level required reconfiguring the entire apparatus on the centrifuge basket so that the collection cylinder was located below the fluid table overflow. All of the 1g prototypes and centrifuge models were placed on the basket and the electronic data acquisition system was used for all tests under the same conditions.

A series of tests was performed to select the best combination of porous stone or

106

filter screen, valves, and tubing. The boundary conditions were found to be sensitive to the type of porous stone or filter screen used at the bottom of the column to retain the sand. The fine filter screens became capillary barriers themselves, even though they were located below the artificial fluid level. Brass, ceramic, and plastic porous stones were used in place of the filter screen. The plastic porous stones were found to perform the best. Table 5.1 and Figure 5.6 show the modeling of models dimensions, g-level, and a schematic of the centrifuge apparatus.

Table 5-1. Model dimensions

Length (cm)	g-level	Location of Transducers (cm)
200.0	1 g	20, 40, 80, 120, 180
20.0	10g	2, 4, 8, 12, 18
13.3	15g	2, 4, 8, 12
10.0	20g	2, 4, 8
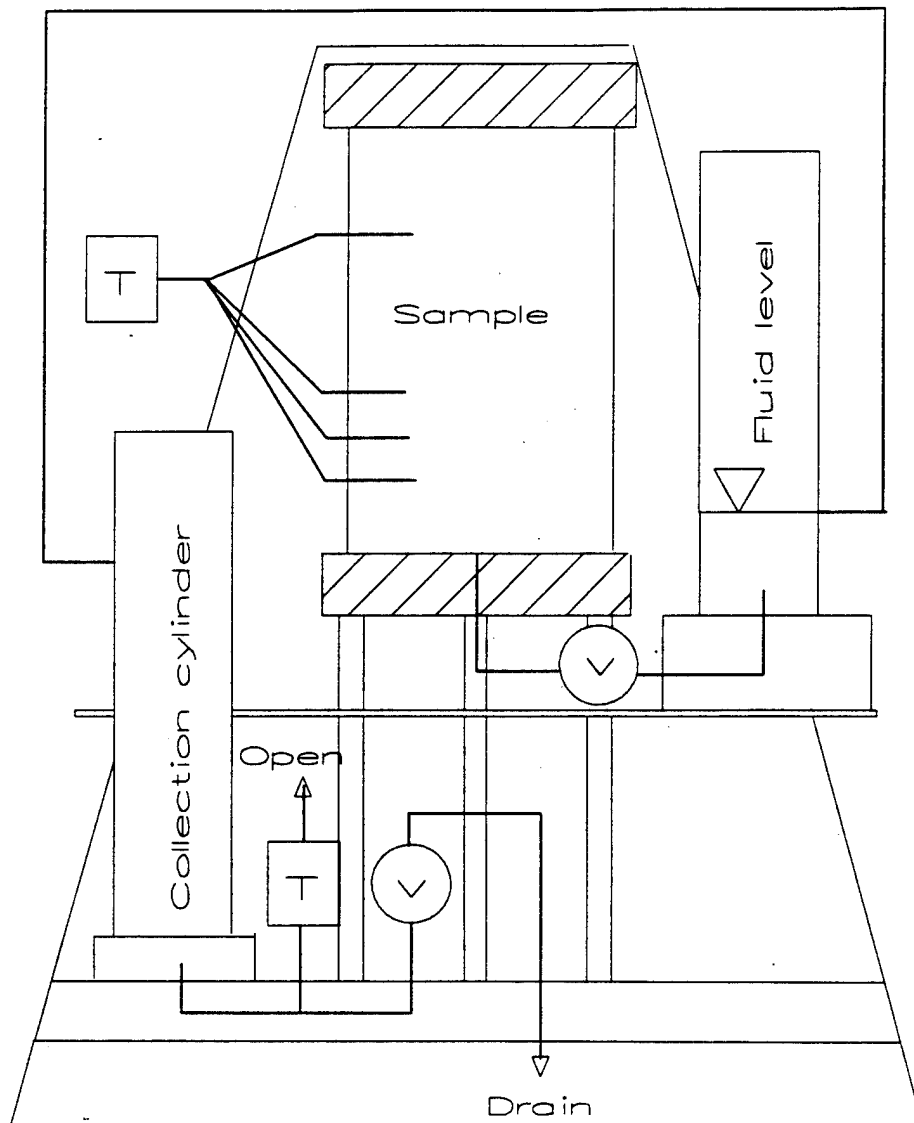
Figure 5-6. Unsaturated flow column (side view)

A major problem was encountered with the selection of the solenoid valve used to control the drainage rate. The solenoid valves used for the saturated flow impeded the flow due to their small orifices and did not perform well in unsaturated flow. Larger orifice solenoid valves, both diaphragm and plunger types, failed to overcome the head loss problem. The solution was to use a 1/2" gate valve driven by an air pressure actuator and mechanical linkage. After verifying the ability of the system to operate properly, the experimental procedure had to be refined.

In the first test series, a significant problem was the inability to completely saturate the sample. Several tests were performed by placing dry sand in the cylinder and then applying suction to the top and allowing the sample to saturate from the bottom. Invariably, air always became entrapped at the plexiglass/sand interface and the internal air distribution was unknown. To overcome this problem, the column was filled with fluid and a known amount of sand was rained through the fluid. The column was tapped and vibrated until the sand height reached the desired level. The fluid level was lowered to the top of the sand column and the unsaturated flow test was performed by draining the column. After the test was complete, the height of the fluid in the collection cylinder was measured and then drained and weighed to provide two independent measures of the total volume. The sand sample was then removed by siphoning the sand from the cylinder by using a plastic hose and fluid. The sand was siphoned into a separate plastic container and, after refilling the test apparatus with fluid, the same sand was rained into the fluid to perform the next test. In this manner, excellent repeatability was ensured with variations in the porosity of only a few percent.

109

5.4 - Pore pressure transducers

The measurement of pore pressures in a desaturating column has previously been shown to be one of the more difficult tasks to accomplish (Ibrahim, 1990; Walser, 1994). Ideally, the transducer should be small, relative to the pore size, to eliminate any influence of the transducer on the flow field. Druck PDCR-81 miniature pressure transducers were selected due to their small size. Their maximum pressure ranges were from 0.70 m to 10.50 m of water column. The transducers have a ceramic porous stone at the end which prevents the porous material from contacting the metal membrane directly. The stone and the space between the stone and the membrane must be saturated for reliable measurements of pore pressures. The transducers were extensively tested using positive and negative heads and kept fully saturated to ensure the calibrations were linear and passed through the zero point.

To calibrate the transducers, they were placed in a calibration cell which was connected to a head source. The calibrations were done at both normal gravity and in the centrifuge. The normal gravity tests were accomplished by using a manometer board and the data acquisition system. The head source was raised or lowered and the manometer board manual reading and data acquisition system voltage were compared. The data acquisition system collected 15 seconds of data which would be averaged to give a voltage for the given head. In the centrifuge, the sample column was used with the transducers installed in the side ports. Increments of four centimeters of water were used, first at 1g, and then with the centrifuge spun to the desired g-level. Figures 5-7 and 5-8 show typical calibration test results of the transducers.
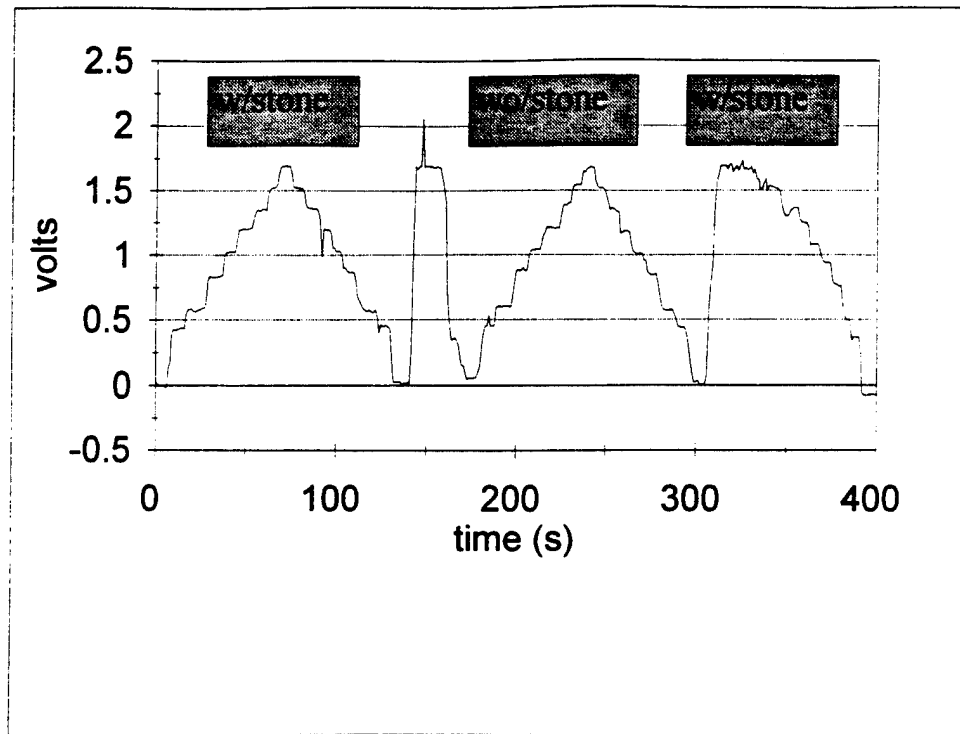
Figure 5-7. Transducer calibration with and without the porous stone.
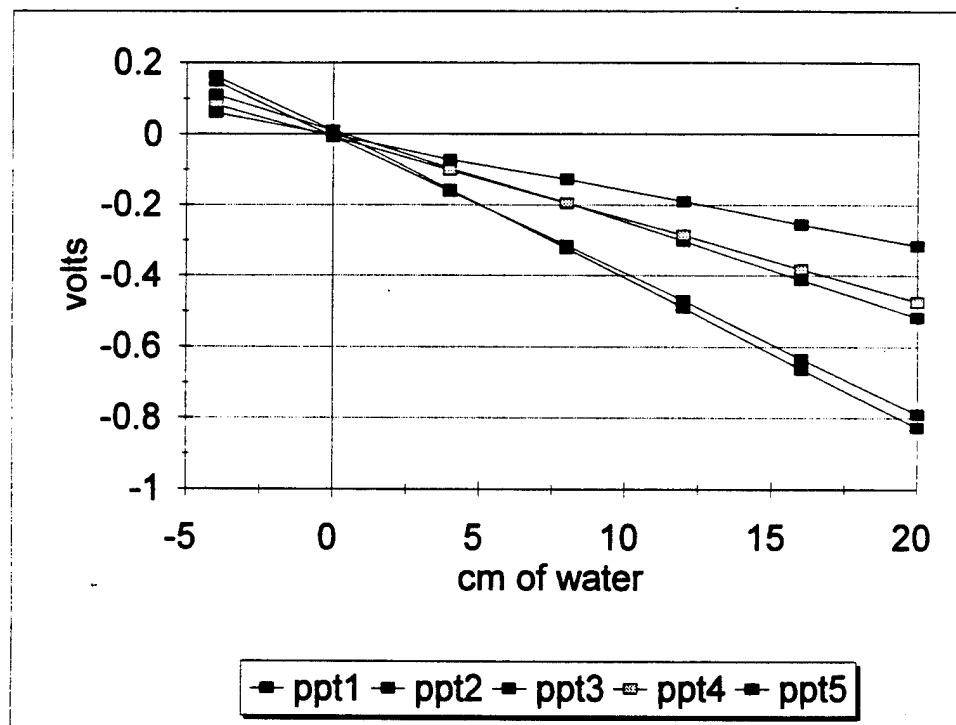
Figure 5-8. Transducer calibration with positive and negative heads

111

Figure 5-7 shows the calibration with the porous stone in place and with the porous stone removed. The steps shown are for different head levels and indicate that the stone and the space behind are fully saturated. The average voltage for different head levels are plotted in Figure 5-8 which shows the transducer's voltage response to each four-centimeter head change is linear and passes through the zero point.

5.5 - Water prototype experimental results

The prototype experiments were conducted using #70 sand in a 200 cm column. The #70 sand was chosen due to its capillary rise and hydraulic conductivity; the capillary fringe is well defined and the hydraulic conductivity is low. The #70 sand used for the unsaturated tests was not the same sand used for the saturated tests due to a change in suppliers. The hydraulic conductivity of the new #70 sand of 0.02 cm/s was slightly greater than the old #70 sand.

Two methods of placing the sand were used: dry and wet. The dry sand was saturated by placing the column under suction for several hours and then adding de-aired water. The wet method involved raining the sand through the water. The dry method did not produce 100% saturation, while the wet method did. The initial fluid level was at the top of the sand, and at the beginning of the drainage test, a gate valve was opened allowing the column to drain. Two tests were conducted to measure cumulative outflow of the water using a small diameter collection cylinder connected to a pressure transducer. The test results are shown in Figure 5-9.

112
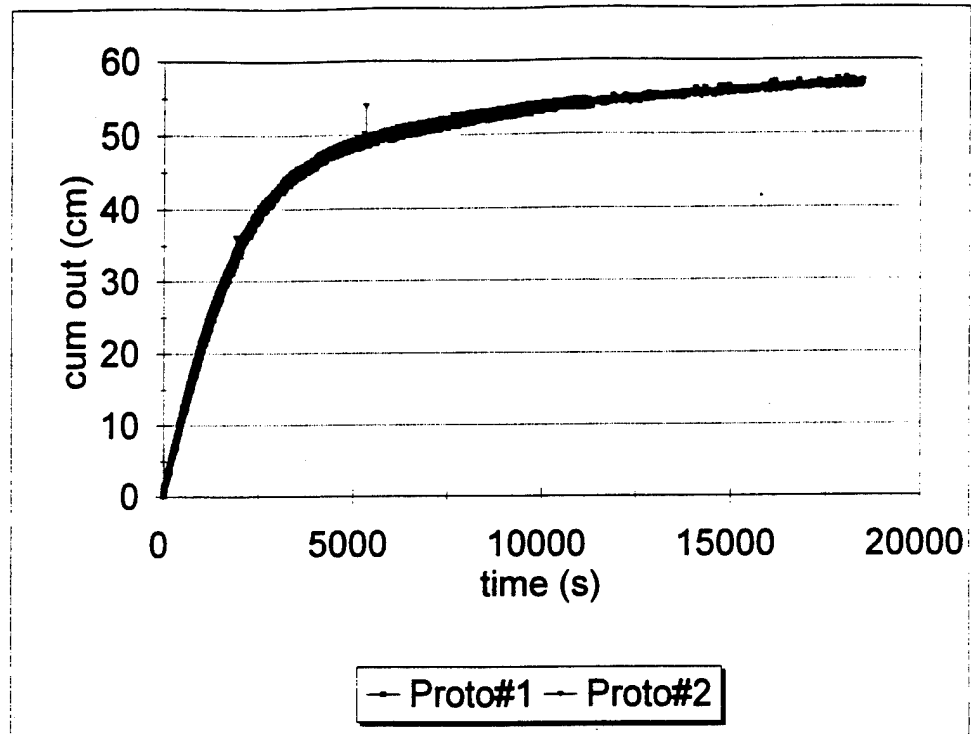
Figure 5-9. Water and #70 sand prototype 200 cm column cumulative outflow

To check the system, the initial portion of the curve was used to compute the initial Darcy velocity which should equal the saturated hydraulic conductivity. The initial experimental hydraulic conductivity from Figure 5-9 is:

$$K_{sat} = \frac{20}{1040} = 0.0192 \ cm/s \tag{5.34}$$

The cumulative outflow fluid volumes were also measured by using calibrated flasks and by weight. Several tests to determine the porosity yielded very consistent results of $\phi = 0.45$ to 0.46.

Having obtained repeatable results for cumulative outflow, the Druck miniature

pore pressure transducers were installed and the tests repeated. The pressure heads measured by the Druck transducer can be compared to the theoretical pressure head distribution shown in Figure 5-10. At the beginning of the test with no flow, the system has a hydrostatic pressure distribution (t = 0-). At the moment when the valve is opened and the drainage process begins, the pressure head instantaneously drops to zero and the total head equals the elevation head, thus giving a gradient of one (t = 0+). After drainage is complete, the new water table is at the bottom of the column and the soil sample is in suction with a negative hydrostatic pressure distribution (t = infinity).
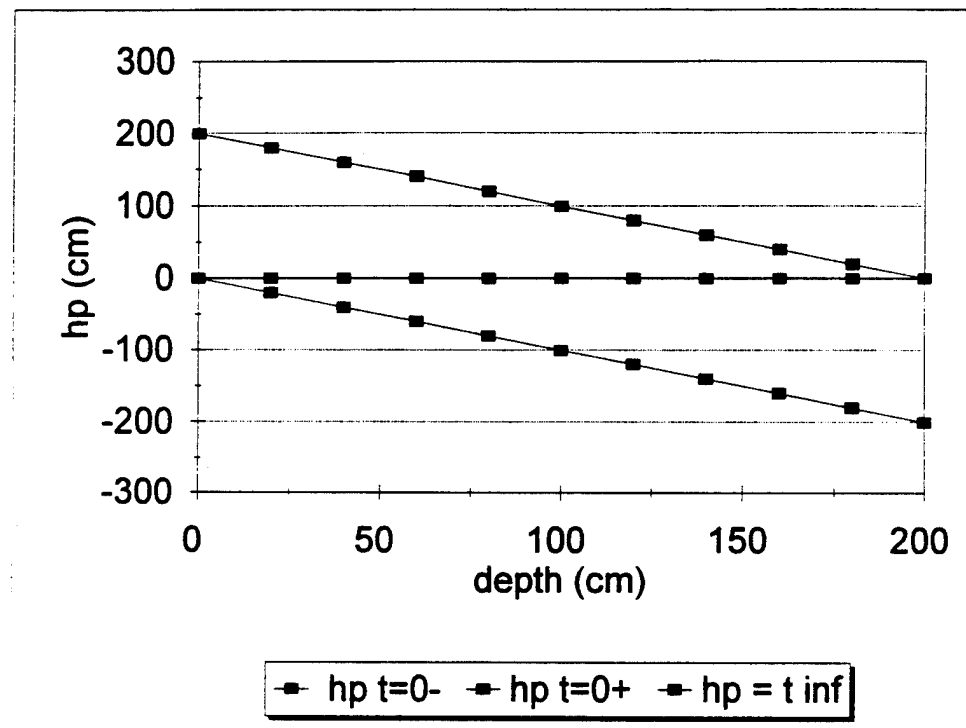
Figure 5-10. Theoretical pressure head distribution

114

The prototype, with the transducers installed, test results are shown in Figures 5-11 and 5-12 in the form of a cumulative outflow curve and pore pressures profiles with time. The cumulative outflow curve shown is the actual collection cylinder measurement and is not corrected for the areas of the collection cylinder and soil sample.

Figures 5-11 and 5-12 show that as the column drains, the transducers go into suction until the pore space fluid becomes discontinuous, at which point the transducers can no longer measure the actual pore pressure. The sudden break indicates the suction reduction takes place at approximately 50 to 60 cm of water column. Figure 5-11 illustrates that two transducers, #3 and #5, are malfunctioning. Transducer 1 is at a location of 20 cm above the water table and is expected to remain fully saturated, based on the height of the capillary fringe.
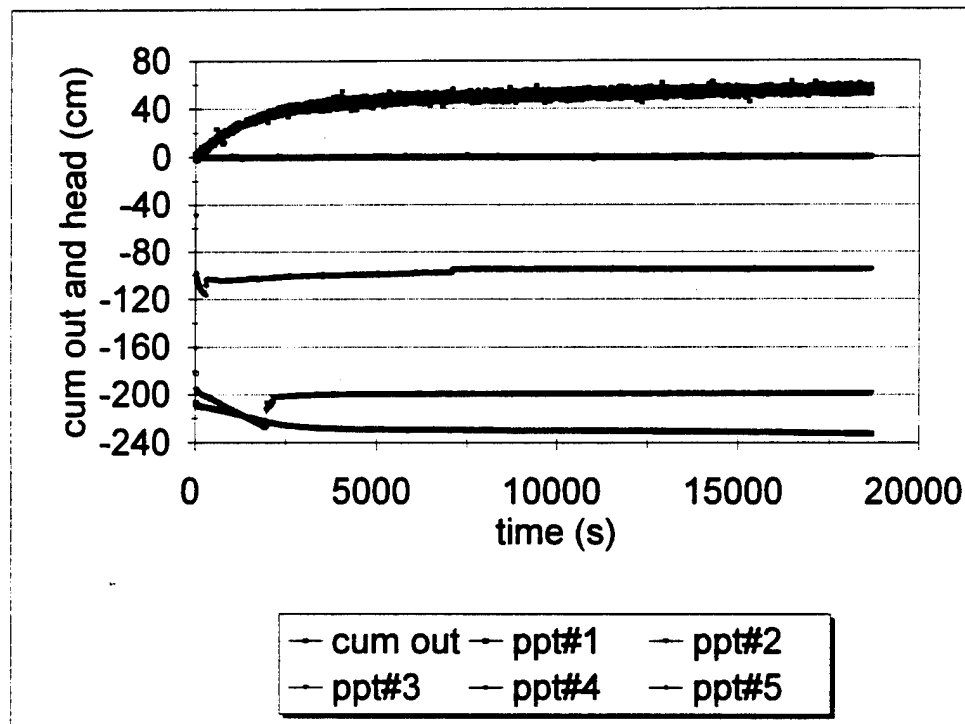
Figure 5-11. Water and #70 sand prototype drainage and pore pressures
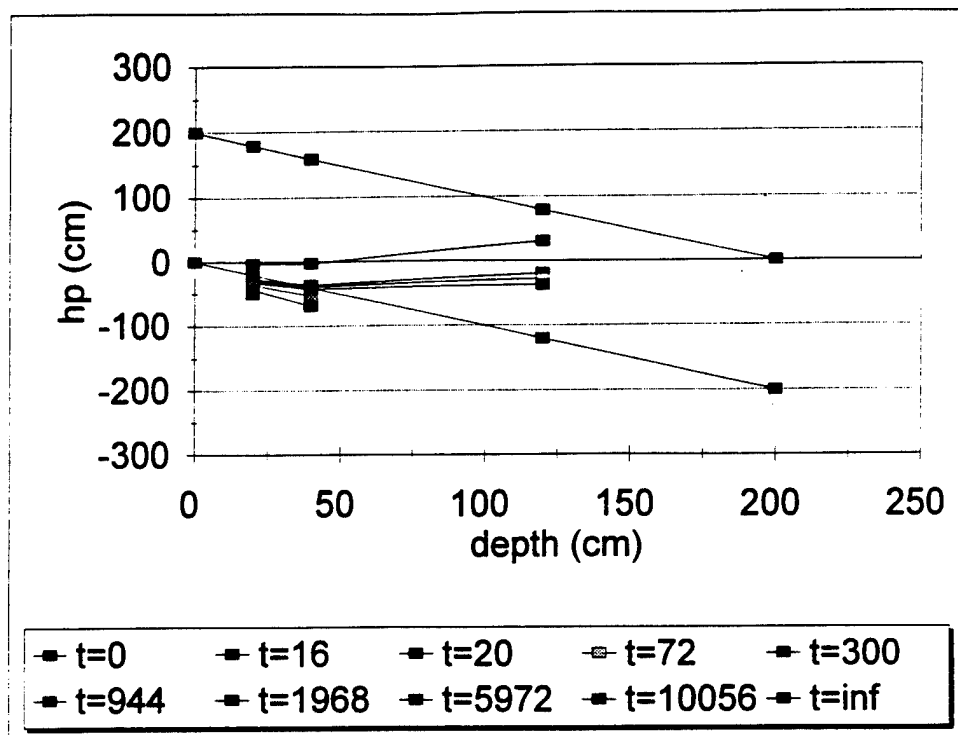
Figure 5-12. Water pore pressure profiles

From Figure 5-12, the pore pressure plots indicate final suctions below hydrostatic values near the bottom boundary. The drainage arrangement at the boundary could be responsible for the effect. To check boundary conditions, the water table was raised 2 cm, a transducer was placed below the water table, and the water prototype test repeated. The results are shown in Figure 5-13. The cumulative outflow curve is shown in Figure 5-14 and falls below the cumulative outflow curves of Figure 5-9. Figure 5-15 was generated by allowing the test to run an additional 24 hours. The pore pressure profiles are shown in Figure 5-16 and in this case, the transducers measured final pressures lower than hydrostatic.
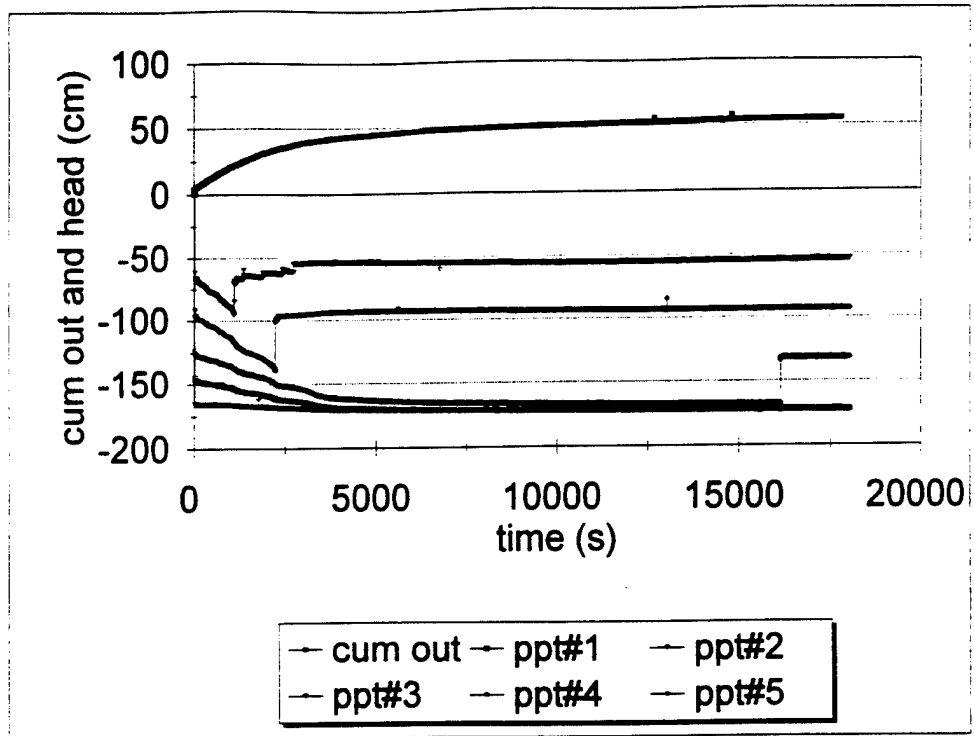
Figure 5-13. Water and #70 sand prototype drainage and pore pressures
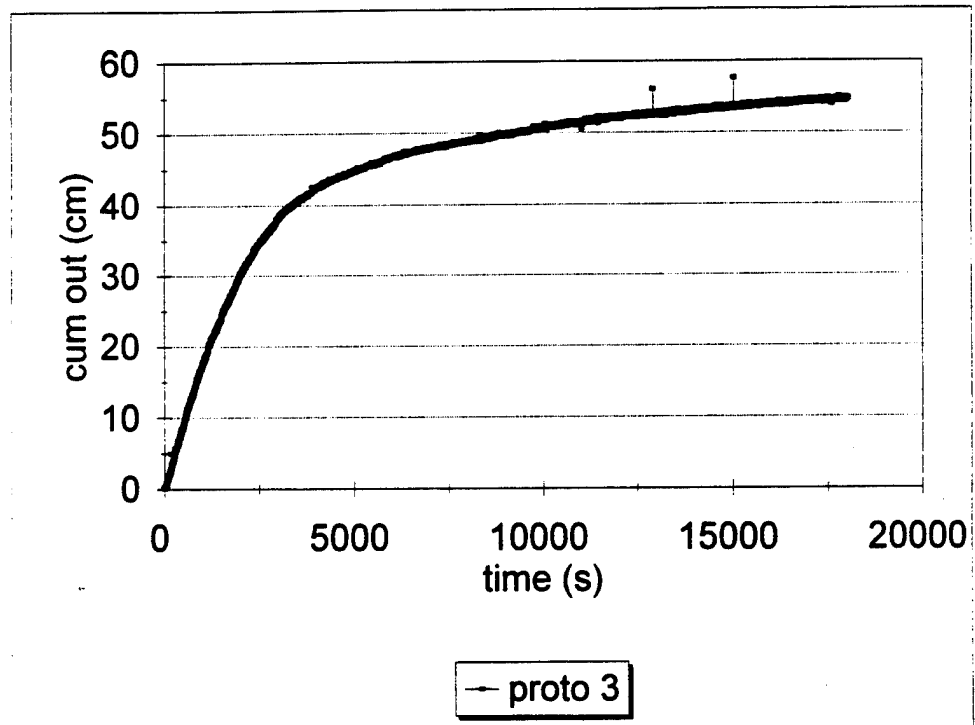
Figure 5-14. Water and #70 sand prototype 200 cm column cumulative outflow

117
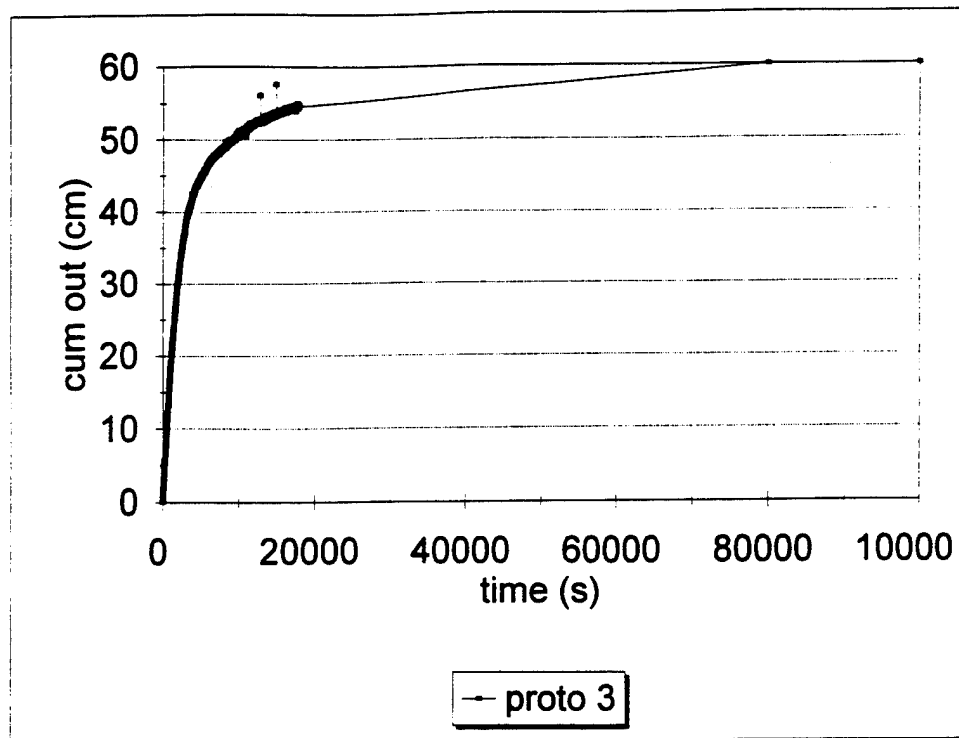
Figure 5-15. Water and #70 sand prototype 200 cm column cumulative outflow
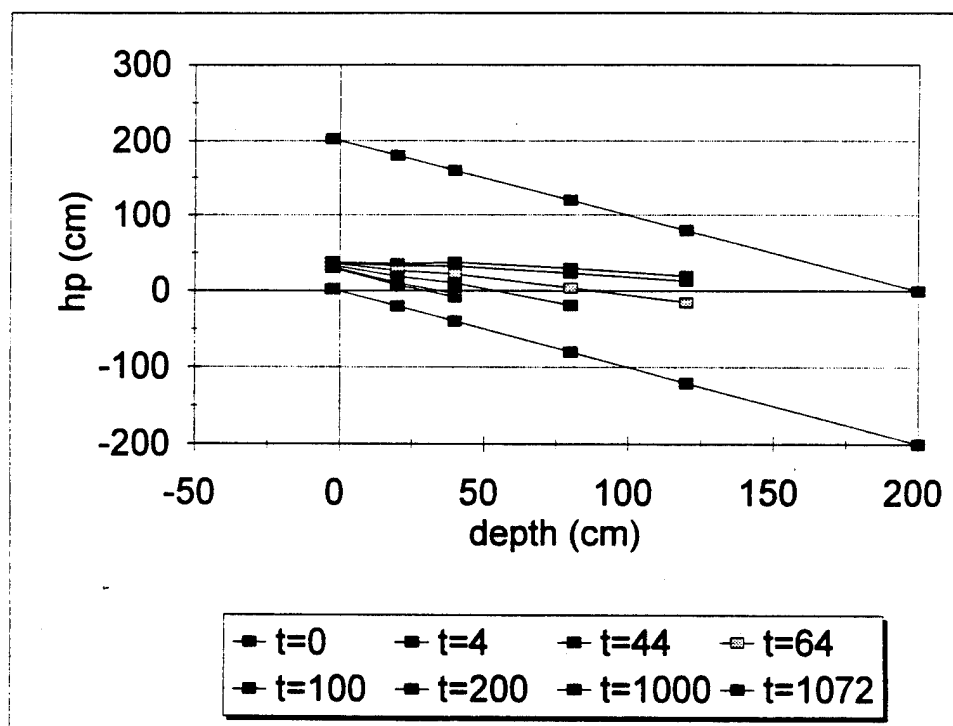
Figure 5-16. Water pore pressure profiles with raised water table

From these experiments, it appears the boundary conditions create an unexplained suction which impacts the drainage rate. Additional suction speeds up the drainage process and reduced suction slows the drainage process. However, the variation in suction does not drastically alter the cumulative outflow curves. The slope of the final pore pressure distributions with either test have the same slope as the theoretical hydrostatic pressure distribution.

5.6 - Soltrol prototype experimental results

The same apparatus and test procedures used for the water experiments were used to perform a drainage test using Soltrol. Figure 5-17 shows the results of the first two tests to determine repeatability. The differences in the density, viscosity, and interfacial tension of the two fluids are reflected in the difference in the shape of the outflow curves. Unexpectedly, the total cumulative outflow volumes for the water and Soltrol were almost identical. If the outflow rates were dependent upon only density and viscosity, then the final drainage time for an equivalent amount of Soltrol would be expected to be six times longer than for water. The lower interfacial surface tension of Soltrol (27 dynes/cm versus 72 dynes/cm) appears to accelerate the drainage. Figure 5-18 illustrates the drainage test with the transducers installed, and Figure 5-19 shows the pore pressures profiles.
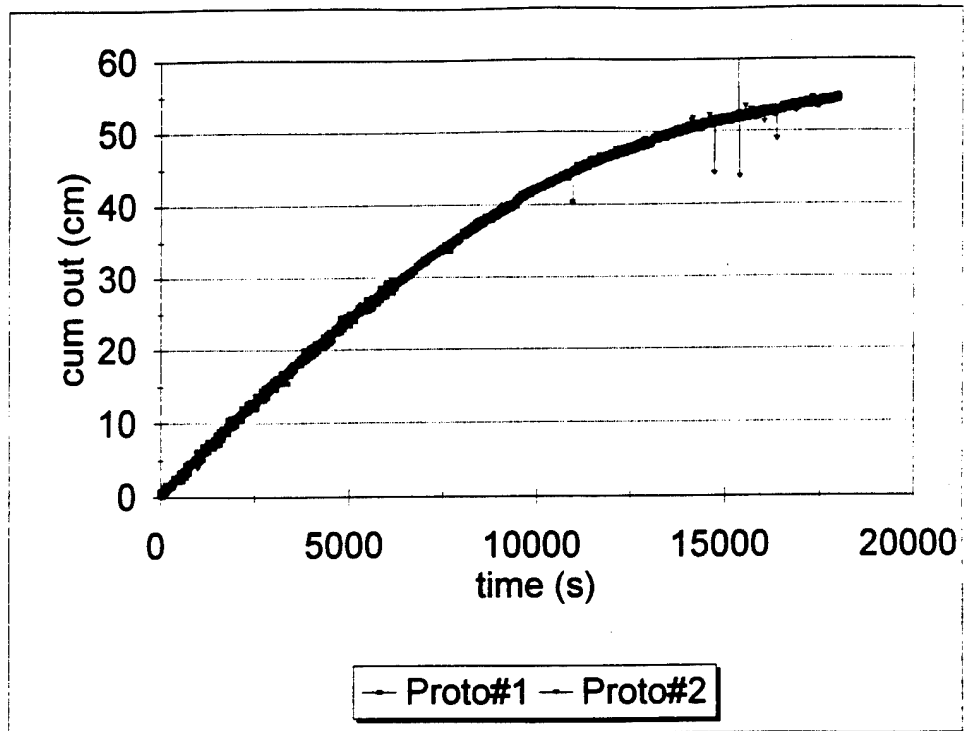
Figure 5-17. Soltrol and #70 sand prototype 200 cm column cumulative outflow
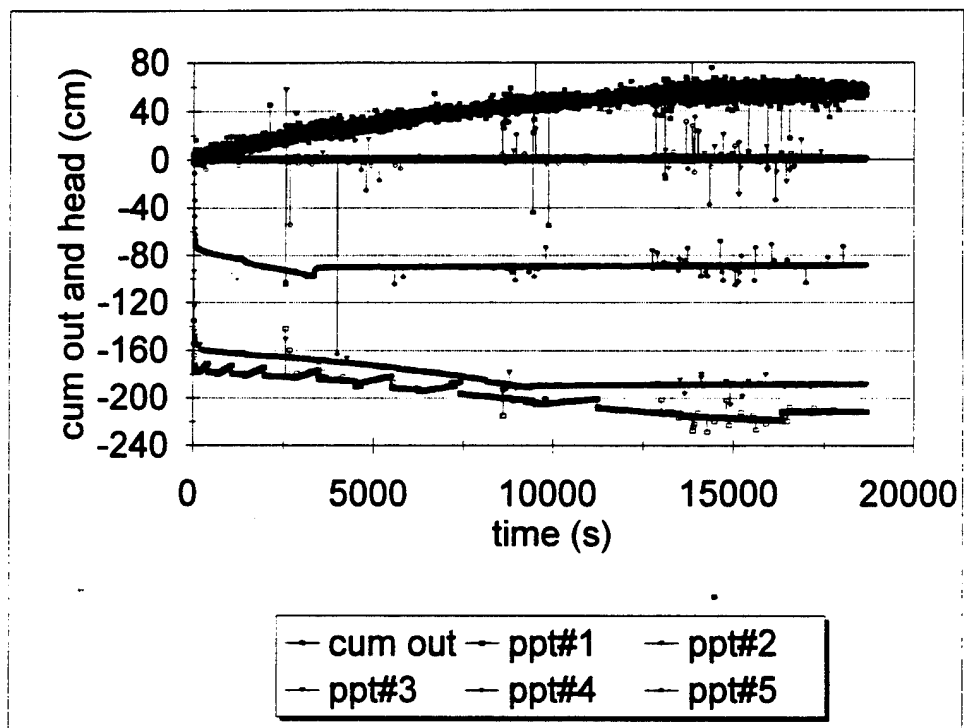
Figure 5-18. Soltrol and #70 sand prototype drainage and pore pressures

120
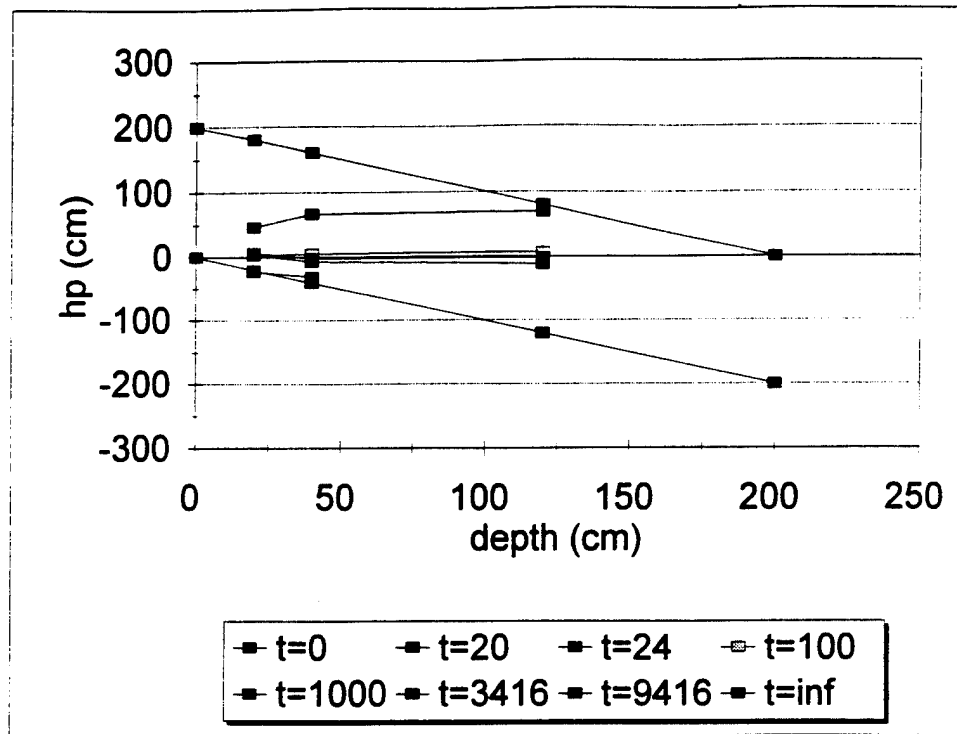
Figure 5-19. Soltrol pore pressure profiles

The prototype experimental data were compared to numerical solutions of the Richards equation. The first code to be used was a commercially available finite element code, PC-SEEP (developed by Geoslope). It is presumed that the program properly accounts for the change in the hydraulic conductivity during the drainage process. The code, however, predicted pore pressure dissipation and cumulative outflows significantly different from those obtained from the experiments. A close examination of the numerical results confirmed that the movement of the drainage front was unrealistic. In discussions with Geoslope, the time stepping algorithm was found to be unreliable for this problem.

A literature review of other researchers' models revealed similar problems. The code developed by Cooke and Mitchell (1991) and plotted in Figure 5-2, for example,

121

was valid only for low permeability soils. The program ran into numerical instabilities when modeling free draining soils. A general code that can be used for this analysis has been developed by Durnford and Marinelli (1995) and was used to predict cumulative outflow and pore pressures for these experiments.

Using the suction-saturation and relative permeability curves of Figure 4-6 and Figure 4-7, the Brooks-Corey parameters were determined and used for model input parameters. The model cumulative outflow results for water are shown in Figure 5-20 and for Soltrol in Figure 5-21. A pressure head plot for water is shown in Figure 5-22. While the models underpredicted the total cumulative outflow, the shape of the cumulative outflow curves is correct and the pressure head plot generally simulates the observed experimental pore pressures.
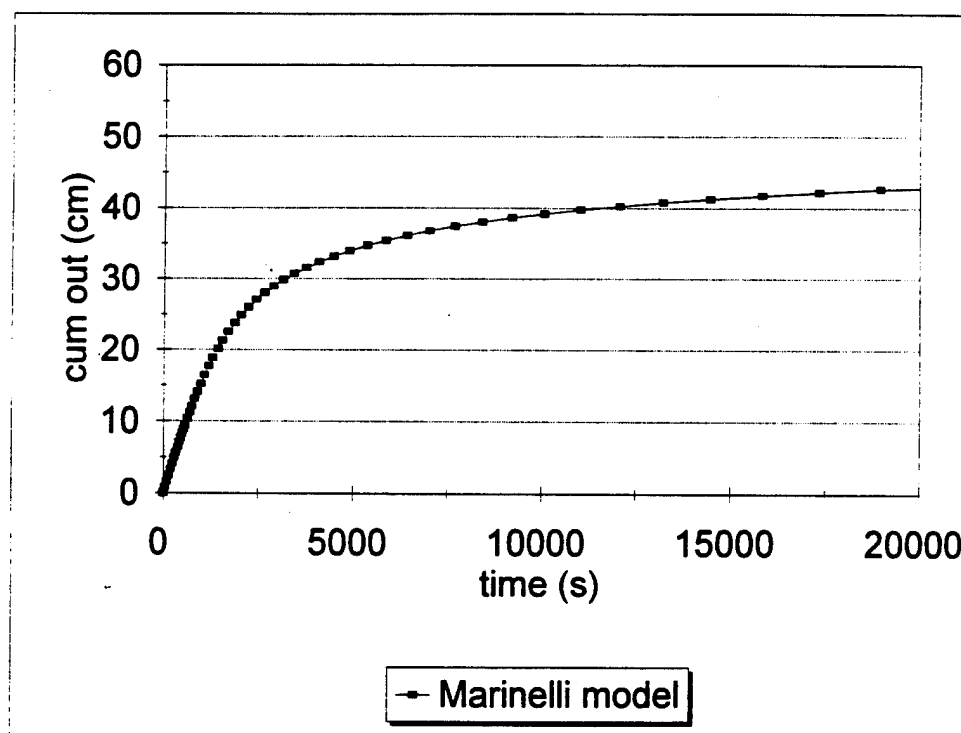
Figure 5-20. Numerical model of prototype water cumulative outflow curve
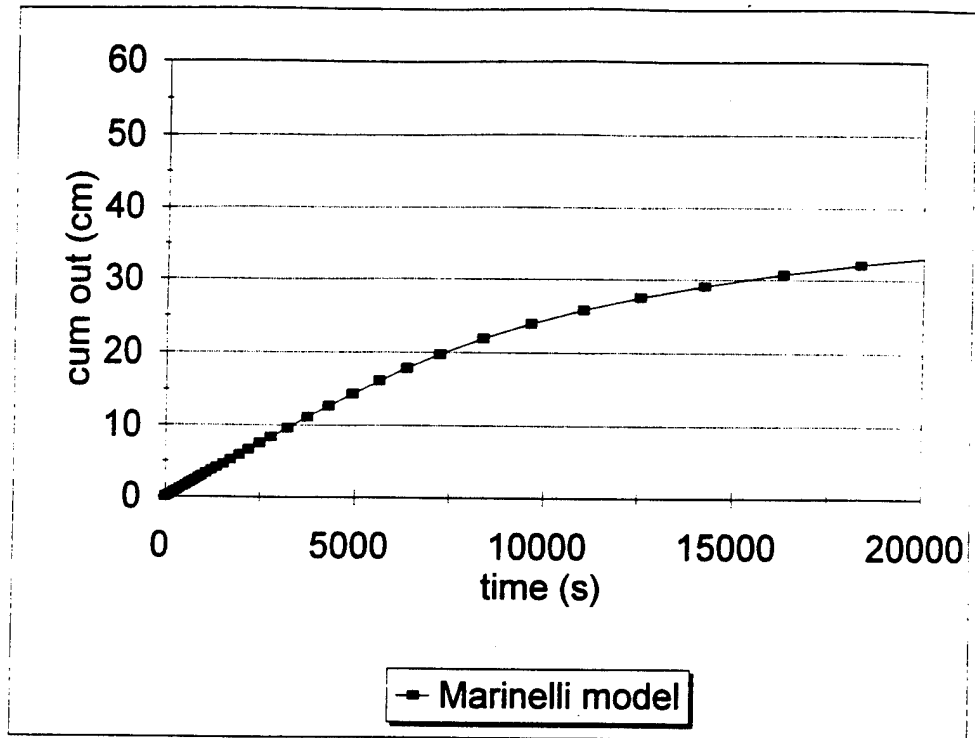
Figure 5-21. Numerical model of prototype Soltrol cumulative outflow curve
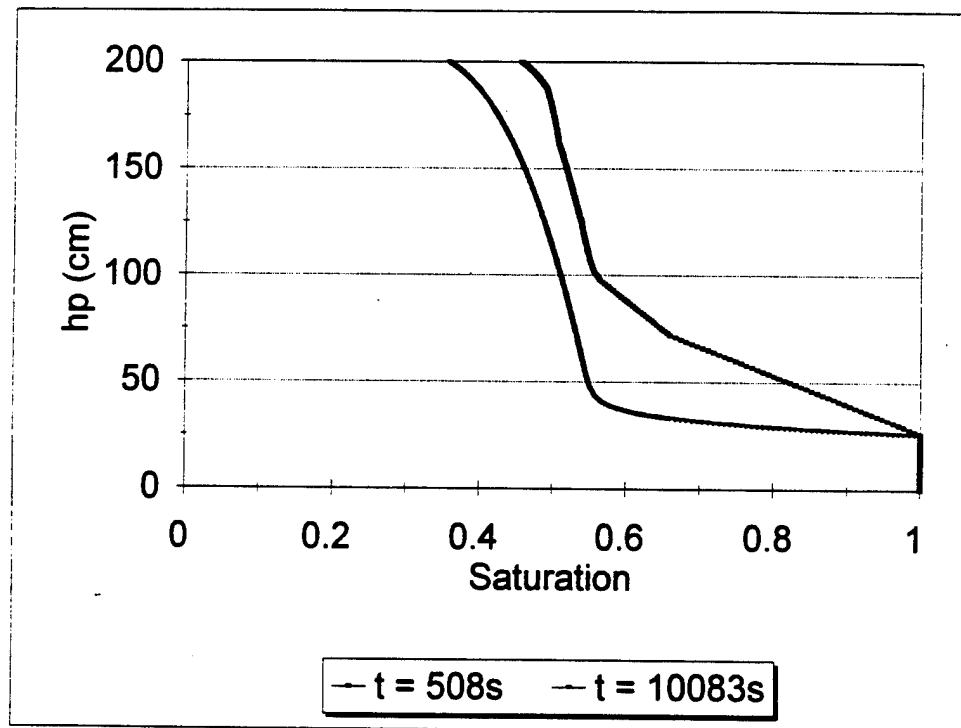
Figure 5-22. Numerical model of prototype water pressure head

5.7 - Modeling of models using water experimental results

The modeling of models tests was conducted in order to verify the scaling relationships described in Section 5.2. Both the small and the large centrifuge were used to determine if the effect of the arm radius as predicted by Corey (1990) was observable. A series of tests was performed with the artificial fluid level at two different locations similar to the prototype tests to determine the effect of the boundary conditions.

The first tests were performed in the small centrifuge with a low artificial fluid level at the bottom boundary similar to the prototype of Figure 5-9. Figures 5-23 through 5-25 are the modeling of models tests raw data using water and #70 sand and show the excellent repeatability of the system. The system configuration and sample preparation procedure appears to overcome the repeatability problems experienced by Goforth et al. (1991).

The first test series cumulative outflow curves in the small centrifuge appear to capture the proper behavior of the prototype. A second series was run with the pore pressure transducers installed. Figures 5-26 through 5-28 are the raw data plots.

The water table was raised 2 cm and a series of tests performed to determine the effect of the boundary condition. Figures 5-29 through 5-31 are the raw data plots.
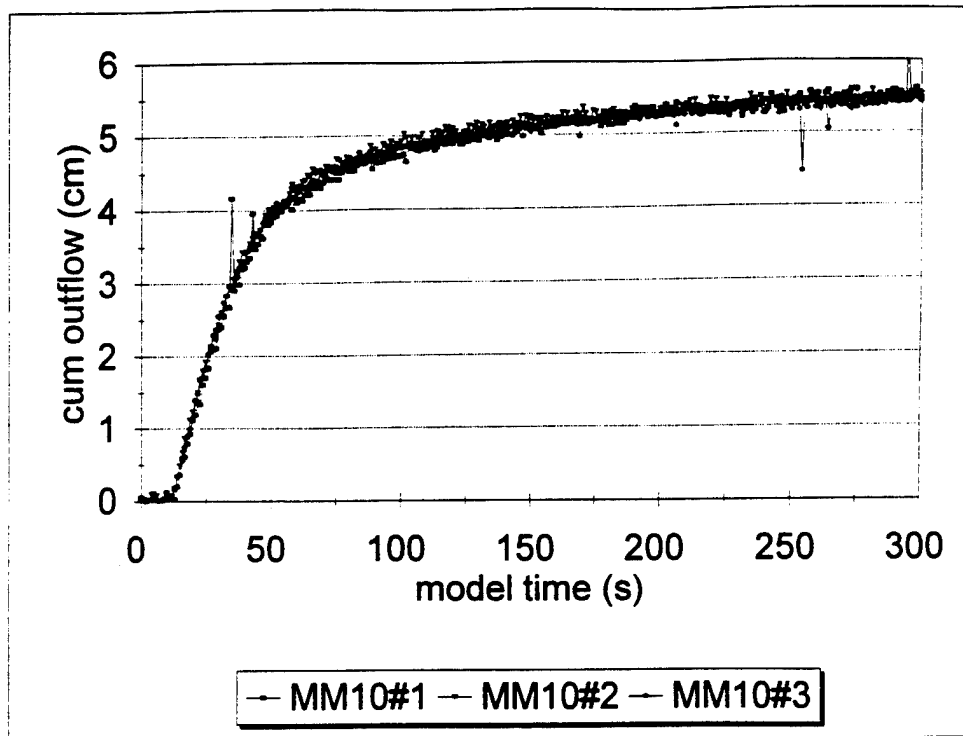
Figure 5-23. Modeling of models 10g tests raw data using water
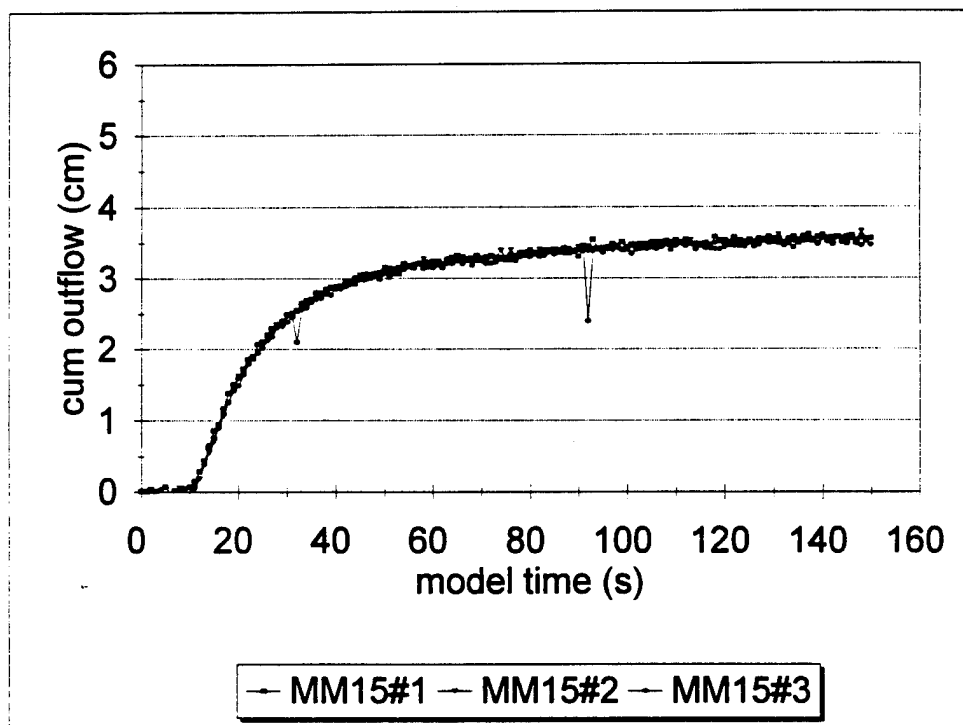
Figure 5-24. Modeling of models 15g tests raw data using water
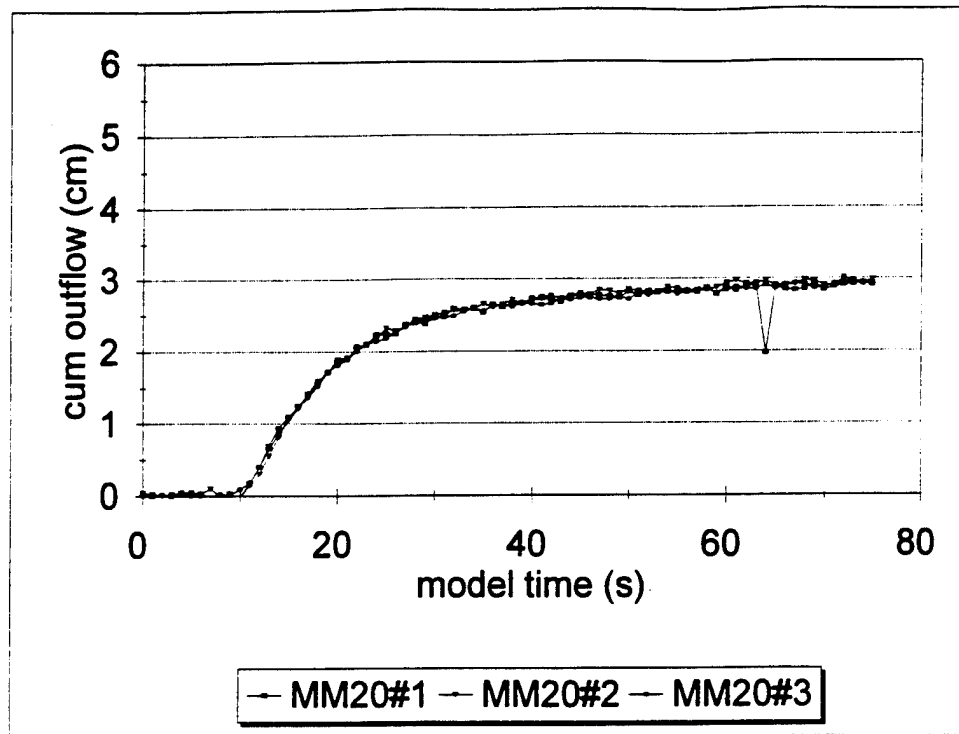
Figure 5-25. Modeling of models 20g tests raw data using water
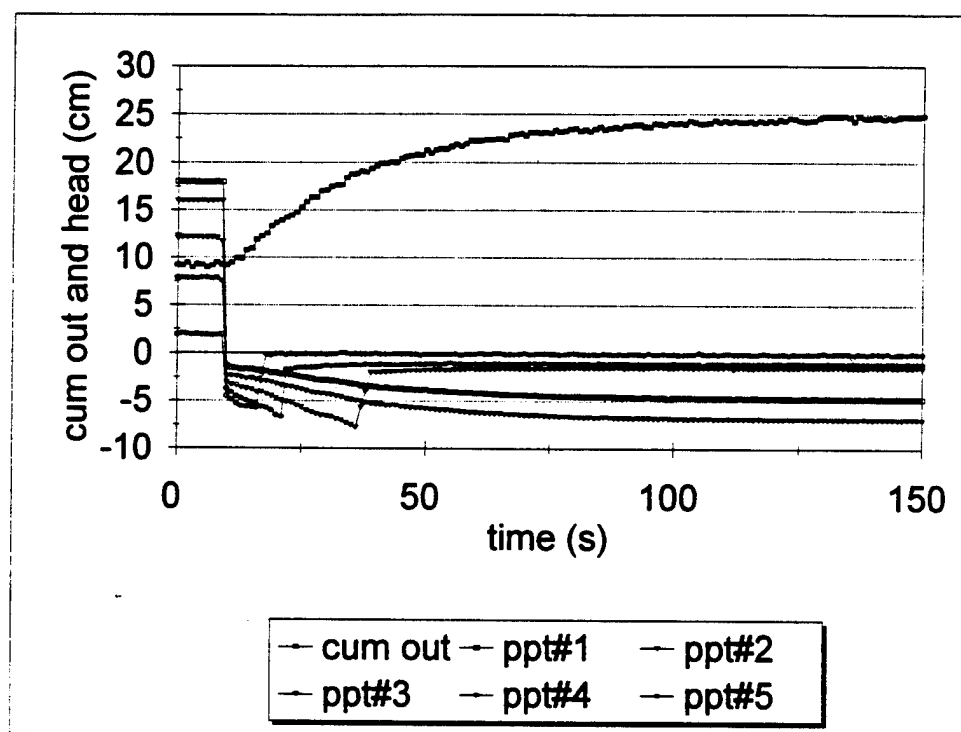
Figure 5-26. Modeling of models 10g test raw data using water

126
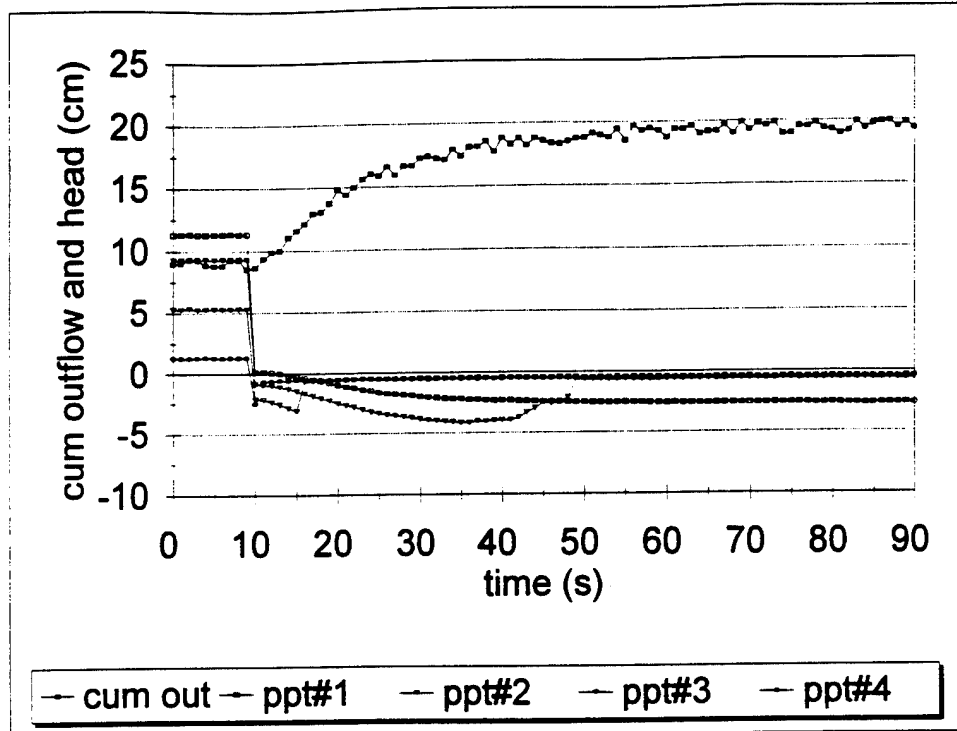
Figure 5-27. Modeling of models 15g test raw data using water
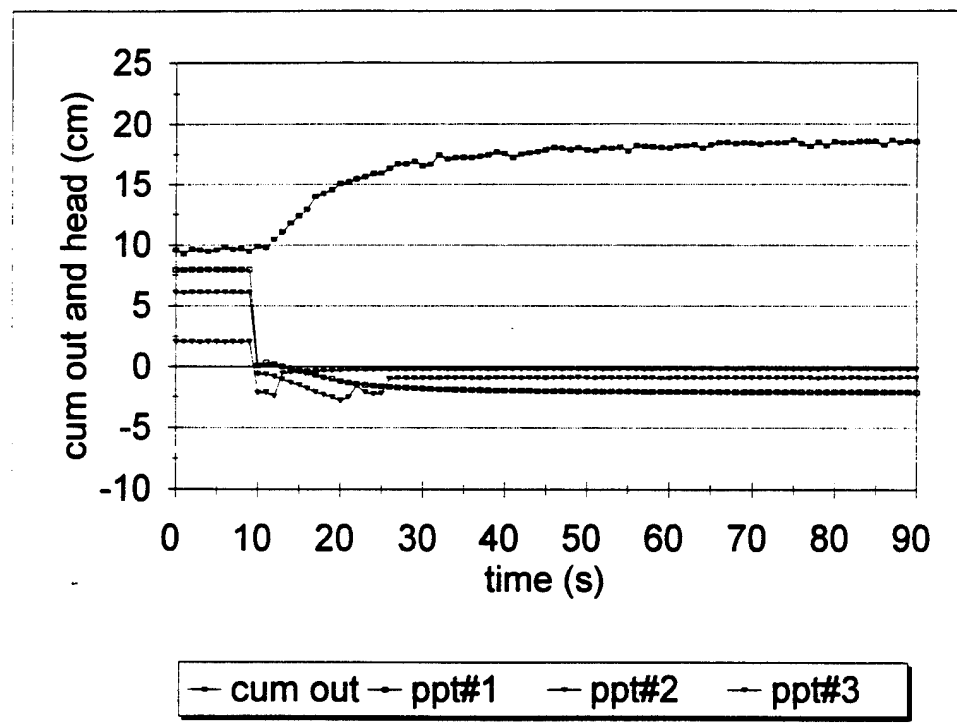
Figure 5-28. Modeling of models 20g test raw data using water

127
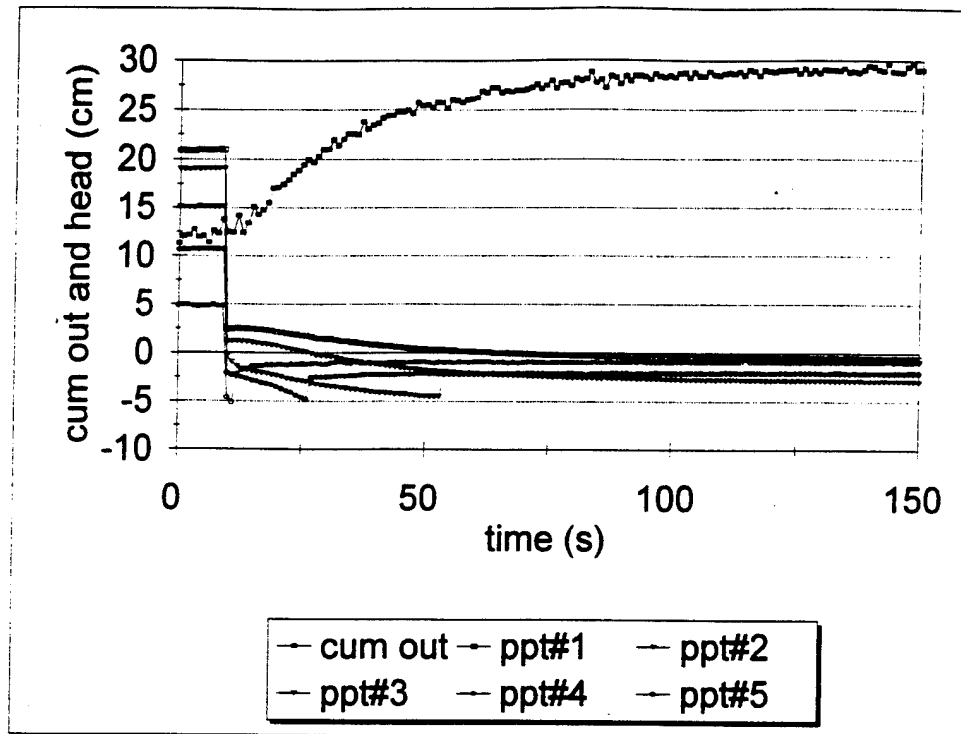
Figure 5-29. Modeling of models 10g test raw data with raised level using water
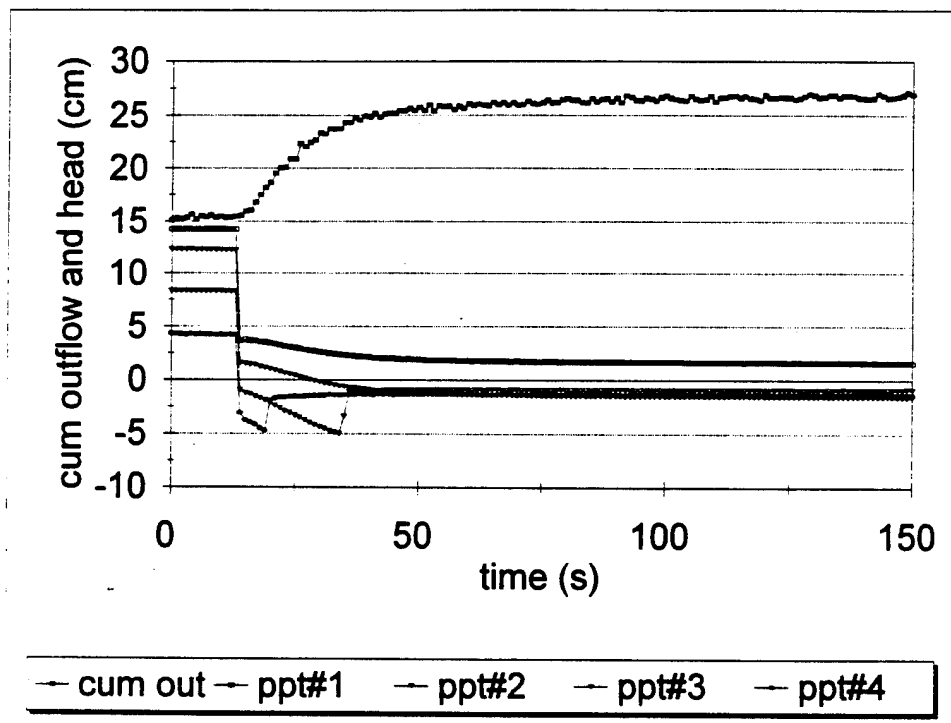
Figure 5-30. Modeling of models 15g test raw data with raised level using water
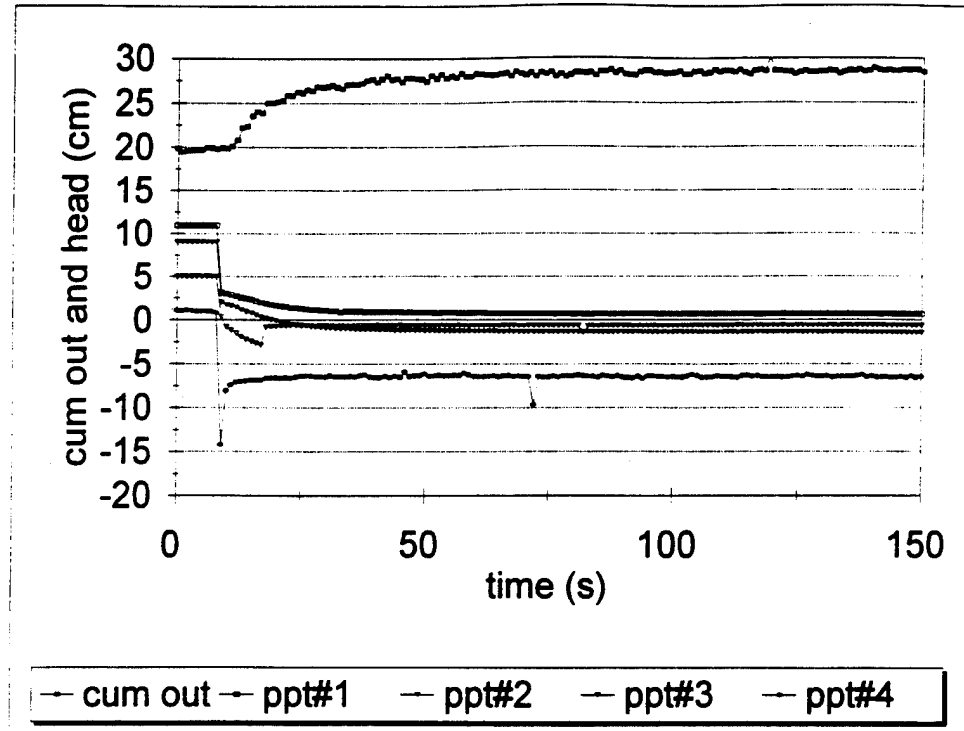
Figure 5-31. Modeling of models 20g test raw data with raised level using water

The following series of tests were run on the large centrifuge. The large centrifuge was able to accommodate a 40 cm column required for a 5g test, but the basket did not rotate into the full horizontal position at 5g's. However, the acceleration vector remained in the axial direction of the sample. This series of tests were run using the lower artificial fluid elevation. Figures 5-32 through 5-35 are the raw data plots.
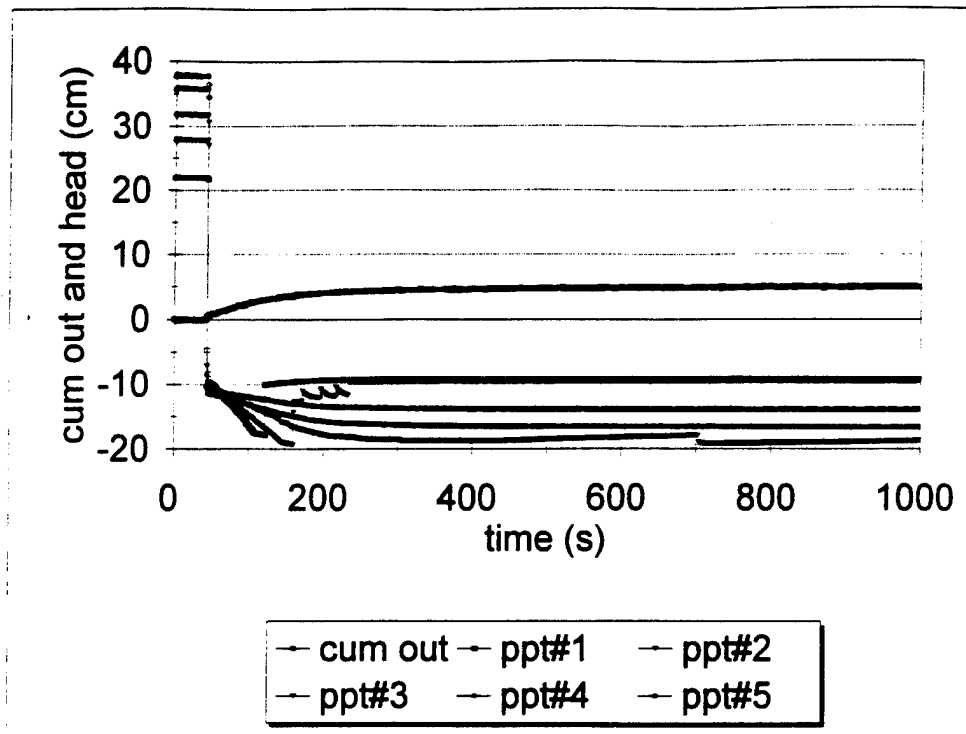
Figure 5-32. Modeling of models 5g test raw data using water in large centrifuge
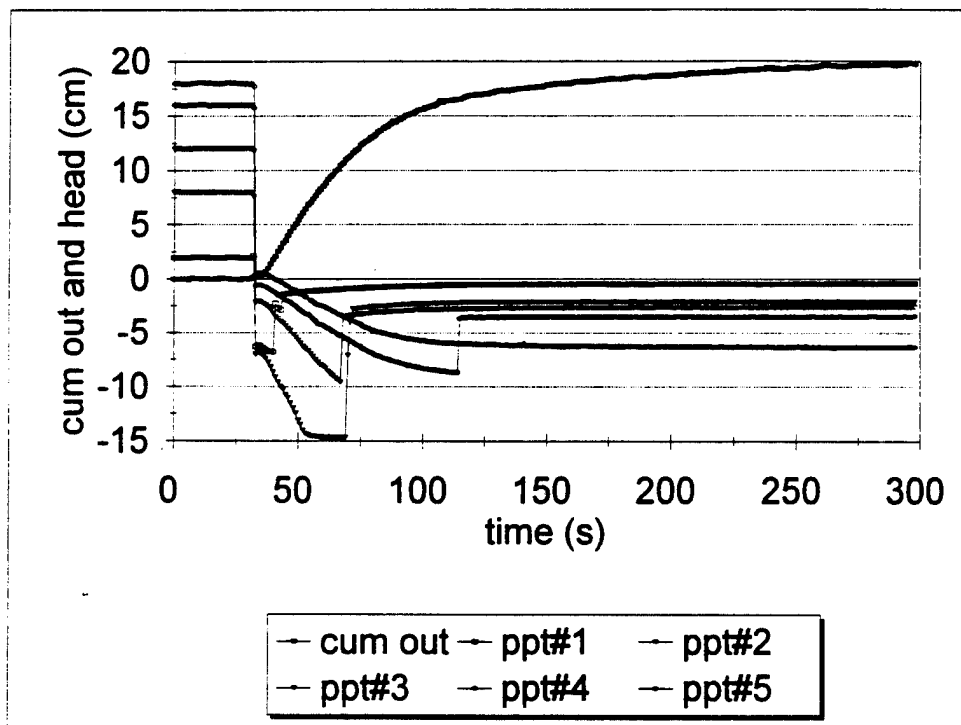
Figure 5-33. Modeling of models 10g test raw data using water in large centrifuge
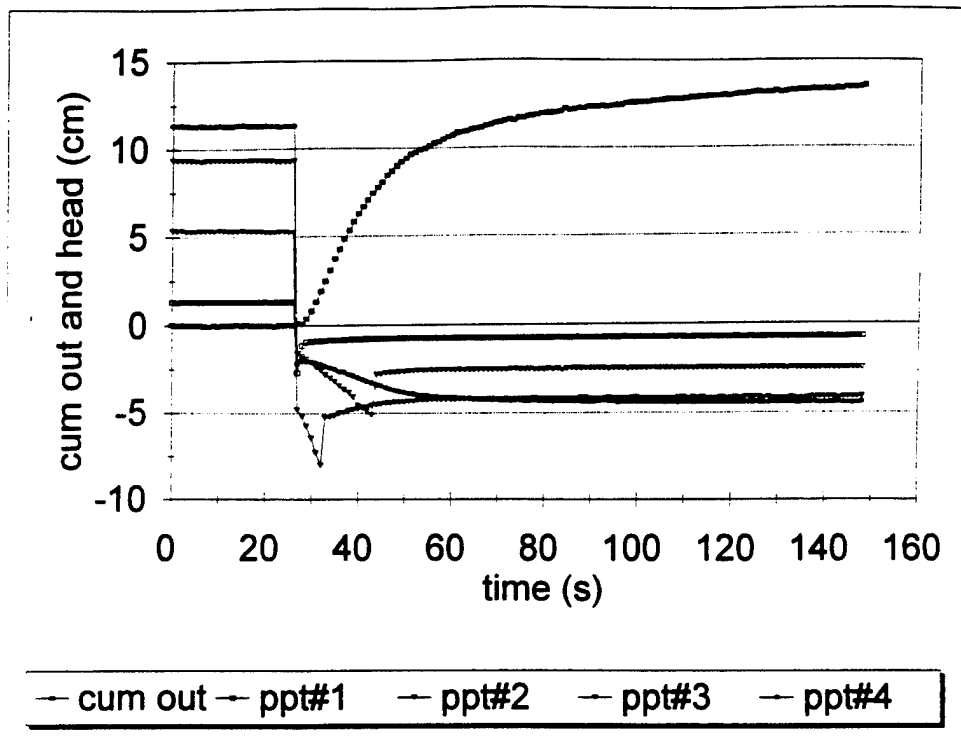
Figure 5-34. Modeling of models 15g test raw data using water in large centrifuge
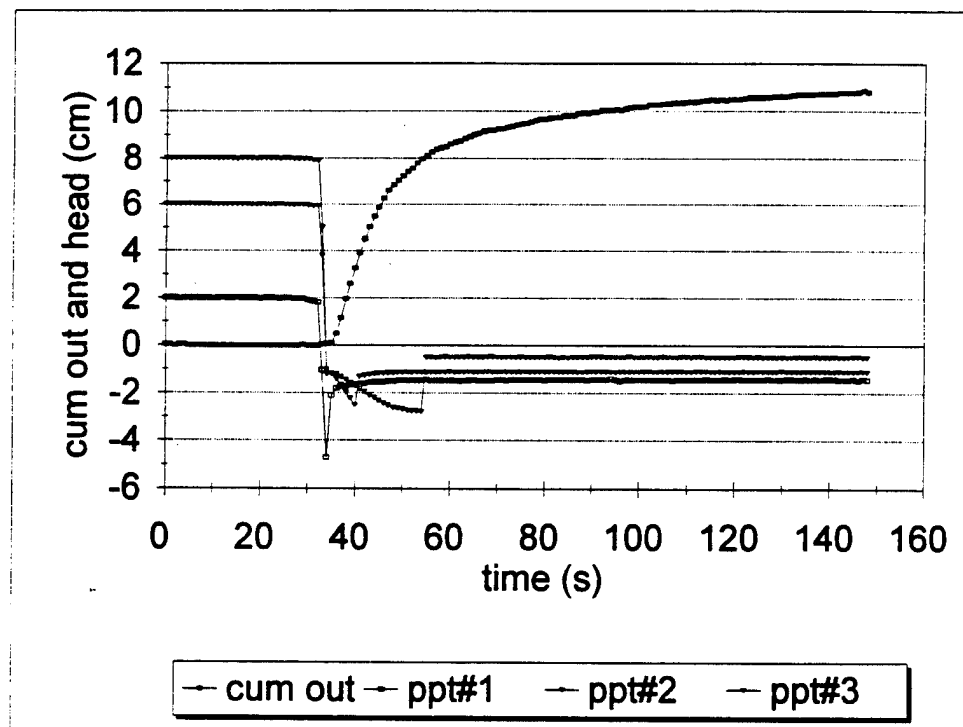
Figure 5-35. Modeling of models 20g test raw data using water in large centrifuge

131

5.8 - Modeling of models using Soltrol experimental results

The same apparatus used for the water tests was used for the Soltrol tests. The

first series of tests was performed in the small centrifuge with a low artificial fluid level

at the bottom boundary, similar to the prototype of Figure 5-17. Figures 5-36 through 5-

38 show the results of the modeling of models tests' raw data using Soltrol and #70 sand

and show the excellent repeatability of the system. The Soltrol curves display some data

scatter; obtaining the same porosity using Soltrol was more difficult compared to water.

The first test series cumulative outflow curves in the small centrifuge appear to capture

the proper behavior of the prototype. A second series of tests were run with the pore

pressure transducers installed. Figures 5-39 through 5-41 are the raw data plots.
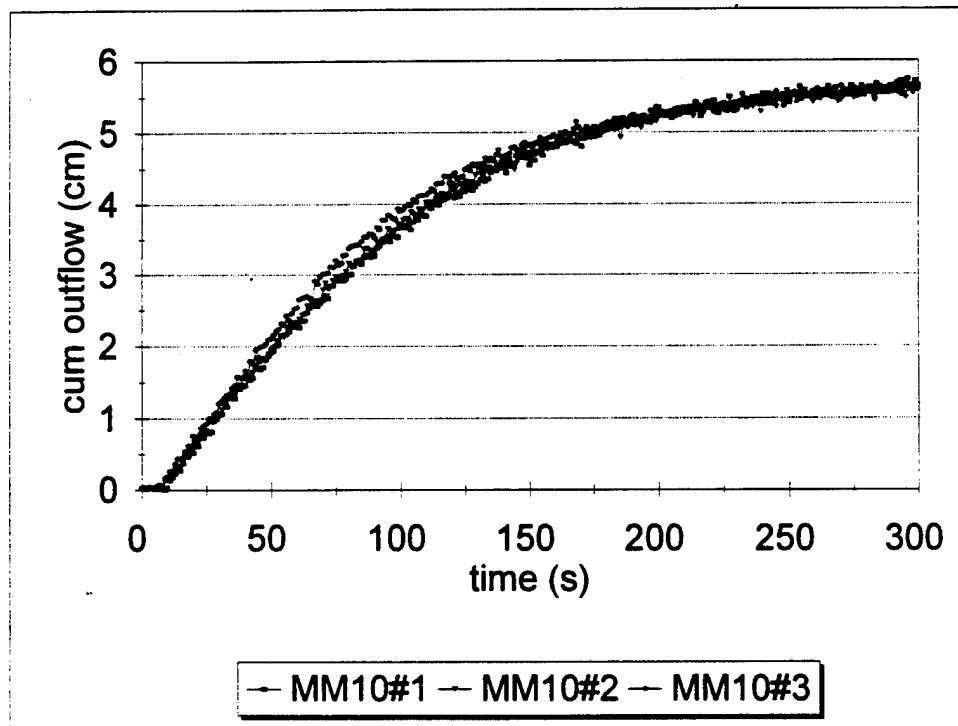
Figure 5-36. Modeling of models 10g test raw data using Soltrol

132
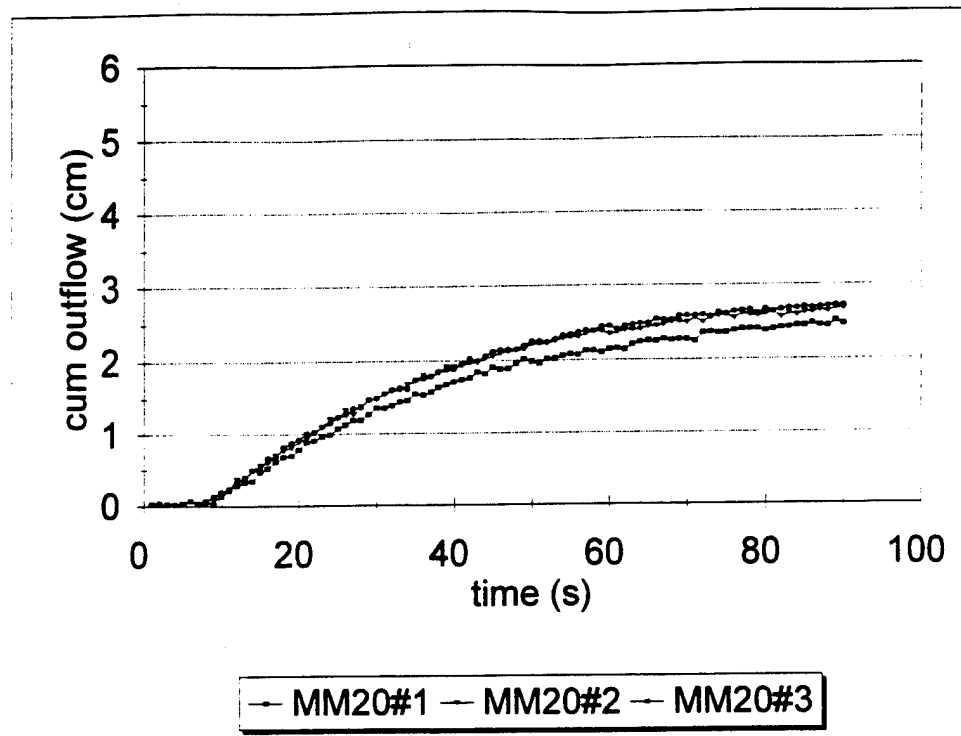
Figure 5-37. Modeling of models 15g test raw data using Soltrol
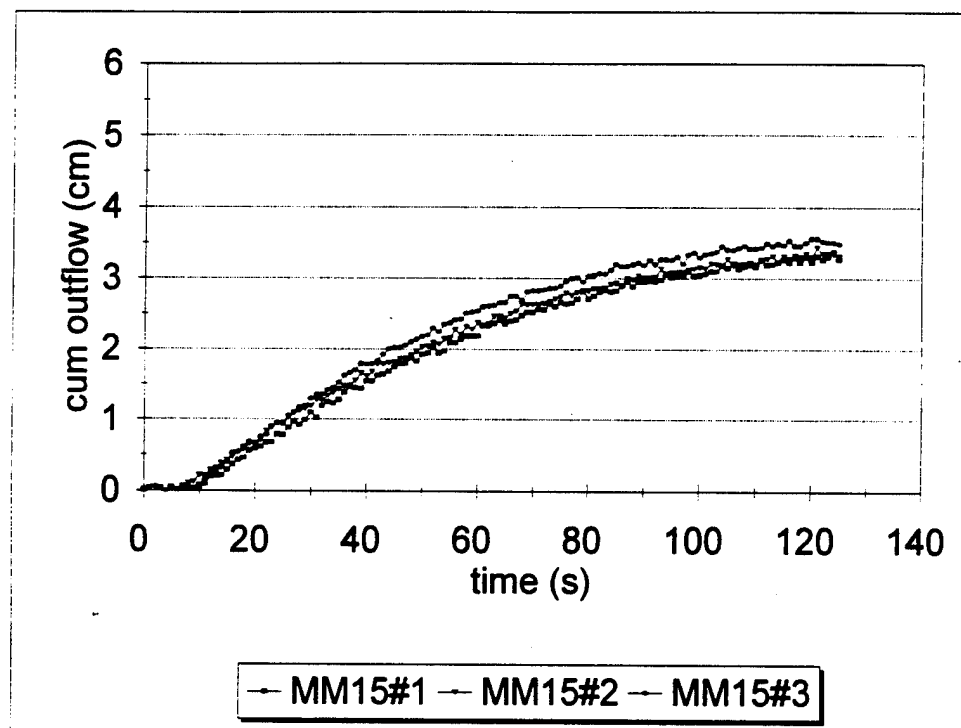
Figure 5-38. Modeling of models 20g test raw data using Soltrol

133
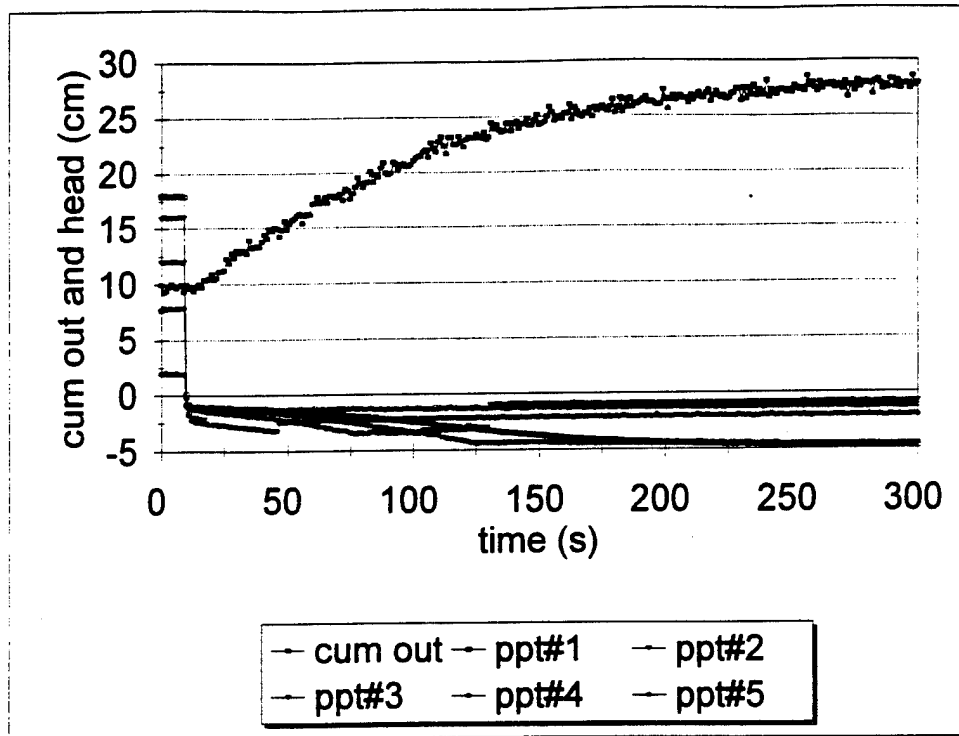
Figure 5-39. Modeling of models 10g test raw data using Soltrol
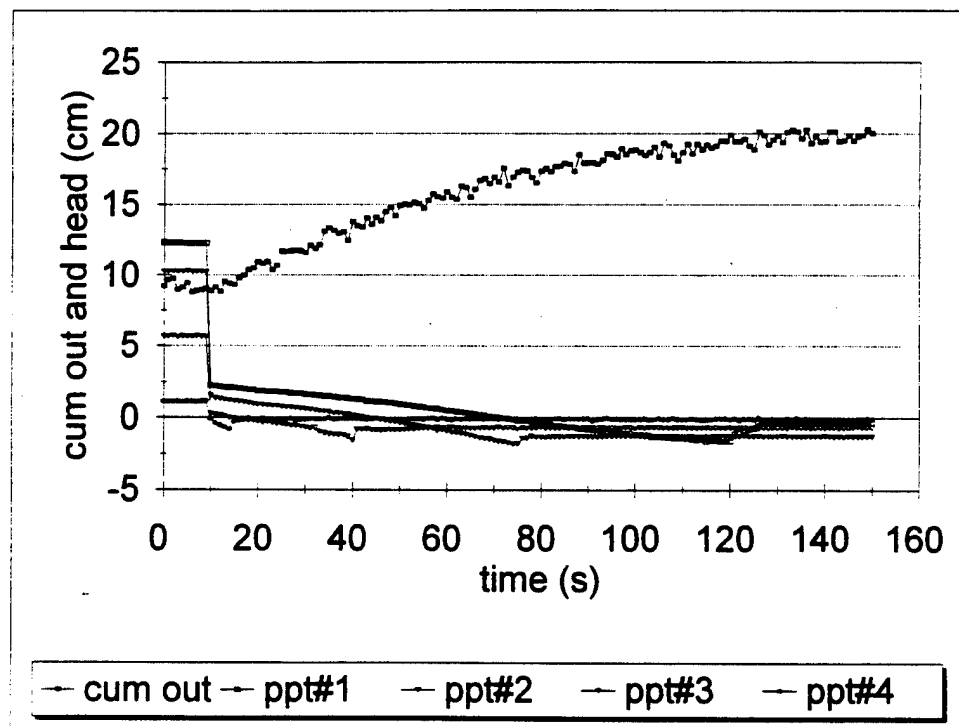
Figure 5-40. Modeling of models 15g test raw data using Soltrol

134
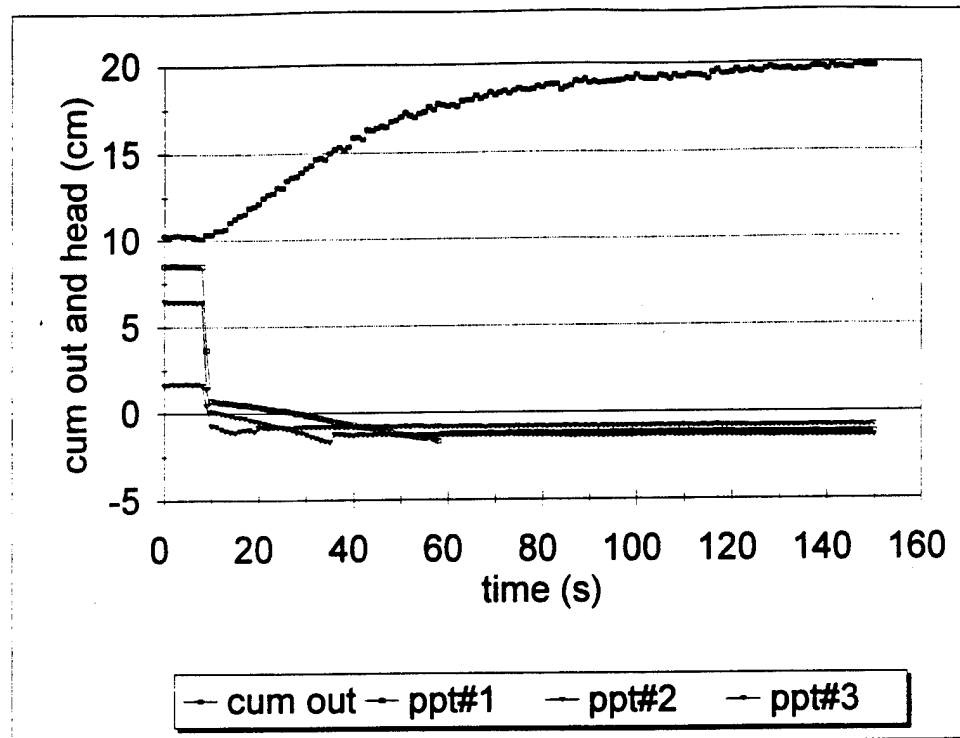
Figure 5-41. Modeling of models 20g test raw data using Soltrol

5.9 - Modeling of models using layered sands experimental results

The layered sands tests were performed in the small centrifuge only. The #70 sand was layered between two #30 layers, as shown in Figure 5-42. The thickness of the layers for the modeling of models was varied as shown in Table 5-2. The layered sands were tested using both water and Soltrol.

Figures 5-43 through 5-45 are the results of the 1g prototype using the higher fluid level similar to the boundary conditions of Figure 5-13. The water outflow curve shape is different than the homogeneous test, and the pore pressures in the two highest transducers which are imbedded in the #70 layer are retarded compared to the homogeneous test.

135
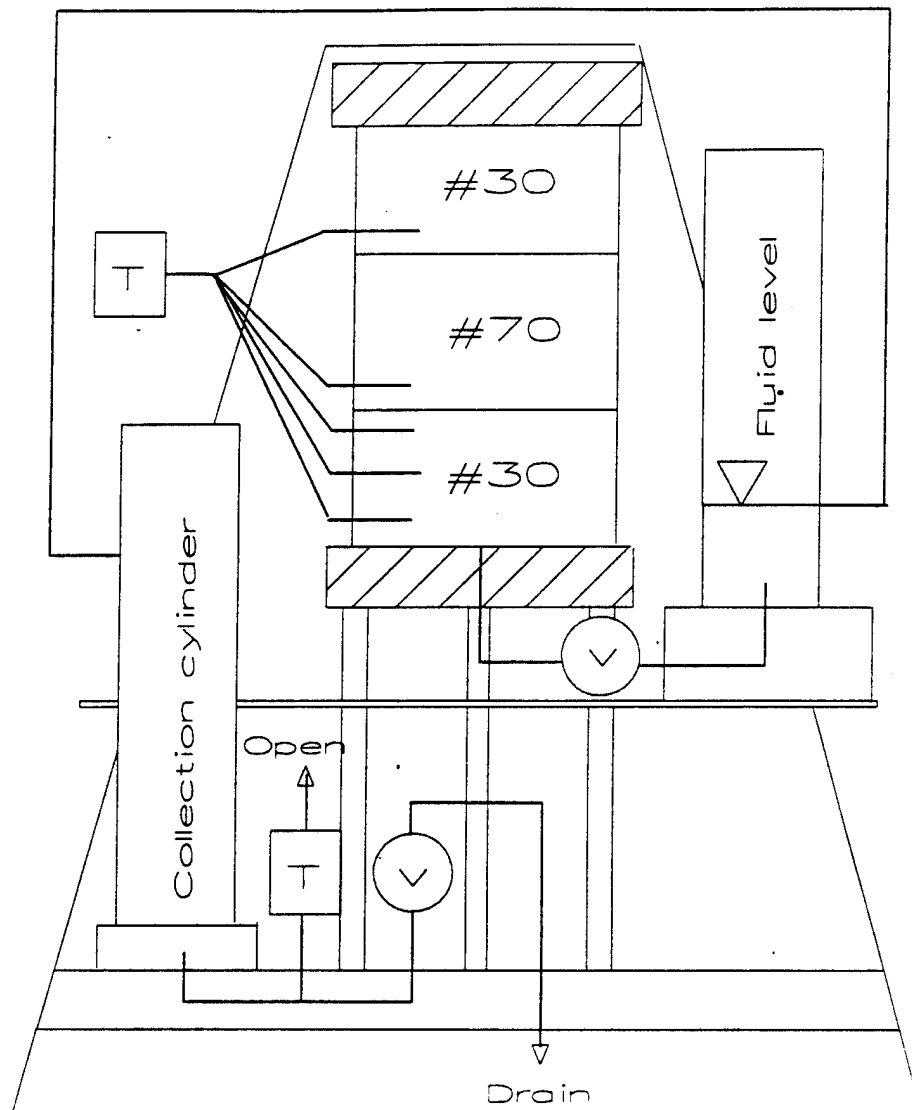
Figure 5-42. Schematic of layered sand columns

136

Table 5-2. Modeling of models for layered sands

	1g	10g	15g	20g
		height (cm)		
#30 layer 1	70	7	4.67	3.5
#70 layer 2	60	6	4	3
#30 layer 3	70	7	4.67	3.5
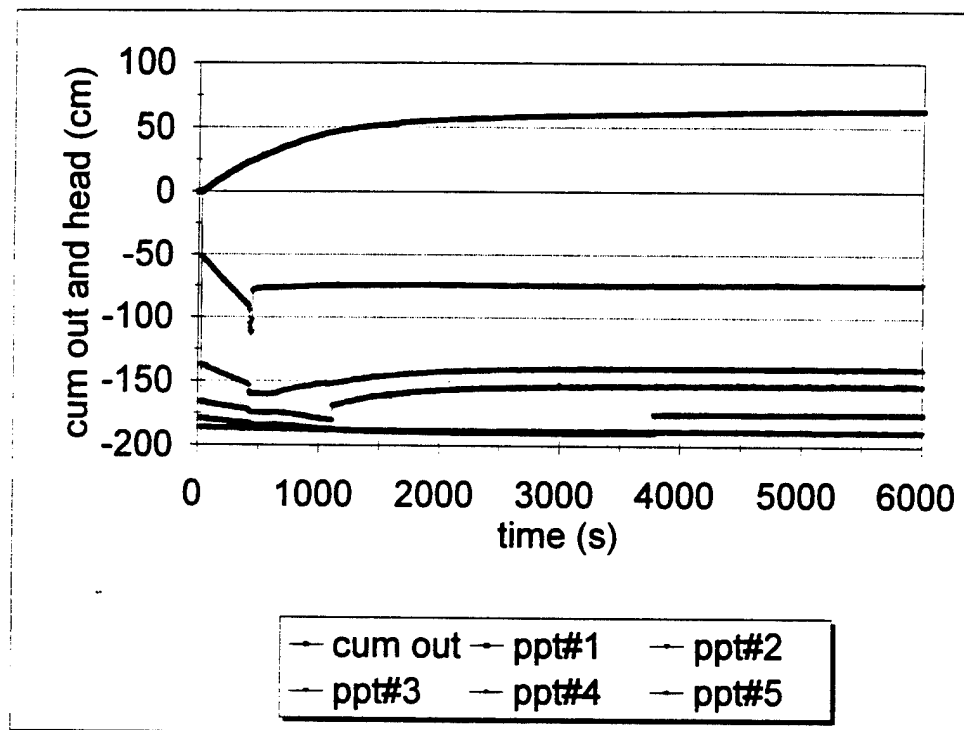
Figure 5-43. Water and #70 sand between layers of #30 sand prototype
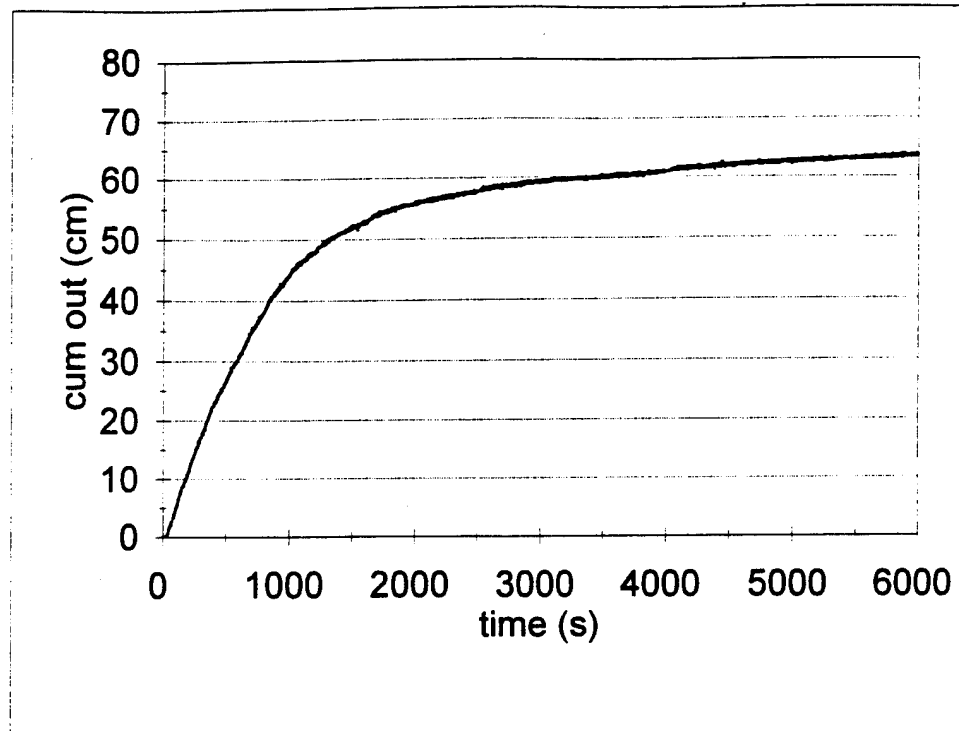
Figure 5-44. Water and layered sand prototype cumulative outflow curve
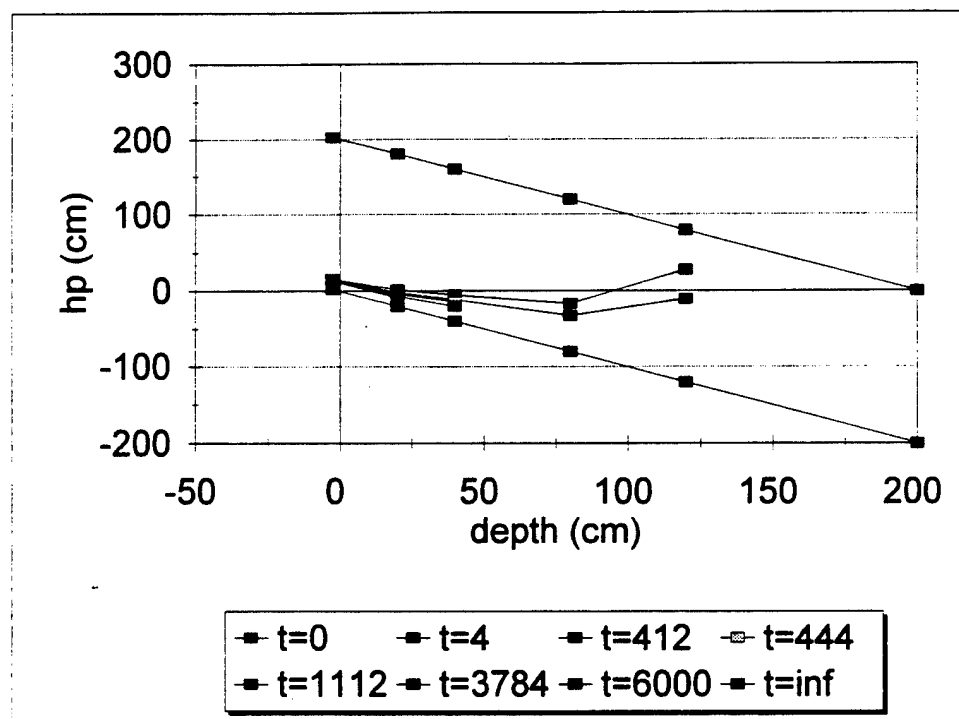
Figure 5-45. Water and layered sands prototype pore pressure profiles

The initial experimental hydraulic conductivity from Figure 5-43 is:

$$K_{sat} = \frac{20}{400} = 0.05 \ cm/s \qquad (5.35)$$

and the theoretical hydraulic conductivity is:

$$K_{sat} = \frac{200}{(\frac{140}{0.131})+(\frac{60}{0.02})} = 0.0492 \ cm/s \qquad (5.36)$$

The modeling of models tests' raw data using water and #70 sand layered between #30 sand are presented in Figures 5-46 through 5-48. Figures 5-49 through 5-51 show the results of the modeling of models tests' raw data with pore pressures measurements using Soltrol and the #70 sand layered between #30 sand. Once again, the shape of the Soltrol outflow curve is different compared to the homogeneous test. After the tests were completed, the fluid entrapment in each layer was clearly visible; the top layer appeared to be at residual saturation, the middle layer appeared residually saturated at the top and fully saturated at the bottom, and the bottom layer appeared residually saturated at the top and fully saturated at the bottom.
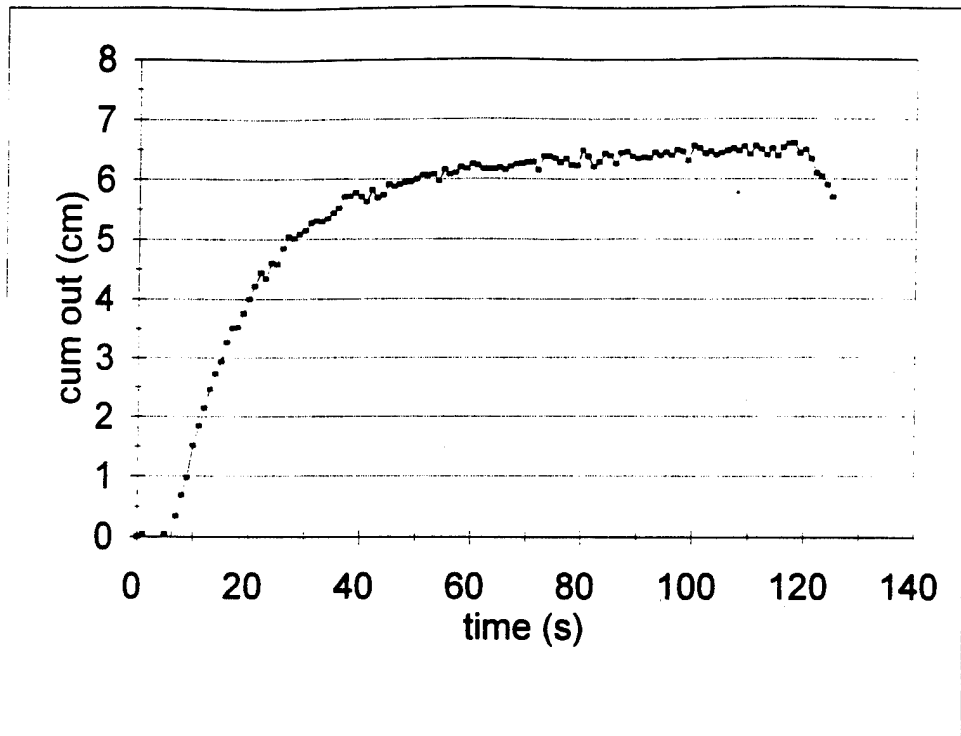
Figure 5-46. Modeling of models #70/#30/#70 sand 10g test raw data using water
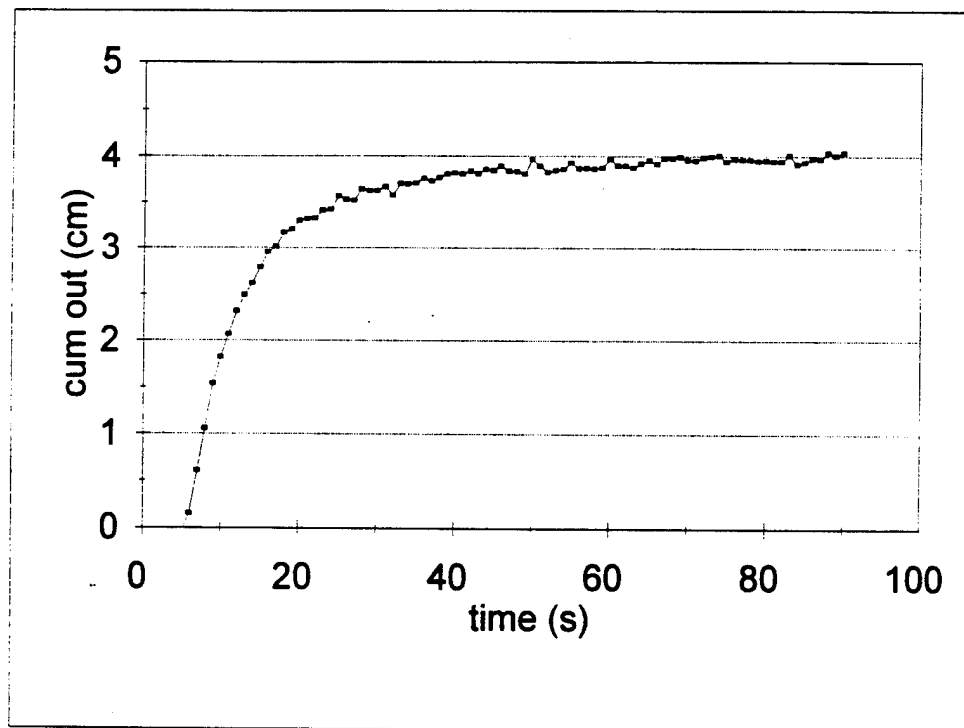
Figure 5-47. Modeling of models #30/#70/ #30 sand 15g test raw data using water

140
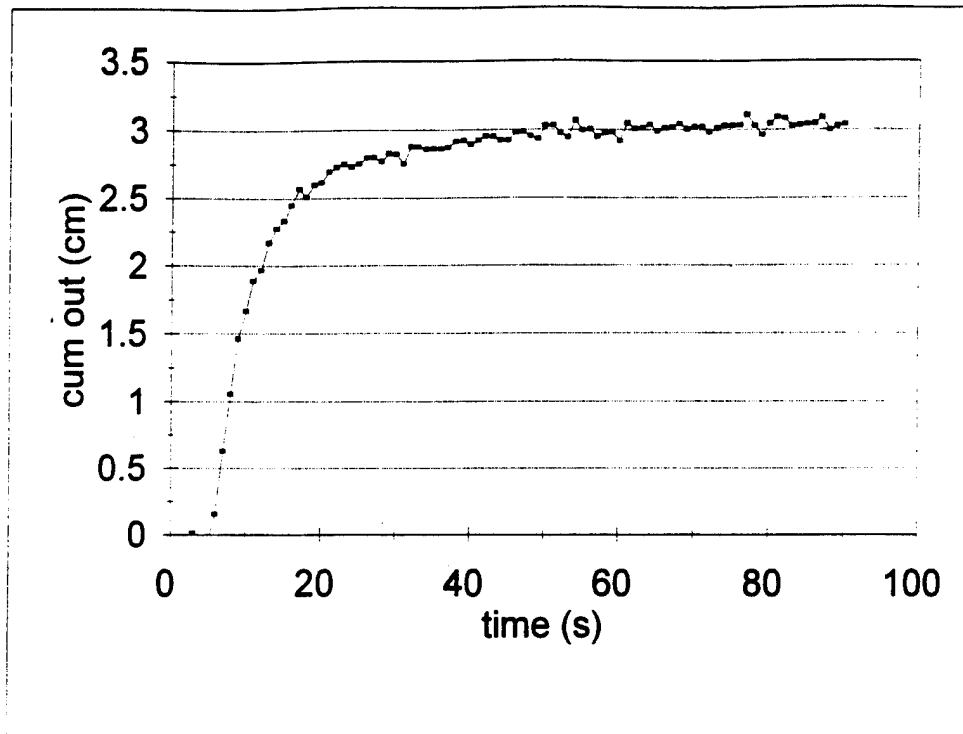
Figure 5-48. Modeling of models #30/#70/#30 sand 20g test raw data using water
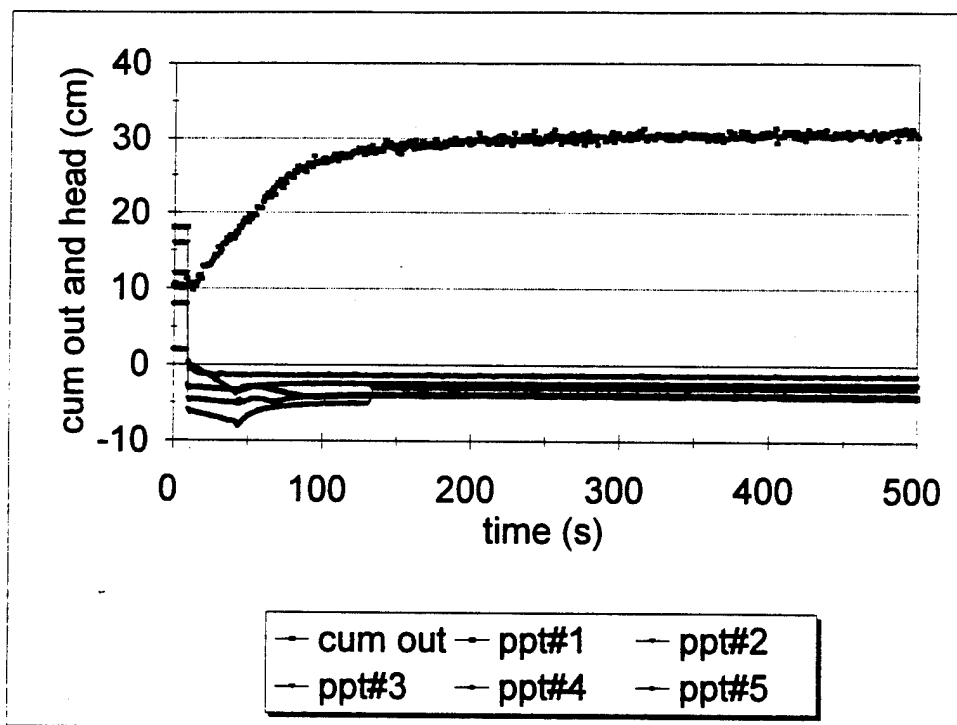
Figure 5-49. Modeling of models #30/#70/#30 sand 10g test raw data using Soltrol

141
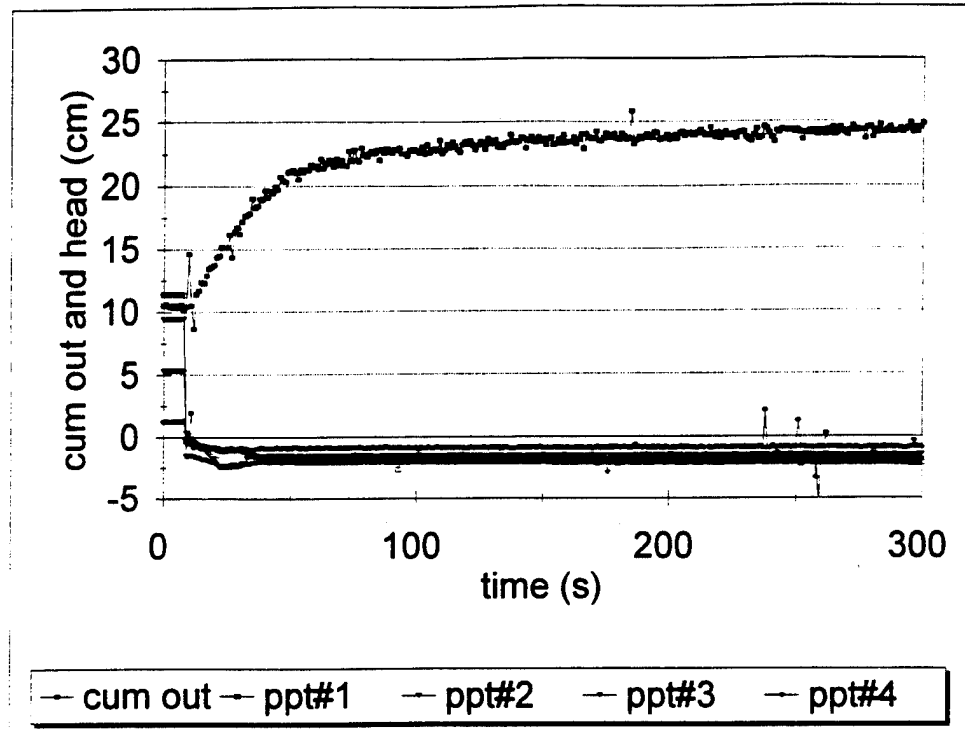
Figure 5-50. Modeling of models #30/#70/#30 sand 15g test raw data using Soltrol
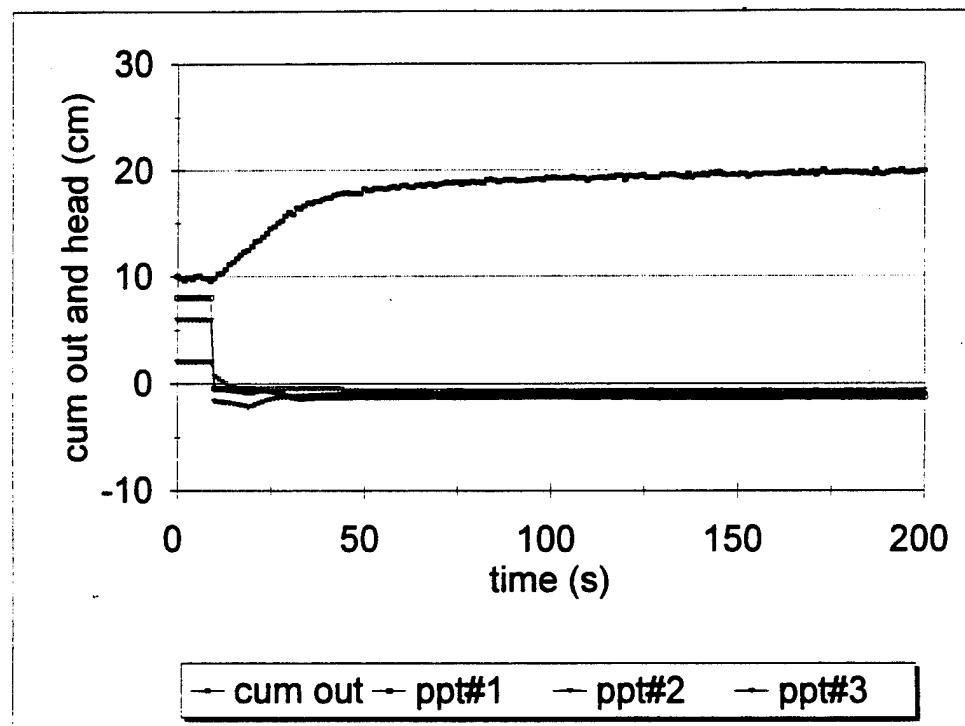
Figure 5-51. Modeling of models #30/#70/#30 sand 20g test raw data using Soltrol

142

5.10 - Experimental results data analysis

The raw data from a modeling of models test can be analyzed in two ways: by comparing it to the prototype and by comparing the results from one model to another model at a different g-level. In saturated flow, because the total head remains constant, an "average" g-level could be defined as the center of the sample. In unsaturated flow, because the total head is determined by the drainage front, the "average" g-level is changing during the test. Therefore, it is not clear *a priori* which g-level should be used for scaling purposes. During the drainage process the flow rate is controlled mostly by the length of the saturated column, which changes with time, and by the capillary forces behind the front. As the position of the front changes with time and the g-level changes with increasing radius to the front, it is reasonable to expect the change in the "average" g-level will influence the results more than in saturated flow.

To eliminate bias in the g-level, the cumulative outflow curve of the model was matched to the prototype cumulative outflow curve in a two-step process. First, a cumulative outflow scale factor N was determined by matching the ultimate cumulative outflow of the model to the prototype. Second, a time scale factor N^a was determined by matching the complete curve using the cumulative outflow scale factor raised to an exponent. The curves were matched visually by trial and error, and were seen to converge rapidly. The final cumulative outflow value shifted the curve up and down, and the time scale factor exponent shifted the curve left to right to align the time axis. The first test series using water will be used as an example.

First, an approximate g-level N required to match the cumulative outflow ultimate

143

value was found; for the 10g test scaled to the 1g prototype the required N is:

$$N = \frac{(cum\ out)_p}{(cum\ out)_m} = \frac{57}{5.5} = 10.36 \qquad (5.37)$$

The time factor was found using:

$$t_p = N^a t_m \qquad (5.38)$$

Both the N value and the exponent "a" were changed until the curves aligned. The data manipulation was performed using Quattro Pro spreadsheets; a typical calculation is shown in Figure 5-52. Figures 5-53 through 5-55 compare the centrifuge models of Figures 5-23 through 5-25 scaled to the 1g prototype of Figure 5-9.

The model curves scaled to the prototype were easily matched by overlaying the predicted curve over the prototype. The cumulative outflow scale factor N was usually very close to the approximate N calculated using Equation (5.37); for the 10g model the calculated N was 10.30. The time factor exponent "a" in Equation (5.38) was usually found in two or three iterations. Similarly for the use of the 10g model as the prototype, the approximate cumulative outflow scale factor N for the 15g test was:

$$N = \frac{(cumout)_p}{(cumout)_m} = \frac{5.5}{3.5} = 1.57 \qquad (5.39)$$

The actual N after matching the curve of Figure 5-54 to Figure 5-22 was 1.55. Figures 5-56 and 5-57 compare the 15g and 20g models scaled to the 10g model of Figure 5-23 as the prototype.

MM10#1		N =	10.3
		N^a =	1.78
Model	Model	Proto	Proto
cum out	time	cum out	time
0	0	0	0
0.0297	1	0.3057	63.511
0.199	2	2.0498	127.02
0.3571	3	3.678	190.53
0.5917	4	6.0946	254.04
0.6155	5	6.3392	317.56
0.7973	6	8.212	381.07
0.9282	7	9.5603	444.58
1.1147	8	11.481	508.09

Figure 5-52. Quattro Pro spreadsheet calculation of 10g model scaled to 1g prototype
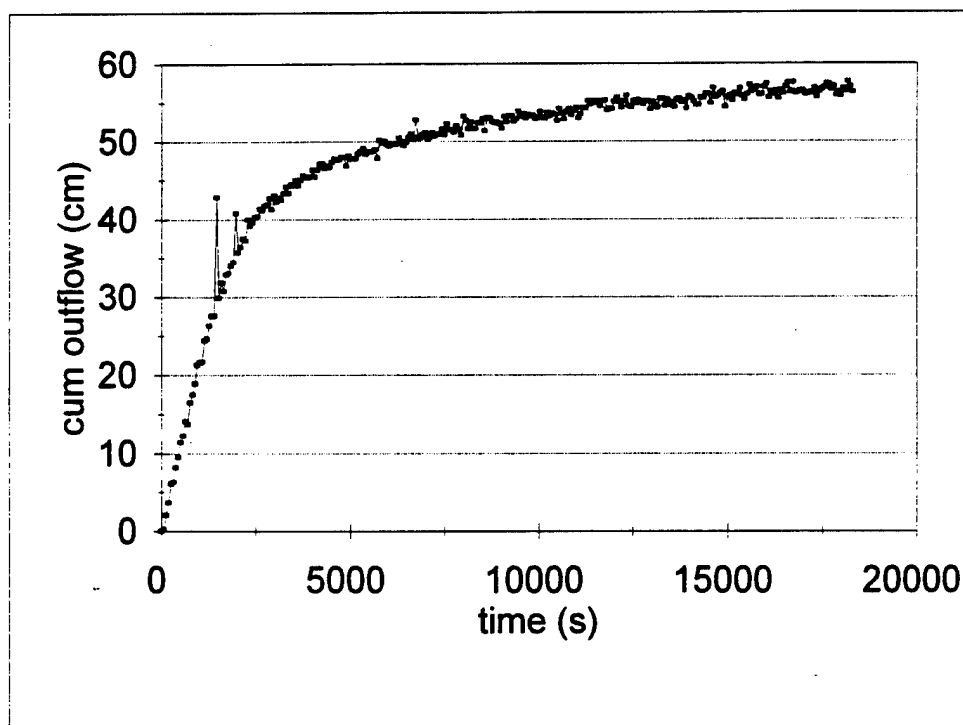
Figure 5-53. 10g scaled to 1g prototype cumulative outflow curve using water

145
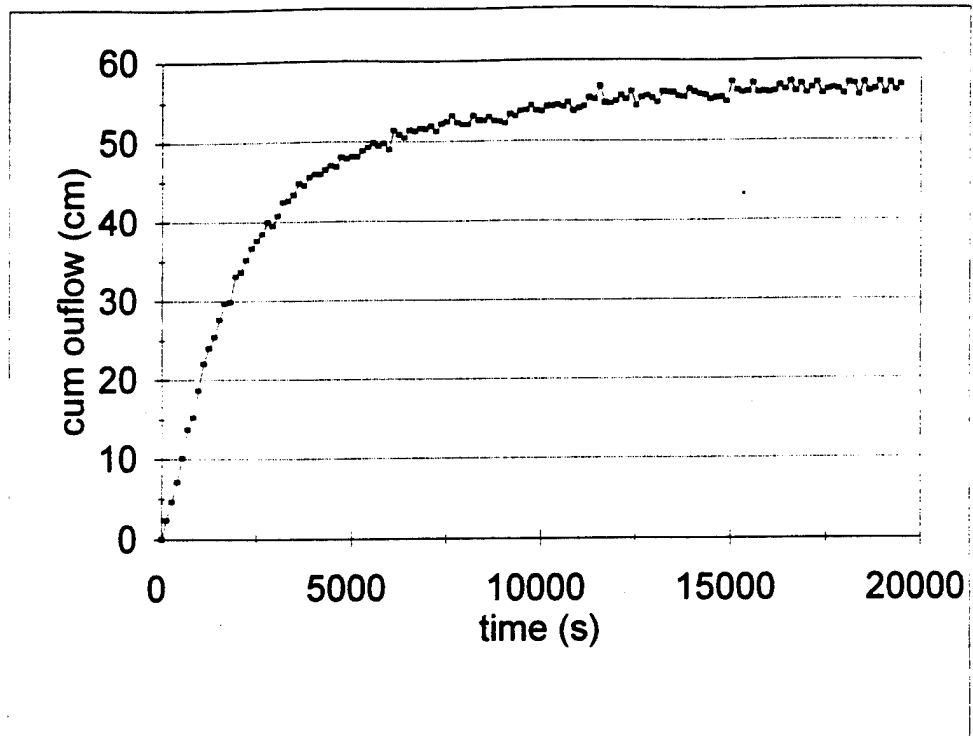
Figure 5-54. 15g scaled to 1g prototype cumulative outflow curve using water
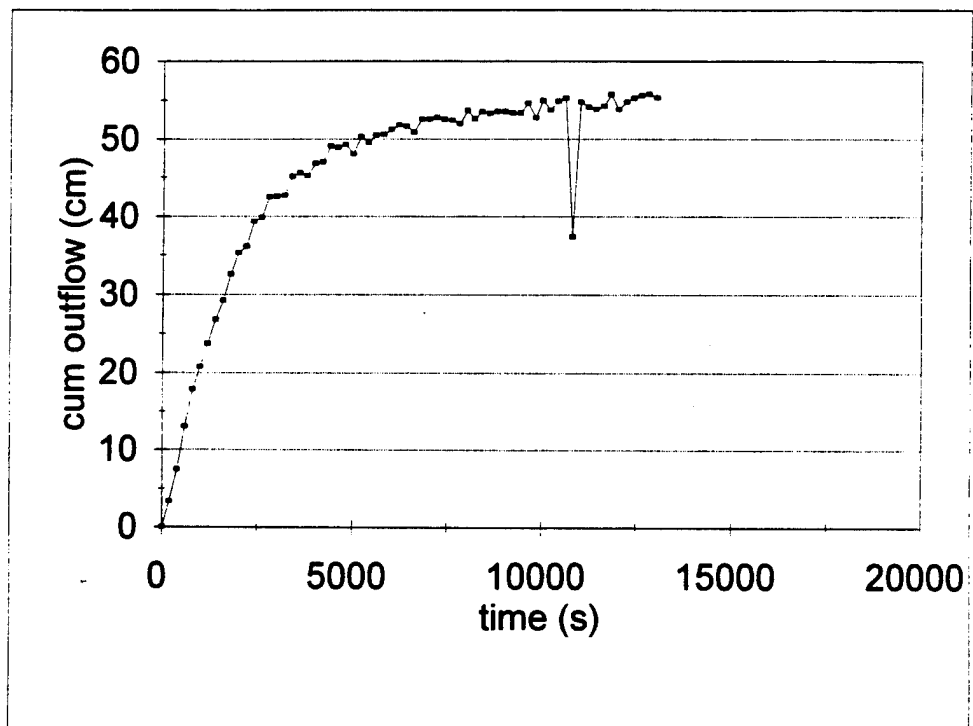
Figure 5-55. 20g scaled to 1g prototype cumulative outflow curve using water

146
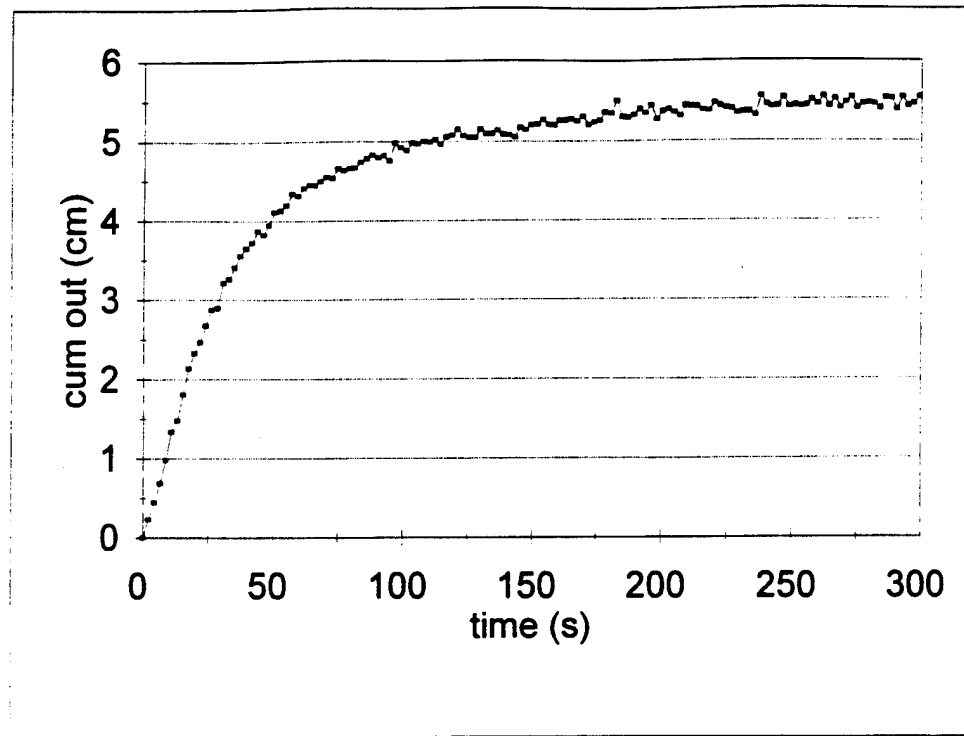
Figure 5-56. 15g scaled to 10g prototype cumulative outflow curve using water
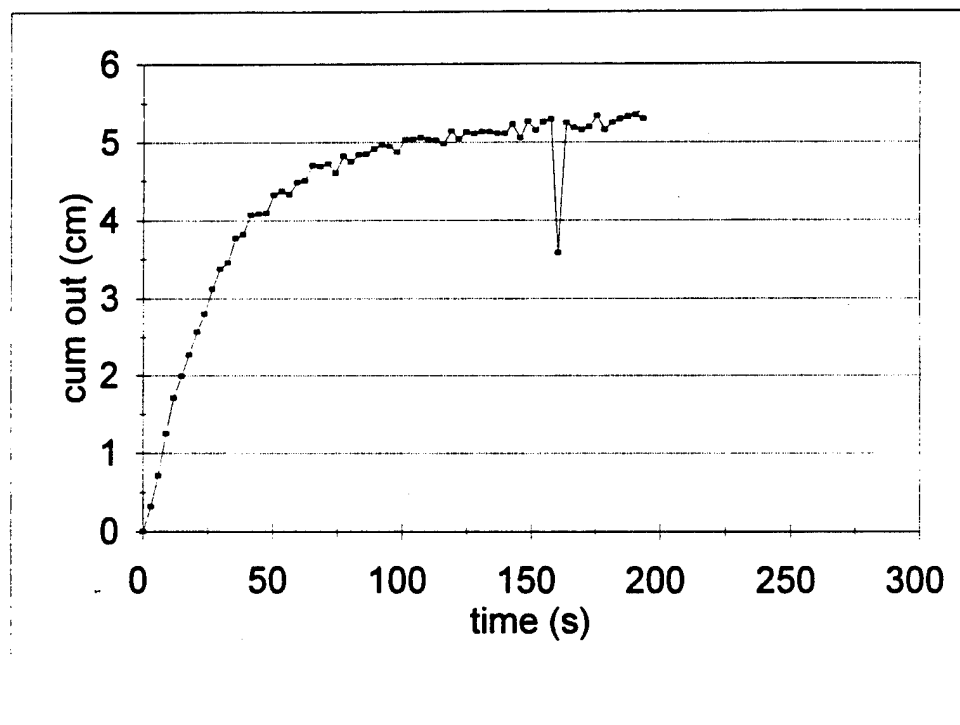
Figure 5-57. 20g scaled to 10g prototype cumulative outflow curve using water

Using the previous methodology, the model tests using the lower fluid level of Figures 5-26 through 5-28 were scaled to the 1g prototype of Figure 5-11 as shown in Figures 5-58 through 5-60. Figures 5-61 through 5-63 are the scaled pore pressure profiles. The scaled pore pressures were determined using the model pore pressure multiplied by the actual g-level at the transducer location. The total radial acceleration is comprised of a horizontal gravity vector imposed by the spinning centrifuge and a vertical gravity vector acting downward due to the Earth's gravity. The total radial acceleration can be found using:

$$a_r = Ng = \sqrt{(\omega^2 r)^2 + g^2} \tag{5.40}$$

where:

a_r = the radial acceleration (L/T^2)

ω = the angular velocity (rad/T)

g = the downward acceleration (L/T^2)

N = the multiple of local gravity

Equation (5.40) can be rewritten as:

$$N = \frac{\sqrt{\dfrac{(\omega^2 r)^2}{g^2} + 1}}{g} \tag{5.41}$$

Using Equation (5.41), the actual g-level for each transducer, as well as the top and bottom of the sample was calculated. From the pore pressure profiles, a very unusual phenomenon appears. At the lower g-levels, the final pore pressure distribution

148

shows higher suctions than the theoretical hydrostatic distribution, similar to the 1g prototype in Figure 5-12. As the g-level increases, however, the final distribution shifts towards the theoretical distribution. This indicates the boundary conditions do not scale with the g-level.

Using Equation (5.41), the g-level at the bottom of the column was calculated to provide a reference g-level to compare with the scale factor N. In general, the scale factor N was slightly larger than the g-level at the bottom of the column, indicating that the experimental apparatus design was not ideal. As the fluid leaves the overflow outlet, it is in free fall in an increasing g-field; the effect may cause a deviation in the time scale (Tan and Scott, 1985).

Figure 5-58. 10g scaled to 1g prototype

Figure 5-59. 15g scaled to 1g prototype

Figure 5-60. 20g scaled to 1g prototype

Figure 5-61. 10g scaled to 1g prototype pore pressure profiles

Figure 5-62. 15g scaled to 1g prototype pore pressure profiles

Figure 5-63. 20g scaled to 1g prototype pore pressure profiles

To verify that the boundary conditions were not scaling, the test results using the elevated fluid level of Figures 5-29 through 5-31 were scaled to the prototype of Figure 5-13, as shown in Figures 5-64 through 5-65. The pore pressure profiles are shown in Figures 5-66 through 5-68, which can be compared to prototype pore pressures shown in Figure 5-14. Pore pressure transducer #1 was beneath the fluid level and pressure transducer #2 was in the suction saturated zone above the fluid level; both transducers should remain fully saturated and accurately capture the pore pressures. In the following plots, the transducers are seen to have a continuous curve without the sharp break typical of the transducers in the upper regions. The scale factor and exponent for all tests are presented in Section 5.11, Summary of unsaturated sands tests.

Figure 5-64. 10g scaled to 1g prototype

Figure 5-65. 15g scaled to 1g prototype

153

Figure 5-66. 20g scaled to 1g prototype

Figure 5-67. 10g scaled to 1g prototype pore pressure profiles

Figure 5-68. 15g scaled to 1g prototype pore pressure profiles

Figure 5-69. 20g scaled to 1g prototype pore pressure profiles

155

Once again the final pore pressure distributions are changing with g-level, moving towards the theoretical distribution. It appears that the boundary condition definitely causes a deviation in the suction from the theoretical distribution, and the deviation does not scale.

The boundary conditions at the top of the sample can also be difficult to analyze. A possible problem using the transducers to measure unsaturated pore pressures is shown in Figure 5-66. Transducer #4 was placed at the 9 cm elevation and had an additional 1 cm of sand above it. At the start of the test, the fluid was to the top of the sand column. As the valve was opened to initiate drainage, the instantaneous pressure drop was shown at lower g-levels as a vertical drop. At the higher g-levels, due to the expansion of the time scale, the drop is no longer vertical; and for transducer #4, the first data point fell below the predicted pressure distribution. It is not unlikely that this pressure drop was an artifact of the transducer set-up (porous stone) and doesn't represent the actual pore pressure in the soil. Since the desaturation was so quick at that instant in time, it is possible that the fluid behind the porous stone in the transducer exhibits high suction before the cavitation can occur. Such a problem is not present at lower elevations and later times during which the desaturation process is more gradual. In those cases, the cavitation takes place without a prior suction increase. The boundary conditions did not appear to be dependent upon the size of the centrifuge arm radius; the results were similar for both the large and small centrifuge.

The effect of a changing centrifuge arm length was explored using the large centrifuge. For true modeling of models (Corey, 1990), the variation of the g-field across

the sample should be equal to:

$$(\omega R)_m = (\omega R)_p \qquad (5.42)$$

which requires a change in the length of the centrifuge arm to have equivalent systems. If the model is a scaled length of the prototype, then the length of the arm should be scaled to the same length. Examining the variation in the g-field for a 10g and a 20g test using a column length x, the variation from the top to bottom is:

$$\delta_{10} = \frac{(\omega^2 R_{10} - \omega^2(R_{10} - x_{10}))}{\omega^2 R_{10}} = \frac{x_{10}}{R_{10}} \qquad (5.43)$$

$$\delta_{20} = \frac{(\omega^2 R_{20} - \omega^2(R_{20} - x_{20}))}{\omega^2 R_{20}} = \frac{x_{20}}{R_{20}} \qquad (5.44)$$

and if both the column length and centrifuge arm are properly scaled:

$$\frac{x_{20}}{R_{20}} = \frac{\dfrac{x_{10}}{2}}{\dfrac{R_{10}}{2}} = \frac{x_{10}}{R_{10}} \qquad (5.45)$$

then the variation in the g-field is:

$$\delta_{10} = \delta_{20} \qquad (5.46)$$

and the two systems are equivalent. However, changing the length of the centrifuge arm is not usually possible, but the model is scaled and the variation in the g-field becomes:

157

$$\delta_{10} = \frac{(\omega^2 R_{10} - \omega^2(R_{10} - x_{10}))}{\omega^2 R_{10}} = \frac{x_{10}}{R_{10}} \qquad (5.47)$$

$$\delta_{20} = \frac{(\omega^2 R_{10} - \omega^2(R_{10} - x_{20}))}{\omega^2 R_{10}} = \frac{x_{20}}{R_{10}} \qquad (5.48)$$

and since only the column length is scaled:

$$\frac{x_{10}}{R_{10}} = \frac{2x_{20}}{R_{10}} \qquad (5.49)$$

and the variation in the g-field in an actual modeling of models test using a scaled soil sample but unchanged arm radius is:

$$\delta_{10} = 2\delta_{20} \qquad (5.50)$$

The large centrifuge was used to examine the effect the variation in the g-field compared to the small centrifuge. The large centrifuge test results shown in Figures 5-32 through 5-35 were scaled to the 1g prototype of Figure 5-9 and are shown in Figures 5-70 through 5-73. Figures 5-74 through 5-77 are the scaled pore pressure profiles.

Data from the large centrifuge are similar to data from the small centrifuge in all respects. The pore pressure distributions show the same behavior, moving towards the theoretical final pressure distribution with increasing g-level. Perhaps the only noticeable improvement was in determining the time exponent; there was less data scatter of the cumulative outflow curves. However, it is possible that the smoother data could be a

result of the smoother ride of the large centrifuge compared to the small centrifuge, and not a result of the variation in the g-field. With a smoother ride, the fluid enters the collection cylinder at a constant rate and does not slosh from side to side within the collection cylinder. The side to side sloshing is reflected in the vertical separation between any two data points.

The scale factor and exponent for all tests are presented in Section 5.11, Summary of unsaturated sands tests.
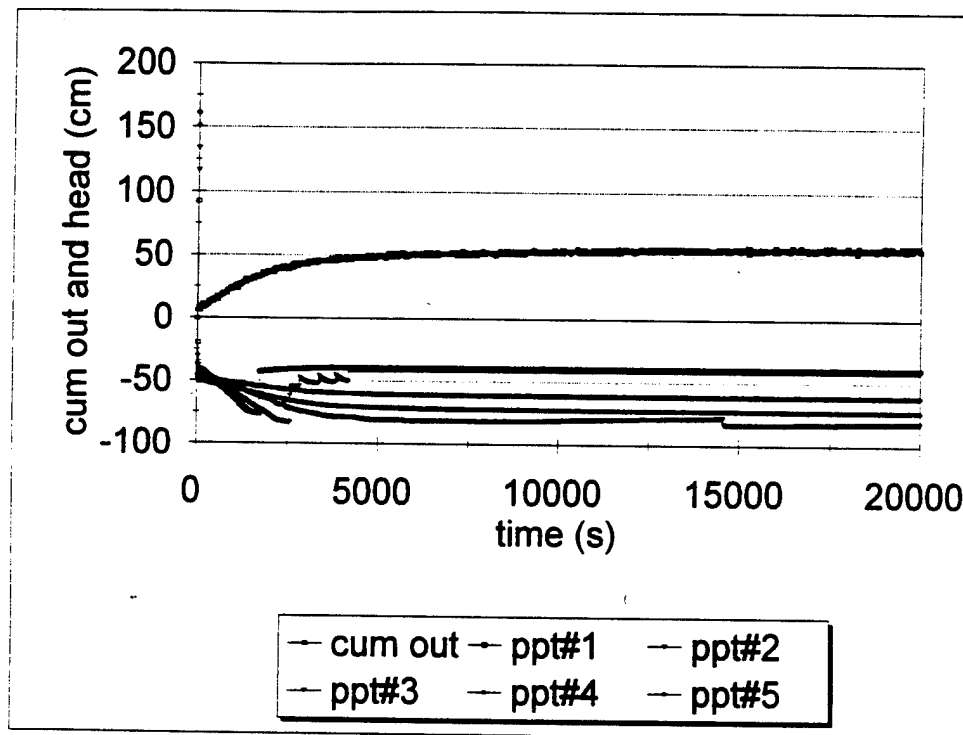
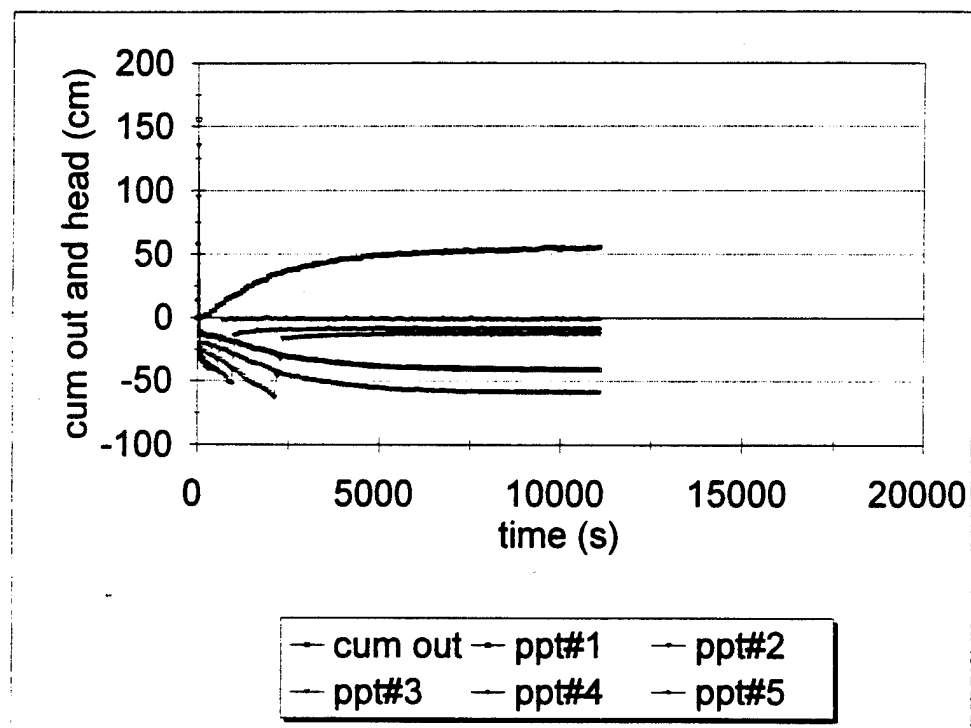Figure 5-70. 5g scaled to 1g prototype
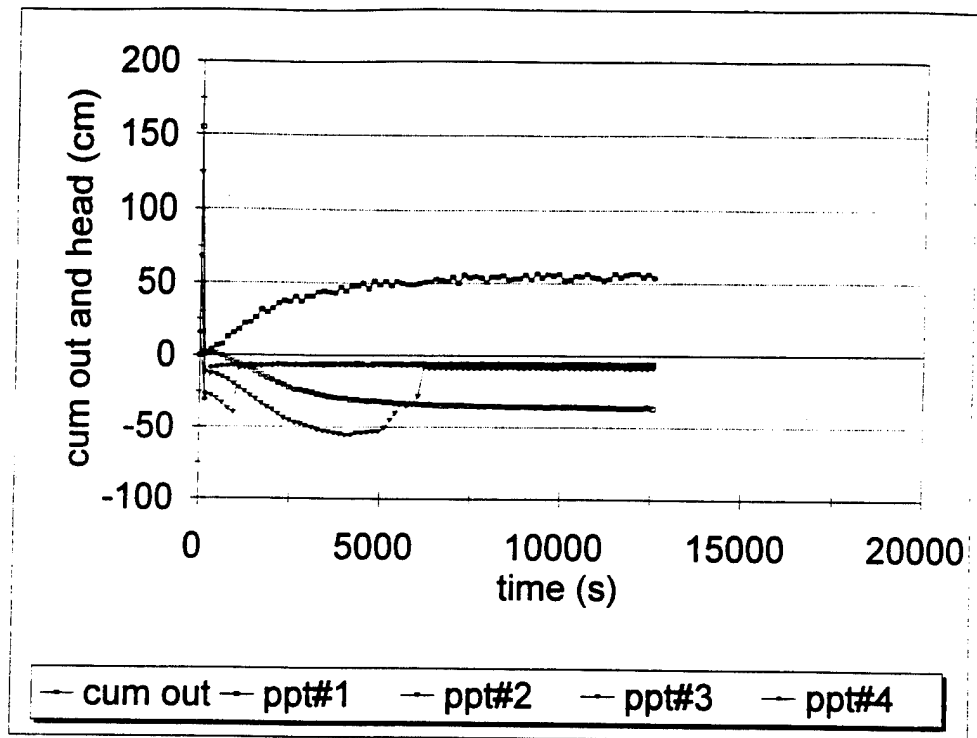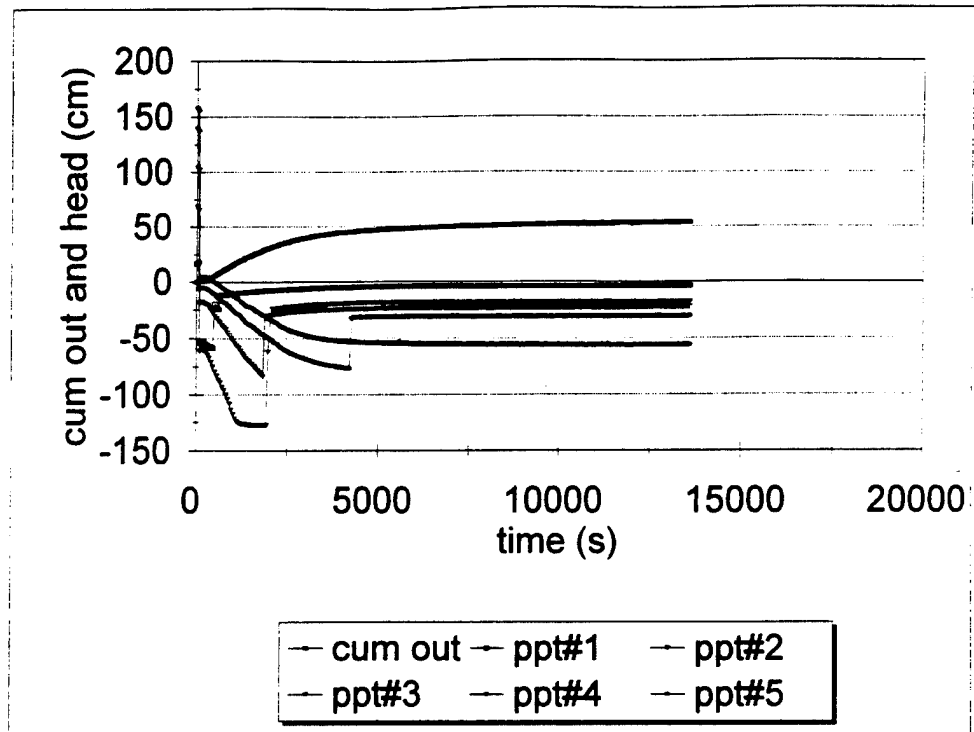
Figure 5-71. 10g scaled to 1g prototype
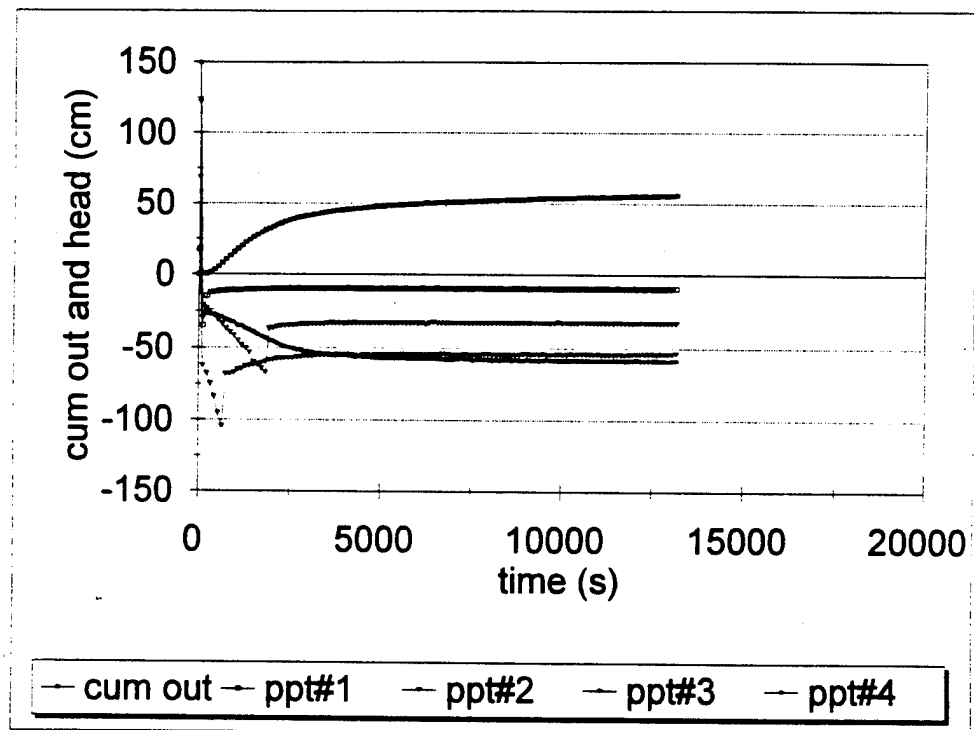
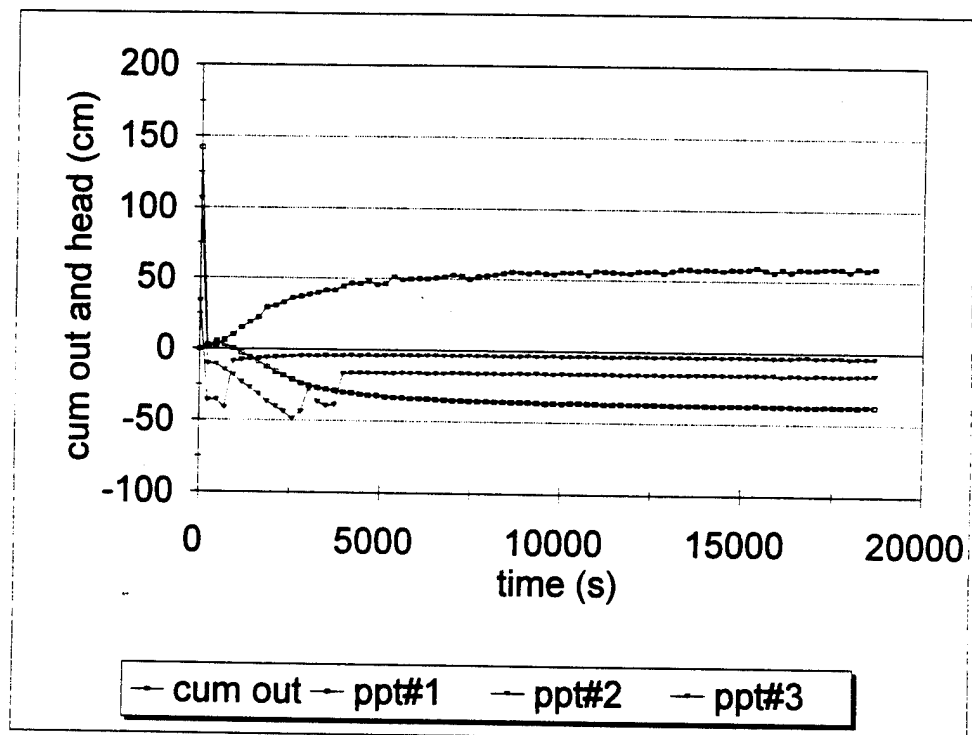**Figure 5-72. 15g scaled to 1g prototype**
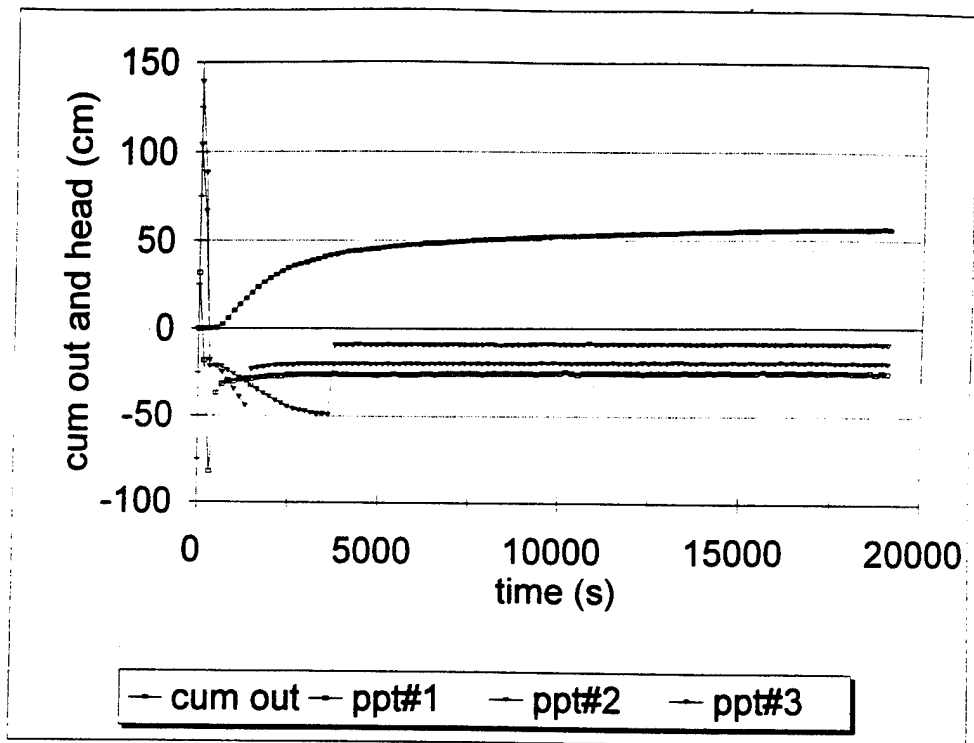
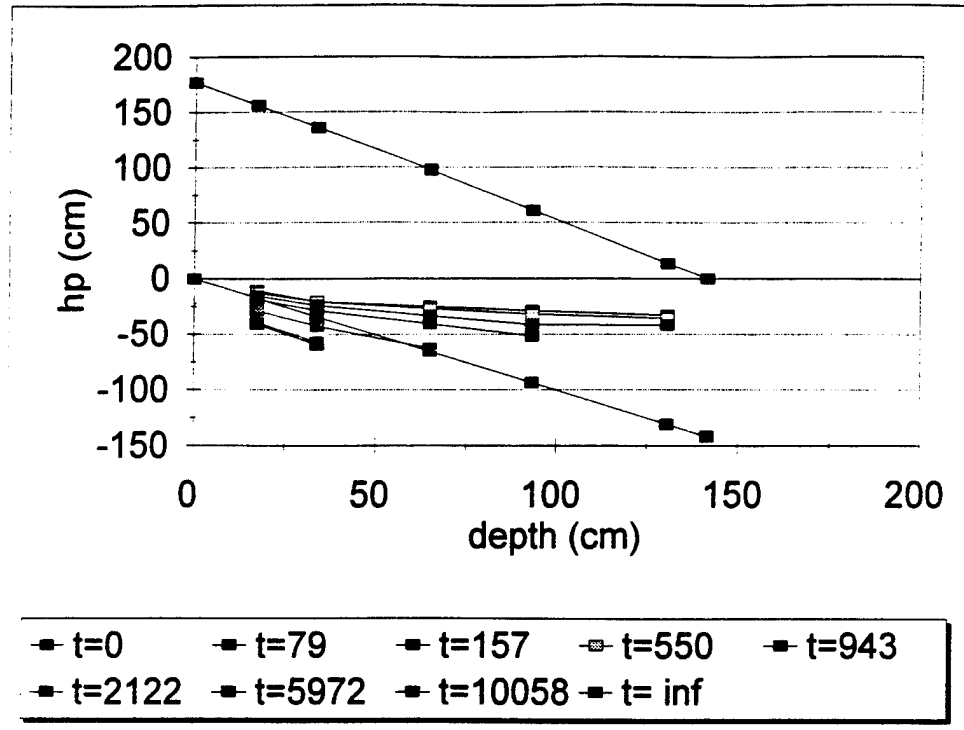Figure 5-73. 20g scaled to 1g prototype
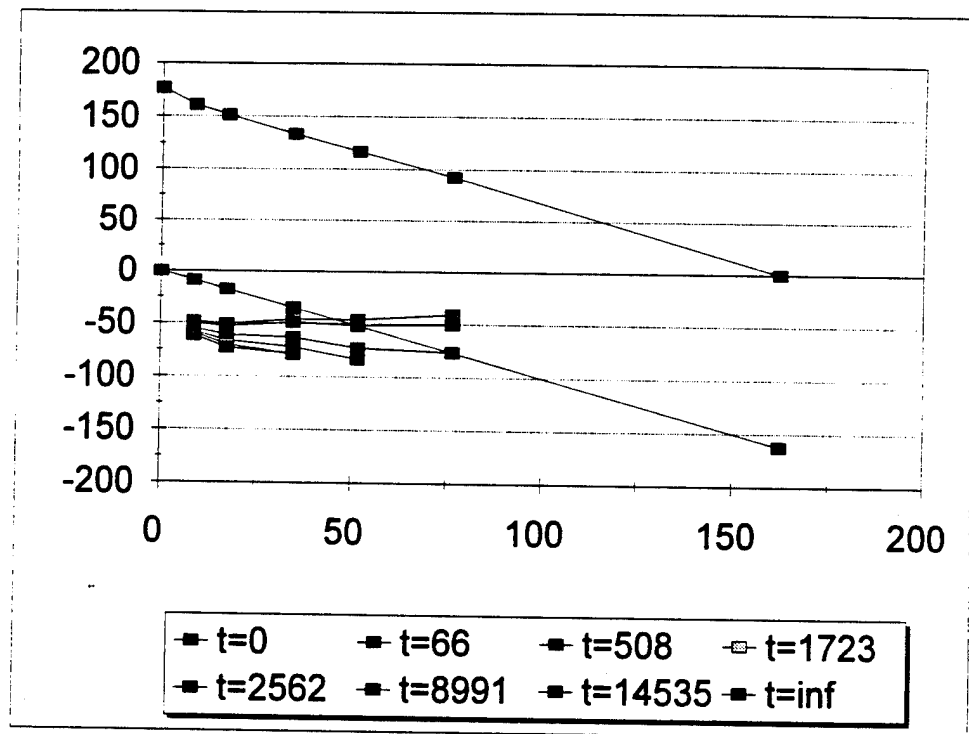
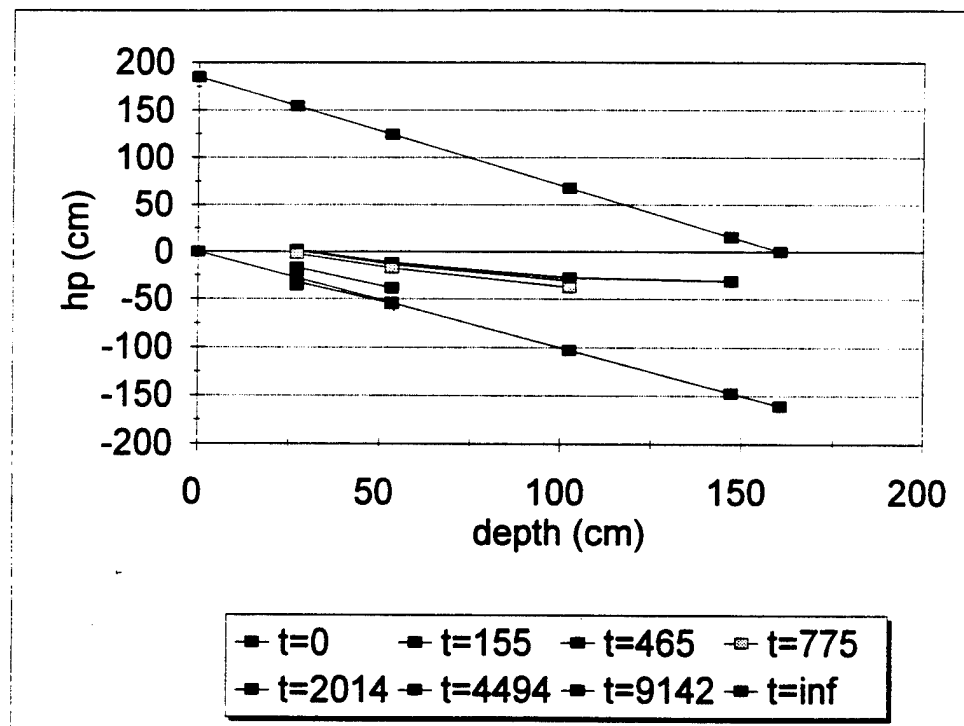Figure 5-74. 5g scaled to 1g prototype pore pressure profiles
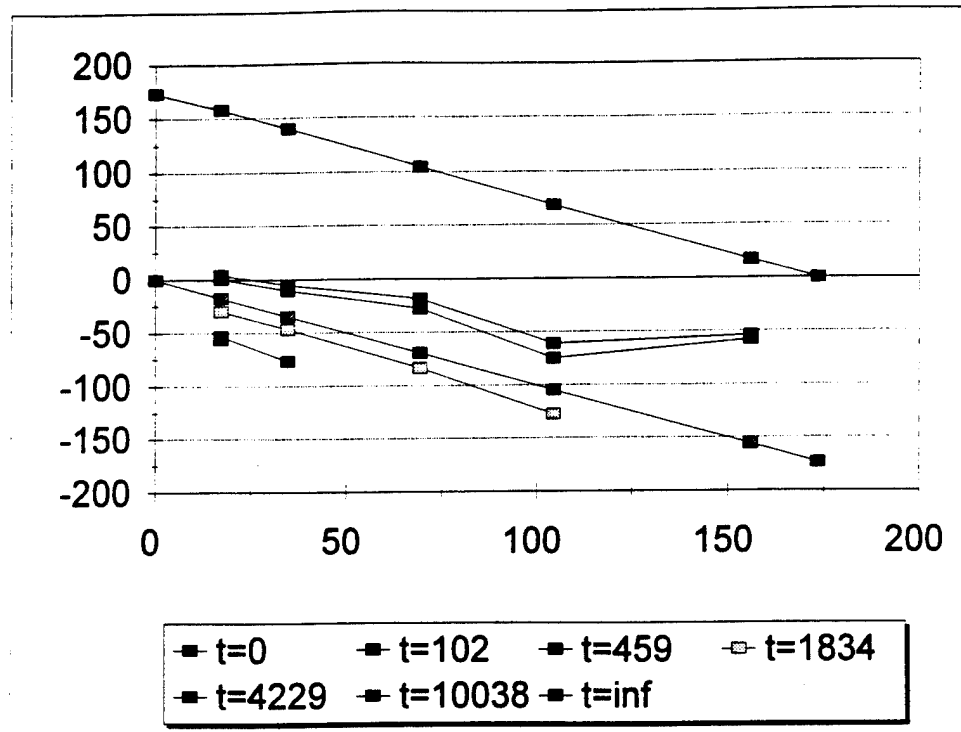
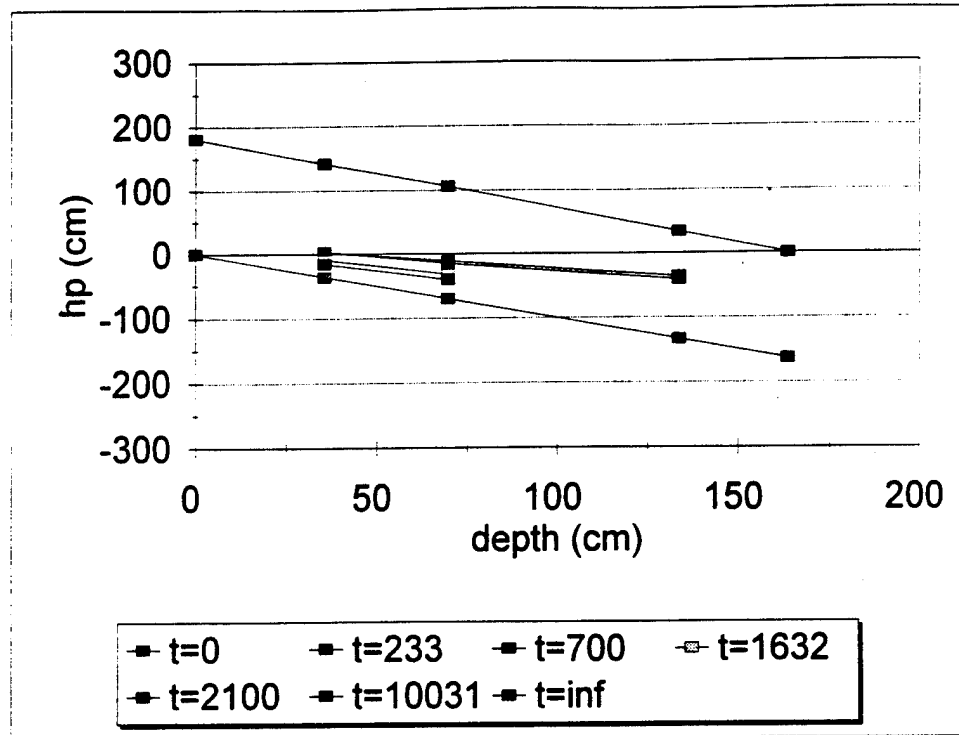**Figure 5-75. 10g scaled to 1g prototype pore pressure profiles**
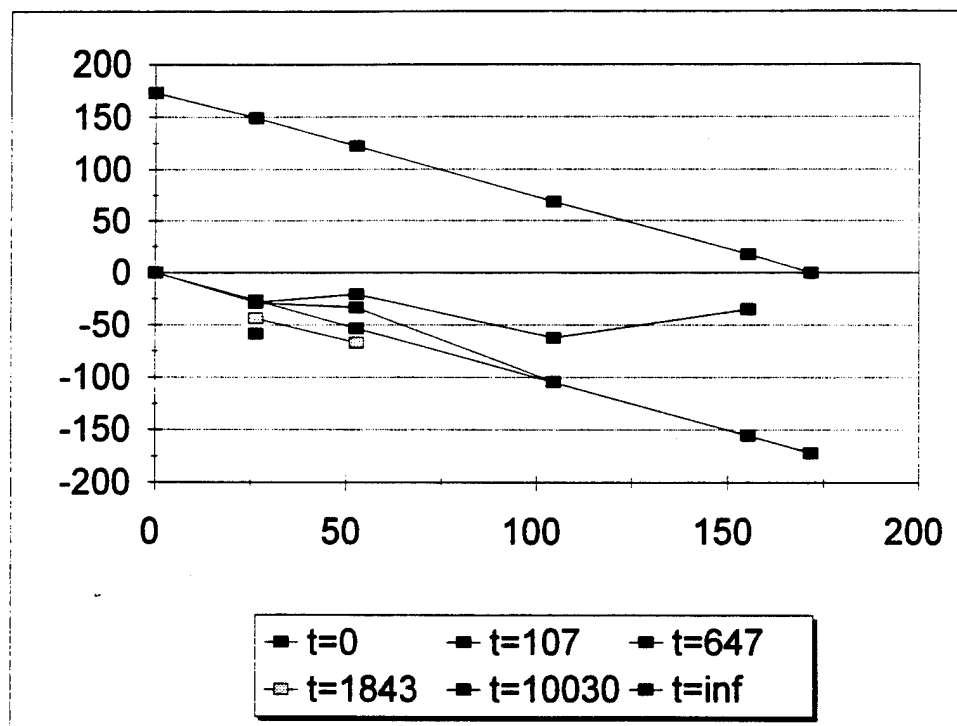
Figure 5-76. 15g scaled to 1g prototype pore pressure profiles

162
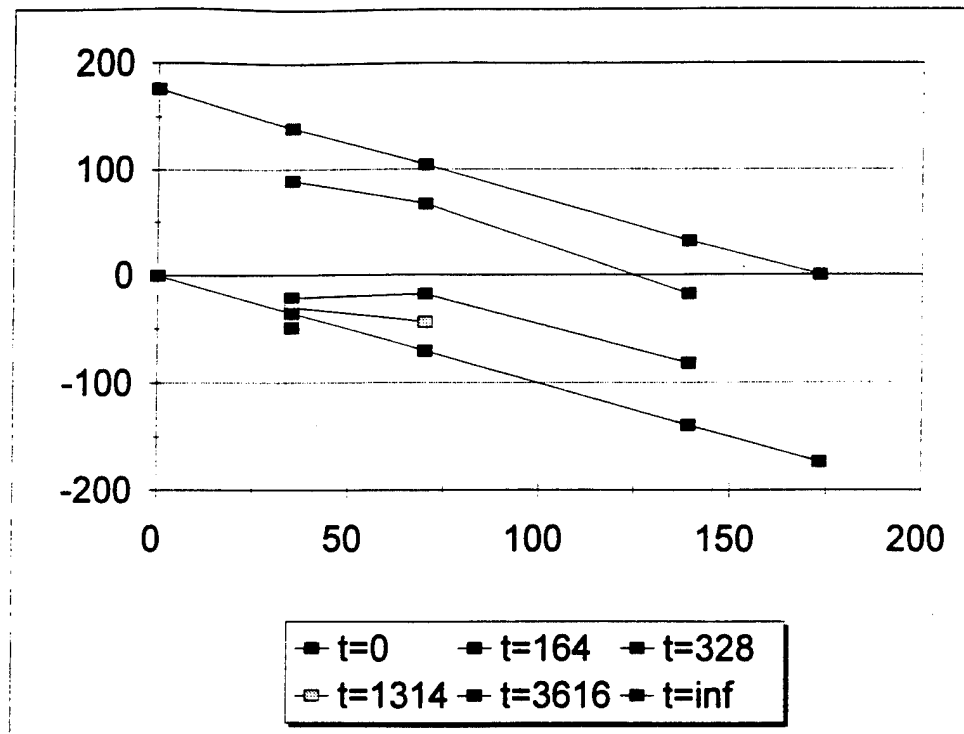
Figure 5-77. 20g scaled to 1g prototype pore pressure profiles

Having verified the ability to accurately model the drainage process using water

as the wetting fluid, the following figures compare the modeling of models tests to the

prototype using Soltrol as the wetting fluid. Figures 5-78 through 5-80 compare the

centrifuge models of Figure 5-36 through 5-38 scaled to the 1g prototype of Figure 5-17.

Figures 5-81 and 5-82 compare the 15g and 20g models scaled to the 10g model as the
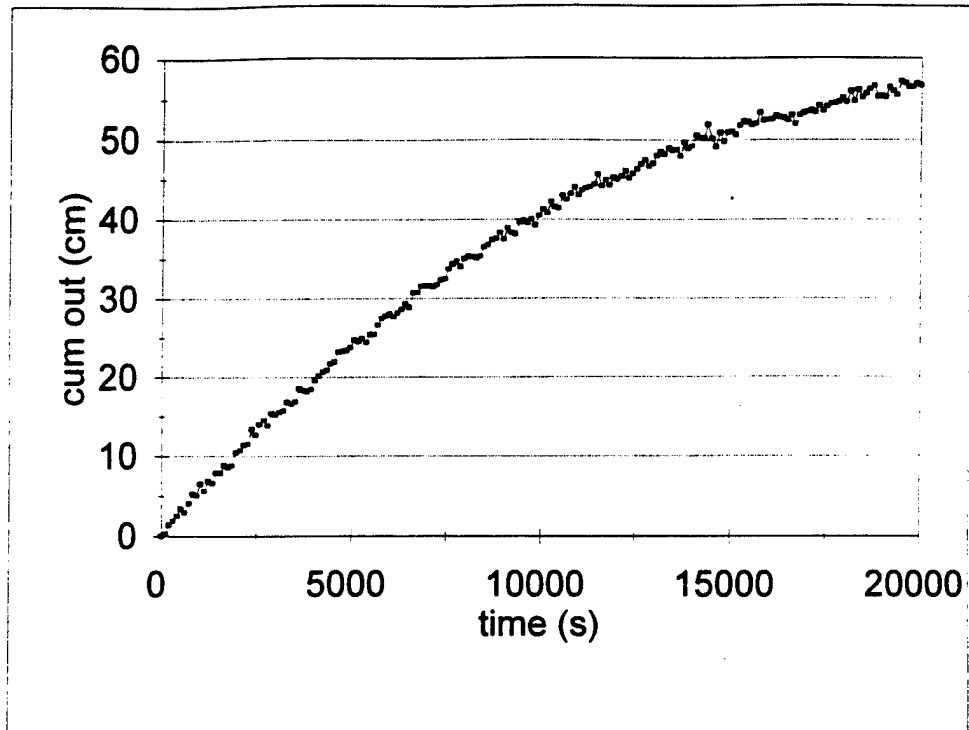
prototype.

Figure 5-78. 10g scaled to 1g prototype cumulative outflow curve using Soltrol
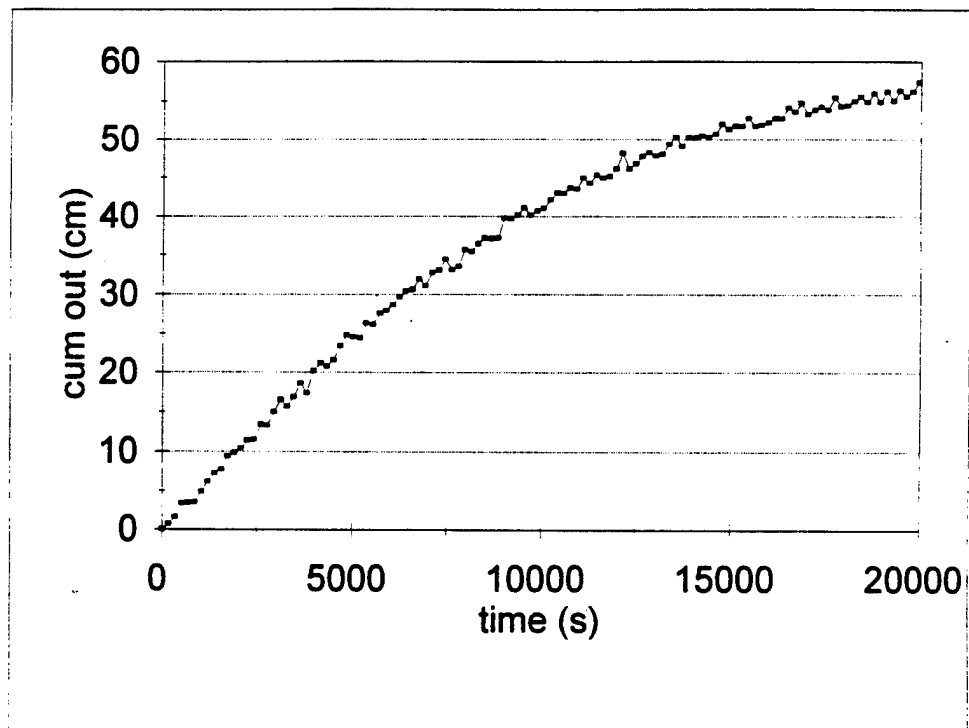
Figure 5-79. 15g scaled to 1g prototype cumulative outflow curve using Soltrol
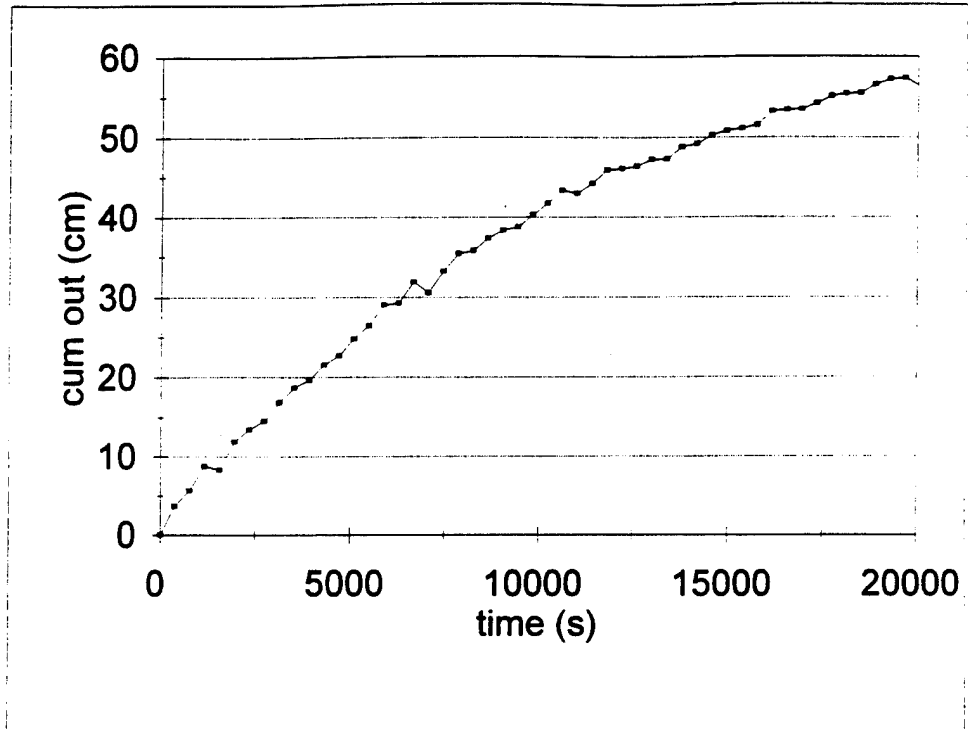
Figure 5-80. 20g scaled to 1g prototype cumulative outflow curve using Soltrol
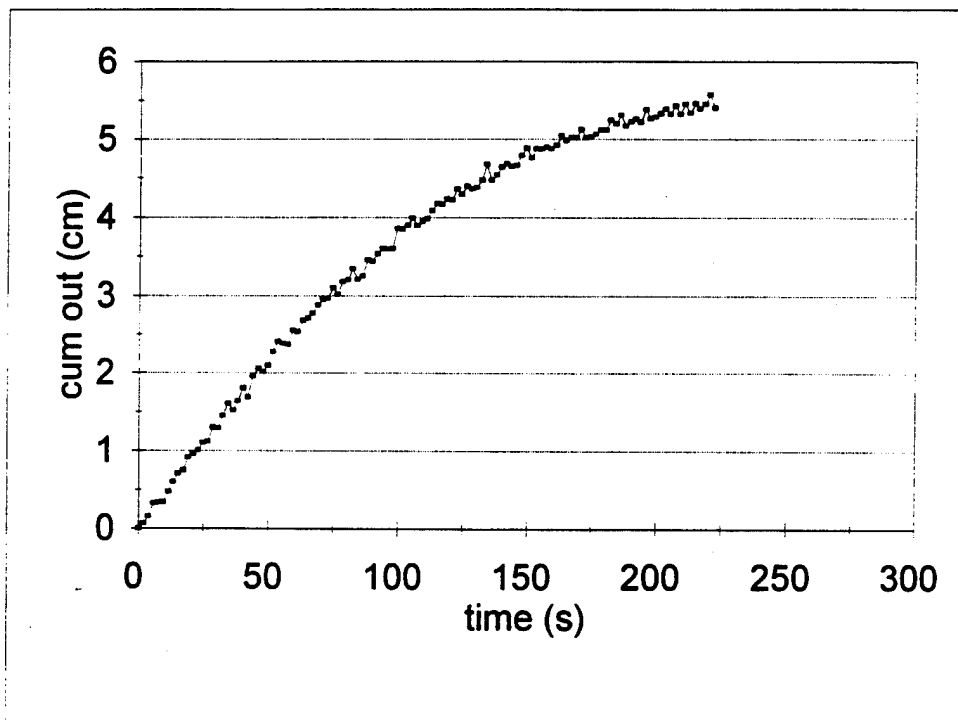
Figure 5-81. 15g scaled to 10 g prototype cumulative outflow curve using Soltrol
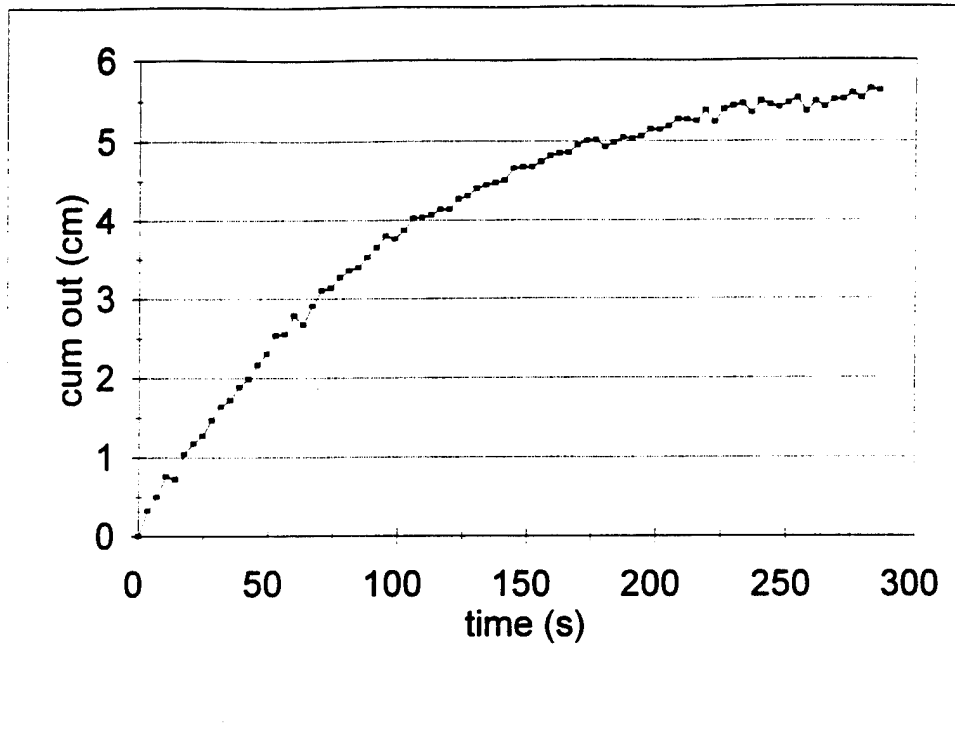
Figure 5-82. 20g scaled to 10g prototype cumulative outflow curve using Soltrol

Using the same analysis procedure developed for water, the test results using Soltrol shown in Figures 5-39 through 5-41 were scaled to the 1g prototype of Figure 5-17 and are shown in Figures 5-83 through 5-85. Figures 5-86 through 5-88 are the scaled pore pressure profiles. All Soltrol tests were run with the fluid table at the lower elevation causing an apparent suction similar to that of the water experiments. From the pore pressure profiles, it is seen that the boundary condition does not appear to scale. The scale factor and exponent for all tests are presented in Section 5.11, Summary of unsaturated sands tests.
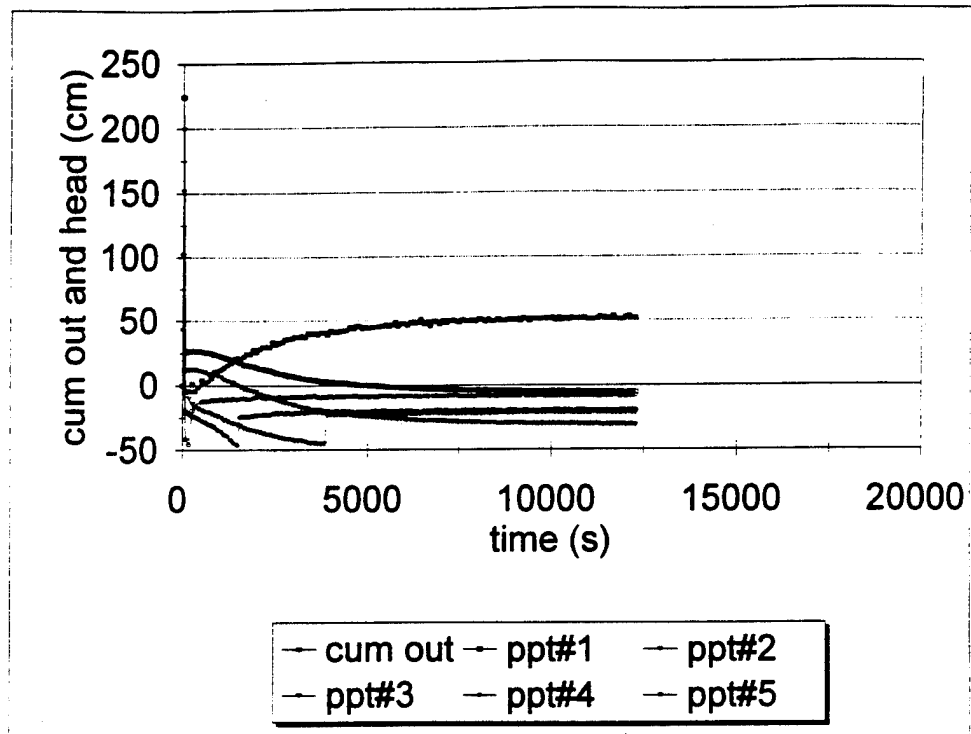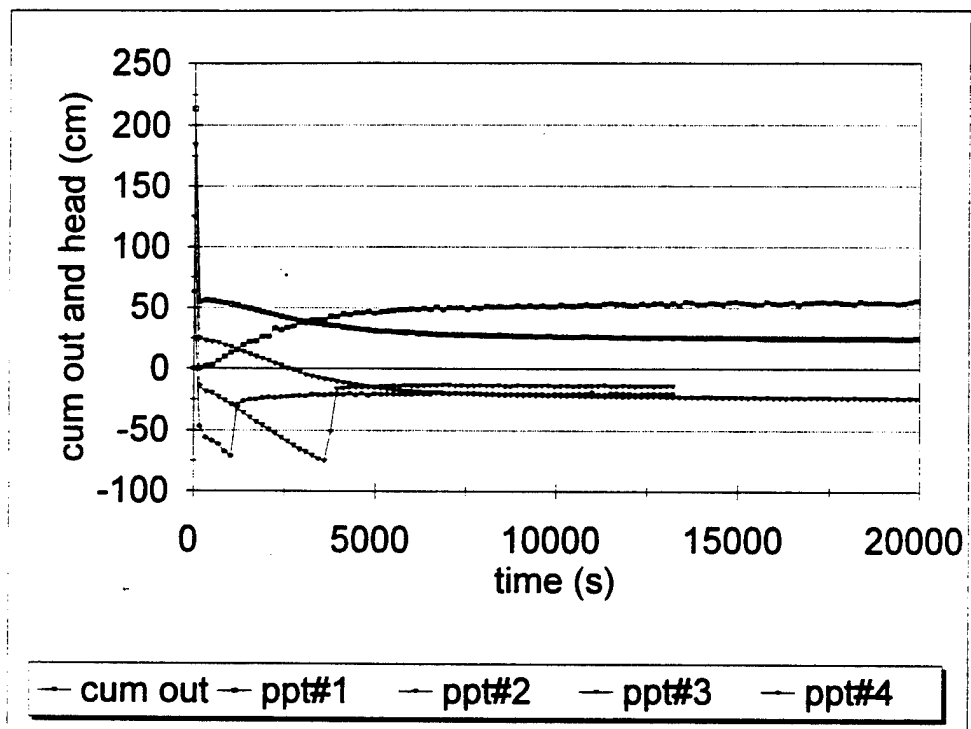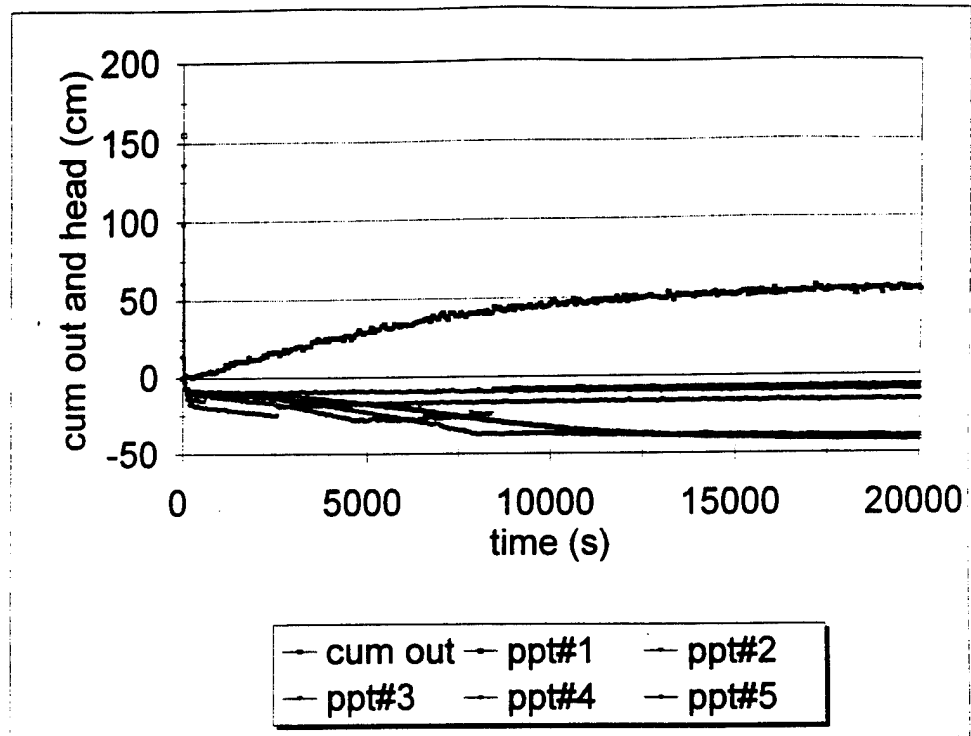
Figure 5-83. 10g scaled to 1g prototype
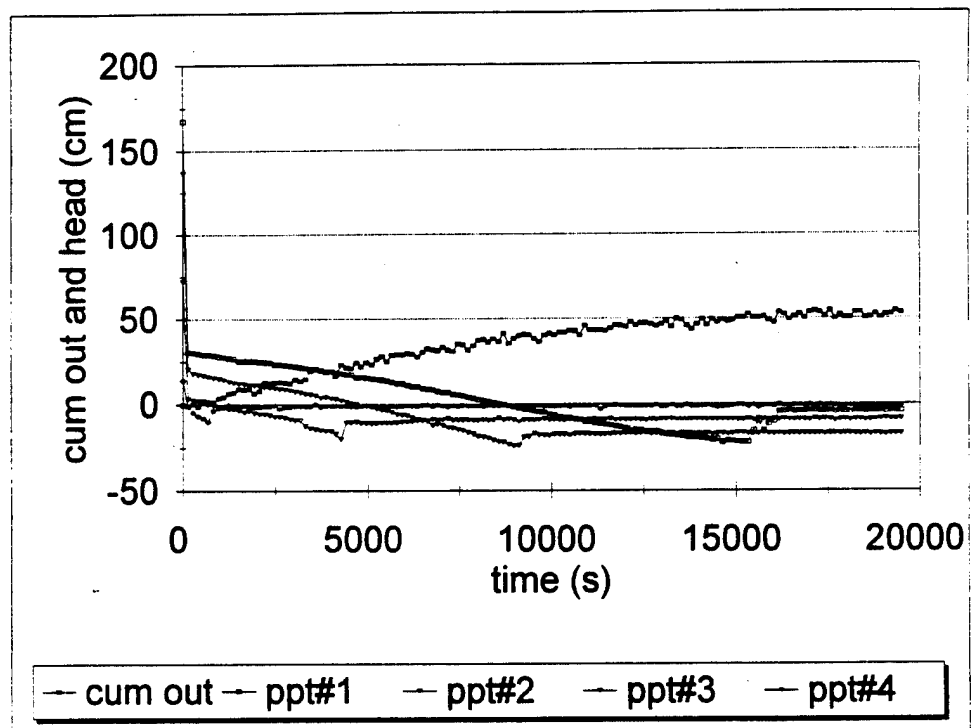
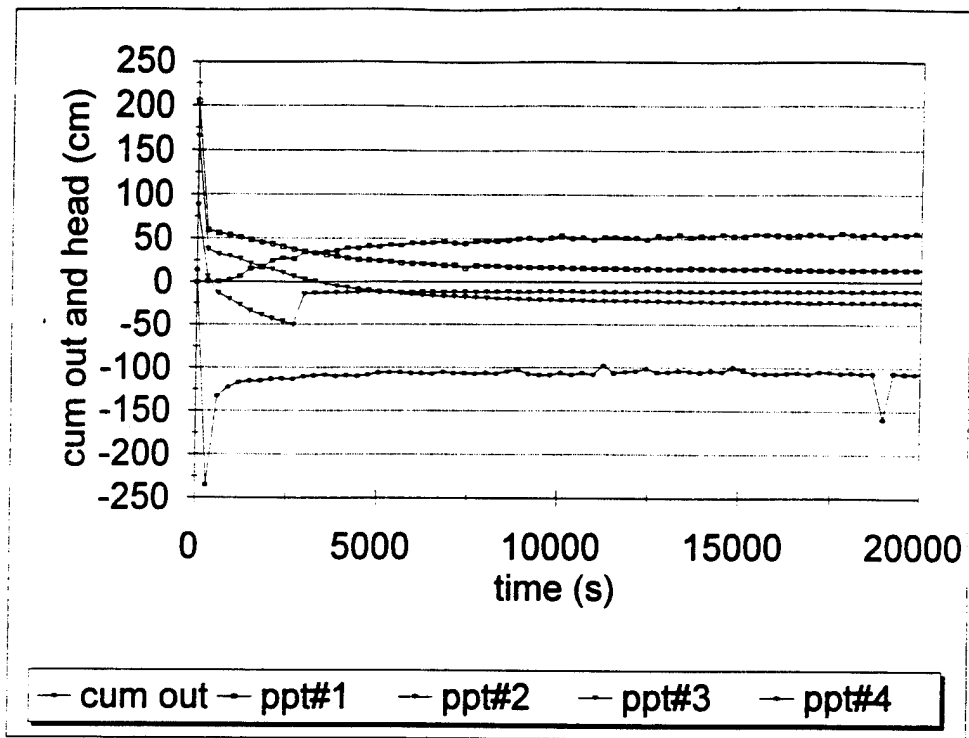**Figure 5-84. 15g scaled to 1g prototype**

167
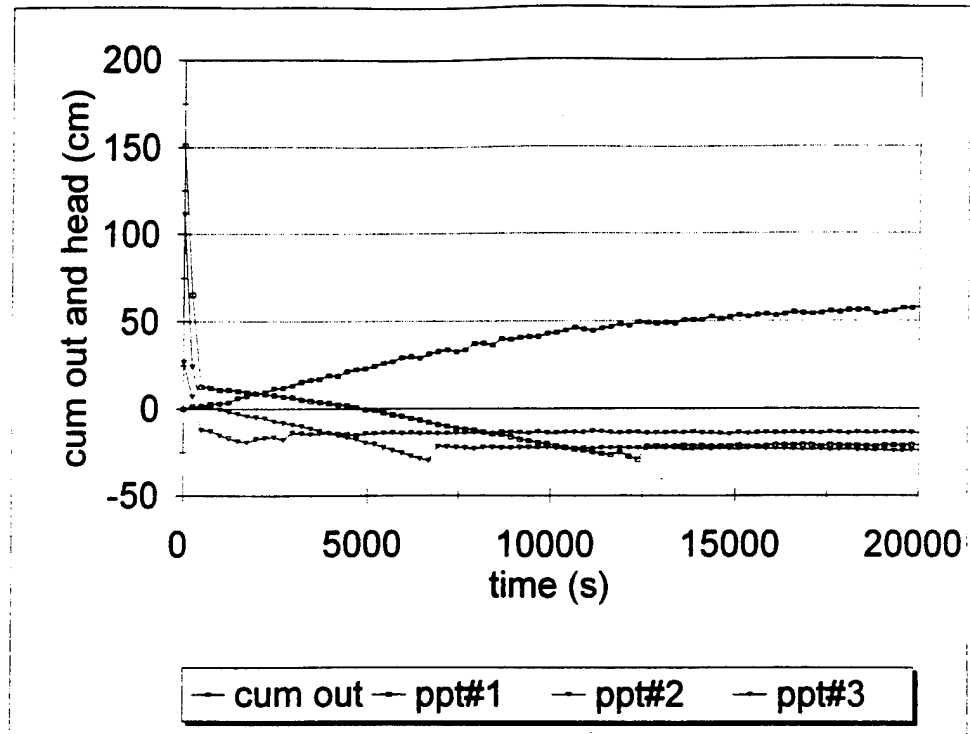
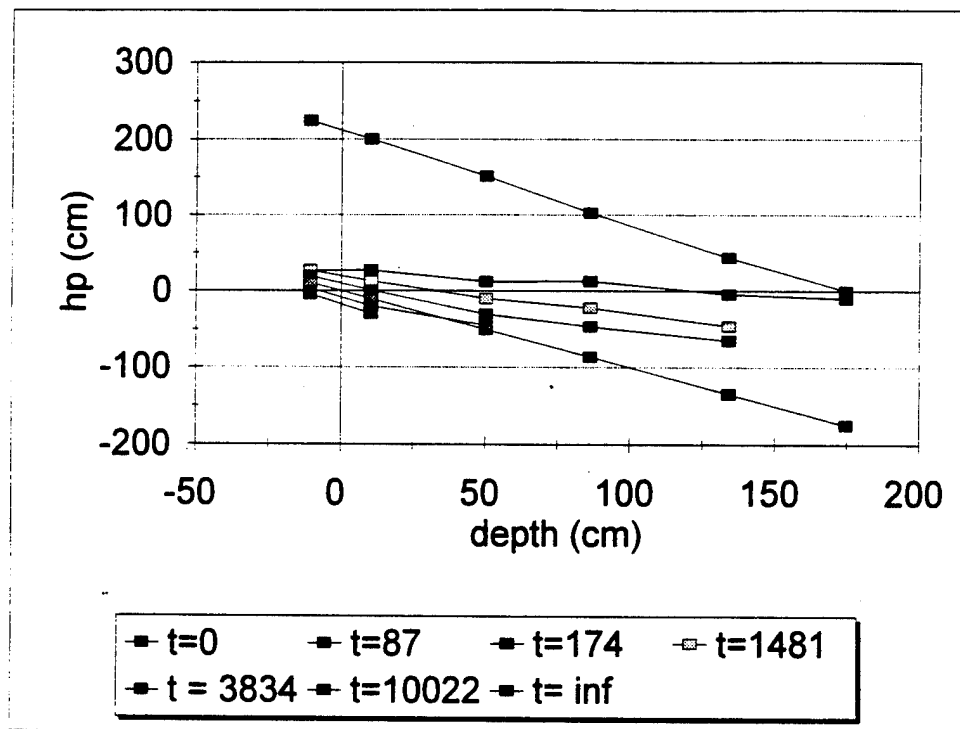Figure 5-85. 20g scaled to 1g prototype
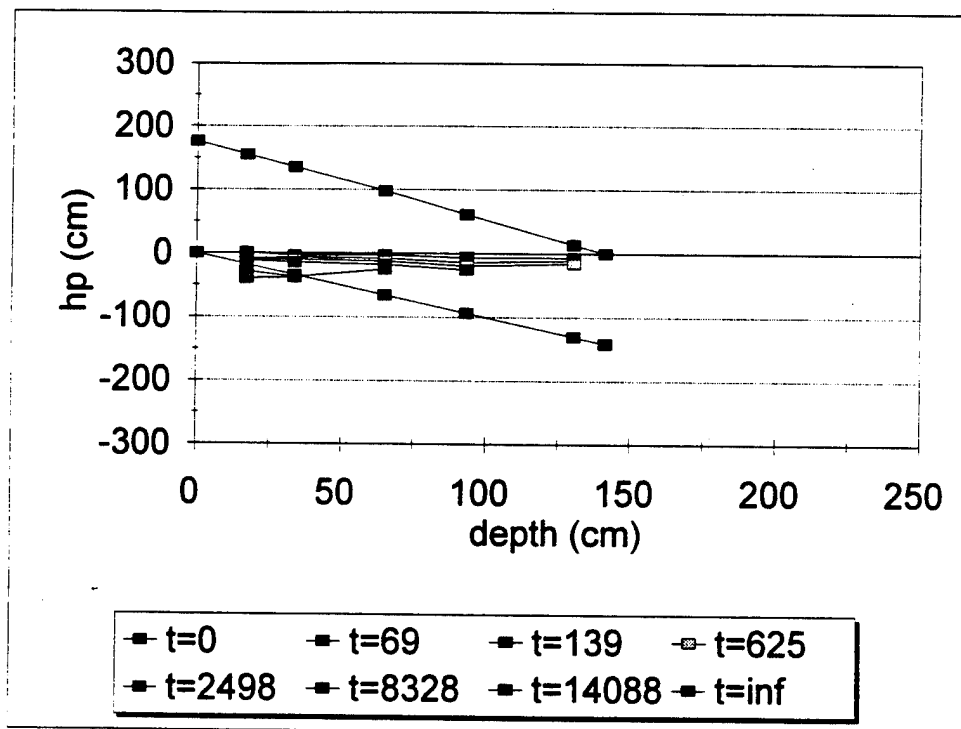
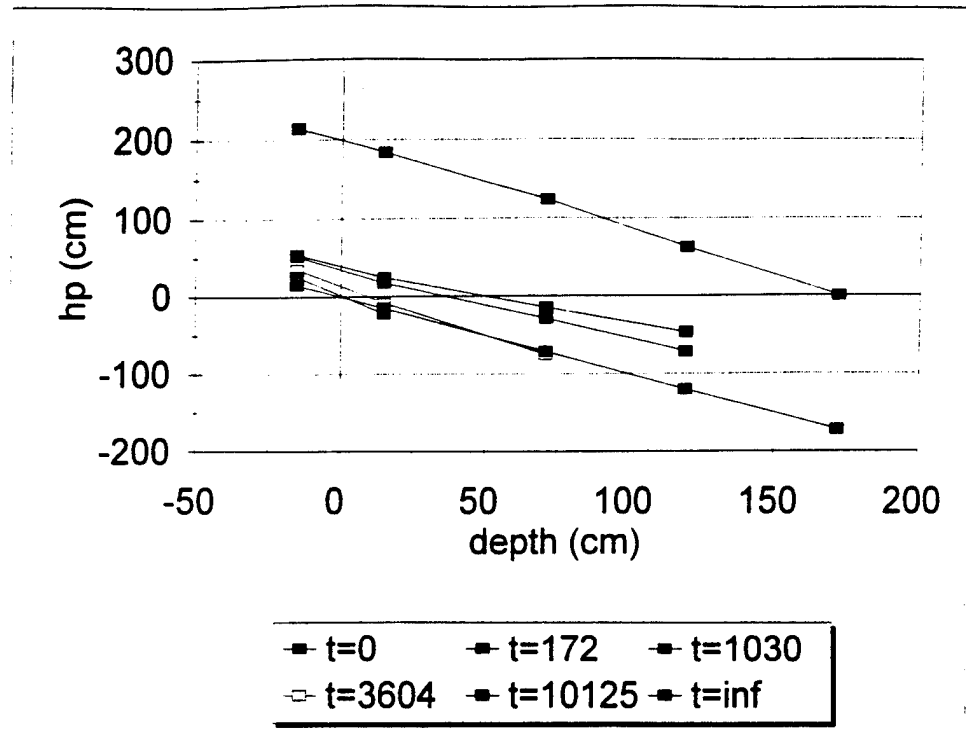Figure 5-86. 10g scaled to 1g prototype pore pressure profiles

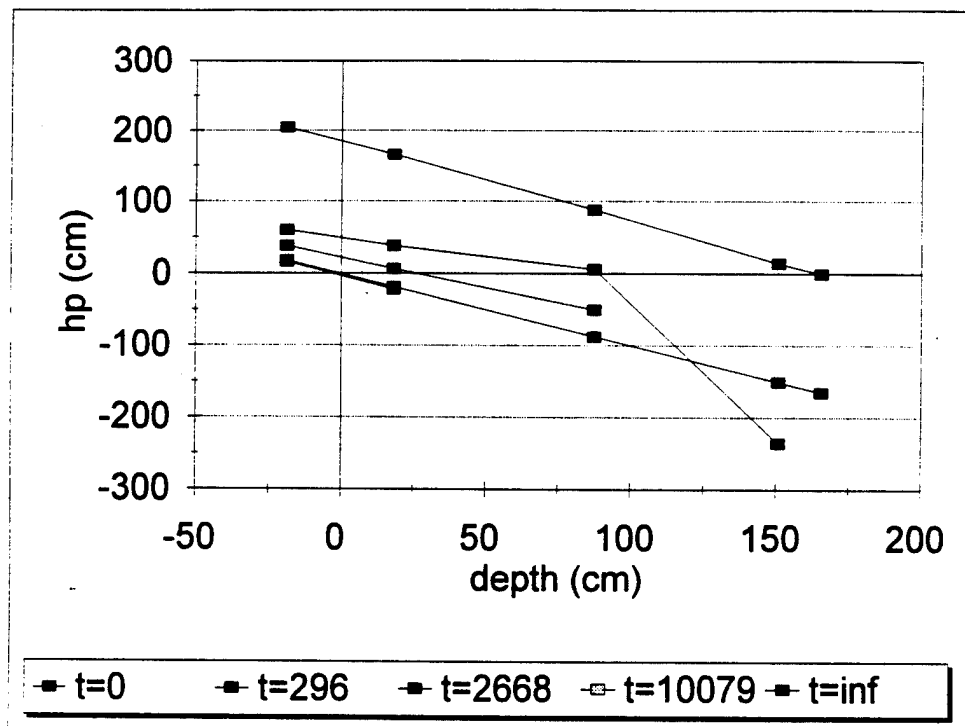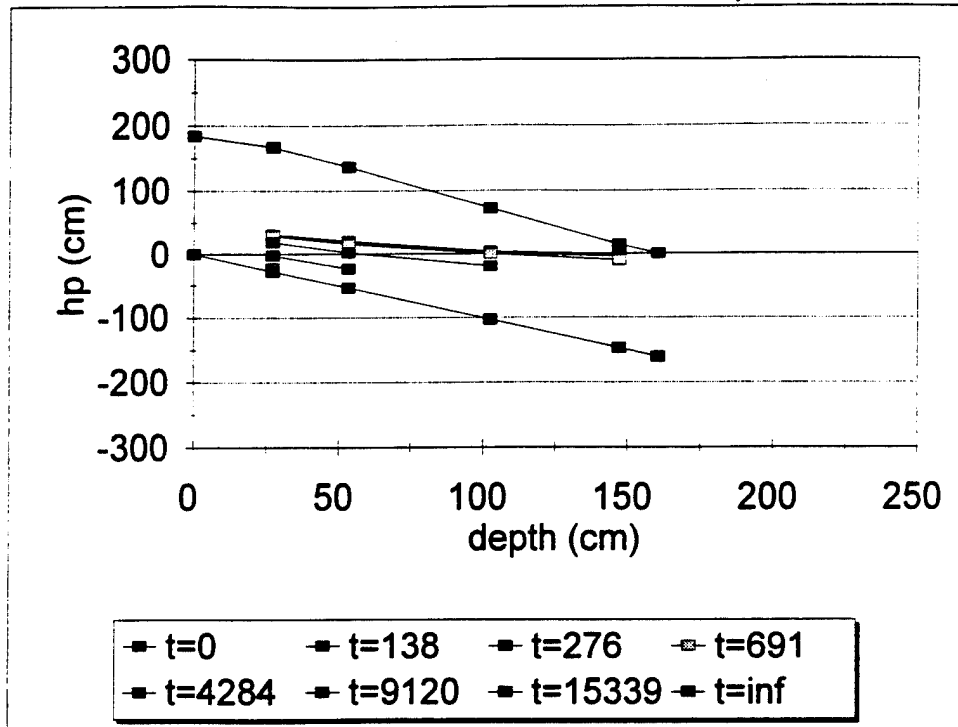**Figure 5-87. 15g scaled to 1g prototype pore pressure profiles**
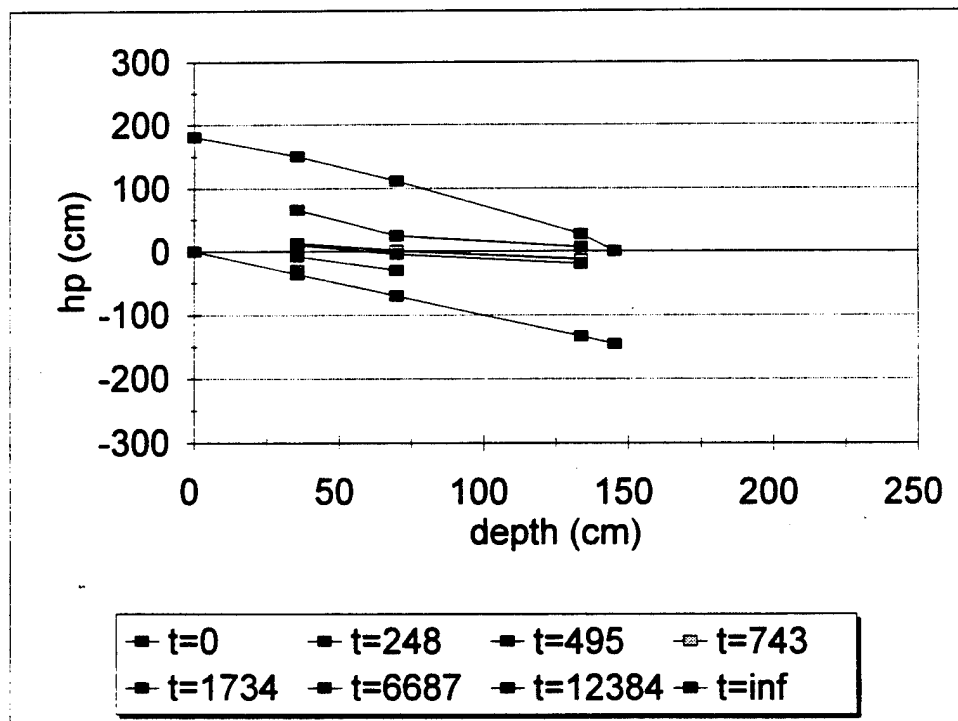
Figure 5-88. 20g scaled to 1g prototype pore pressure profiles

169

The homogeneous sands models appear to properly capture the prototype behavior. Both the cumulative outflow curve and the pore pressure distributions show the same characteristics, whether performed in a 1g or a multi-g environment, and the homogeneous sands tests verify the applicability of using the centrifuge to model unsaturated flow problems. The problems of repeatability, data measurement, and transducer functionality appear to have been overcome.

The next series of tests involved the layered sands. The layered sands models of Figures 5-46 through 5-48 were scaled to the prototype of Figure 5-44 and are shown in Figures 5-89 through 5-91.
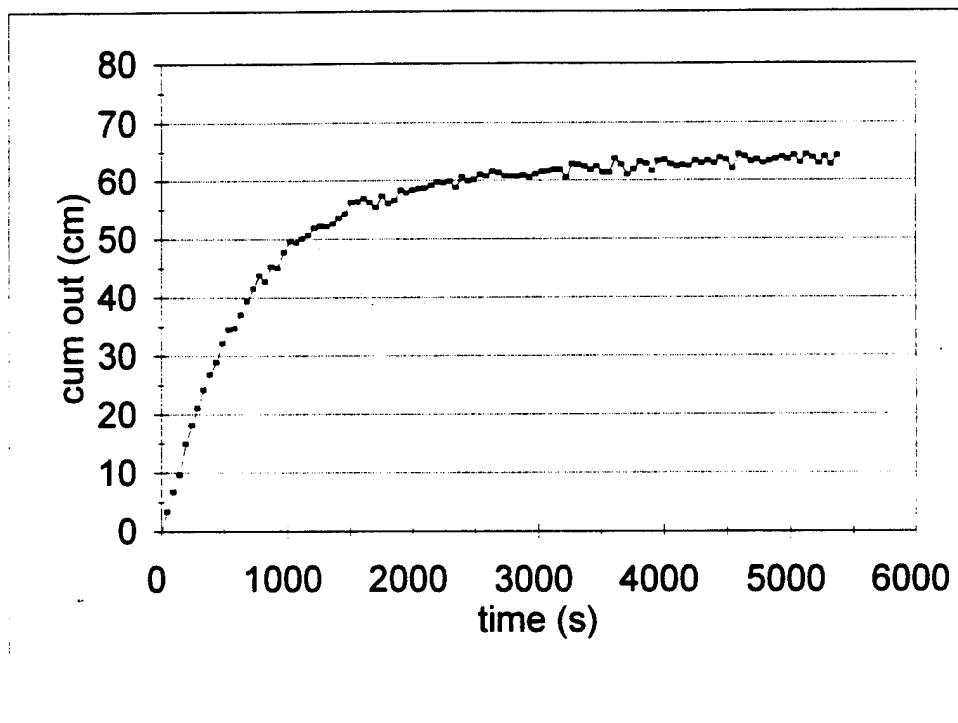
Figure 5-89. 10g scaled to 1g prototype
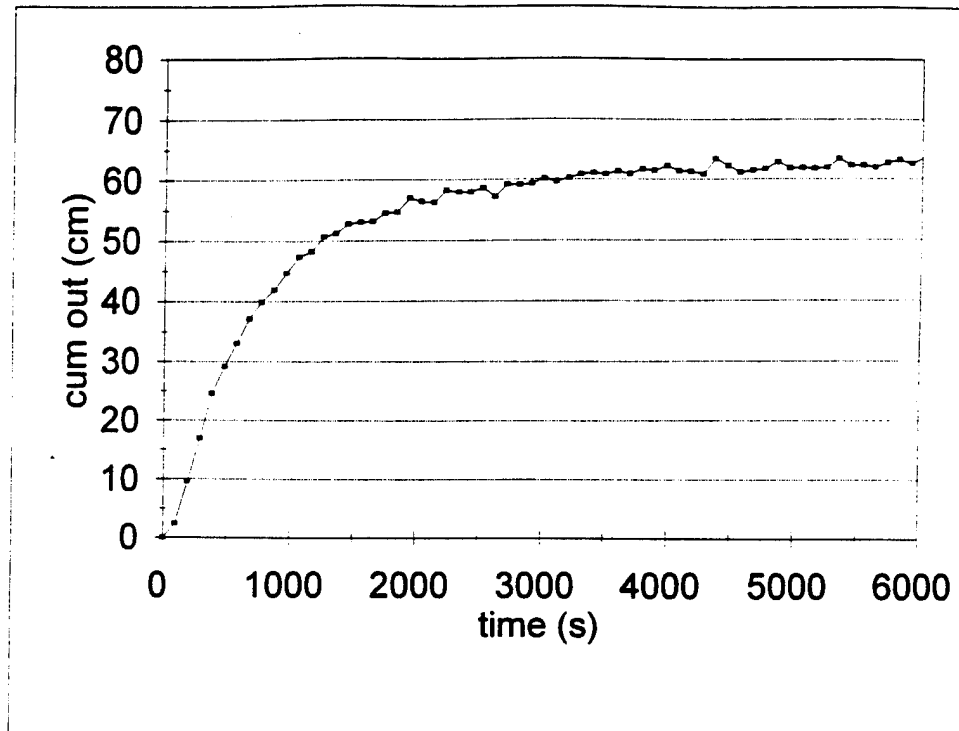
Figure 5-90. 15g scaled to 1g prototype
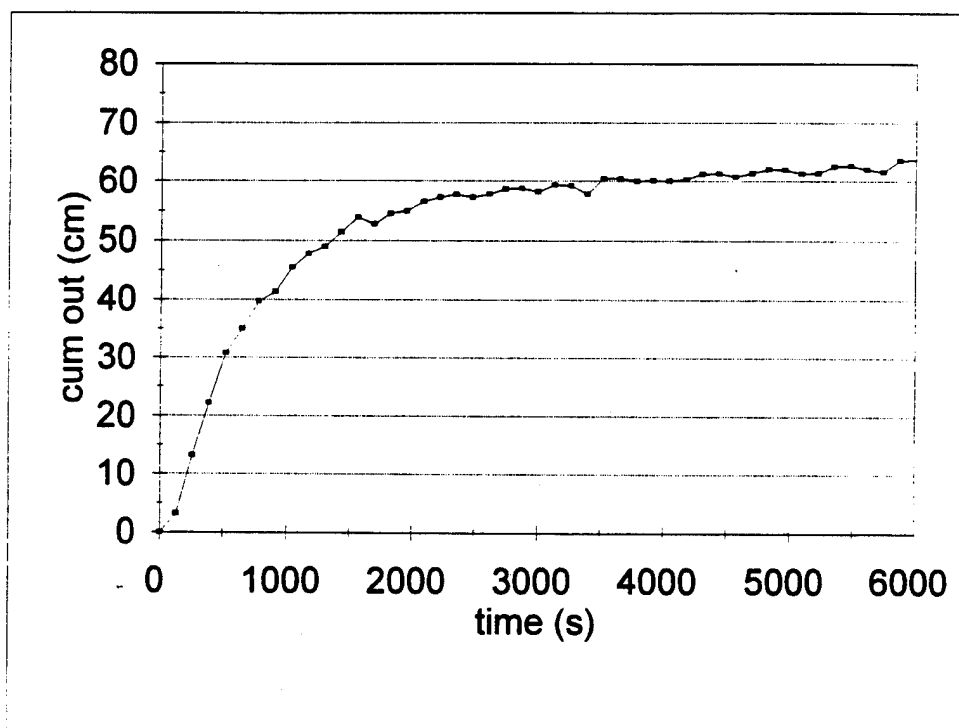
Figure 5-91. 20g scaled to 1g prototype

The previous tests were performed using water and without pore pressure measurements. The time exponents were found to be significantly lower than for the homogeneous case and varied significantly between each g-level. To verify these results, the tests using Soltrol shown in Figures 5-49 through 5-51 were scaled using the 10g model as the prototype. The scaled results are shown in Figures 5-92 through 5-94. The scaled pore pressure profiles are shown in Figures 5-95 through 5-97. The calculated scale factors and exponents for all tests are presented in Section 5.11, Summary of unsaturated sand tests.
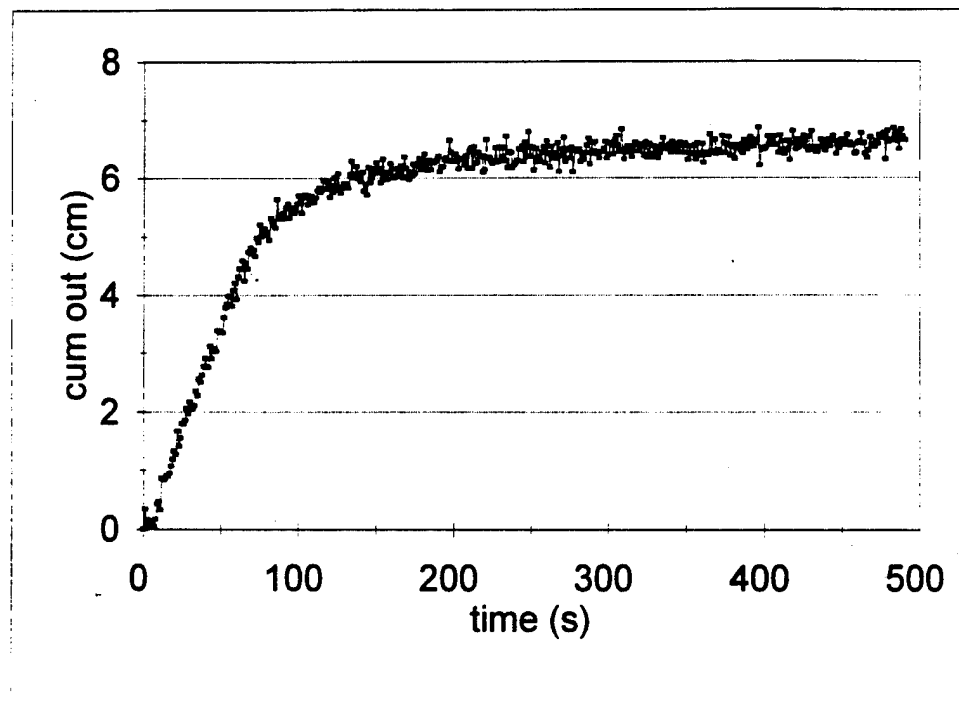
Figure 5-92. 10g as prototype using Soltrol

172
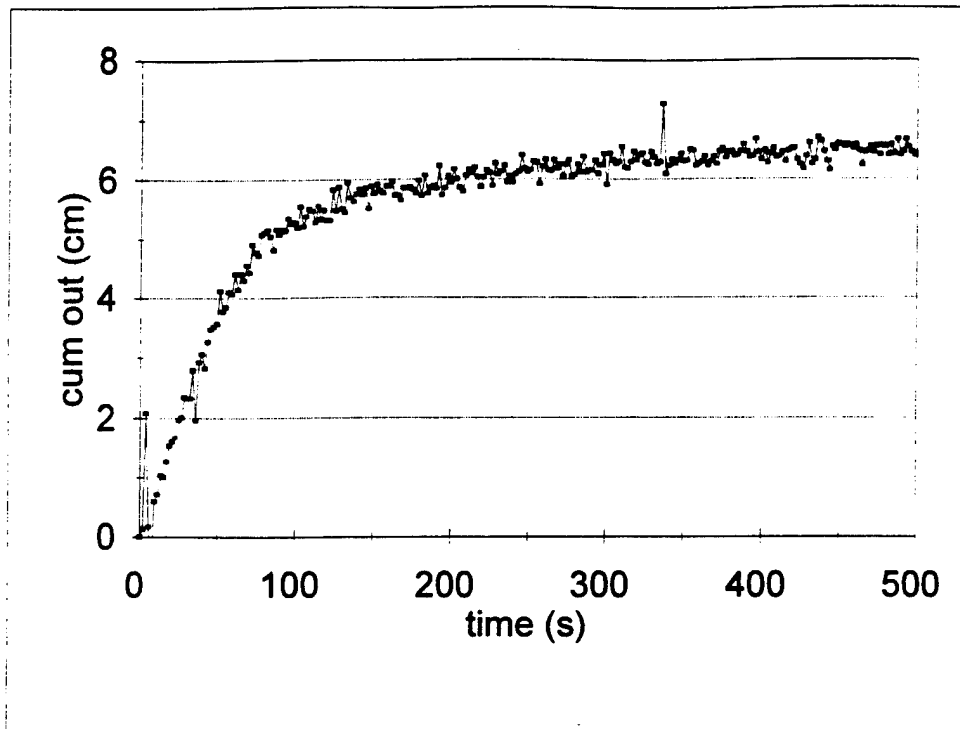
Figure 5-93. 15g scaled to 10g as prototype using Soltrol
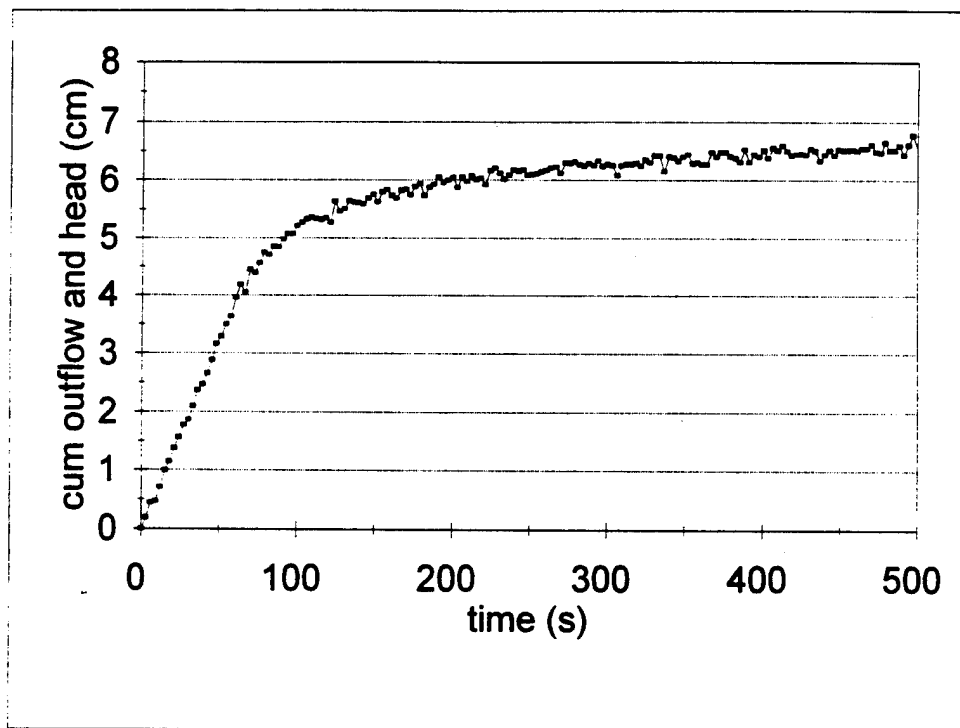
Figure 5-94. 20g scaled to 10g as prototype using Soltrol

173
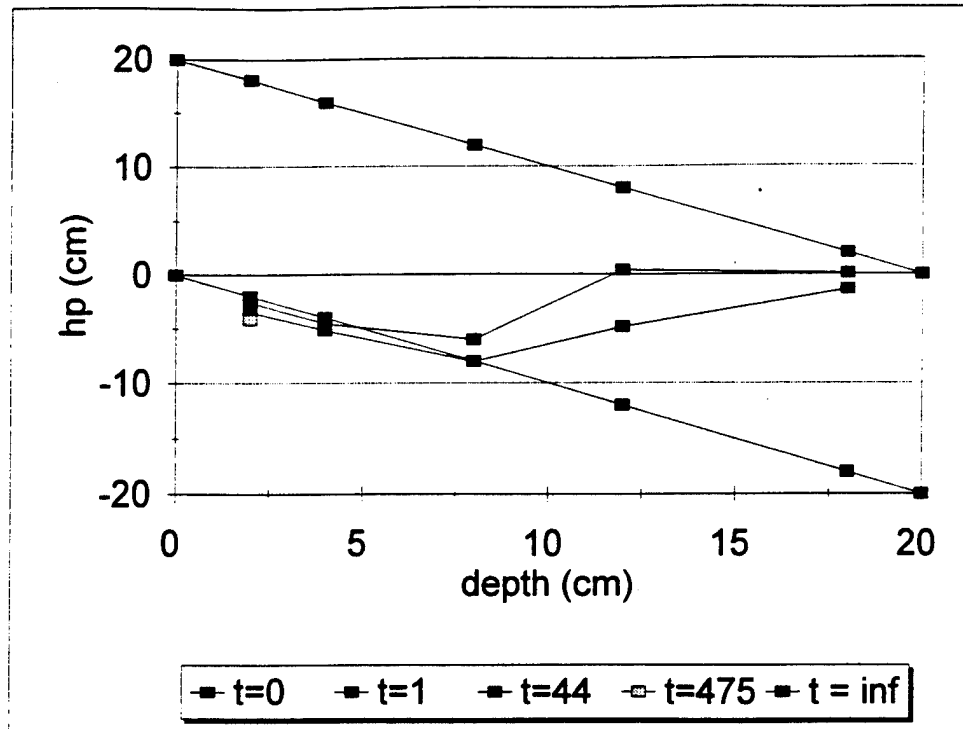
Figure 5-95. 10g as prototype pore pressure profiles
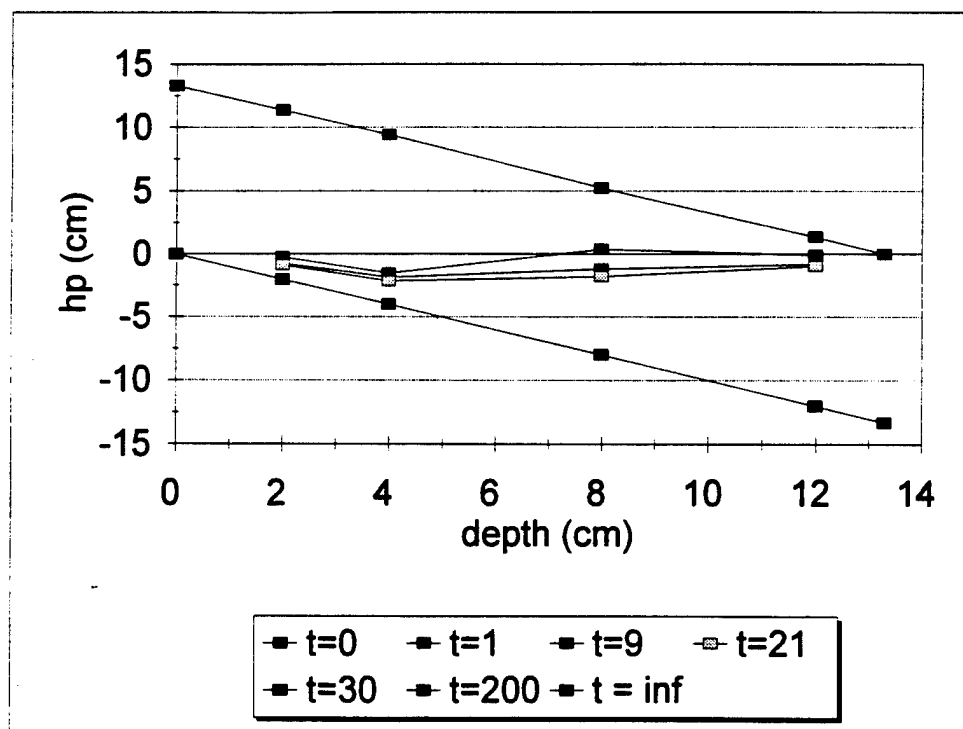
Figure 5-96. 15g scaled to 10g as prototype pore pressure profiles

174
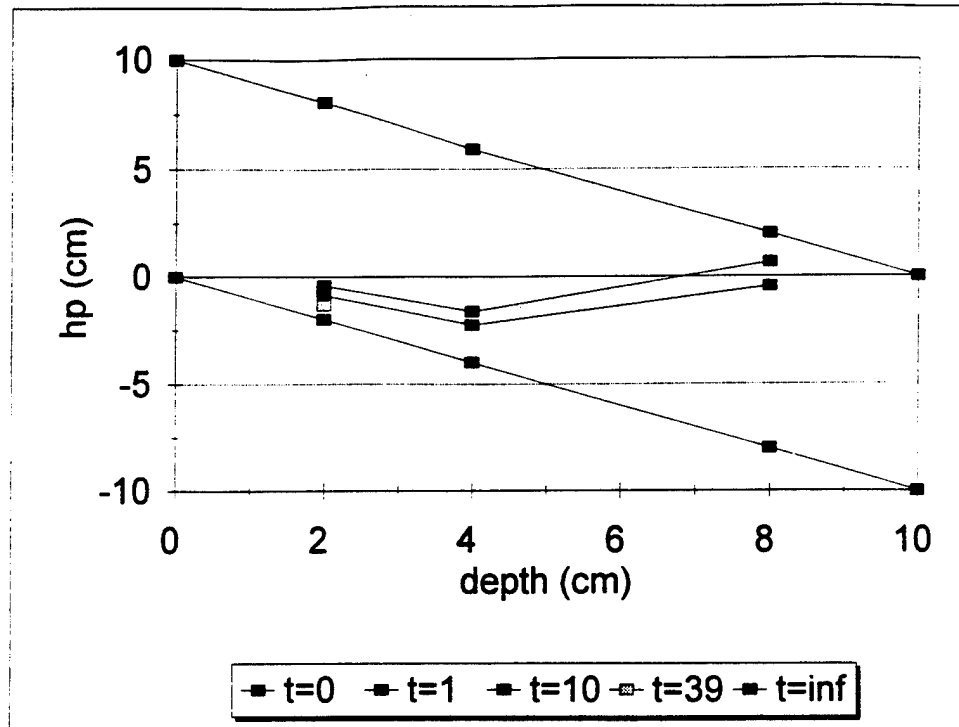
Figure 5-97. 20g scaled to 10g as prototype pore pressure profiles

From the pore pressure plots, the effect of the middle layer of #70 sand can be seen as a retardation of the drainage from the upper layer, similar to that obtained with the prototype of Figure 5-45. Once again, the final pore pressure distribution changes with g-level, approaching the theoretical distribution with increasing g-level.

The capillary fringe measured in each layer was found to be N times less than the prototype capillary fringe. For the #30 sand at 20g's the model fringe was measured as 0.2 cm and the scaled fringe is:

$$h_{cp} = Nh_{cm} = (20.4)(0.2) = 4.1 \ cm \tag{5.51}$$

which compares with a capillary rise of 3 cm shown in Figure 4-6. For the #70 sand at

175

20g's the model fringe was measured as 1.0 cm and the scaled fringe is:

$$h_{cp} = Nh_{cm} = (20.4)(1.0) = 20.4 \ cm \tag{5.52}$$

which compares with 20 cm of saturated capillary rise from Figure 4-6.

After drainage had occurred, some entrapped fluid remained within the pore space. The final saturation is assumed to be independent of the gravity level. The saturation can be calculated for each model and the total volume of fluids extracted can be compared. From Figure 4-6, the suction-saturation plot for #70 sand, the residual saturation is approximately 0.27 for the 1g prototype at suctions of approximately 60 cm and higher. The total volume that is at residual saturation in the 200 cm column (Area = 80.12 cm², $\phi = 0.45$) is:

$$V_1 = (0.45)(200-60)(80.12) = 5048cm^3 \tag{5.53}$$

The volume remaining entrapped in the upper 140 cm of the column and at residual saturation is:

$$E_1 = (0.27)(5048) = 1363cm^3 \tag{5.54}$$

The total volume that is in the capillary fringe between 20 cm and 60 cm of suction is:

$$V_2 = (0.45)(60-20)(80.12) = 1442cm^3 \tag{5.55}$$

The volume remaining entrapped in the capillary fringe, assuming a triangular approximation between S= 0.27 and S = 0.45 is :

176

$$E_2 = (0.27)(1442) + \frac{(0.45 - 0.29)}{2}(1442) = 519 cm^3 \tag{5.56}$$

The total theoretical cumulative fluid drained from the column is:

$$Cum\ out = (V_1 - E_1) + (V_2 - E_2) = (5048 - 1363) + (1442 - 519) = 4608 cm^3 \tag{5.57}$$

From Figure 5-11, the total experimental cumulative fluid drained is:

$$Cum\ out = (57)(80.12) = 4567\ cm^3 \tag{5.58}$$

which suggests that the prototype column is essentially at residual saturation. The centrifuge models can be checked in the same manner. Table 5-3 compares the theoretical versus experimental results of the large centrifuge tests of Figure 5-32 through Figure 5-35.

Table 5-3. Theoretical and measured cumulative outflow

Test	Theoretical Cum out cm^3	Measured Cum out cm^3
5g	769	748
10g	425	391
15g	284	264
20g	214	213

The measured cumulative outflow values for all tests in both the large and small centrifuge only varied 5% from the values shown in Table 5-3, with the variation probably due to different values of porosity. For example, a 1% increase in porosity, from 45% to 46%, results in an increase of the prototype total volume $V_1 + V_2$ from 6490 cm^3 to 6633 cm^3, giving a 2.2% variation.

With only a 1% variation in the porosity, the effect at multi-g levels becomes pronounced. For example, the 10g test where the scale factor N has been calculated for a sample with 45% porosity is:

$$N = \frac{(cum\ out)_p}{(cum\ out)_m} = \frac{57}{5.5} = 10.36 \tag{5.59}$$

For the same 10g test with a 46% porosity, the scale factor N is:

$$N = \frac{(cum\ out)_p}{(cum\ out)_m} = \frac{57}{5.62} = 10.13 \tag{5.60}$$

and using the time factor Equation (5.38) for the 45% sample gives a final theoretical time of:

$$t_p = (10.36^2)(300) = 32199s \tag{5.61}$$

and for the 46% sample gives a final theoretical time of:

$$t_p = (10.13^2)(300) = 30785s \tag{5.62}$$

For the two systems to be equivalent, the time factor exponent "a" of the 45% porosity sample would have to be reduced from 2 to 1.98. Finding the actual time factor is complicated by another problem. For the analysis of the centrifuge models, it has been assumed that an "average" scale factor N could be found such that the prototype and model cumulative outflow curves would coincide. However, what the soil sample is experiencing is a variable g-field which is changing as the drainage front moves downward. From the cumulative outflow curve there is no apparent method to determine where the front is with respect to time. Examining the 10g test of Figure 5-23; at the top of the soil sample the g-level is 8.44g, the midpoint has a g-level of 9.05g, 5 cm above the bottom the g-level is 9.30g, and the bottom g-level is 9.65g. From the cumulative outflow curve of Figure 5-23, it is seen that 90% drainage occurs within the first 45 seconds of the test. Applying the time factor using the actual g-levels for each 15 second intervals of the first 45 seconds of drainage gives:

$$t_p = (8.44^2)(15)+(9.05^2)(15)+(9.30^2)(15)+(9.65^2)(255)=27340s \qquad (5.63)$$

which requires the time exponent "a" to be reduced from 2 to 1.93 for the "average" scale factor N equal to 10.36g. If the actual g-level of 9.65g at the bottom of the sample is used as the scale factor N, the time exponent "a" becomes 1.85.

An additional error is incorporated when draining the fluid down to the level of the sand prior to the start of a test; a 1mm variation at the top surface is equivalent to 8.01 cm^3 of fluid. Comparing with Table 5-3, the variation of 8 cm^3 of fluid is 1% to 4% of the total cumulative outflow.

179

The ability to prepare consistent samples is shown in the water cumulative outflow curves of Figures 5-23 through 5-25. Using the same sample preparation techniques, the Soltrol cumulative outflow curves of Figures 5-36 through 5-38 illustrate the variability in cumulative outflow curves. The variability of the Soltrol curves could be due to sample preparation, or due to physical factors such as surface tension, viscosity, density, and wettability of the Soltrol compared to water.

Finally, it should be noted that the centrifuge is only accurate to plus or minus 2 RPM. For the nominal 9.65g test, the actual g-level could be as low as 9.24g or as high as 10.06g. The corresponding time exponent "a" could be as low as 1.82 or as high as 1.89. The cumulative outflow scale factor N and the time exponent "a" are clearly very sensitive to both the sample preparation and the imposed g-level.

5.11 - Summary of test results

The experimental tests program was designed to validate the scaling laws for the hydraulic conductivity and the time, and to test the requirement for a changing arm radius for the modeling of models technique. In multiphase flow, the hydraulic conductivity is a function of the degree of saturation. For homogeneous sands, the change in saturation is continuous, while in layered sands, the interfaces cause a discontinuity. Layered systems are the norm rather than the exception for most contamination problems.

The scaling factor N for the cumulative outflow curve and the time exponent "a" for all tests are presented in Table 5-4. N was obtained by matching the final cumulative outflow value, while the exponent was obtained by matching the complete cumulative

outflow curves. From Sections 4.2 and 5.2, it can be seen that the theoretical value of the hydraulic conductvity is N, and the time exponent "a" is 2. The cumulative outflow curves are a plot of the hydraulic conductivity with time. The ratio of the calculated scale factor N to the actual g-level N_{act} is denoted as λ. Figure 5-98 and Figure 5-99 are plots of λ and "a" versus N_{act}.

Table 5-4. Summary of unsaturated sand tests

Test	Fluid	Sand	N_{act}	N	a	λ
1g	water	#70 low fl	1	1		
1g	water	#70 elev fl	1	1		
1g	water	#30/#70/#30	1	1		
1g	Soltrol	#70 low fl	1	1		
10g to 1g	water	#70 low fl	9.65	10.30	1.78	1.07
15g to 1g	water	#70 low fl	14.15	16.00	1.78	1.13
20g to 1g	water	#70 low fl	19.52	19.00	1.80	0.97
15g to 10g	water	#70 low fl	1.47	1.55	1.80	1.05
20g to 10g	water	#70 low fl	2.02	1.82	1.82	1.11
10g to 1g	water	#70 low fl	8.66	11.00	1.82	1.27
15g to 1g	water	#70 low fl	13.66	15.50	1.84	1.13
20g to 1g	water	#70 low fl	17.82	20.00	1.82	1.12

Table 5-4. Summary of unsaturated sand tests (continued)

Test	Fluid	Sand	N_{act}	N	a	λ
5g to 1g	water	#70 low fl	4.43	4.70	2.00	1.06
10g to 1g	water	#70 low fl	8.86	8.67	1.70	0.98
10g to 1g	water	#70 low fl	8.86	8.67	1.82	0.98
15g to 1g	water	#70 low fl	13.66	13.09	1.82	0.96
15g to 1g	water	#70 low fl	13.66	13.09	1.82	0.96
20g to 1g	water	#70 low fl	17.82	16.50	1.82	0.93
20g to 1g	water	#70 low fl	17.82	16.50	1.82	0.93
10g to 1g	water	#70 elev fl	10.91	10.50	1.90	0.96
15g to 1g	water	#70 elev fl	15.46	15.00	1.90	0.97
20g to 1g	water	#70 elev fl	19.04	20.00	1.90	1.05
10g to 1g	Soltrol	#70 low fl	10.06	10.80	1.95	1.07
15g to 1g	Soltrol	#70 low fl	14.90	17.00	1.82	1.14
20g to 1g	Soltrol	#70 low fl	20.40	24.00	1.88	1.18
15g to 10g	Soltrol	#70 low fl	1.48	1.65	1.30	1.11
20g to 10g	Soltrol	#70 low fl	2.03	2.10	1.70	1.03

Table 5-4. Summary of unsaturated sand tests (continued)

Test	Fluid	Sand	N_{act}	N	a	λ
10g to 1g	Soltrol	#70 low fl	8.60	9.10	1.92	1.06
15g to 1g	Soltrol	#70 low fl	13.66	15.00	1.82	1.10
20g to 1g	Soltrol	#70 low fl	17.82	20.00	1.84	1.12
5g to 1g	Soltrol	#70 low fl	4.43	4.70	1.82	1.06
10g to 1g	Soltrol	#70 low fl	8.86	10.00	1.75	1.13
15g to 1g	Soltrol	#70 low fl	13.28	16.00	1.90	1.20
20g to 1g	Soltrol	#70 low fl	17.70	16.50	1.95	0.93
10g to 1g	water	#30/#70/#30	9.85	9.85	1.82	1.00
15g to 1g	water	#30/#70/#30	15.4	16.00	1.65	1.04
20g to 1g	water	#30/#70/#30	20.40	21.00	1.60	1.03
15g to 10g	water	#30/#70/#30	1.56	1.70	1.40	1.09
20g to 10g	water	#30/#70/#30	2.07	2.20	1.30	1.06
20g to 15g	water	#70/#30/#70	1.32	1.45	1.30	1.10
15g to 10g	Soltrol	#30/#70/#30	1.52	1.43	1.80	0.94
20g to 10g	Soltrol	#30/#70/#30	1.98	2.00	1.60	1.01
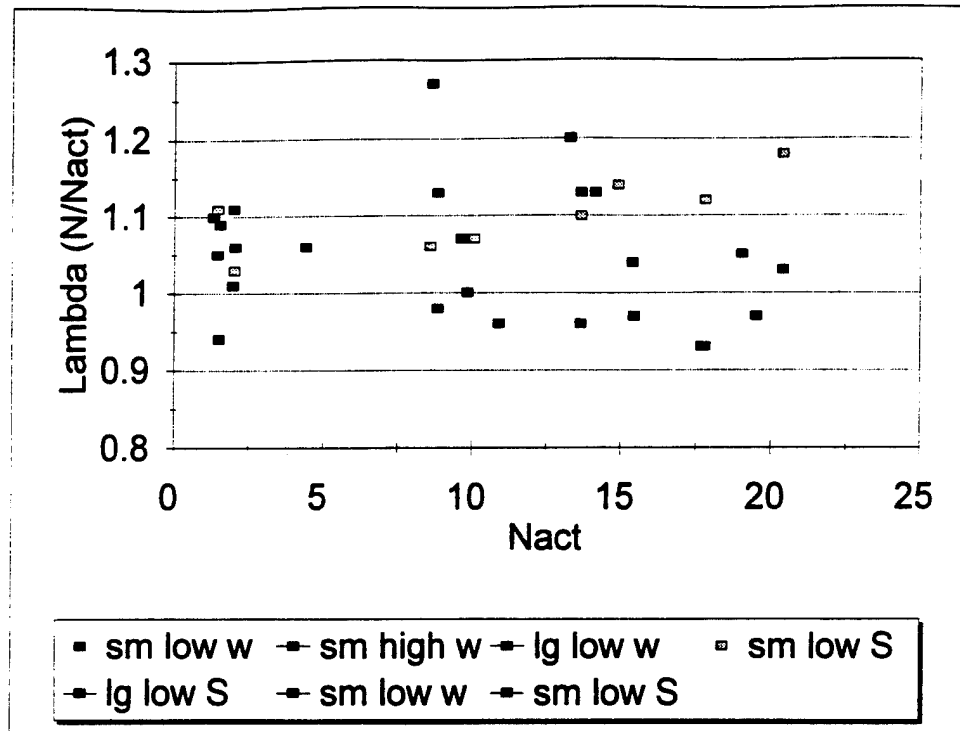
Figure 5-98. λ versus N_{act}
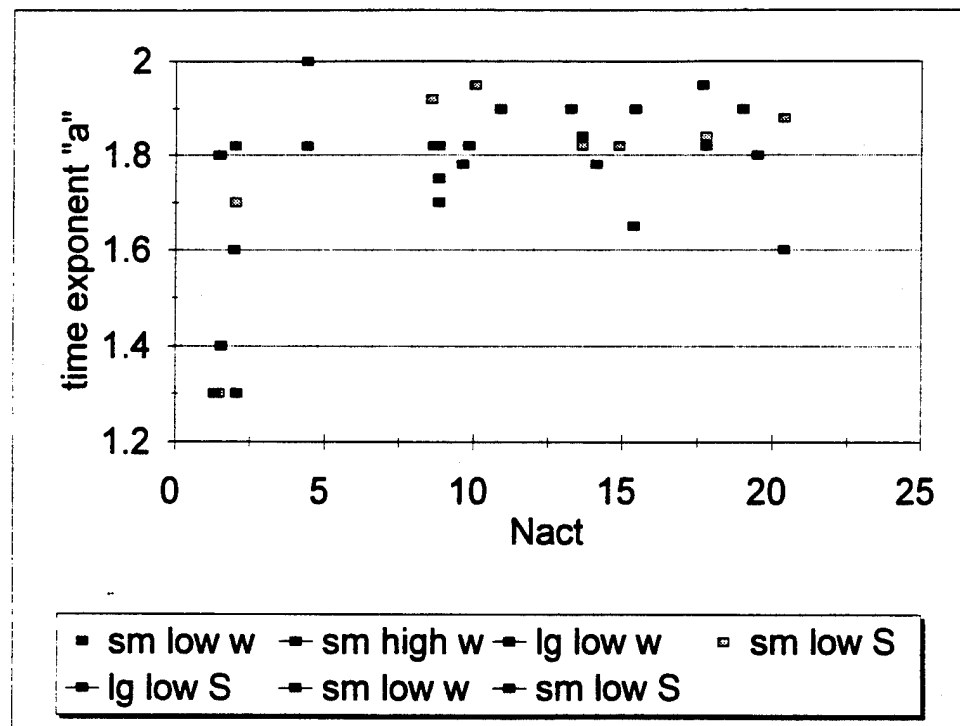
Figure 5-99. "a" versus N_{act}

5.12 - Analysis and discussion of results

The experimental results for unsaturated flow verify the scaling relationship for the cumulative outflow and therefore the hydraulic conductivity as:

$$K_m = N K_p \quad \text{(hydraulic conductivity)}$$

and the scaling of the time as:

$$t_p = N^a t_m \quad \text{(time)}$$

The scale factor N and the time exponent "a" appear to be dependent upon the boundary conditions imposed at the bottom of the column. Originally, the bottom boundary of the soil column was designed in such a way that the free water table level was exactly at the bottom of the soil sample and porous stone interface. The pore pressure measurements revealed that such an arrangement resulted in suction being applied to the bottom of the column. From the prototype pore pressures shown in Figure 5-12, an additional 25 cm of suction is applied at the interface. For the centrifuge models, the initial value of 25 cm decreased to 0 cm with increasing g-levels, as seen in Figures 5-61 through Figure 5-63.

In order to avoid the suction problem, the water table was raised 2 cm above the porous stone in subsequent experiments. For the prototype pore pressures shown in Figure 5-16, the pore pressure measurements for this arrangement revealed the boundary condition caused 25 cm of positive pressure head (impedance to flow). For the centrifuge models, instead of 25 cm of impedance, an additional 25 cm of suction reappears at 10g's,

and decreases to 0 cm at 20g's, as shown in Figure 5-67 through Figure 5-69.

It is clear that the boundary conditions in the tests did not properly scale and that the variation at the boundary affected the outflow rates in the experiments. Indeed, in the experiments with the higher suction, the cumulative outflow curve lies above the corresponding curve with the impeded boundary, as can be seen by comparing Figure 5-11 and Figure 5-13. The cumulative outflow curve with suction indicates higher outflow rates, as should be expected for the given boundary conditions.

As previously discussed, sample preparation and the chosen method of analysis can affect the scale factor N. A variation in the scale factor N as high as 10% would not be unreasonable. As illustrated by Figure 5-98, the average λ for all tests is 1.05, indicating the cumulative outflow scale factor N is approximately 5% greater than the actual g-level. The higher scale factor N indicates a bias, implying more fluid is extracted from the centrifuge models compared to the prototype. As illustrated by Figure 5-99, the average time exponent "a" is 1.87. This average does not include the layered sands exponents, however, they are included in Figure 5-99 for comparison purposes. The time exponent indicates that the drainage process is occurring faster than theoretically predicted. Both the increase in the scale factor N and the reduction in the time exponent "a" reflect an accelerated drainage rate. This higher drainage rate is consistent with the additional suction applied to the bottom of the sample.

The layered sands results are more difficult to interpret. While the scale factor N is similar to the homogenous sands, the time exponent drastically changes with increasing g-levels. The time exponent is seen to decrease with increasing g-level, indicating the

drainage process occurs at an even higher rate. From the initial portion of the cumulative outflow curve, the initial drainage rate is seen to be the saturated hydraulic conductivity of a theoretically equivalent homogeneous system. The hydraulic conductivity indicates the system in initially saturated flow does not experience the effect of the interlayering, and therefore, the time exponent must be close to the theoretical value of 2. As the column undergoes further drainage, the process must be severely affected by the interlayering, causing a sudden and dramatic drop of the time exponent "a" to a value near 1. After drainage is complete, the entrapped fluid distributions are visually seen to be properly scaled; i.e., the capillary fringe and transition to residual saturation in each layer are properly duplicated. At this time, the relationship between the g-level and layered sands behavior is unexplainable. Further research on the change in the hydraulic conductivity as a function of the sand layering and type of fluid must be done at normal gravity levels.

The search for a numerical model capable of modeling the drainage process for the various sand packings and fluids was not successful. Although numerical techniques to solve the Richards equation have been in existence for many years, the solutions are very conditional upon the boundary conditions and the change of the hydraulic conductivity with changes in saturation. Regardless of the complexity and elegance of the numerical technique, the numerical modeling results will only be as accurate as the input parameters. The input parameters can only be obtained by accurately determining the porous medium material and fluid properties.

The requirement for true modeling of models to change the length of the

centrifuge arm to have equivalent g-field variations does not appear to be crucial. The discrepancy of ignoring the constant arm radius is probably within the ability to accurately reproduce a modeling of models sample and collect the data.

A significant advantage of the centrifuge models was the ability to qualitatively assess the degree and nature of entrapment quickly. Both the homogeneous and layered sand packings provided very definite capillary fringes which were easily measured. The capillary fringe height was found to scale as the g-level.

The unsaturated flow experiments have verified the scaling relationships for the hydraulic conductivity and time for homogeneous sands. Use of the macroscopic parameters of cumulative outflow and pore pressures have been found to adequately describe the one-dimensional drainage process for both normal gravity levels and centrifuge models. The layered sands experiments indicate that the same macroscopic processes can be used to relate the models to prototype, however, the time exponent is no longer a constant. Tests in both the large and small centrifuges yielded similar results, indicating that the size of the centrifuge arm did not appear to be a crucial factor. Although many equipment modifications and new analysis techniques will be required before attempting to model two-dimensional flow in sands, the results of this chapter can be used to qualitatively explore one-dimensional multiphase flow in sands. Chapter 6 will explore the stability criteria of Chapter 3 using the experimental and analysis techniques developed for two-phase flow in this chapter.

CHAPTER 6

MULTIPHASE FLOW

6.1 - Objective and theory

The objective of the multiphase flow experiments is to address qualitatively the feasibility of using the centrifuge to model multiphase flow problems. Based on the results of Chapters 4 and 5, adding an additional phase to the problem should not invalidate the scaling laws as long as the order of fluids is chosen so that sharp front behavior is induced. The governing equations for multiphase fluid flow under normal gravity conditions are coupled, highly non-linear, and obtained by combining Darcy's law, Equation (3.4), and the continuity equation, Equation (3.3) for each phase. Faust (1986) and later researchers have used these equations as the basis to derive equations that explain multiphase flow and are given as:

$$\frac{\partial(\phi \rho_w S_w)}{\partial t} = q_w + \nabla[\frac{k\rho_w k_{rw}}{\mu_w}(\nabla p_w - \rho_w g \nabla z)] \qquad (6.1)$$

$$\frac{\partial(\phi \rho_n S_n)}{\partial t} = q_n + \nabla[\frac{k\rho_n k_{rn}}{\mu_n}(\nabla p_n - \rho_n g \nabla z)] \qquad (6.2)$$

$$\frac{\partial(\phi \rho_a S_a)}{\partial t} = q_a + \nabla[\frac{k\rho_a k_{ra}}{\mu_a}(\nabla p_a - \rho_a g \nabla z)] \qquad (6.3)$$

where:

w = the water phase

n = the nonaqueous phase

189

a = the air phase

k = the intrinsic permeability (L^2)

ρ = the density (M/L^3)

k_r = the relative permeability (dimensionless)

μ = the dynamic fluid viscosity(M/LT)

p = the fluid pressure (M/LT^2)

g = the gravitational acceleration (L/T^2)

z = depth (L)

q = the mass source/sink (M/T)

ϕ = the porosity (dimensionless)

S = the volummetric saturation (dimensionless)

∇ = the del operator

t = time

For each phase, a physical interface exists and the capillary pressure is defined as:

$$P_c = P_{nw} - P_w \qquad (6.4)$$

where p_{nw} is the pressure in the nonwetting phase and p_w is the pressure in the wetting phase. The wetting phase is defined as the interface with the convex surface. For the air, oil and water phases, Equation (6.4) gives:

$$P_c = P_n - P_w \qquad (6.5)$$

$$P_c = P_a - P_n \qquad (6.6)$$

190

A constitutive relationship that must be satisfied is that the summation of all saturations of each phase present must equal unity and can be expressed as:

$$S_n + S_w + S_a = 1 \qquad (6.7)$$

Related to the saturation is the relative permeability. Relative permeabilities can be determined for each fluid using:

$$k_{rn} = k_{rnw}^*[(\frac{k_{rnw}}{k_{rnw}^*}+k_{rw})(\frac{k_{rna}}{k_{rnw}^*}+k_{ra})-(k_{rw}+k_{ra})] \qquad (6.8)$$

where k_{mw}^* is the relative permeability of the nonaqueous phase at the residual water saturation in a water-nonaqueous phase system, k_{mw} is the relative permeability of the nonaqueous phase in a water-nonaqueous phase system, and k_{ma} is the relative permeability of the nonaqueous phase in an air-nonaqueous phase system. The flow equations can now be simplified using the following assumptions:

1. The pressure gradients in the air are negligible and the air is at atmospheric pressure;

2. For shallow systems the densities and viscosities are independent of the pressure;

3. The capillary pressure between the nonaqueous phase and water is dependent on the water saturation; and,

4. The capillary pressure between the nonaqueous phase and air is dependent on the air saturation.

Equations (6.1) and (6.2) can be rewritten as:

191

$$\frac{\partial(\phi \rho_w S_w)}{\partial t} = q_w + \nabla[\frac{k\rho_w k_{rw}}{\mu_w}(\nabla p_n - \rho_w g \nabla z)] \qquad (6.9)$$

$$\frac{\partial(\phi \rho_n (1-S_w-S_a))}{\partial t} = q_n + \nabla[\frac{k\rho_n k_{rn}}{\mu_n}(\nabla p_n - \rho_n g \nabla z)] \qquad (6.10)$$

The objective of this chapter is to explore the use of the centrifuge to model multiphase flow problems. Peterson and Cooke (1994) claim that any multiphase flow problem involving water and NAPL will not scale properly due to the reduction in the size of the ganglia with increasing g-levels. Based on the results of Chapters 4 and 5, the ordered pair of fluids can be chosen such that the front always remains sharp and stable, and the formation of ganglia can be prevented. For these multiphase flow conditions, the centrifuge may properly capture prototype behavior.

Examining Equations (6.9) and (6.10), several variables must be measured directly to properly predict prototype behavior. Measurement techniques have been in development over the last five years, but 1g tests are difficult to run and obtain consistent results (Armbruster, 1990; Campbell, 1993; Walser, 1994). In addition, for two-phase unsaturated flow, the model time scale was found to be very difficult to correlate to the prototype time for the cumulative outflow. Measurement of the pore pressure using transducers and correlation to prototype behavior is yet to be resolved. In view of these difficulties, the results in this chapter should be viewed as giving only qualitative evidence of the applicability of the centrifuge modeling of multiphase flow problems. Quite a few measurement issues will have to be resolved before quantitative results of high quality can be obtained.

Several numerical solutions to Equations (6.9) and (6.10) have been developed, and all numerical solutions require extensive input parameters. The centrifuge can be used to provide both microscopic input parameters required for the numerical models while also providing macroscopic data such as cumulative outflow and pore pressures. Some of the input parameters will have to be determined at 1g (i.e., relative permeabilities, porosity, saturation) and some of the parameters could be measured in the centrifuge (i.e., phase pressures, saturation of each phase). These issues are beyond the scope of this research at this time, however, the macroscopic cumulative outflow and pore pressures can be used qualitatively to examine the use of the ordered pairs of fluids.

6.2 - Soltrol over water experimental results

Peterson and Cooke (1994) argued that the pore scale ganglia formed by any advancing fluid front would not scale properly. A method to solve the problem of instability of the front is to eliminate the possibility of ganglia formation by placing the lighter fluid above the denser fluid and forcing sharp front behavior so that all pore spaces go to residual saturation. In this experiment, the sharp front behavior was observed with the Soltrol displacing the water in the sand pore space as shown in Figure 6-1. In the collection cylinder, both fluids accumulated and the pore pressure transducer measured the passing of the fluid interface. The sand was at residual Soltrol saturation as indicated by the color change.
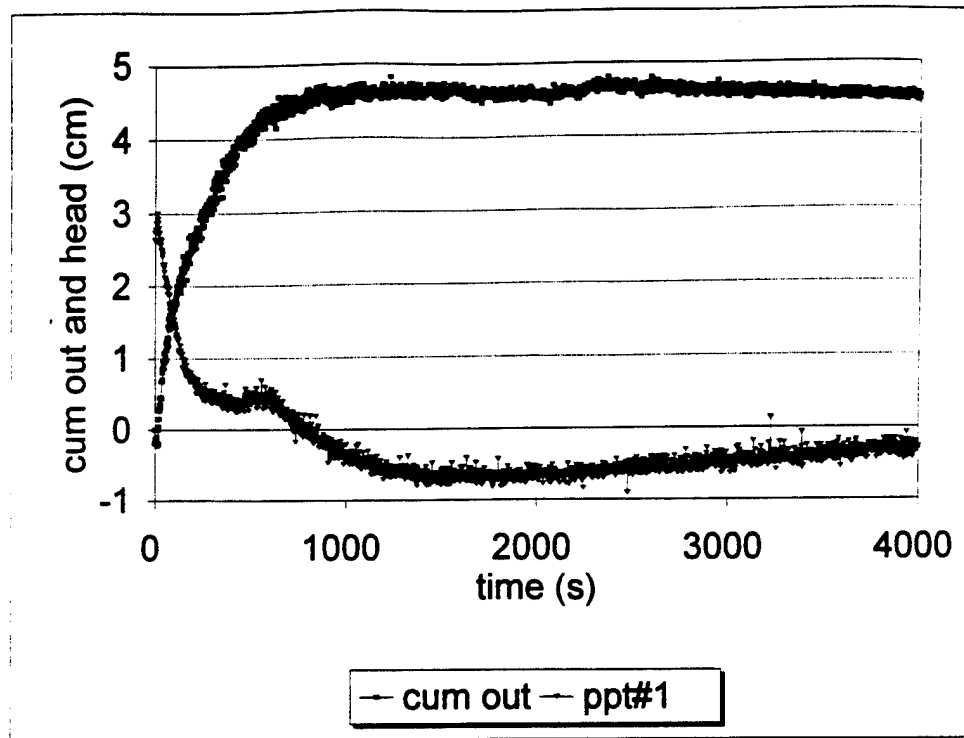
Figure 6-1. Soltrol over water saturated #70 sand

6.3 - Water over Soltrol experimental results

To test the concept of the mobility ratio and critical velocity, the water was placed over the sand saturated with Soltrol. Due to the very fine pore space, the water remained on top of the Soltrol and could not be induced to finger at the normal 1g gradients used for the saturated experiments. The sand column could be vigorously shaken and even rodded, yet viscous fingering did not occur. Figure 6-2 shows the cumulative outflow curve and pore pressure measurement at 20g's. The water penetrated the sand in several fingers and left very visible channels. The pore pressure measurement appears to capture a finger forming and passing.
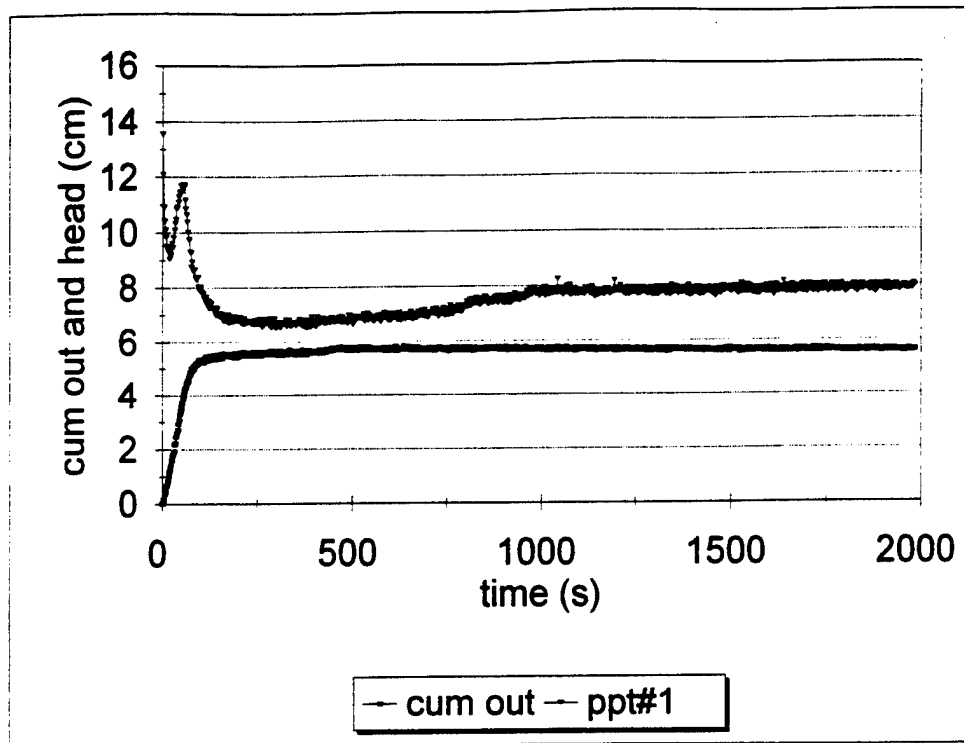
Figure 6-2. Water over Soltrol saturated #70 sand

6.4 - Analysis and discussion of results

The modeling of multiphase problems in the centrifuge appear to obey the expected physics qualitatively. As predicted, the sharp front and viscous fingering behaviors can be directly controlled. To obtain quantitative results, further testing will require oil-water separators and transducers to measure each fluid as it leaves the porous media, and some method to measure the individual phase pore pressures. In addition, the modeling of models will become extremely difficult to perform, however, the modeling of models will be the only method to determine the time exponent to predict prototype behavior.

This chapter concludes the experimental test program using sands as the porous

medium. To further validate the applicability of using the centrifuge in modeling environmental problems, Chapters 7 and 8 will explore fissure flow. Natural systems are often characterized by fissures, whether in a clay or in a rock matrix, and the fissures can dominate the fate and transport of organic chemicals. Fissures have much larger hydraulic conductivities than the surrounding matrix, therefore, the fissures become preferential flow channels. Chapters 7 and 8 will examine flow in a single fissure, using the concept of an "effective hydraulic conductivity". In the field, the "effective hydraulic conductivity" is measured over a length of a fissure network, however, the hydraulic conductivity must be shown to properly scale for a single fissure before networks can be modeled. Fissure flow also provides a method to model two-dimensional flow; any variation of the fissure aperture generates a non-uniform flow field. Unlike the sands, the flow fields in a fissure can be visually seen by injecting a dye tracer. Verification of fissure flow will show the scaling relationships are valid over a large range of material properties and for two-dimensional flow.

CHAPTER 7

SATURATED FISSURE FLOW

7.1 - Objective and theory

The first objective of the saturated flow through fissures experiments is to verify the scaling relationship for the hydraulic conductivity in one-dimensional flow and find the upper limit of the Reynolds number for laminar flow. The second objective is to verify the scaling relationship for the hydraulic conductivity for two-dimensional flow and find the upper limit of the Reynolds number for laminar flow.

The term "porous medium" is somewhat of a misnomer, as a rock fissure can also be considered a porous medium. A rock mass is normally faulted and jointed by fissures; flow through the rock mass can occur through both the rock matrix and within the individual fissures. The interconnected fissures create a fissure network which tends to have much larger hydraulic conductivities than the rock matrix (Goodman, 1989). Within a single fissure, the flow has been found to be a function of the aperture distribution (Moreno et al., 1990; Zimmerman et al., 1991; Amadei and Illangasekare, 1992). The hydraulic conductivity of a network of fissures is used to calculate an equivalent "average" single fissure aperture. The aperture and fracture spacing then provide a quantitative index of rock mass quality.

The aperture distribution of a fissure is generally measured as the "average" distance between two parallel plates. The "average" distance is complicated by the

protrusions of single mineral grains. The wall surface of the fissure is usually comprised of sand or mineral grains embedded in a cement matrix and have edges protruding into the aperture. If the aperture is small and the grains are contacting the opposite wall grains over large areas, the fissure behaves essentially like a sand, with the fluid flowing through the interparticle space and the overall flow field is controlled by microscopic variables. As the aperture becomes larger, the particles do not touch, but the particle edges cause the fluid flow to be extremely tortuous and head loss occurs due to shear forces near the wall surfaces. The microscopic variables are transitioning to macroscopic variables as the regions of the high and low contact now determine overall fluid flow. As the aperture becomes even larger, the effect of the grain edges becomes negligible and fluid flow becomes similar to flow between two parallel plates. The aperture distribution within a large rock matrix now controls fluid flow and the macroscopic variables determine the fluid flow. The aperture distribution can be thought of as the "porosity" of the system.

Determining the aperture distribution and particle edge penetration for a real fissure is for most cases not possible, just as determining the actual porosity of a nonhomogeneous sand is not possible. A possible solution is to use some "average" which captures the microscopic variables as some macroscopic parameters.

For saturated sands, the solution of the Laplace equation in one-dimensional flow yields only the constant head contour lines which are uniformly spaced along the length of the sample. The velocity field is also uniform and no information of the microscopic tortuosity of the velocity field is presented. For two-dimensional flow in saturated sands, any local variation in grain size or porosity will cause a variation in both the local head

and velocity fields, but this variation is lost due to the averaging over the whole sample domain. The one dimensional homogeneous saturated sand flow field can be generated., however, using a fissure with two walls coated with uniform sand grains interlocking with zero aperture. For two walls with regions of different sand grains and zero aperture, a two-dimensional nonhomogeneous saturated sand flow field would be generated. As the aperture is opened, various one or two-dimensional saturated fissure flow fields are generated.

To date, there are no published experimental investigations of fissure flow in a centrifuge. The most thorough evaluation of fissure flow at normal gravity was by Louis (1969); he explored the transition of laminar-to-turbulent flow for a variety of surface roughness and geometric configurations. Fryberger (1990) examined in detail the fissure flow through two concrete slabs with a variety of surface roughness and aperture distributions. Fryberger's (1990) work was used in the design of the centrifuge models for this research.

Based on the literature, the majority of effort is now placed on numerical modeling of fissures and fissure networks, with minor emphasis on experimental verification. Experimental investigations of field materials at field scale are usually cost prohibitive, thus the move to numerical modeling. If the centrifuge is to be used to model field problems, designing the experimental apparatus to duplicate accurately field conditions may be the most difficult problem to overcome, in part due to the lack of experience with small models.

The flow analysis of fluid flow through parallel plates has been developed by many

199

researchers. The following analysis is from Fryberger (1990), but variations appear in standard fluid texts and in Bear (1972).

For fissure flow, Equation (3.5) is the starting equation. The form of Darcy's law changes slightly, however, when working with rock fissures. A rock fissure is represented as two smooth parallel plates with a velocity distribution, as shown in Figure 7-1.
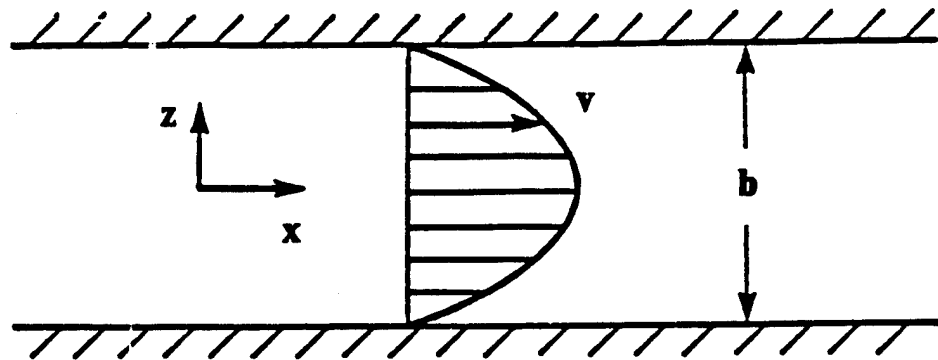
Figure 7-1. Parabolic velocity distribution in a fissure (From Fryberger, 1990)

From Figure 7-1, the y-axis projects outward normal from the plane of the paper. If the flow is two dimensional in the x-y plane, uniform, and at steady state then:

$$v \frac{\partial^2 v_x}{\partial z^2} - g \frac{\partial h}{\partial x} = 0 \tag{7.1}$$

by observing that h is independent of z we can solve for:

$$v_x = \frac{g}{2v} \frac{\partial h}{\partial x} z^2 + c_1 z + c_2 \tag{7.2}$$

where c_1 and c_2 are the constants of integration. Substituting the boundary conditions $v_x = 0$ at $z = + b/2$ and $- b/2$:

$$v_x = \frac{g}{2\nu}\frac{\partial h}{\partial x}(z^2 - \frac{b^2}{4})$$

(7.3)

and Equation (7.3) is often referred to as Poiseuille flow for a laminar closed conduit flow. The maximum velocity in the x direction occurs at the midpoint where $z = 0$ and is found by taking the derivative of Equation (7.3) with respect to x and can be written as:

$$v_{x,max} = \frac{-gb^2}{8\nu}\frac{\partial h}{\partial x}$$

(7.4)

By integrating Equation (7.4) over the fracture aperture b, the average velocity is:

$$v_{x,avg} = \frac{1}{b}\int_{-b/2}^{b/2} v_x dz = -\frac{gb^2}{12\nu}\frac{\partial h}{\partial x}$$

(7.5)

and a similar equation is obtained for $v_{y,avg}$. The average discharge per unit width in a parallel walled tube is then:

$$Q = \frac{gb^3}{12\nu}-\nabla h$$

(7.6)

and Equation (7.6) is called the cubic law for fissure flow. By analogy with Darcy's law in porous media, the hydraulic conductivity can be defined as:

$$K = \frac{gb^2}{12\nu}$$

(7.7)

The Reynolds number changes form slightly due to the hydraulic diameter of a tube. For parallel plate flow, the hydraulic diameter is equal to four times the hydraulic

201

radius, where the hydraulic radius is the ratio of the cross-sectional area of flow to the wetted perimeter. Therefore:

$$R_h = \frac{bw}{2(b+w)} \approx \frac{b}{2} \qquad (7.8)$$

because the width w is much greater than the aperture b. The hydraulic diameter becomes:

$$D = 4R_h = 2b \qquad (7.9)$$

and the Reynolds number becomes:

$$R_e = \frac{vD}{\nu} = \frac{2vb}{\nu} \qquad (7.10)$$

where:

v = Darcy velocity (L/T)

b = the aperture width (L)

ν = the kinematic viscosity (L^2/T)

For a fissure, the range in Reynolds number will be much higher than that for a fine grained soil due to the aperture width versus the d_{10} particle size. Lomize (1953) and Louis (1969) conducted a multitude of tests to determine the Reynolds number range and to verify the laminar-to-turbulent transition using a variety of apertures and surface roughness. Figure 7-2 is a schematic of the test set-up used by Louis. Figure 7-3 is the compilation of experimental data obtained by Louis presented in the form of a Moody diagram (similar to the sands friction factors) where:

$$\lambda = \frac{96}{R_e} \tag{7.11}$$

and

$$\lambda = \frac{2b(\frac{\Delta h}{\Delta l})}{\frac{v^2}{2g}} \tag{7.12}$$

the "roughness" of the fissure walls effect on the hydraulic conductivity was found to be:

$$\tag{7.13}$$

$$K = \frac{gb^2}{12v[1+8.8(k/D_h)^{1.5}]}$$

The ratio k/D_h is the "relative roughness" of the aperture and is a measure of the side walls and mineral grains penetrating into the open channel of the aperture.

Fryberger's (1990) experimental investigation examined the effect of wall roughness, tortuosity, and flow rate on single fissure flow using a large concrete slab. The definition of the aperture and roughness is shown in Figure 7-4 and typical results of a rough parallel plate test are shown in Figure 7-5. For a uniform aperture distribution, the head loss is seen to be linear along the length of the fissure.

1. Pump h = 25m, Q = 360m³/h
2. Airvessel V = 3000 l
3. Dirt trap ⌀ 250mm
4. Pressure reducer ⌀ 250mm
5. Waterflow metre (Venturi)
6. Movable connection

7. Inlet funnel (width 0.50m)
8. Joint model
9. Pressure metre (water -, mercury columns)
10. Pitot tubes
11. Measuring weirs (total flow rate)
12. Precision measuring weir (measuring in a certain point)
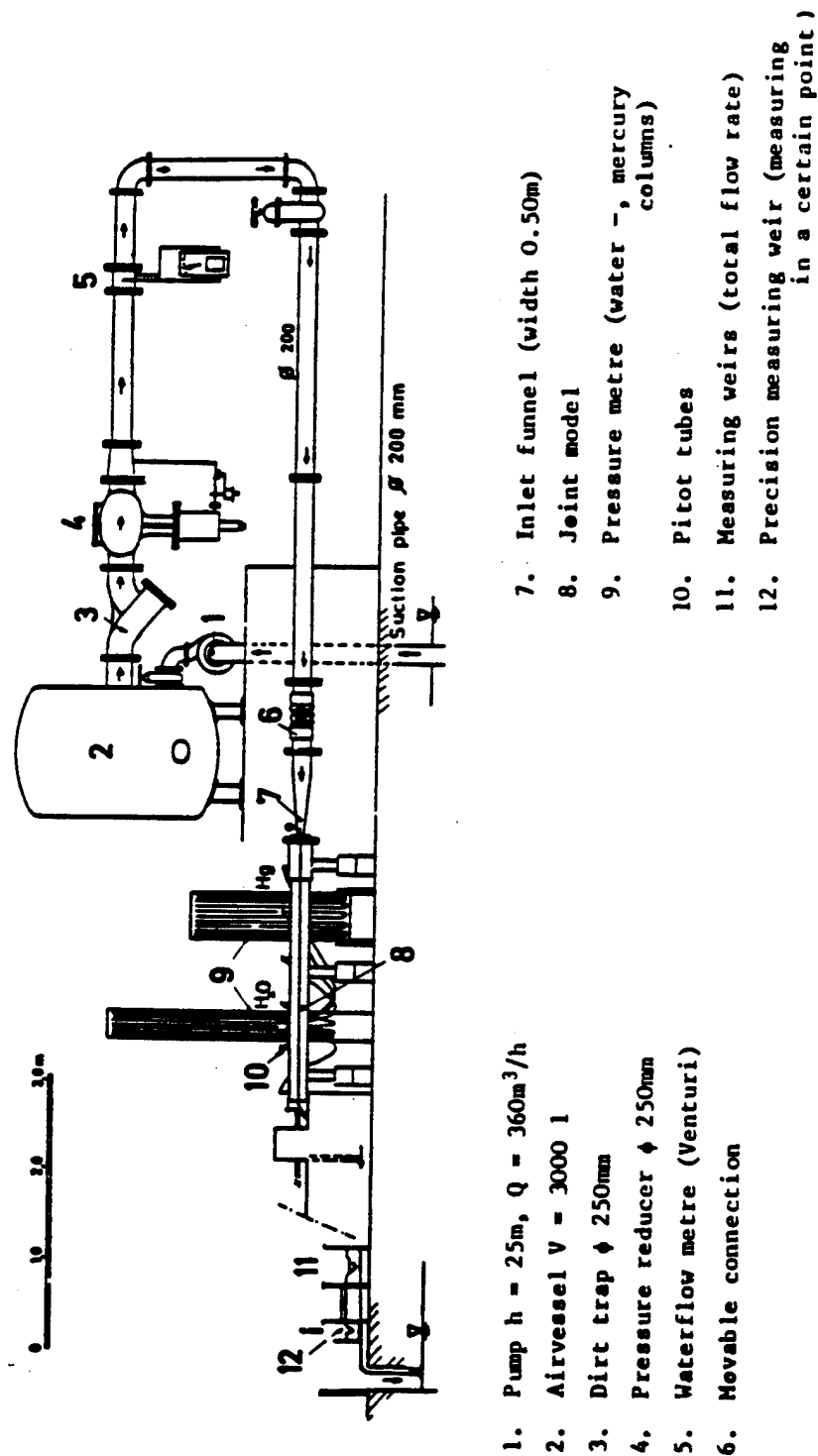
Figure 7-2. Schematic of test set-up of Louis (from Louis, 1969)

204

Figure 7-3. Uniform flow in a joint (from Louis, 1969)

205
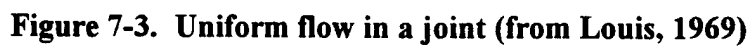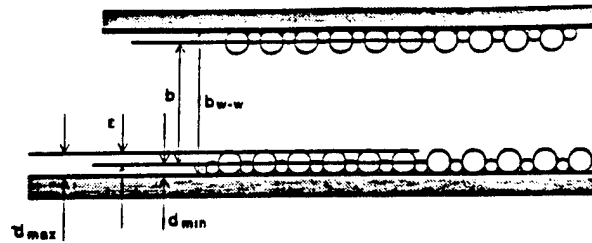
bw-w : MEASURED WALL-TO-WALL APERTURE
b   : MECHANICAL APERTURE
ε   : ABSOLUTE ROUGHNESS HEIGHT
dmin : MINIMUM DIAMETER OF SAND GRAINS
dmax : MAXIMUM DIAMETER OF SAND GRAINS

Figure 7-4. Aperture roughness for parallel plates (from Fryberger, 1990)
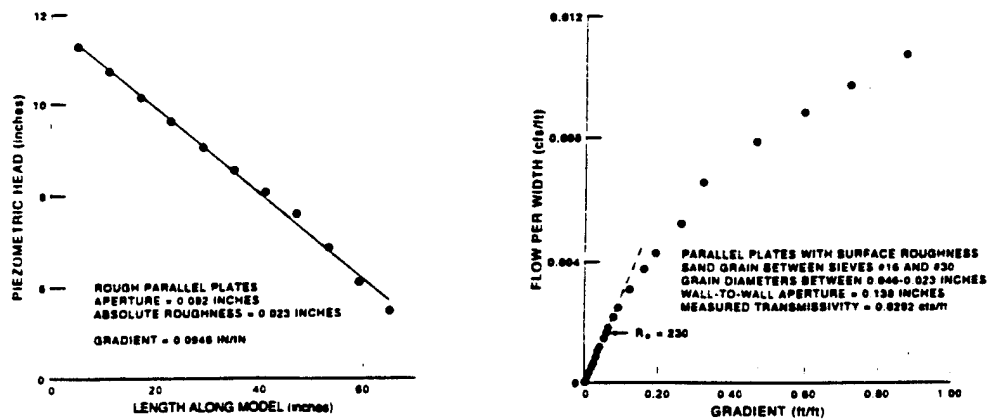
Figure 7-5. Typical test results of rough parallel plates (from Fryberger, 1990)
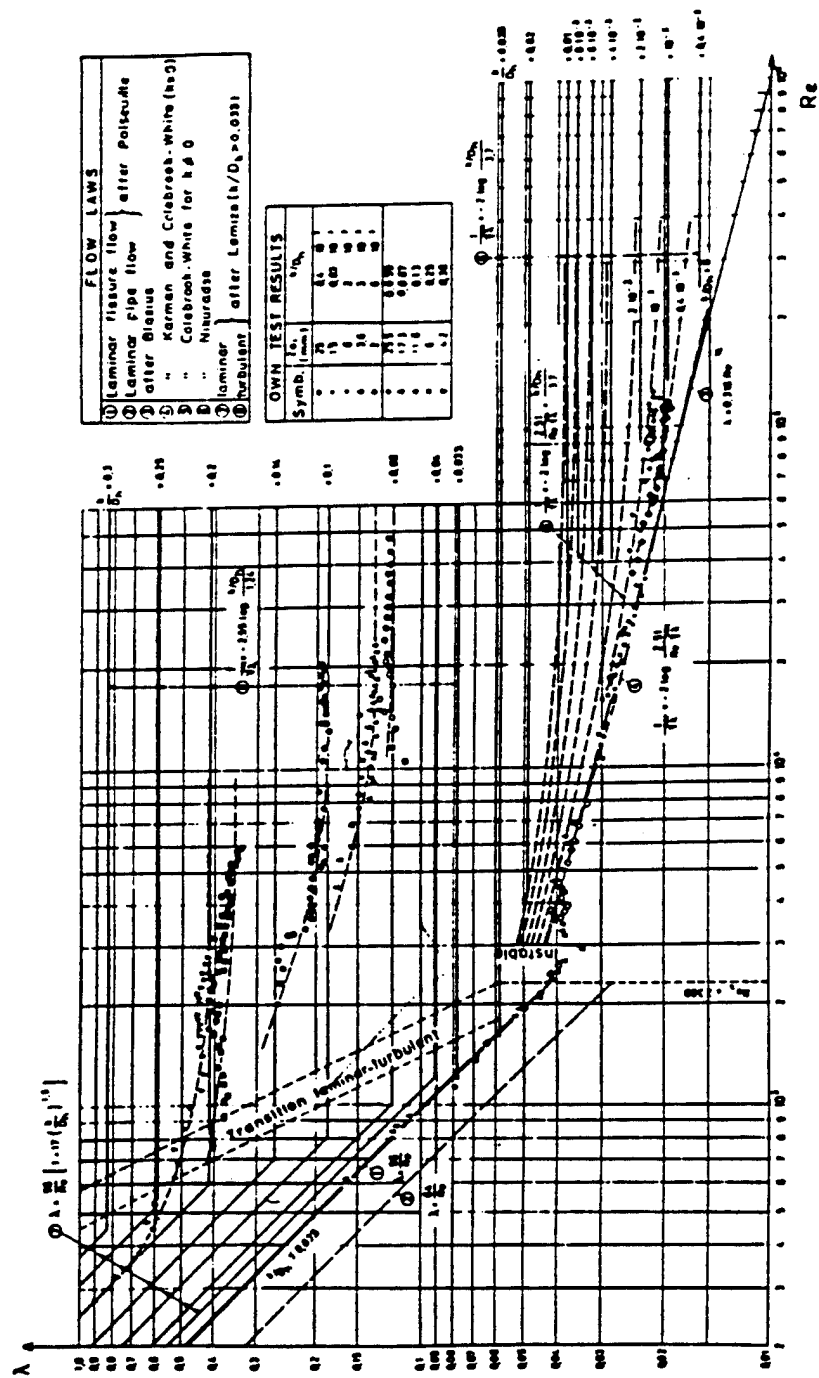
Figure 5-3. Uniform flow in a joint (from Louis, 1969)

center of each quadrant. Edges and constant head reservoirs were sealed using foam rubber stripping, rubber gaskets, and silicone caulking. Several C-clamps at equally spaced distances were used along the edges of the plexiglass plate models to hold the fissure together. Head bolts were used for the aluminum plate models.

The two-dimensional fissures were created using foam rubber placed in a geometric pattern similar to that described by Amadei and Illangasekare (1992). Another two-dimensional fissure was created by using the foam rubber to create an "S" pattern.

The test fluids used were Soltrol 220 and Metolose, similar to the sands tests presented in Section 4.4. The Metolose was thinned with water to obtain a viscosity closer to that of the Soltrol. The prototype tests used both water and Soltrol as test fluids. The centrifuge models used water and the thinned Metolose to simulate the Soltrol. A major problem encountered with the Soltrol and fissures was the choice of the edge sealant; the Soltrol aggressively attacked the foam rubber and silicone caulking.

5.4 - Centrifuge set-up

The same constant head source, solenoid valves, and pressure transducers used for the sand experiments were used for the fissure experiments. The model was placed on the centrifuge basket in the vertical direction. From the constant head source, the system was configured to force the fluid to flow from the bottom to the top of the sample. The head loss was measured at the outermost centerline ports. Figure 7-6 is a schematic of the fissure model on the centrifuge basket.
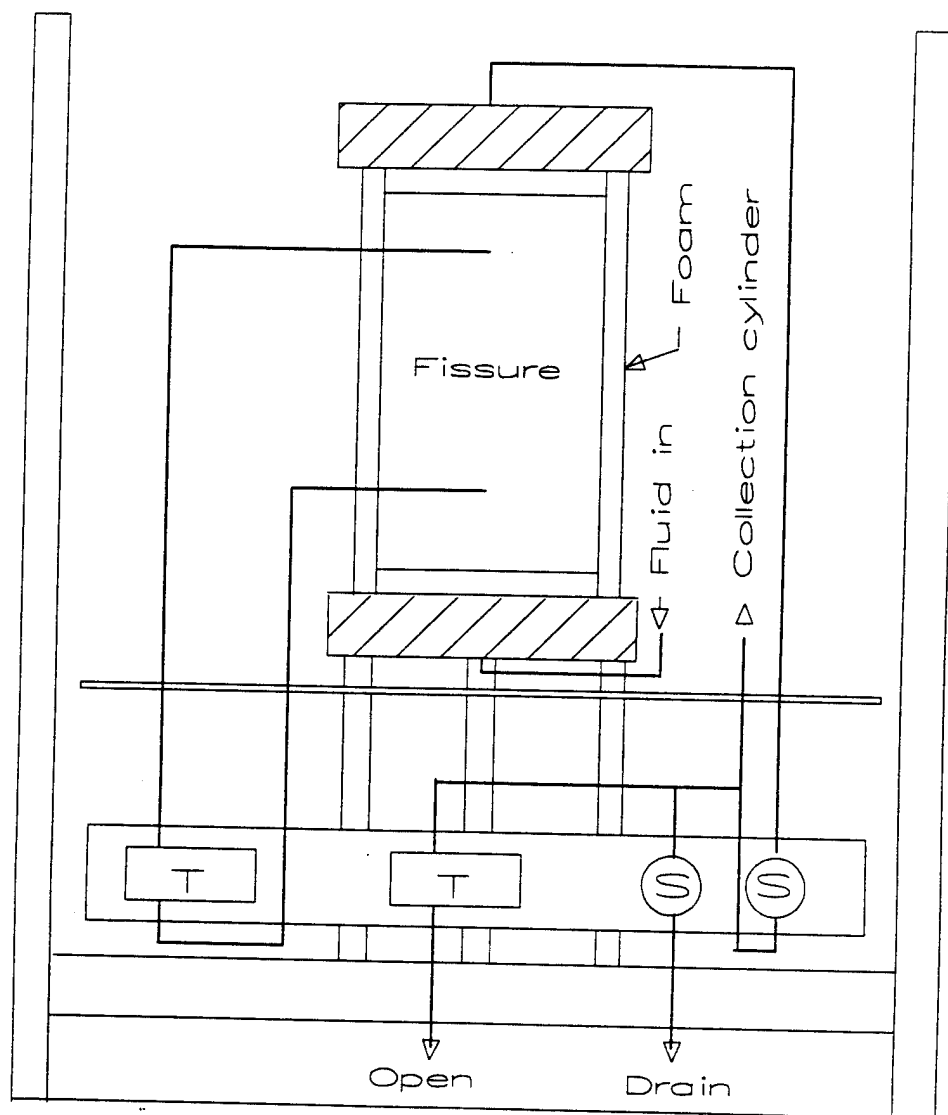
Figure 7-6. Fissure model

To run the experiment, the centrifuge was brought to the appropriate RPM. The MDAS was zero referenced and the data collection started. The MDAS ran for 30 seconds without flow, to ensure that a reliable zero reference had been obtained. After 30 seconds, the solenoid valve controlling the flow was opened. Most tests for water were run for 300 seconds; at higher g-levels, they did not require as long a time period. For Soltrol and Metolose, because of their higher viscosities, longer times were required. The MDAS data files were then imported into a Quattro Pro spreadsheet where the data manipulation was performed. Flow rate and head across the sample were plotted, as shown in Figure 7-7.
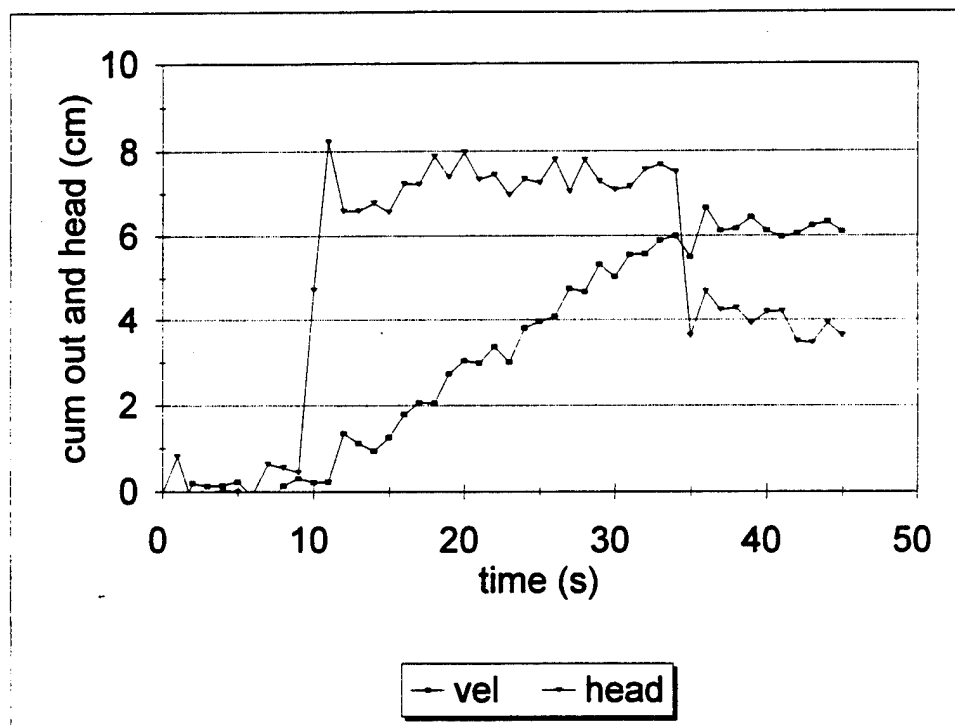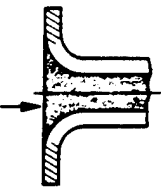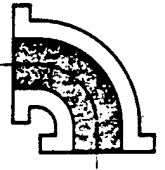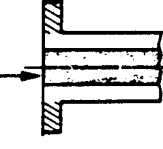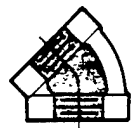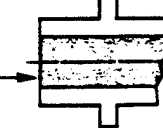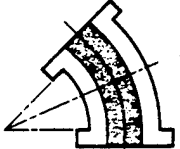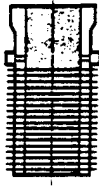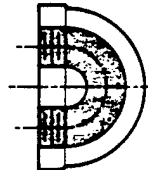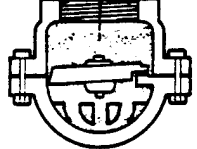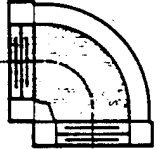
Figure 7-7. Typical head and velocity measurements

7-5. Head loss distribution through the system

To ensure the head loss measured through the fissure is controlling the flow, the head loss distribution through the system of tubing, valves, and manifolds was measured. Head loss in a system varies depending upon the roughness of the tubing, number of sharp corners or edges, number of 90-degree bends, etc., as shown in Figure 7-8. To limit head losses through these areas, sharp corners were rounded and a total of only three 90-degree bends were used. The length of tubing necessary for connections was kept to a minimum; of the four pieces of tubing required, the longest was 12 cm long.

The constant head source supplying the fluids was a plastic bottle which reduced to a standard Swagelock fitting at the top. The tubing connected to the top of the bottle and directly to the inlet manifold. The outlet manifold tubing connected directly to the constant head collection cylinder. Since the highest heads were at the inlet manifold side, the highest percentage of head loss is expected to occur near the entrance.

To measure the head loss distribution, a manometer board was used to measure the fluid heights at several system locations; 1) at the supply constant head source, 2) before the inlet manifold, 3) after the inlet manifold, 4) before the outlet manifold, 5) after the outlet manifold, 6) the exit constant head. Two types of tests were run: one test with the constant head source connected to the plastic bottle in-line to measure head loss through the bottle, and one test with the constant head source connected directly to the inlet manifold. The 1g tests were usually run with the head source connected to the plastic bottle in-line and the centrifuge tests were run using the plastic bottle as the constant head source.

211

Well-rounded entrance; or bell-mouth inlet $K = 0.05$	Flanged 90° elbow $K = 0.31$ (regular) $K = 0.22$ (long radius)
Square-edged inlet $K = 0.5$	Threaded 45° elbow $K = 0.35$ (regular)
Reentrant inlet or inward-projecting pipe $K = 1.0$	Flanged 45° elbow $K = 0.17$ (long radius)
Basket strainer $K = 1.3$	Threaded return bend $K = 1.5$ (regular)
Foot valve $K = 0.8$	Flanged return bend $K = 0.30$ (regular) $K = 0.20$ (long radius)
Threaded 90° elbow $K = 1.4$ (regular) $K = 0.75$ (long radius)	

Note: Many fittings have losses that vary with nominal diameter D_n; K for threaded fittings is taken at $D_n = 1$ in.; K for flanged fittings is taken at $D_n = 4$ in.

Figure 7-8. Head loss coefficients (from Engineering Data Book)

212

Figure 7-9 shows the head loss distribution through the system, and that the head loss through the fissure is very low. Louis (1969) used a very long system, while Fryberger (1990) used an eight-foot long system and could only obtain a maximum of one foot of total head loss. The plexiglass system is also eight feet long, with the initial four feet used to ensure parallel laminar flow and the pattern is in the final four feet. The highest head losses occur in the inlet manifold, with little head loss actually occurring in the fissure. Overall, between 75 to 85 percent of the available head is used just getting the water into the fissure. The head loss of coefficients of Figure 7-8 do not appear to apply; the coefficients were determined using large separations distances on either side of the connection. As the separation distance decreases, the head loss coefficients must "feel" the next connection and become larger, as seen in Figure 7-9.
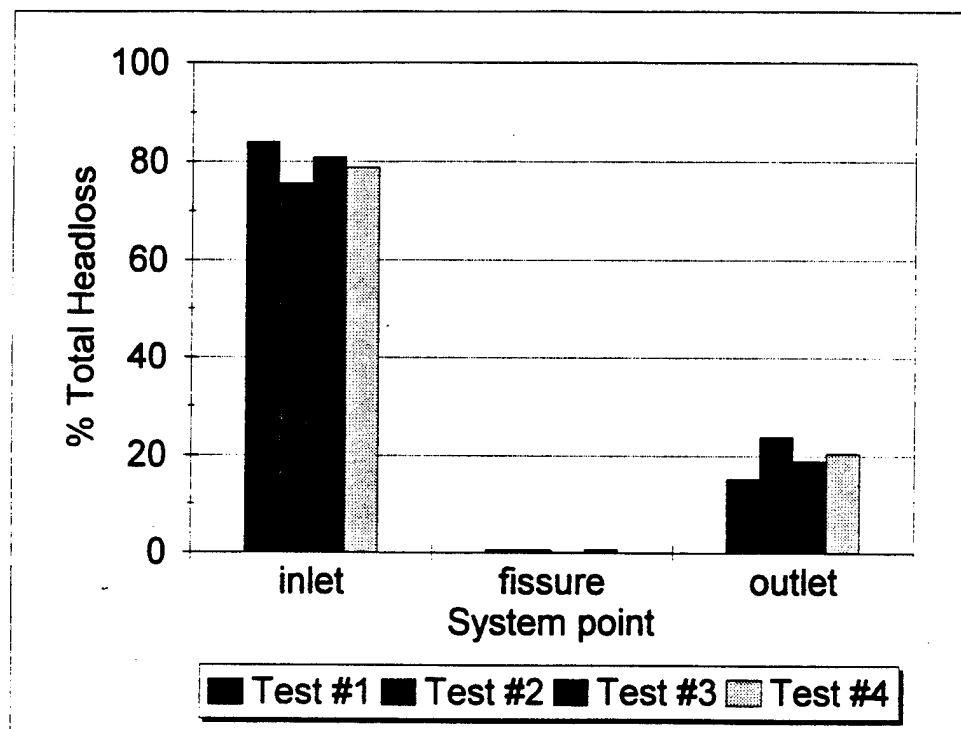
Figure 7-9. Head loss distribution in fissure

213

7.6 - Experimental results for prototype model

Unlike the sands experiments, there is no established data base of hydraulic conductivities for fissures. Therefore, to ensure the planned centrifuge fissure experiments would provide reliable data, a large scale prototype fissure was first constructed using the same materials as the centrifuge models.

The prototype apparatus and methods were based on previous work by Fryberger (1990), in which he verified the cubic law using large parallel concrete slabs having a variety of surface roughness coefficients. The first prototype apparatus design consisted of two 2' X 8' X 3/4" plexiglass sheets with 15 brass flush mounted aperture/pressure measurement ports. The two sheets were mated with a constant aperture, and constant head reservoirs were attached to each end. The initial tests used a smooth, unobstructed constant aperture to verify laminar flow, ensure constant head boundaries, and confirm linear head loss with length. The aperture was measured using a dial gage with an extension that fit through the brass ports. After verification of unobstructed system performance, a standard channel pattern was installed to model an ideal fissure, as shown in Figure 7-10. Figure 7-11 shows the aperture distribution and Figures 7-12 through 7-14 are pictures of the actual fissure being injected with dye and clearly showing the streamlines. The center streamline remains well defined while the outer streamlines show smearing due to mixing at the pattern edges. Aperture distribution, flow rate, and the type of fluid were varied to obtain prototype performance for a variety of conditions.
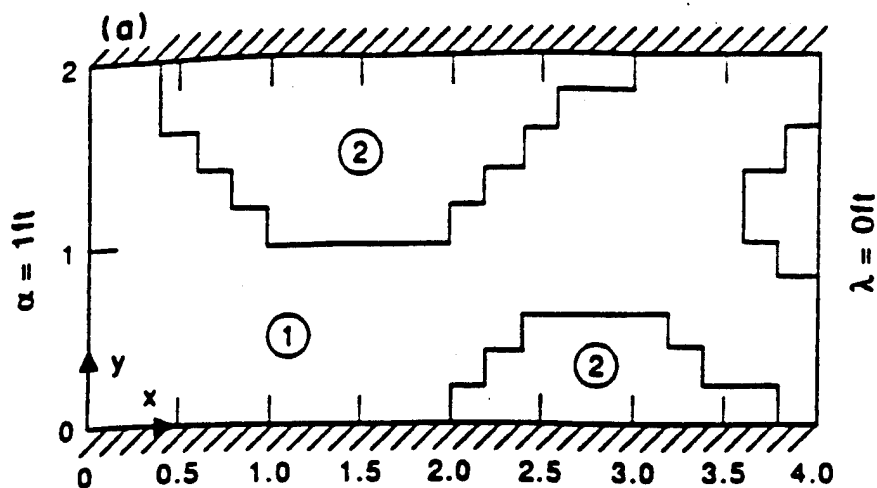
Figure 7-10. Standard channel pattern for an ideal fissure
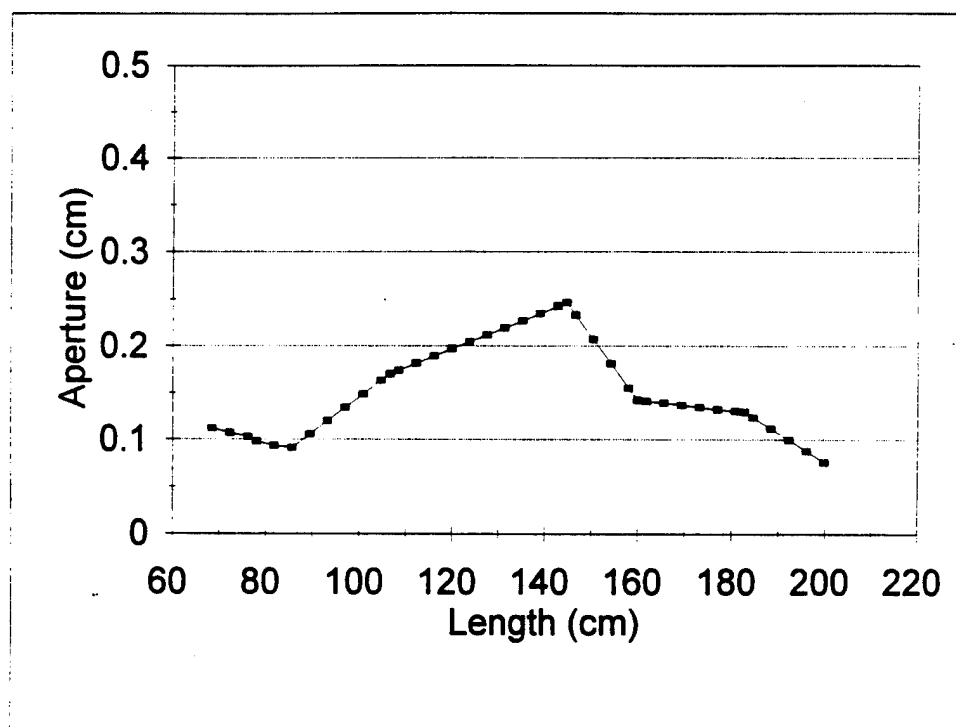
Figure 7-11. Aperture distribution for prototype

215
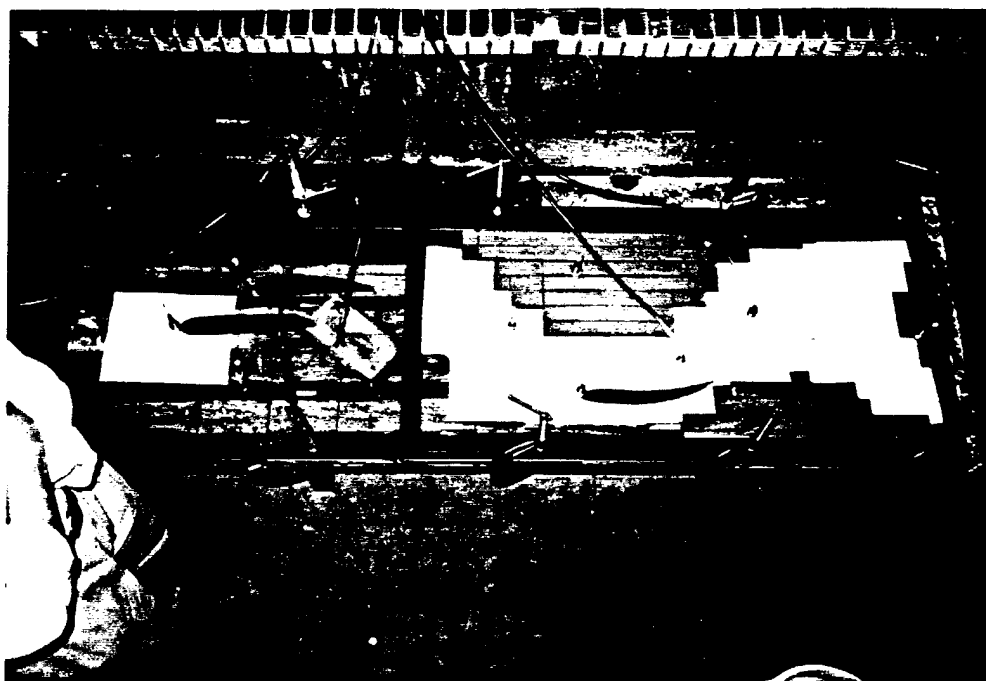
Figure 7-12. Prototype fissure with dye injection
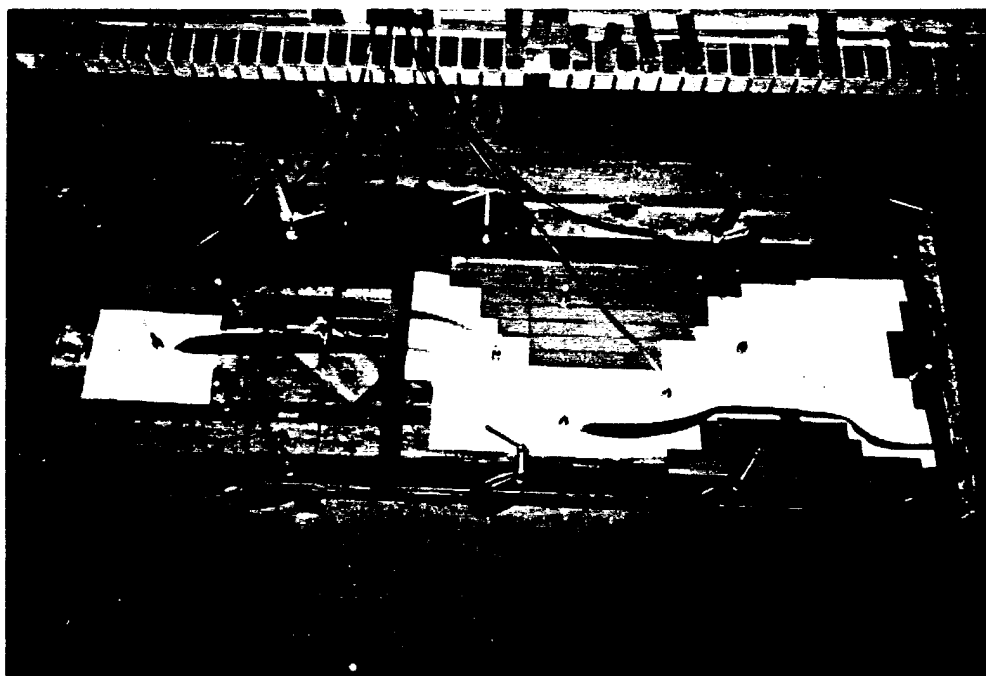
Figure 7-13. Prototype fissure with dye injection
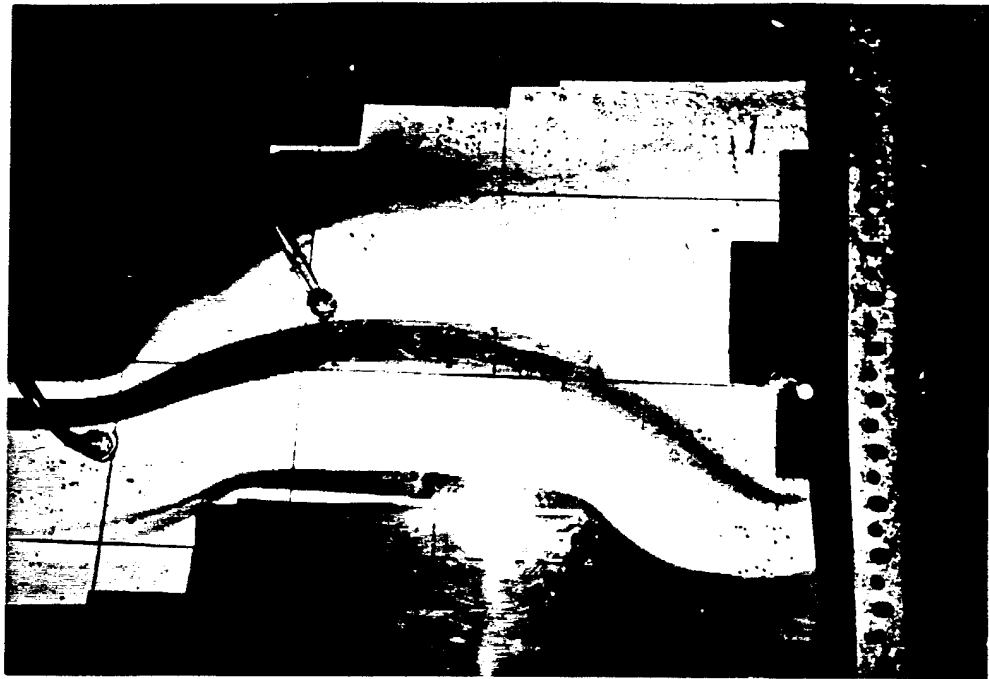
Figure 7-14. Prototype fissure with dye injection

To analyze the data, Amadei and Illangasekare (1992) developed an analytic solution to steady flow in non-homogeneous and anisotropic fissures which provides a method to analyze both one- and two-dimensional flow problems. Table 7-1 compares the numerical model output to the experimental measured values. Figure 7-15 shows the head distribution and velocity field generated by the numerical model, with and without the end pattern. The velocity vectors of the numerical model match the experimental streamlines of Figure 7-14.

The numerical model calculates an average aperture which includes all cells. The blocked patterns are regions of zero aperture and are included in the cell average. The equivalent aperture is defined as a single aperture which gives the same flow rate Q.

Table 7-1. Numerical versus experimental measured results for prototype

Test	Fluid	dh (in)	Q_{exp} (ft^3/s)	Q_{mod} (ft^3/s)	b_{exp} (in)	b_{mod} (in)	b_{eqi} (in)
1	water	0.197	0.000201	0.000198	0.091	0.080	0.075
2	water	0.276	0.000297	0.000219	0.068	0.066	0.057
3	water	0.551	0.000297	0.000304	0.061	0.050	0.040
4	water	0.669	0.000303	0.000386	0.065	0.047	0.052
5	water	1.614	0.000307	0.000476	0.055	0.035	0.043
6	water	2.913	0.00150	0.00148	0.060	0.051	0.050
7	water	3.544	0.00144	0.00147	0.054	0.053	0.045
8	Soltrol	0.748	7.3E-5	5.4E-5	0.091	0.080	0.075
9	Soltrol	6.181	0.000172	6.1E-5	0.043	0.032	0.018
10	Soltrol	7.126	0.000205	7.0E-5	0.043	0.032	0.018

b_{exp} is the average of 15 measured apertures

b_{mod} is the average of all node apertures of the numerical model

b_{eqi} is the equivalent aperture calculated by the numerical model
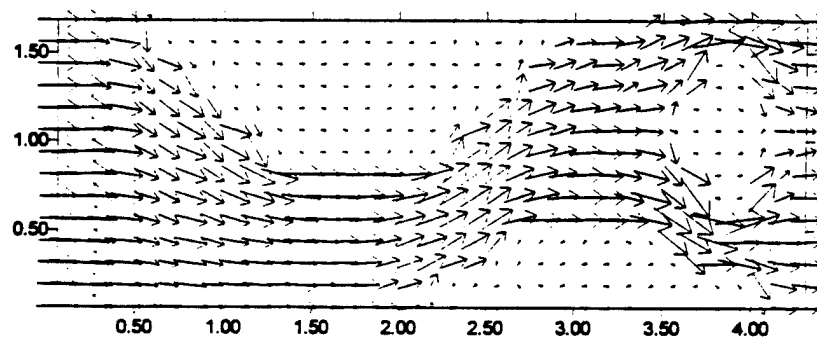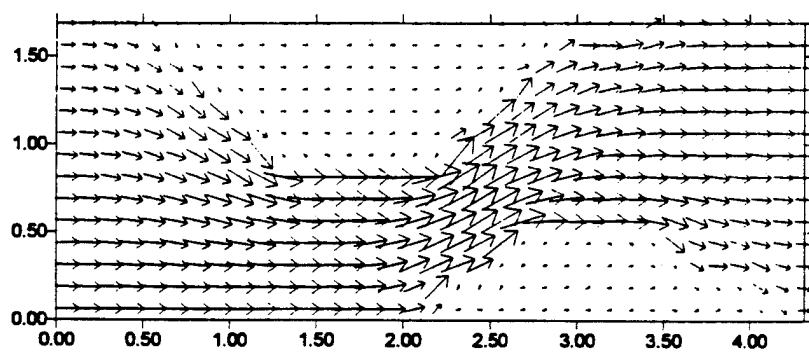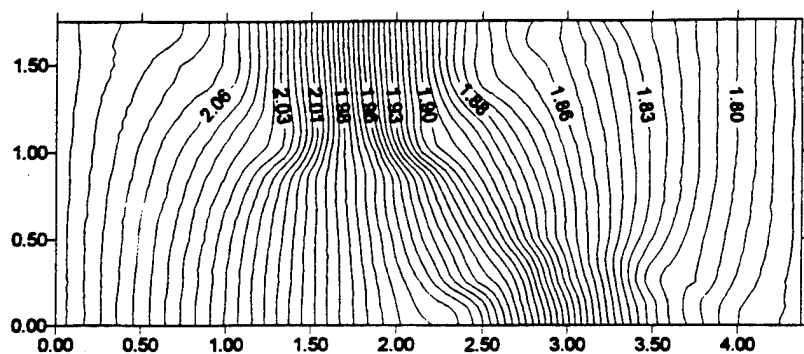
Figure 7-15. Numerical model head and velocity distribution

The plexiglass surface was chosen for its smoothness and to eliminate the evaluation of a relative roughness coefficient. This presented a problem, however, in obtaining head loss through the fissure; in many cases only millimeters of head loss could be obtained over a 7'-6" length with most head loss occurring at the entrance to the fissure. All measurements were made manually using manometers and by timing the flow into a 1- or 2-liter collection cylinder. One of the objectives was to obtain a constant aperture between the two mated sheets, however, this proved to be almost impossible. Even using spacers and weights, the aperture varied significantly due to imperfections in the plexiglass surface and warpage, as seen in Figure 7-11. The first attempts at running the numerical model used the average value of the 15 aperture measurements; the results were quite variable. When the actual aperture values were used, the model predicted very similar results to the experimentally measured flow rates, head distributions, and velocity fields, as shown in Table 7-1.

Another problem encountered was the head source and air bubbles. Tests were run using a constant head reservoir placed at different elevations connected to the inlet reservoirs and using the pressurized building water supply hooked directly to the inlet reservoirs. The constant head reservoirs worked very well but could only provide low flow rates. To obtain higher flow rates, the building water supply was used, however, the building water supply had a large amount of dissolved air which came out of solution inside the fissure and was found to be unsuitable for use. Obtaining 100% saturation was also impossible. The model was too large and heavy to stand vertically so it was placed horizontally with a slight uphill incline. Air bubbles collected at various points in the

fissure and grew in size as the experiment progressed. The best results were obtained by completely draining the system, opening the fissure and hand drying it, reassembling the system, and flooding the fissure from the inlet end with the outlet end slightly raised. The water would evenly wet the plexiglass and force almost all the air out of the system.

The prototype experiment verified the ability to use standard laboratory materials to simulate an ideal fissure. A significant problem to overcome is the fact that the head loss through the fissure is a function of the length of the model. As the size of the model decreases, the head loss through the fissure dramatically decreases.

7.7 - Experimental design of centrifuge models

The centrifuge models were scaled down versions of the 2' X 8' prototype model and consisted of two 12" X 14" X 3/4" plexiglass sheets with two solid aluminum machined constant head reservoirs. The models were designed to fit into the small centrifuge and use the multichannel data acquisition system (MDAS). Several models were designed; both plexiglass sheets coated with various sizes of sand grains, smooth open fissures with the standard pattern, and one sheet of plexiglass replaced by a cast of a rock surface. Water and Metolose were used as the test fluids. A total of 15 aperture/pressure ports were installed.

Based on the large prototype inlet reservoir performance, the centrifuge model inlet reservoir was modified to reduce the inlet head loss. To reduce head loss, all edges were rounded with a 5 cm transition zone before and after the fissure. The predicted head loss coefficients shown in Figure 7-8 are based on the length of pipe or channel being

much longer than the centrifuge model. The reduced length of the centrifuge model so drastically affected the head loss distribution throughout the system that using smooth plexiglass for the ideal fissure, even with high flow rates, yielded no measurable head loss across the fissure.

To overcome this problem, two different approaches were taken: increasing the surface roughness and increasing the fissure length. To increase the surface roughness, the plexiglass sheets were coated with a single grain layer of sand. To increase the fissure length, foam strips were installed perpendicular to the width to form an "S" pattern. The foam strips were butted to one edge and had a 1 cm gap at the opposite edge, in alternating rows. The 20 cm long fissure became a 200 cm long fissure.

7.8 - Experimental results of #30 sand layer and 1 mm aperture fissure

To verify one-dimensional constant aperture flow, two sheets of plexiglass were coated with a single grain layer of #30 sand and spaced with an aperture of 1 mm, measured from plexiglass sheet to plexiglass sheet. Figure 7-16 is a plot of the centerline aperture which remains very uniform compared to the prototype model. The 1g tests were run using a constant head source placed at various levels and also using air pressure. These tests were run manually using manometers and timed flows. Figure 7-17 shows the head loss versus length to confirm that the head loss is linear for a variety of flow rates; the slight deviation of head at the highest flow rate near the entrance indicates possible turbulence. Figure 7-18 is the flow rate versus gradient plot similar to the plot in Figure 7-5.
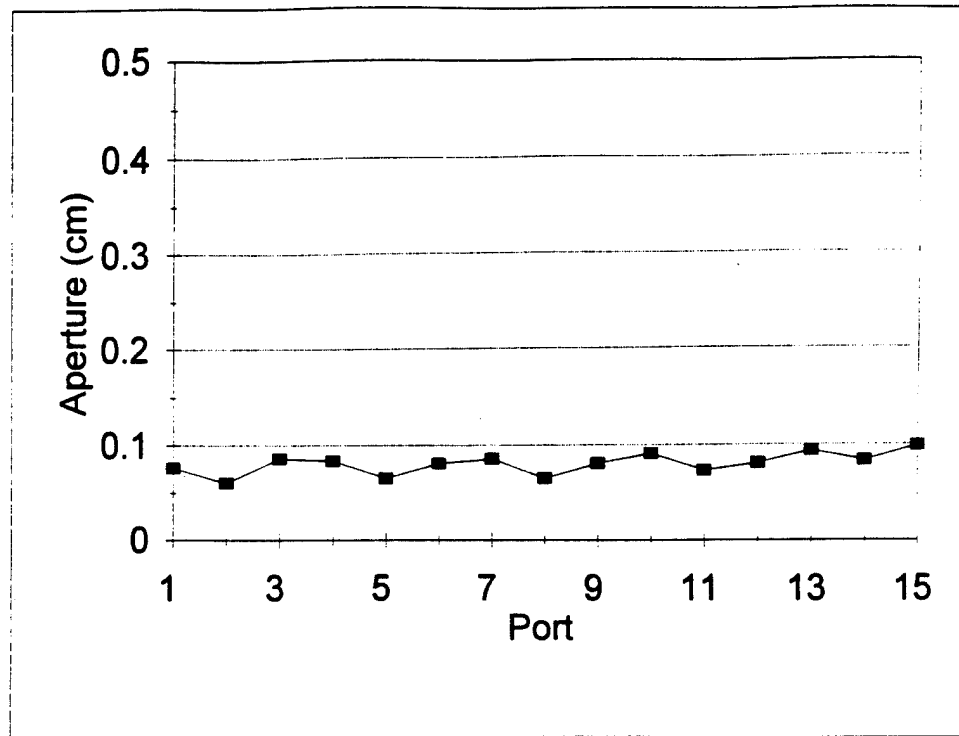
Figure 7-16. Aperture distribution for model
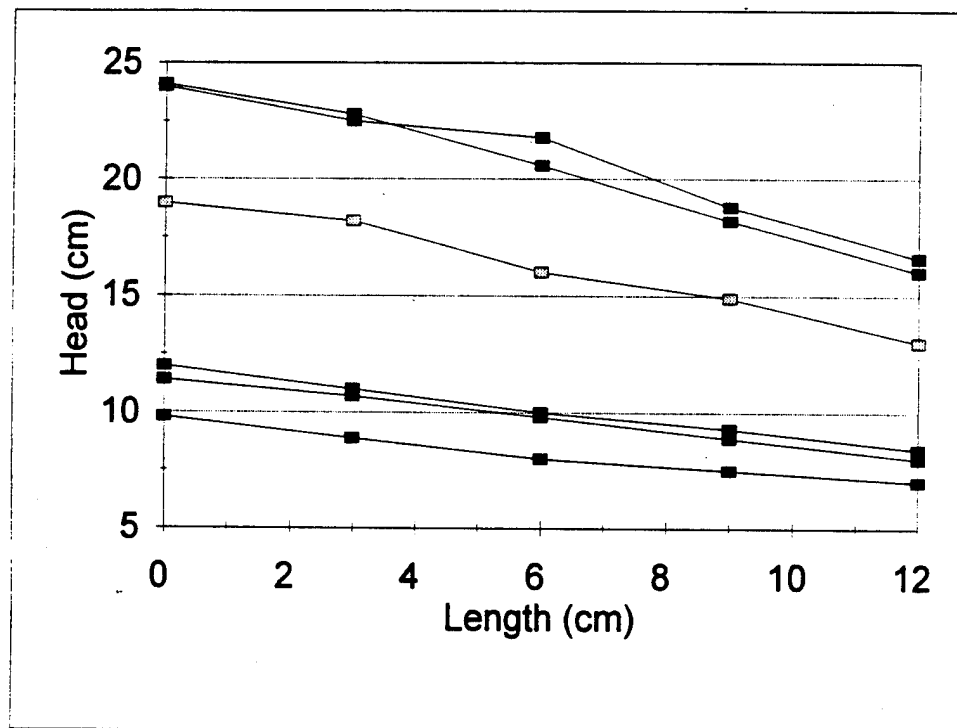
Figure 7-17. Head loss versus length

223
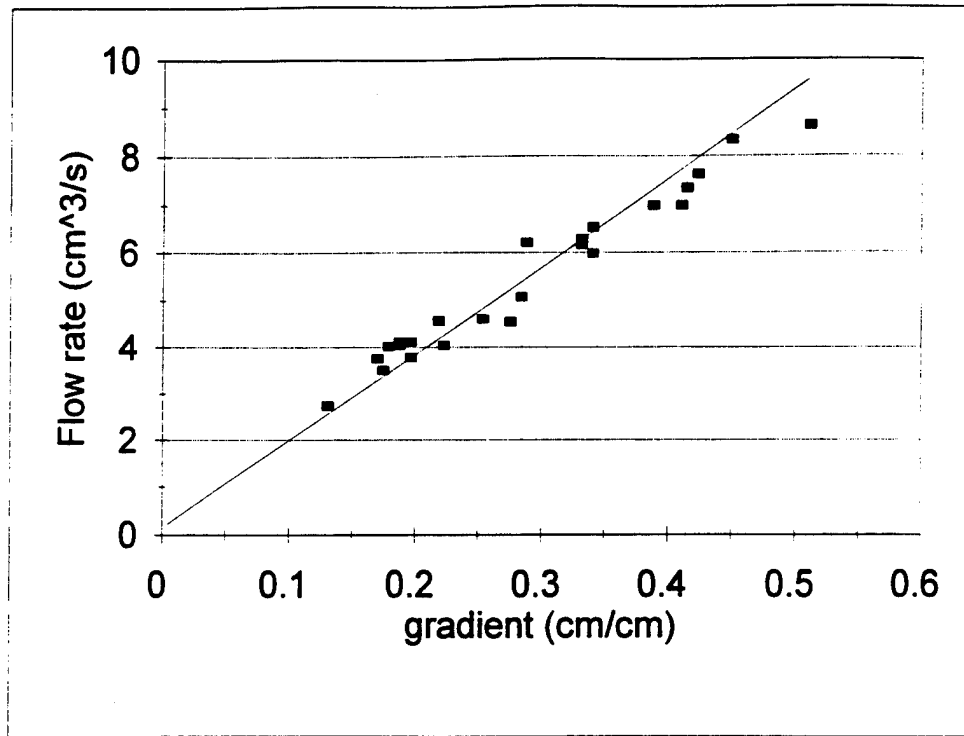
Figure 7-18. Flow rate versus gradient for #30 sand coated fissure

The transition zone into the turbulent regime was not reached, even though the maximum pressure available was used. The high flow rate test caused the sealant on the edge to fail, therefore, centrifuge tests could not be performed.

The numerical model was used to predict the head distribution, velocity field and flow rate for the model. Table 7-2 compares the numerical model results with the experimentally measured values. Figure 7-19 is a plot of the velocity field showing the variation in the velocity field due to the variation in the aperture.

Table 5-2. Numerical versus experimental measured results for model

	b_{avg} (in)	Q (ft^3/s)
Experimental	0.0318	1.60E-4
Numerical	0.0314	1.35E-4
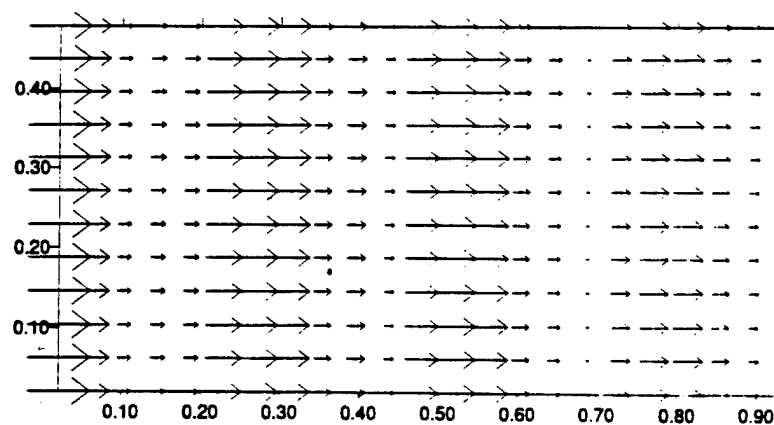
Figure 7-19. Velocity distribution

7.9 - Experimental results of #16 sand layer and 2 mm aperture fissure

Having satisfied the linear head loss for the 1 mm fissure and validating that the centrifuge model worked, the model was rebuilt using #16 sand and a 2 mm gap. The coarser sand was chosen to provide a higher roughness coefficient and the 2 mm aperture was chosen to match the prototype. To prevent the edge sealant from failing, additional silicone caulking and C-clamps were used. The model was placed into the centrifuge in the vertical direction, and connected to the water supply cylinder with a high air pressure line. The head ports and collection cylinder were connected to the same pressure transducers used for the sands tests. At 1g, the pressure transducers are capable of measuring 500 to 600 cm of water and therefore require at least several centimeters of head loss to give consistent results. The 2 mm aperture required high flow rates to create measurable head loss using the pressure transducers.

To test the system, the air pressure to the water supply was increased in increments of 2 psi up to 24 psi and then decreased in the same manner. The flow rate and head were measured using the data acquisition system. Figure 7-20 clearly shows the effect increasing pressure has upon the plexiglass system. The system initially responds linearly, but as the pressure increases, the response becomes non-linear, and in fact, reverses. As the pressure decreases, the system returns close to its initial condition with a slight increase in the hydraulic conductivity, possibly due to a slight permanent widening of the aperture. Since the flow rate is a cubic function of the aperture, even a slight expansion will have a large impact.
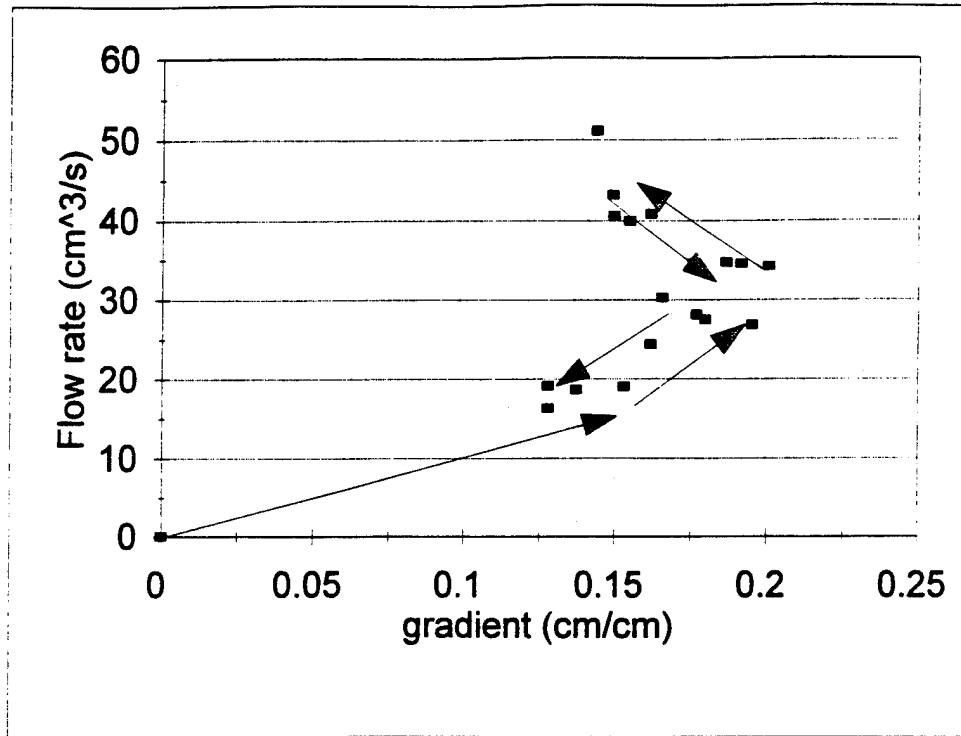
Figure 7-20. Flow rate versus gradient at 1g using air pressure

From Figure 7-20, for a flow rate of 35 cm³/s, the gradient changes from 0.2 to

0.15. The aperture corresponding to this change can be found using Equation (7.6) as:

$$b_{0.15} = (\frac{b_{0.2}i_2}{i_1})^{0.333} = (\frac{(2)(0.20)}{(0.15)})^{0.333} = 2.20 \ mm \tag{7.14}$$

A mere 10% expansion of the fissure has a dramatic effect on the effective

hydraulic conductivity. It appears that the higher flow rates cause the plexiglass to bow

outward. To control the expansion, square metal tubing held by C-clamps was installed

at the third points along the fissure model.

Figure 7-21 shows the "effective hydraulic conductivity" versus g-level for the #16

227

sand coated constant aperture model using water as the test fluid. To verify the use of a higher viscous fluid, a series of tests were run using Metolose, as shown in Figure 7-22. Since the flow rate is a cubic function of the aperture, any expansion of the fissure will cause large variations in the measured flow rate and is reflected in the data scatter. The hydraulic conductivity and the Reynolds number for fissure flow are much larger than the sands.
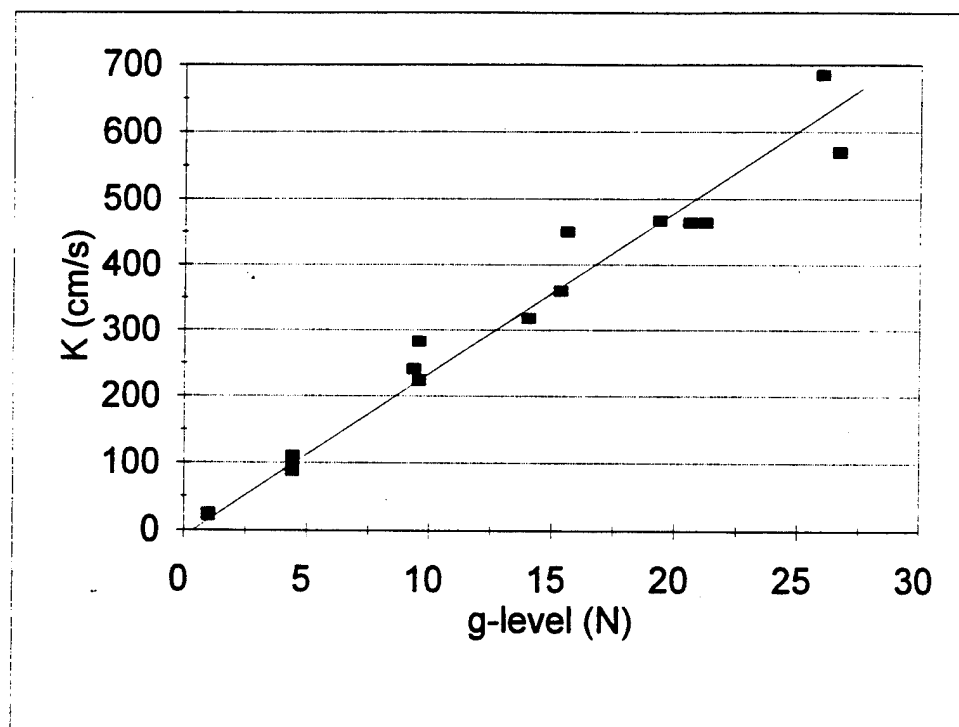
Figure 7-21. Hydraulic conductivity versus g-level for 2 mm fissure and water
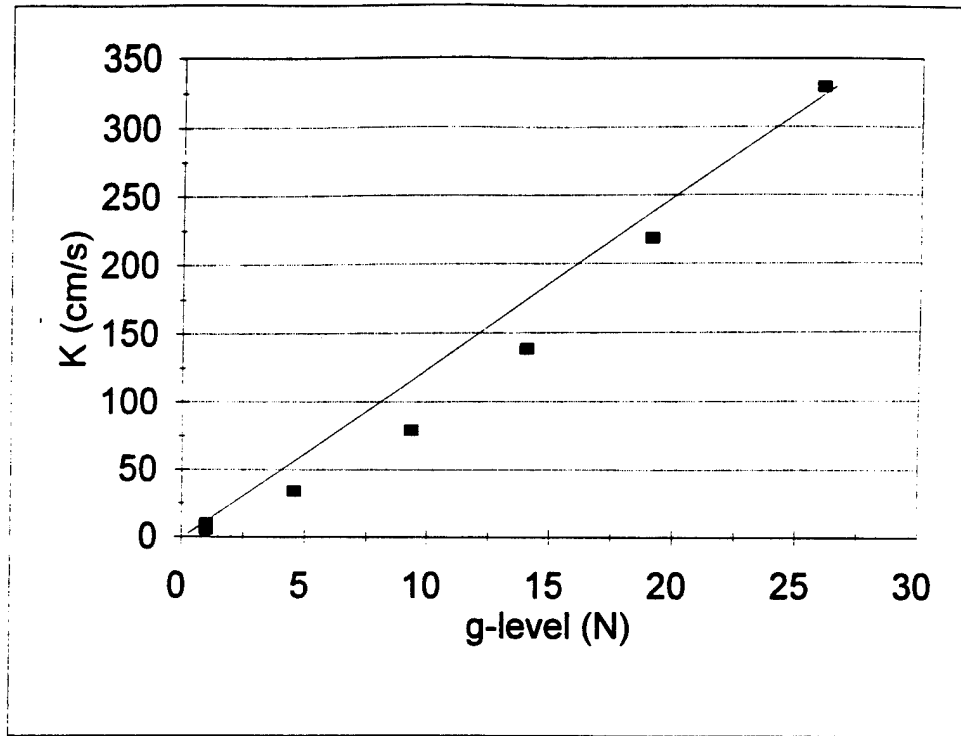
Figure 7-22. Hydraulic conductivity versus g-level for 2 mm fissure and Metolose

Using equation (4.15), the viscosity ratio can be compared as:

$$\frac{\nu_{met}}{\nu_w} = \frac{K_w}{K_{met}} = \frac{23.45}{11.5} = 2.04 \ cs \tag{7.15}$$

which is significantly different from the measured value of 4.68 cs. Looking at the two curves, it appears that as the g-level increases, the curves are not really linear. Using the 1g values, the viscosity ratio is:

$$\frac{\nu_{met}}{\nu_w} = \frac{K_w}{K_{met}} = \frac{21.75}{5.28} = 4.11 \ cs \tag{7.16}$$

229

and it appears that even with stiffeners the plexiglass fissure is expanding. Using the maximum flow rate of the 25g test, the maximum Reynolds number for the fissure with water using Equation (7.10) is:

$$Re = \frac{2bv}{v} = \frac{(2)(0.2)(5.91)}{0.01002} = 236 \tag{7.17}$$

and for Metolose is:

$$Re = \frac{2bv}{v} = \frac{(2)(0.2)(5.10)}{0.0468} = 44 \tag{7.18}$$

Comparing the maximum Reynolds numbers to Figure 7-3 indicates the fissure is well within laminar flow conditions.

7.10 - Experimental results of fissure with standard pattern

To verify two-dimensional flow, the standard pattern used in Figure 7-10 was duplicated in the centrifuge model as shown in Figure 7-23. To control the expansion, the square tubing was placed at the third points and clamped to the sides of the channel. Figures 7-24 and 7-25 show the hydraulic conductivity versus g-level using water and Metolose.
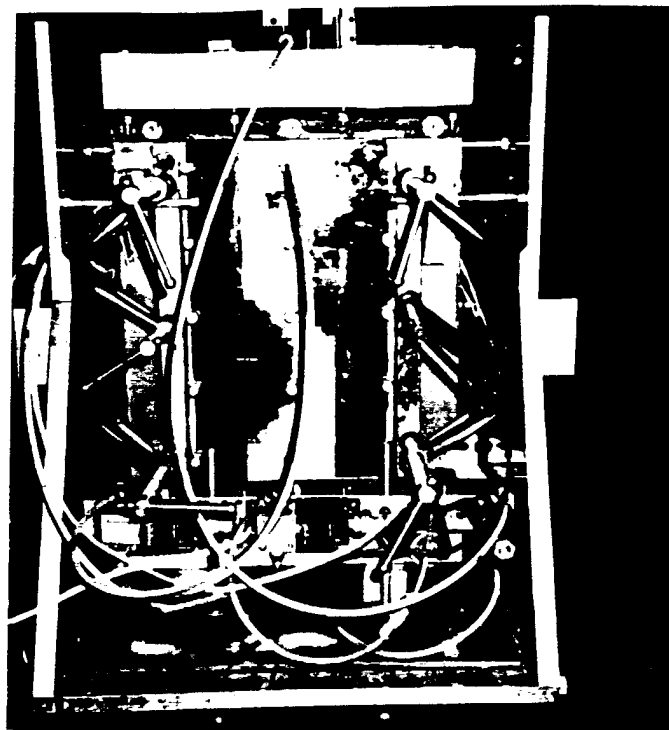
Figure 7-23. Model of standard pattern in centrifuge
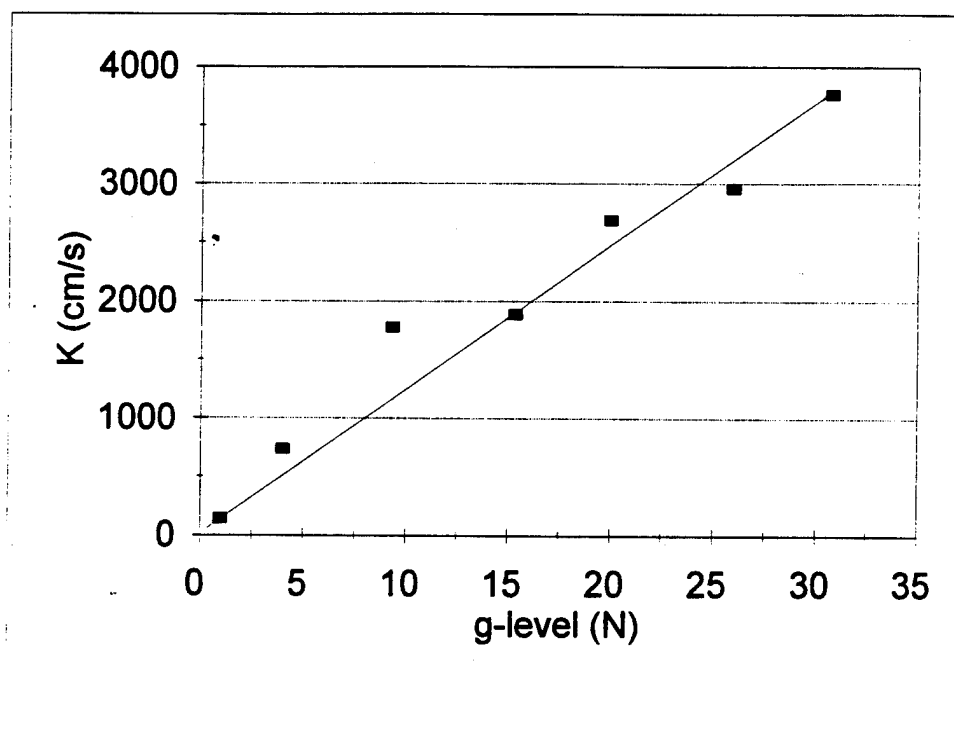
Figure 7-24. Hydraulic conductivity versus g-level with pattern fissure and water
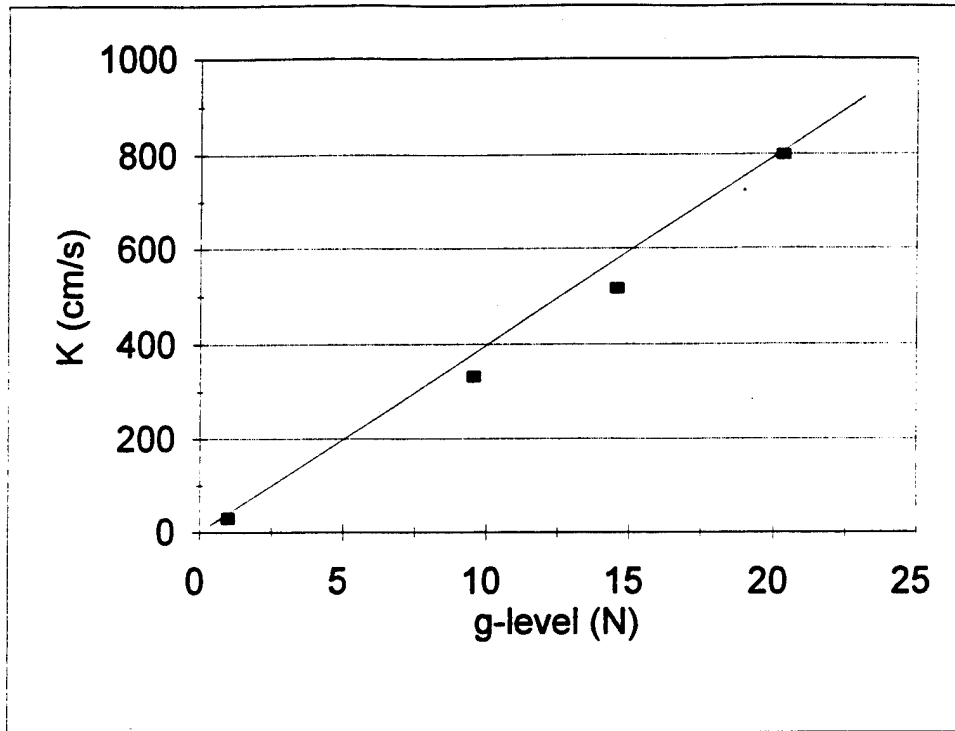
Figure 7-25. Hydraulic conductivity versus g-level with pattern fissure and Metolose

Using equation (4.15), the viscosity ratio is:

$$\frac{v_{met}}{v_w} = \frac{K_w}{K_{met}} = \frac{111.75}{38.83} = 2.88 \ cs \tag{7.19}$$

but the curves are seen to be non-linear similar to the previous experiment using a uniform

aperture. Using the 1g values gives a viscosity ratio of:

$$\frac{v_{met}}{v_w} = \frac{K_w}{K_{met}} = \frac{145.17}{29.77} = 4.88 \ cs \tag{7.20}$$

which compares to the measured viscosity of 4.68 cs. Using equation (7.10), the

Reynolds number for water is:

$$Re = \frac{2bv}{v} = \frac{(2)(0.2)(20.66)}{0.01002} = 825 \tag{7.21}$$

and for Metolose is:

$$Re = \frac{2bv}{v} = \frac{(2)(0.2)(8.90)}{0.0468} = 76 \tag{7.22}$$

which is still within the laminar flow condition. However, even with a narrow fissure channel and stiffeners, the plexiglass appears to be expanding with increasing g-level.

7.11 - Experimental results of "S" pattern channel

The "S" pattern channel experiments were designed to verify two-dimensional flow. To overcome some of the expansion problems encountered using the sand coated plexiglass, the partitioned channel model was constructed from solid aluminum plates. The aluminum plates were very smooth and initial tests at 1g gave only 0.3 cm of head loss across the unpartitioned fissure, similar to the plexiglass experiments.

To obtain higher head losses, the fissure was broken into a smaller channel. The partitions consisted of foam strips placed to give a 2 mm deep by 25.4 mm wide channel winding in an "S" fashion from inlet to outlet, as shown in Figure 7-26. The overall length of the channel was 178.4 cm.
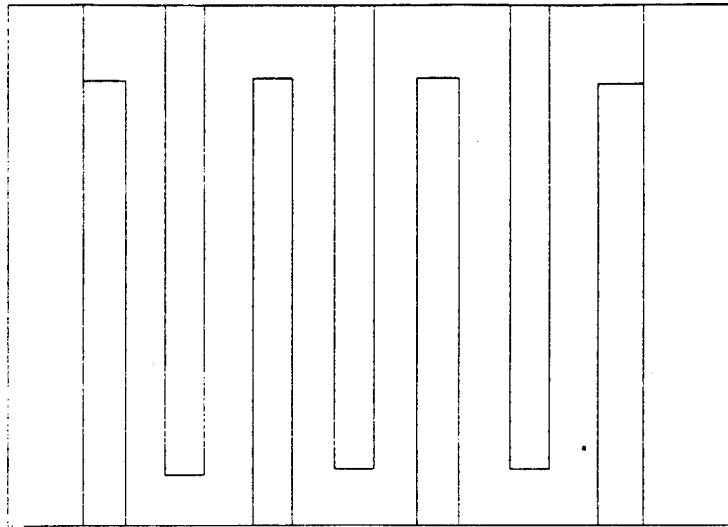
Figure 7-26. "S" pattern channel fissure

Unlike the previous fissure experiments, the "S" pattern model was placed on the centrifuge basket in the horizontal position. In the vertical position the upper head reservoir acts in the plane of acceleration, causing an additional downward force which tries to expand the fissure. In the horizontal position, the head reservoir does not add an additional force. The horizontal top aluminum plate does have an additional downward force component which would counteract the upward acting force caused by the fluid pressure.

The 1g tests using both constant head and the building pressurized water supply yielded excellent results of the flow rate versus gradient, as shown in Figure 7-27, which compares with Fryberger's (1990) results of Figure 7-5.
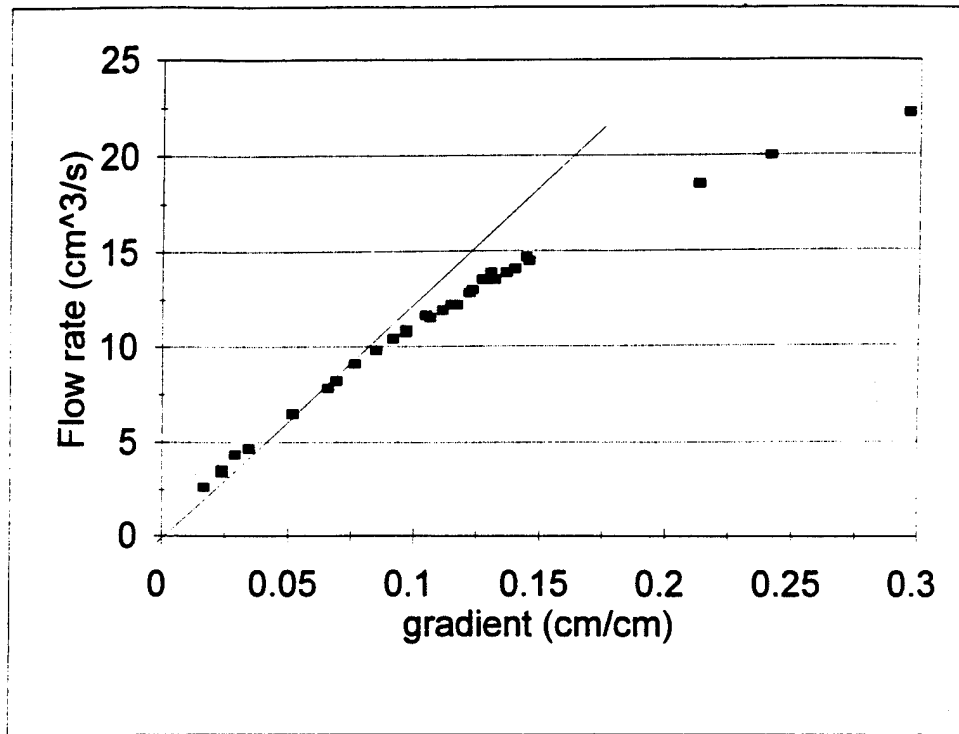
Figure 7-27. Flow rate versus gradient for "S" pattern channel

The "S" pattern fissure displays the characteristic curvature delineating laminar flow from turbulent flow. Previous fissure experiments were not able to reach this range. The transition point can be used to predict centrifuge performance. From Figure 7-27, the flow rate of 7.5 cm^3/s gives a Darcy velocity of 14.76 cm/s. In the centrifuge, the velocity should be N times greater, or for the 20g test, approximately 295 cm/s. At 1g, the upper limit Reynolds number is approximately 589. Using a Darcy velocity of 295 cm/s, the centrifuge theoretical Reynolds number is 11,776.

Mounting the partitioned channel fissure in the centrifuge required moving the solenoid valves and transducers to a position below the model. The collection cylinder was mounted at the same elevation as the fissure. Figure 7-28 shows the head loss

distribution for the "S" pattern fissure. The head loss within the fissure is dramatically increased, however, the head loss through the solenoid also increases significantly. Similar to the problem encountered using the solenoid valves for unsaturated sand flow, at elevated g-levels, this configuration can cause the solenoid to control the flow. The solenoid has a 0.32 cm orifice which at high flow rates causes non-linear head loss to occur proportional to the square of the velocity. Within the centrifuge, since the solenoid was at a lower level than the fissure, the imposed g-level is higher.

Figure 7-29 shows the hydraulic conductivity versus g-level plot for the "S" pattern channel. The solenoid valve does not appear to be controlling flow up to 20g's. Above 20g, the system failed at the gasket connecting the inlet head reservoir to the fissure.
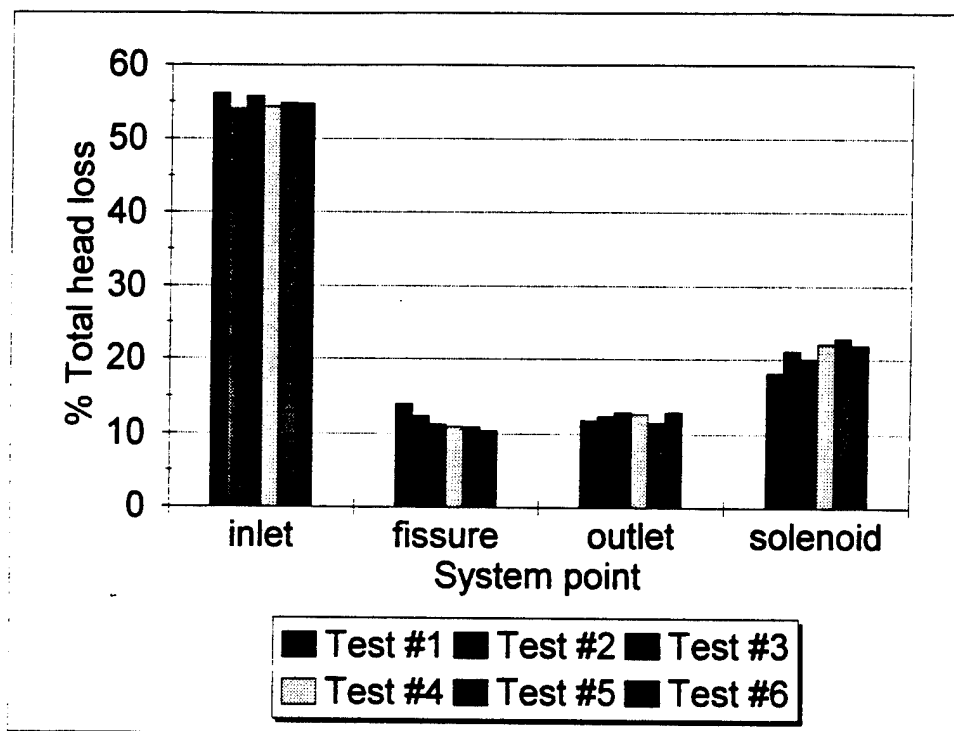
Figure 7-28. Head loss distribution for "S" pattern channel
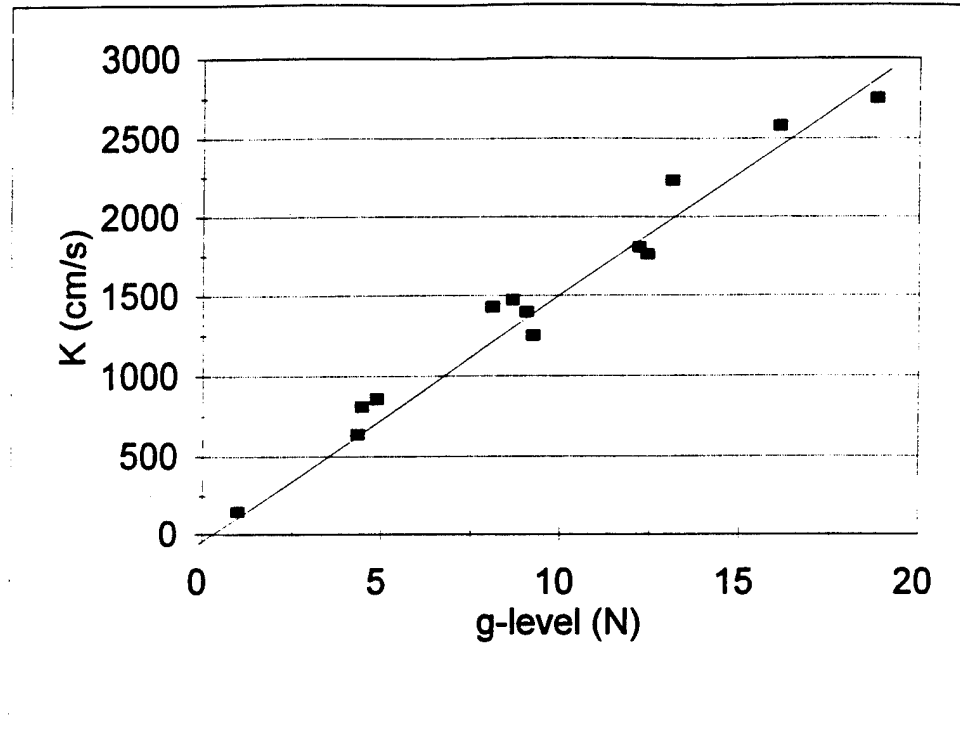
Figure 7-29. Hydraulic conductivity versus g-level for "S" fissure and water

It appears that using aluminum plates for the walls and placing the model in the horizontal position eliminated the expansion problem. The Reynolds number for the 20g test is:

$$Re = \frac{2bv}{v} = \frac{(2)(0.2)(34.72)}{0.01002} = 1386 \tag{7.23}$$

which is within the laminar flow condition previously predicted. To obtain higher Reynolds numbers, higher g-levels are required. Tests at higher g-levels, however, become increasingly more difficult to perform.

7.12 - Summary of results

The saturated fissure experiments were designed to validate both one- and two-dimensional scaling of the hydraulic conductivity. While the expected linear relationship was evident, the non-radial symmetry of a two-dimensional system allowed the fissure to expand, causing significant deviation as indicated by the viscosity and hydraulic conductivity ratios. Because fissure flow is extremely sensitive to the cube of the aperture, and head loss was difficult to measure, the results should be considered qualitative and not conclusive at this time. Table 7-3 is a summary of all centrifuge model saturated fissure tests.

Table 7-3. Summary of saturated fissure tests

Test	Fluid	K1g (cm/s)	KNg (cm/s)	Re
1 mm & #30 sand	water	17.94	N/A	54
2 mm & #16 sand	water	21.75	23.45	236
2 mm & #16 sand	Metolose	5.28	11.30	44
2 mm and standard pattern	water	145.17	111.75	825
2 mm and standard pattern	Metolose	29.77	38.83	76
2 mm and "S" pattern	water	147.80	145.08	1386

The saturated fissures results can be compared to the results obtained by Louis (1969) by using Equation (7.11). Figure 7-30 is a plot of the friction factor versus Reynolds number for the water tests, similar to Figure 7-3 presented by Louis (1969). The plot clearly shows the fissures remain within the laminar flow condition. The "S" pattern links the range of the uniform fissure and the standard pattern fissure.
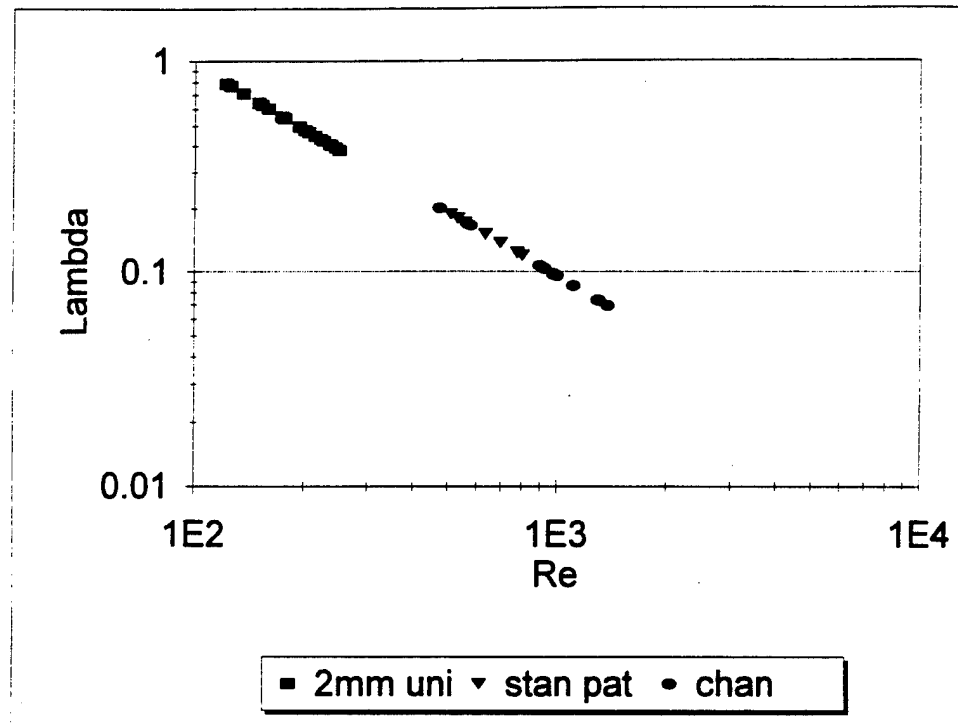
Figure 7-30. Friction factor versus Reynolds number

7.13 - Analysis and discussion of results

The experimental results for saturated fissure flow qualitatively verify the validity of the scaling relationship for the hydraulic conductivity for both one-dimensional and two-dimensional flow as:

$$K_m = NK_p \qquad \text{(hydraulic conductivity)}$$

The hydraulic conductivity versus g-level plots exhibited essentially linear behavior, however, the results do not appear conclusive. The fissures appeared to expand with increasing g-level. The expansion of the fissures would result in an increase in the flow rate and a possible decrease in the measured head losses.

For one-dimensional flow with a constant fissure aperture, the hydraulic conductivity should scale similarly to sands. The test using water appeared to display the linear relationship of increasing hydraulic conductivity with g-level, but had data scatter at the higher g-levels. Using Metolose as the test fluid, a non-linear, but consistently increasing hydraulic conductivity with g-level relationship was observed. The increasing hydraulic conductivity with g-level was consistent with the fissure undergoing expansion. The Reynolds number indicated the flow remained laminar for all tests. Due to the high hydraulic conductivities for even the smallest apertures, extremely high g-levels would be required to attain turbulent flow conditions.

Two-dimensional flow using the standard pattern displayed the same behavior as the one-dimensional flow tests. The "effective hydraulic conductivity" of the system scaled linearly for water but had large data scatter. Using Metolose as the test fluid, the "effective hydraulic conductivity" displayed a slight increase in hydraulic conductivity with g-level. The two-dimensional flow using the "S" pattern yielded very consistent results, but may not be indicative of real fissure flow. The Reynolds number indicated the flow remained laminar for all tests.

Saturated fissure flow proved to be much more difficult than saturated sand flow due to its non-radial symmetry. In the saturated sands, the cylindrical plexiglass column was essentially rigid and non-deformable. With the fissures, the model was two-dimensional and the choice of materials greatly influenced the quality and repeatability of the results. Since the flow rate is dependent upon the cube of the aperture, even a slight expansion of the system will cause an increase in the hydraulic conductivity. In the centrifuge, this effect is multiplied by the g-level. The increased g-level causes the weight of the system to increase, the head of fluid to increase, and, if the valves/solenoids are not placed on the same plane as the fissure, a variation in the fluid velocity through the system. The variation in the fluid velocity creates non-linear head loss through the system components.

The major obstacle to overcome in modeling fissures in the centrifuge is the head loss distribution of the system. As the size of the model decreases, the head loss through the fissure becomes smaller and the head loss coefficients shown in Figure 7-8 may not be not valid. Any additional tubing, valves, or system components only aggravate the problem. Ideally, the fissure should be in direct contact with the upper and lower constant head reservoirs. This alignment, however, presents an additional problem, in that the fissure would then be horizontal to the induced g-field and the weight of the overlying fissure walls would then be normal to the fissure aperture causing it to decrease with increasing g-level.

The numerical model predictions agreed very well with the experimental results, however, the aperture distribution for each cell must be manually input. Use of the

average aperture (determined from the 15 port measurements) in the model did not accurately capture the flow field or outflow rate. To obtain the model cell aperture, the fissure aperture had to be measured and discretized in both horizontal directions and then a smooth curve plotted between all points in two dimensions. For the model, over one thousand cell aperture values had to be manually entered, a very time intensive endeavor.

The saturated fissure experiments qualitatively validate the scaling relationship for the hydraulic conductivity. The determine the scaling relationship for time, the modeling of models technique, similar to the sands experiments of Chapter 5, would have to be used. The drainage process occurs so fast at 1g, however, for the centrifuge models, it would be extremely difficult or impossible to obtain measurements in-flight. Therefore, the determination of the scaling relationship for time in a fissure was not attempted. Although the time relationship was not determined, during the saturated flow experiments, the filling and draining of the fissure highlighted another aspect of unsaturated fissure flow. Unsaturated fissure flow can offer a significant advantage in exploring the stability criteria of Chapter 3. Unlike a uniform sand, the aperture is variable and the radius of curvature causes very distinct interfaces which are easily seen. Chapter 8 explores the stability criteria using fissures initially saturated and allowed to drain.

CHAPTER 8

TWO-PHASE UNSATURATED FLOW THROUGH FISSURES

8.1 - Objective and theory

The original objective in studying two-phase flow through fissures was to verify the scaling relationships of the hydraulic conductivity and time. However, the preliminary 1g tests indicated that the drainage process occurred so quickly at normal gravity that measuring the process in the centrifuge was not possible. As the 1g tests were being performed, anomalies at the fluid interfaces appeared, related to the critical velocity concepts presented in Section 3.5. This chapter will explore the use of ordered pairs of fluids, a variable aperture distribution, and their effects on the fluid-fluid interface.

Two-phase unsaturated flow in fissures is governed by the same equations as unsaturated flow in sands, and an equation similar to the Richards equation can be written for fissures. In a sand, the radius of the pore space determines the capillary pressure across the two fluid interface. In a fissure, the aperture distribution determines the capillary pressure across the interface of the two fluids. A standard test used to evaluate the capillary pressure effects of two different fluids and variable flow rates is the Hele-Shaw cell, shown in Figure 3-19. The viscosity and density are related to the flow rate through the use of the mobility ratio, Equation (3.13) and the critical velocity, Equation (3.14). The stability criteria for the critical velocity of Equation (3.14) can be addressed qualitatively using Equation (3.15).

8.2 - Experimental set-up

The experimental apparatus was constructed using the same constant head reservoirs and plexiglass sheets used in the saturated fissure flow experiments. One plexiglass sheet was replaced by a gypsum cement cast of a local sandstone. The cement cast was made in two steps. First, a negative cast of the sandstone was made with a silicone rubber molding compound. Second, the gypsum cement was poured over the silicone rubber compound. After the gypsum cement had cured, the rubber negative could be flexed and "peeled" away from the gypsum cement cast. This procedure allowed the gypsum cement to capture the various asperities of the real sandstone which would be broken off had the gypsum cement been poured directly onto the sandstone.

The gypsum cement cast was mated to a sheet of plexiglass, with foam rubber sealant used to seal the edges. The model was placed in the vertical direction on the centrifuge basket. The bottom head reservoir drained to the collection cylinder. The same pressure transducers used for the saturated fissures tests were used to measure the collection cylinder fluid. A manually operated Swagelock valve controlled flow.

The aperture distribution was variable and ranged from 0 mm to 5 mm. The interior apertures were measured using the dial gage inserted through the brass ports. Additional aperture measurements were made along the edges of the mated sheets. The sandstone/gypsum cast had an extremely variable distribution: a region of large aperture could exist next to a region of zero aperture due to flaking of the sandstone layers. The tests fluids were water and Soltrol.

8.3 - Experimental results of fissure with a water and air interface

The water and air interface test was designed to verify sharp front behavior. From the stability criteria, if the heavier fluid is always below the lighter fluid, the front is always stable regardless of the flow rate.

The water was dyed using green food coloring to provide color contrast to the white gypsum cement. Figures 8-1 through 8-4 show the water drainage front moving down as a sharp front. Within the fissure, zero and large apertures caused visible color variations and the variable aperture distribution resulted in a change in the front due to the difference in capillary pressures. The cumulative outflow curve is shown in Figure 8-5 and displays the same characteristic shape as the sands of Chapter 5.
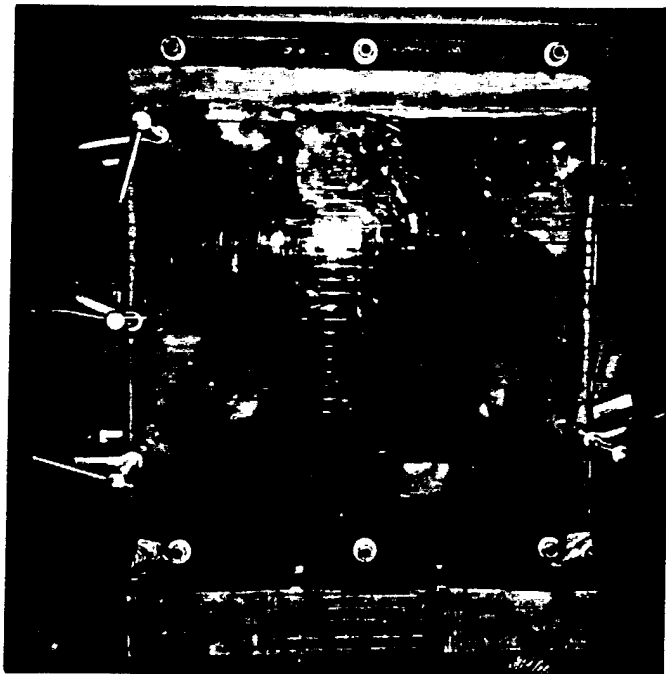
Figure 8-1. Water and air sharp front before drainage
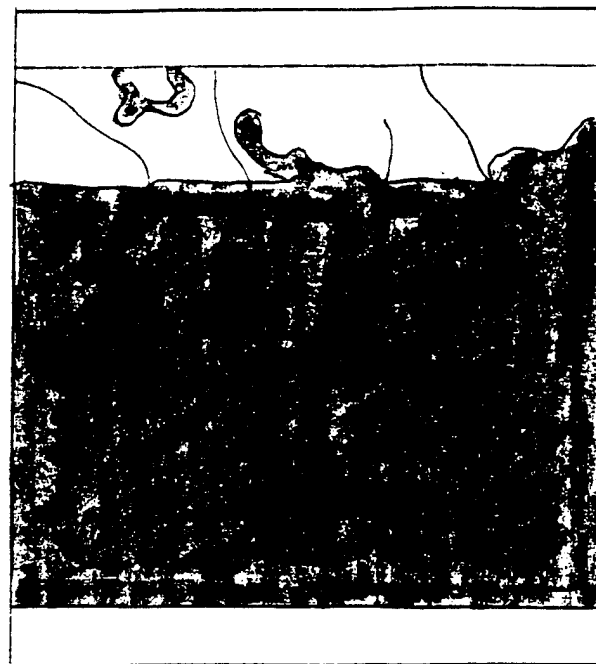
Figure 8-2. Water and air sharp front
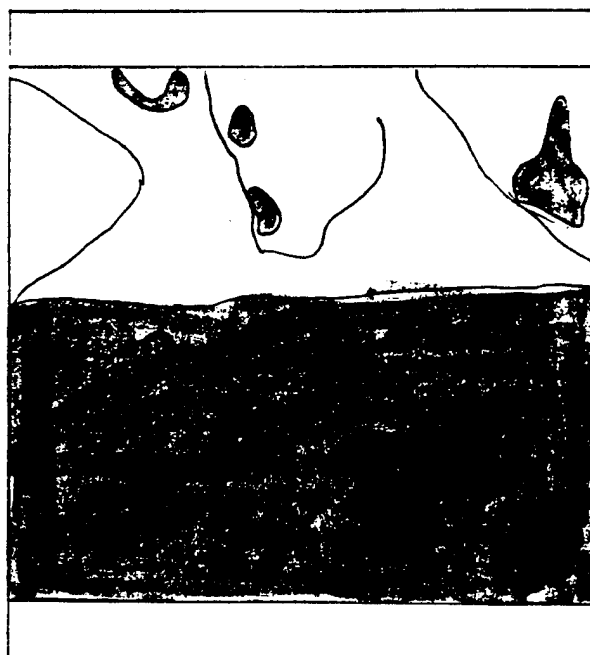
Figure 8-3. Water and air sharp front

Figure 8-4. Water and air sharp front
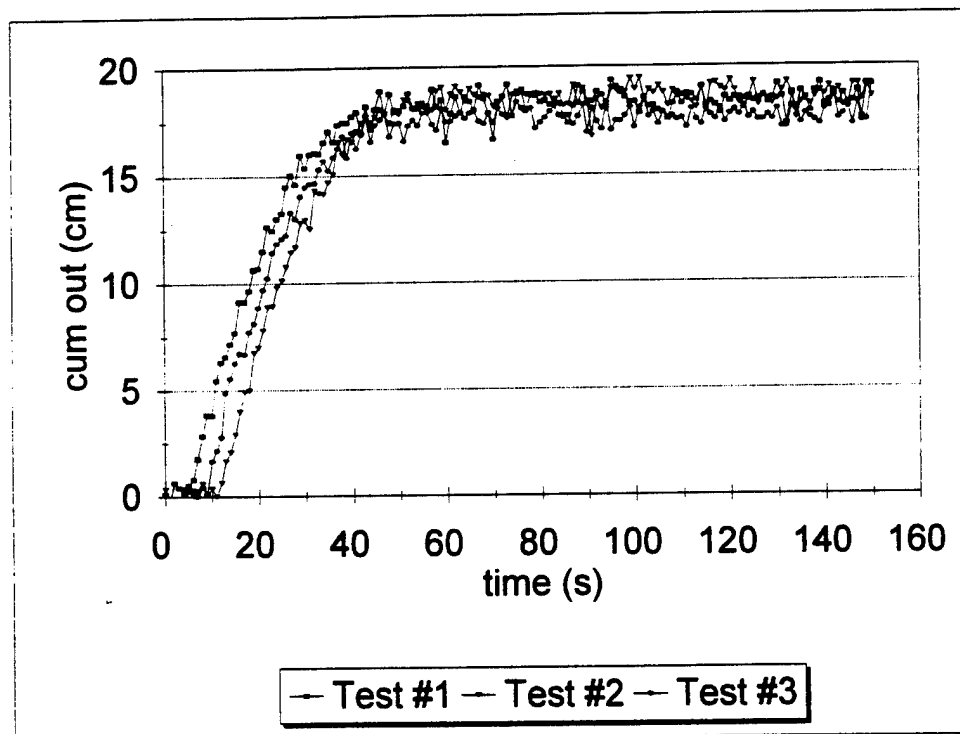
Figure 8-5. Water and air cumulative outflow curves

247

At 1g, the fissure was completely drained in approximately twenty seconds, as seen in the cumulative outflow curves of Figure 8-5. In the centrifuge at 20g's, this drainage rate would correspond to a model time of 0.05 seconds for a complete test. Visual inspection of the drained fissure revealed little entrapped fluids. The regions of zero aperture would be expected to retain significant amounts of fluid due to the high capillary pressures generated. In Figure 8-4, these areas appear at the upper left top and mid-right edge and are seen as the darker color.

The cumulative outflow curves shown were generated with the valve controlling flow in the fully opened position. Several tests with the valve at various openings yielded similar results. The entrapped fluids always appeared in the same regions and were outlined with a black marker for each test. The regions and area of entrapped fluid did not vary with the flow rate.

8.4 - Experimental results of fissure with a Soltrol and air interface

The Soltrol and air interface test was designed to verify sharp front behavior. According to the stability criteria, if the heavier fluid is always below the lighter fluid, the front is always stable regardless of the flow rate. The interfacial tension of Soltrol is approximately one third that of water and the distribution of entrapped fluids is expected to be different from the water distribution.

The drainage front of the fissure with a Soltrol and air interface was visually identical to the water and air interface. Figure 8-6 shows the cumulative outflow curve for Soltrol. The outflow curves are similar to the sands described in Chapter 5.
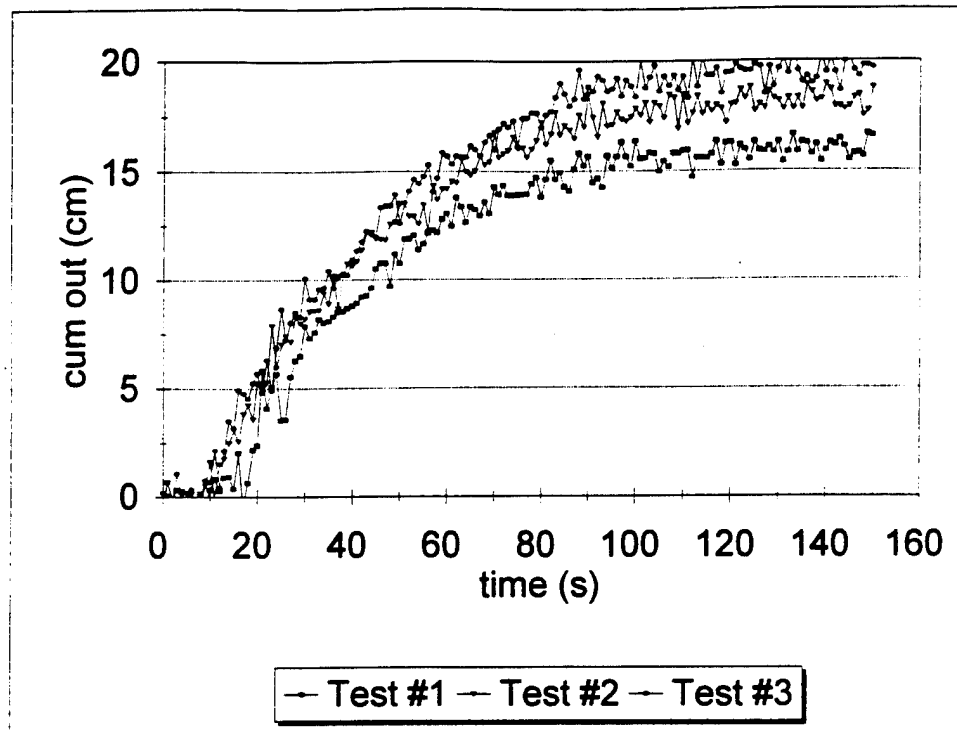
Figure 8-6. Soltrol and air cumulative outflow curves

The entrapped Soltrol was in the same region as the water, but occupied smaller areas. The photos of the Soltrol and air interface did not have enough contrast for the fluid interface to be visible.

8.5 - Experimental results of fissure with a water and Soltrol interface

The water and Soltrol interface test was designed to verify sharp front behavior for two simultaneous drainage fronts, water and Soltrol and Soltrol and air. According to the stability criteria, if the heavier fluid is always below the lighter fluid, the front is always stable regardless of the flow rate. In this experiment, the water and Soltrol interface would be expected to be similar to the water and air interface.

The fissure was filled with water to the bottom of the upper inlet reservoir. The upper reservoir was filled with 2 cm of Soltrol. The drainage front remained sharp with the water and Soltrol interface visually the same as the water and air interface, as shown Figure 8-7 through Figure 8-9. The Soltrol and air drainage front also remained sharp.

No instability of the fronts could be induced, even with the valve in the fully open position. The change in the interface of the water and Soltrol in Figure 8-8 can be compared to the water and air interface of Figure 8-3. The majority of entrapped fluid was Soltrol, forming a coat over the entire gypsum cement cast. Small amounts of water were entrapped in areas which did not normally entrap fluids, as seen in Figure 8-9. It appeared that the Soltrol acted as the wetting fluid, contrary to the assumed order of wetting fluids.
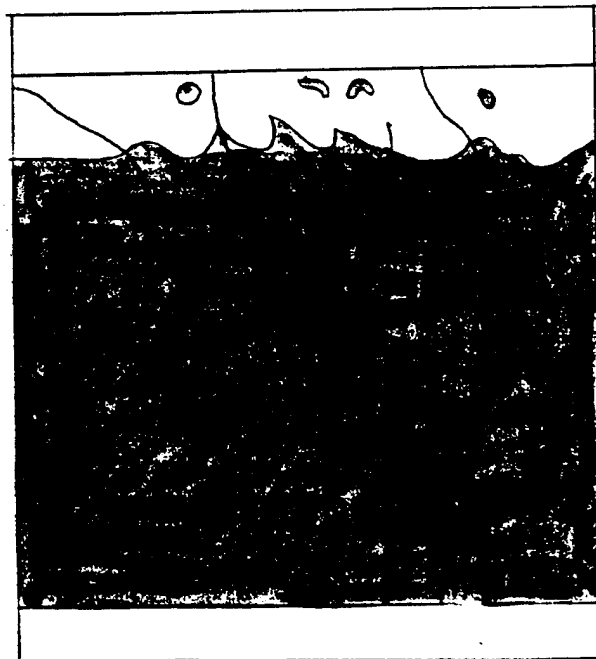
Figure 8-7. Water and Soltrol sharp front
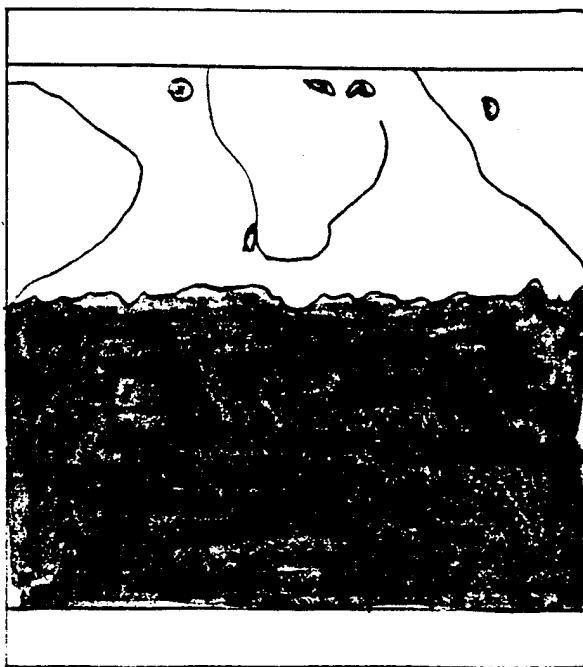
Figure 8-8. Water and Soltrol sharp front
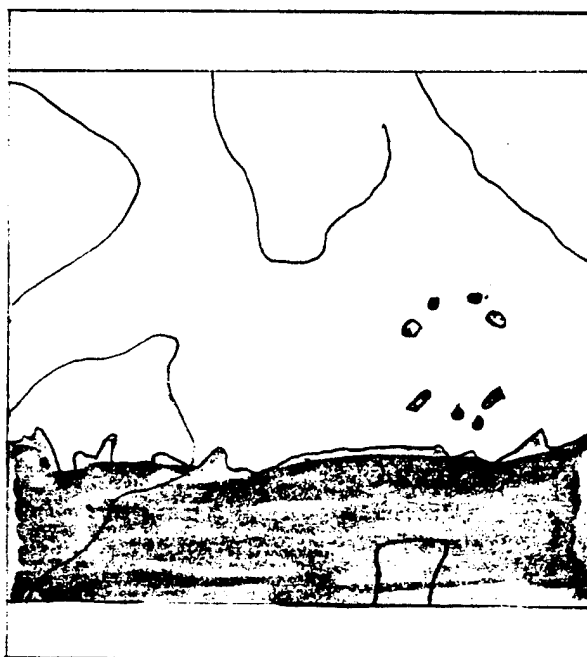
Figure 8-9. Water and Soltrol sharp front

251

8.6 - Experimental results of fissure with a Soltrol and water interface

The Soltrol and water interface test was designed to verify unstable front behavior. According to the stability criteria, if the heavier fluid is above the lighter fluid, the front may be stable. The multiphase tests with uniform sand, described in Chapter 6, showed the front to be stable at 1g and at low drainage rates. At an elevated g-level and with a high drainage rate, fingering occurred.

To test instability, the ordered pairs of fluids were reversed. The fissure was filled to the bottom of the upper inlet reservoir with Soltrol. Using a syringe, water was slowly injected into the upper reservoir. Water pooled to a depth of 2 mm. At that depth, the Soltrol and water interface became unstable and viscous fingering occurred. Figures 8-10 through 8-12 show the fingering phenomenon.
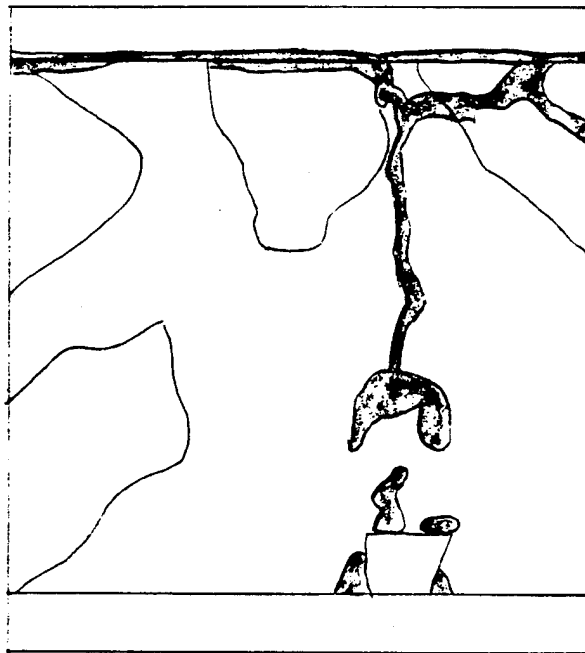
Figure 8-10. Soltrol and water unstable viscous fingering
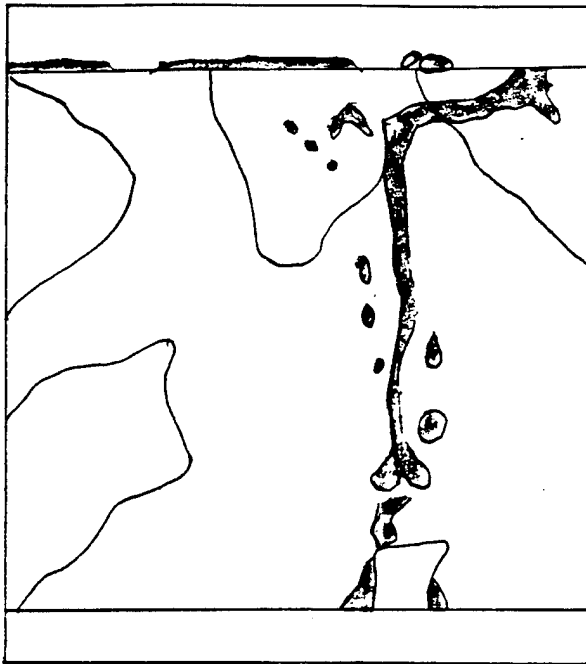
Figure 8-11. Soltrol and water unstable viscous fingering
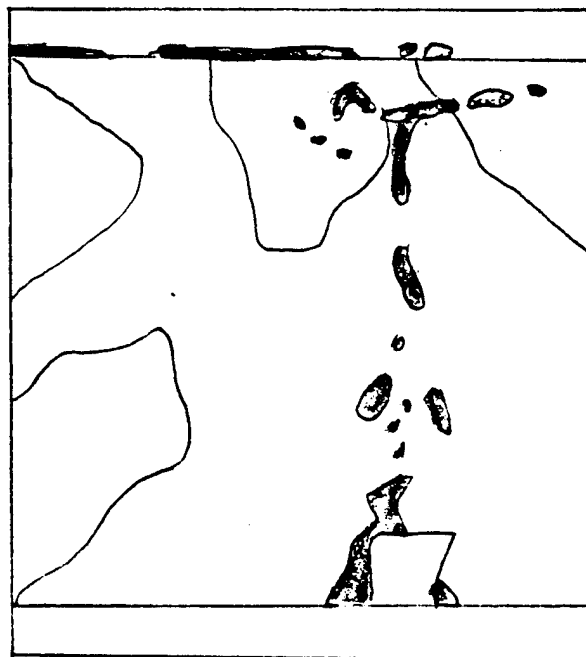
Figure 8-12. Soltrol and water unstable viscous fingering

The point where the fingering occurred was the largest aperture opening at the top. If the top of the Soltrol front were lowered to a different position, a different channel would form. As the finger passed through the Soltrol, some residual water would remain on the gypsum cement, as is seen by the slight green discoloration of the gypsum cement.

8.7 - Analysis and discussion of results

For unsaturated fissure flow, the ordered pair of fluids, densities, and interfacial tensions of the wetting and nonwetting fluid determines stable or instable behavior. For any fissure undergoing gravity drainage with water or Soltrol as the wetting fluid and air as the non-wetting fluid, the fluid front is always stable and basically sharp with the cumulative outflow curve being a function of the viscosity and interfacial tension. For any fissure with multiple light fluids overlaying denser fluids, the drainage front will still remain sharp and the cumulative outflow curve will retain the shape of the denser fluid.

A denser fluid overlying a lighter fluid can be stable or instable. For water overlying Soltrol, water droplets accumulate until a uniform layer of water is formed up to some critical depth, at which point the water penetrates into the largest pore space and the pooled layer of water flows through this pore space. As the water flows downward through the Soltrol, it does not flow vertically, but rather searches for the largest unobstructed pore space. Significant lateral flow occurs and as the pore spaces become slightly water filled, the water column above diverts into a different pore space. For every test, only the initial pore space at the top where the pooled water entered remained constant. All other flow paths varied for each test.

254

Qualitatively, the experiments of this section validate the stability criteria described in Section 3.4. More importantly, the results indicate that ordered pairs of fluids can be chosen such that the analysis presented by Peterson and Cooke (1994) described in Chapter 5 is not applicable. The variable aperture gypsum cement cast clearly illustrated the effect the radius of the pore space has on determining the capillary pressure across the fluid interface. Due to the extremely high drainage rate, it does not appear that there is any advantage to modeling unsaturated flow through fissures in the centrifuge. The process occurs so rapidly at 1g that the time scale is not a factor, and for any real fissure the length factor is not scalable. Only idealized smooth fissures would be appropriate, and as seen in Chapter 7, these models are of limited use.

CHAPTER 9

GEOCHEMICAL OBSERVATIONS

9.1 - Objective

During the research, several observations were made of behavior not theoretically predicted nor previously mentioned in prior studies. These observations are presented in this chapter with an attempt to relate their significance to the flow problems being studied.

9.2 - Color change of the porous media

In the test program, several sands of various gradations, sandstone rock, gypsum cement rock, and ceramic stones were used. Normal porosity and saturation and tests were conducted for all of the sands using water, Soltrol, and Metolose. Using water, any sand exposed to the fluid underwent a slight color change but when dried returned to its original condition. Using Metolose, the same color change as water was noticed, but when dried, a light white residue remained. The residue was the cellulose fibers and, when mixed with water, would return to Metolose. Using Soltrol, a very different color change occurred. The sand color started similar to the water but then became much darker, taking only minutes for the transition to occur. The finer the sand, the darker the color change. Very coarse sands (#8 and #16) showed little change, indicating that the surface area seemed to be the key factor. This color change was initially observed for dry sand and Soltrol. During the unsaturated experiments, the sands were drained to residual

water saturation and then exposed to Soltrol. Once again, the instantaneous color change occurred, indicating that the Soltrol was displacing the water from the sand surfaces. Theoretically, water is the wetting fluid and Soltrol is the non-wetting fluid which requires the water to be preferentially absorbed to the mineral grains. If Soltrol is replacing the water at the mineral grains surface, the concept of preferential wetting is not valid.

To determine the effect that Soltrol was having on the mineral grains, it must be known if the Soltrol is binding to the individual grains and to what degree the partitioning occurs. Evaporation tests were conducted using Soltrol in an evaporation pan, dry sand/Soltrol, and residual water/sand/Soltrol to determine the partition coefficients. Soltrol is a clear/slightly yellow fluid which has a relatively low vapor pressure and evaporates very slowly at normal room temperatures. The samples were placed in the geotechnical oven at 98° C and allowed to dry for several days.

Figure 9-1 shows the Soltrol evaporation rate for the Soltrol placed in the evaporation pan. At the end of the test, a very viscous, yellow sludge similar to petroleum jelly remained. Figure 9-2 is the evaporation rate for the dry sand/Soltrol. At the end of the test, the sands had undergone a very pronounced color change, almost to a grey/black. Every grain was affected but no residue or viscous sludge could be observed and no measurable mass of Soltrol remained on the sand grains. It appears that the Soltrol alkane fractions carbon had bonded to the sand silicon and the alkane hydrogens had been removed.
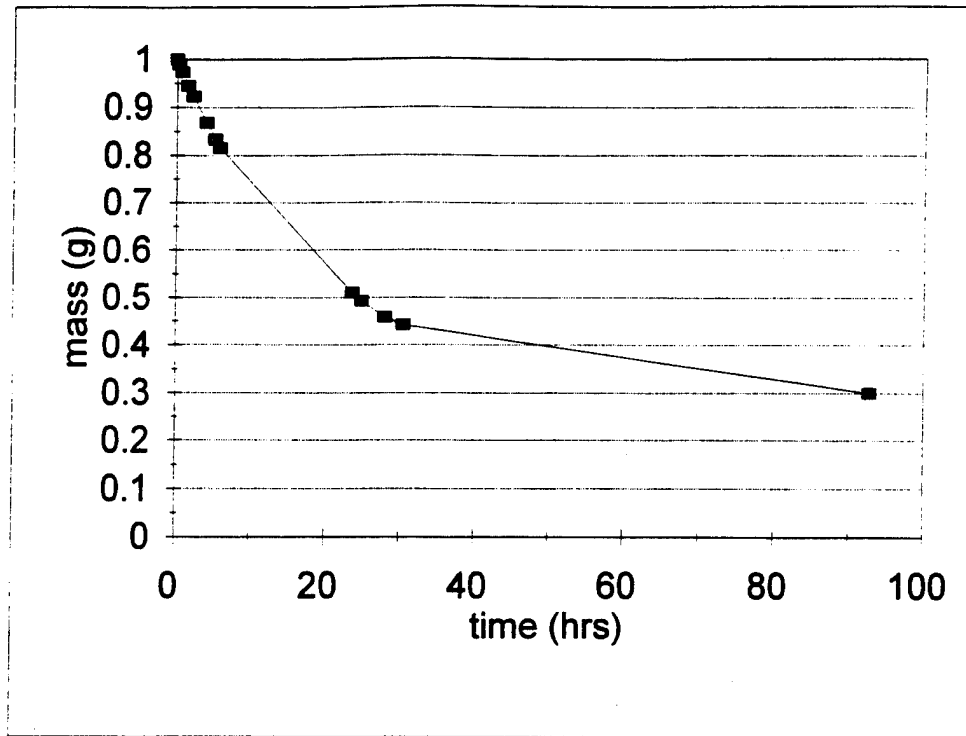
Figure 9-1. Soltrol in evaporation pan
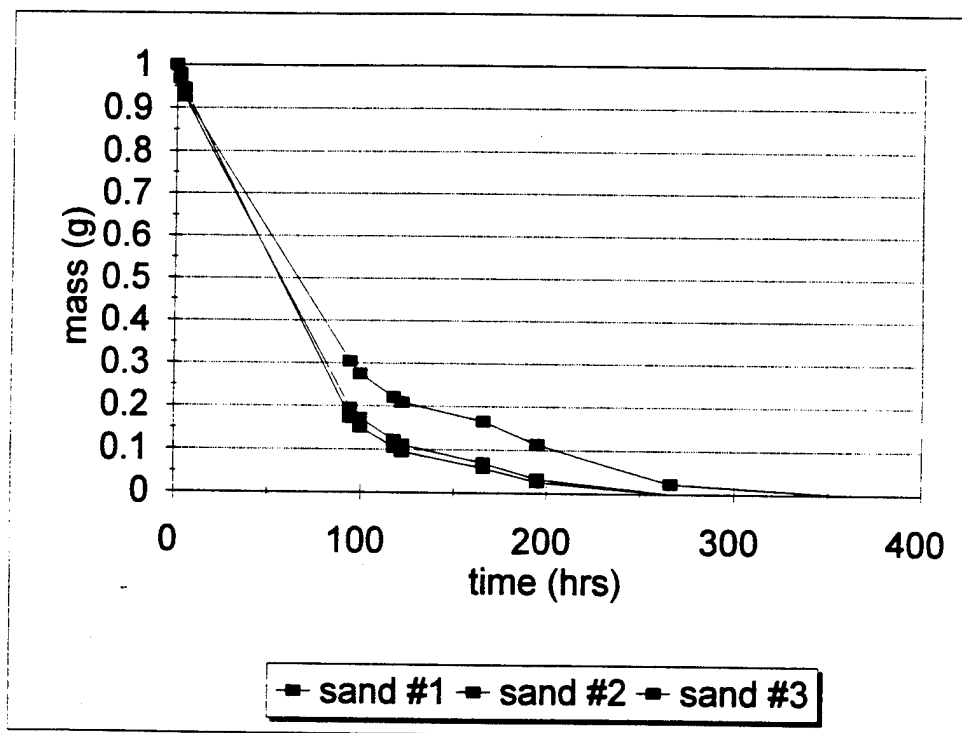
Figure 9-2. Dry sand/Soltrol evaporation

To test the effect of organic composition, different fluids were chosen representing alcohols, alkanes, and benzenes to determine if the color change could be related to straight chain or ring structures. Table 9-1 is a compilation of the results.

Table 9-1. Effect of organic composition and structure

Organic	Saturated				Oven dried			
	#16	#30	#70	#F75	#16	#30	#70	#F75
Iso-propyl	N	N	Y	Y	N	N	N	N
Glycerol	N	N	Y	Y	N	N	N	N
Acetone	N	N	Y	Y	N	N	N	N
Soltrol	N	Y	Y	Y	N	Y	Y	Y
Pump oil	Y	Y	Y	Y	Y	Y	Y	Y
Motor oil	Y	Y	Y	Y	Y	Y	Y	Y

N = No color change   Y = Color change

It appears that there are two physical phenomena occurring related to the organic structure and the surface tension/viscosity. The alcohols and ketones do not show any residual traces but have very high vaporization rates and low viscosities. The heavier oils which have alkane chains or benzene rings are also much more viscous and have very slow evaporation rates. These competing physical properties must be better understood

before they are used in the centrifuge where evaporation rates are accelerated due to the high air velocity caused by the spinning arm.

The effect of Soltrol on sands must be related to some chemical reaction occurring on the sand grains. To test for a possible mechanism, the sandstone rock, gypsum cement rock, and ceramic porous stones were exposed to Soltrol. They did not display any color change upon submersion into the Soltrol. The fragments were left in the Soltrol for several days and still no color change was observed. The fragments were then placed into the oven to dry and still no color change occurred. The sandstone would be expected to have characteristics similar to the silica sands, however, the sandstone has ferrous iron incorporated in the rock matrix and any color change may be obscured by the presence of the iron. The gypsum cement and ceramic porous stone are completely inert and the Soltrol did not appear to react in any manner with these substances.

9.3 - Fluid and surface interactions

The definition of wetting fluid and nonwetting fluid is based upon the contact angle formed by the fluids with the solid surface as shown in Figure 9-3. In Figure 9-3, oil is the wetting fluid and mercury is the nonwetting fluid. For water-NAPL systems, water is assumed to always be the wetting fluid and Soltrol is the nonwetting fluid. There are no published experiments on contact angles for water and Soltrol.

Air

Oil drop

$\theta < 90°$

Air

Mercury drop

$\theta > 90°$
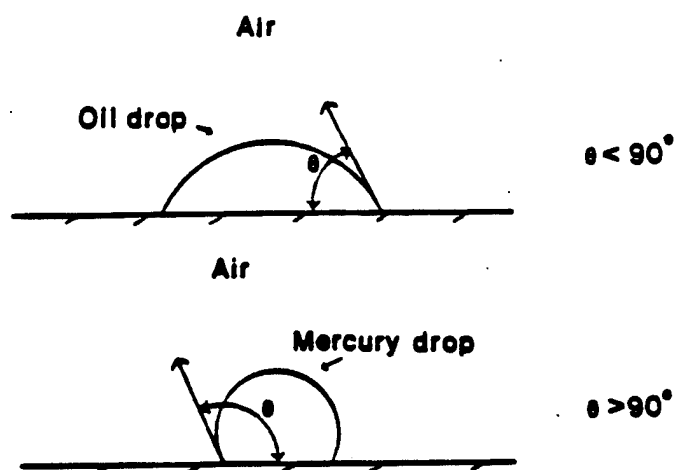
Figure 9-3. Wettability contact angles

Other researchers known to be working with Soltrol were contacted to see if contact angles were available. Prof Deanna Durnford (CSU) and Prof Helen Dawson (CSM) have the required equipment but have not measured Soltrol contact angles. The CU lab does not have the required equipment, so the following results are qualitative versus quantitative. A hypodermic needle was used to place droplets on the surface of a variety of common engineering materials used in the laboratory. Table 9-2 is the compilation of the results. Figure 9-4 shows typical droplet configurations. Water formed very symmetrical droplets on all surfaces. Water was absorbed by the sandstone over a period of time. Soltrol acted more like a penetrating oil, forming very thin films on nonporous materials and was immediately absorbed into the pore space of porous materials. The Soltrol went directly into the pore space of the sandstone with residual water. The more viscous organics formed droplets.

261

Table 9-2. Wettability of various surfaces

	Glass	Plexiglass	Sandstone	Gypsum
water	D	D	D	D
Soltrol	ND	ND	ND	ND
water/Soltrol	D/D	D/D	D/ND	D/D
Soltrol/water	ND/D	ND/D	ND/D	ND/D
Iso-propyl	ND	ND	ND	ND
Acetone	ND	ND	ND	ND
Glycerol	D	D	D	D
Motor oil	D	D	D	D
Hydraulic oil	D	D	D	D

D = droplet formed   ND = no droplet formed
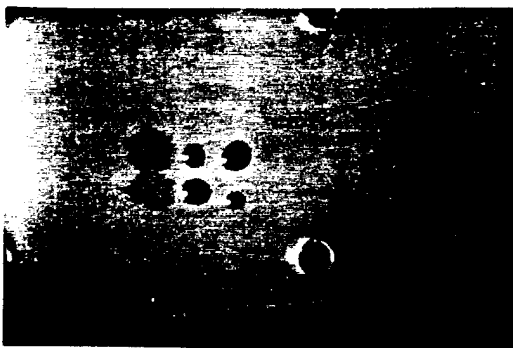
Figure 9-4. Water and Soltrol on various surfaces

9.4 - Capillary pressure and wetting

The experiments using sand saturated with Soltrol and with water above, could be made to display sharp front drainage behavior as long as some "critical velocity" was not exceeded. The uniformity of the grains and porosity ensured a fairly uniform capillary pressure distribution across any horizontal section, as shown by Figure 4-6. The Soltrol saturated rock fissure showed no such behavior; as soon as a continuous water layer of approximately two millimeters was formed, the water broke through the largest aperture channel. If the water layer was only one millimeter thick and drainage allowed, a different drainage channel could be induced. To examine the effect of the aperture on the capillary pressure and the wetting fluid, a series of tests using water and Soltrol placed as droplets was conducted.

The rock fissure was completely dry and open to the atmosphere. A small hypodermic needle was used to place droplets within the aperture opening across the width. The droplets were doubled, tripled, etc., and at some point when the weight of the droplet exceeded the surface tension and capillary pressure, the droplets fell to a lower elevation. At the lower elevation, the entry pressure of the opening was greater than the available pressure of the droplet. Figure 9-5 illustrates the process occurring for water. The initial droplets are quite uniform, and the largest aperture is slightly past the middle on the right-side. The final sequence shows several droplets being spread out due to the small aperture distribution on the left side while the largest aperture allows the water to fall to a lower elevation. Repeating the process with Soltrol, droplets could not be formed, no matter how small the droplet.
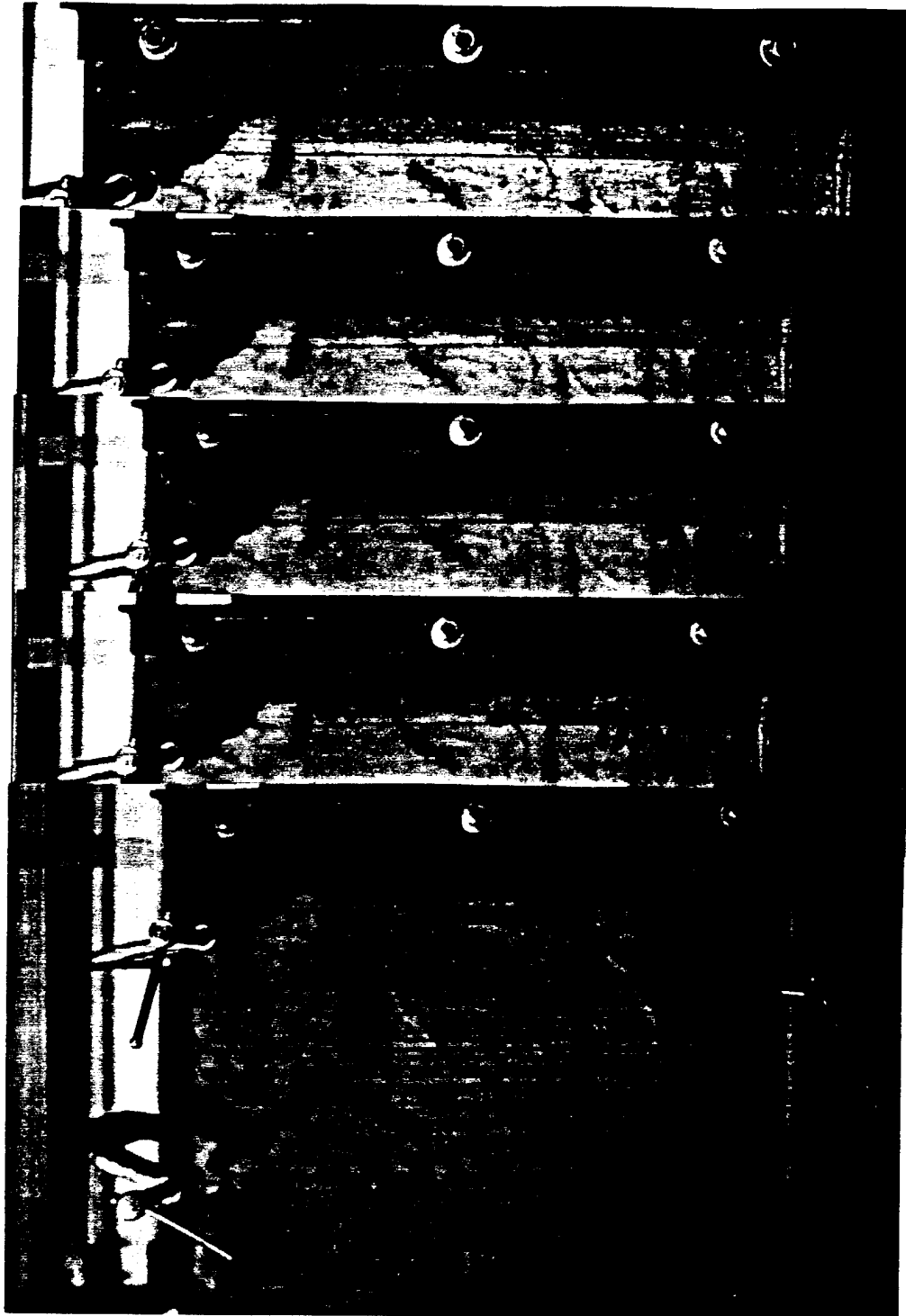
Figure 9-5. Capillary pressure distribution for water droplets in air

9.5 - Analysis and discussion

In discussions with other researchers, many of the same type of observations have been made which contradict the assumed order of wetting. These observations have not been documented before, but they certainly are playing a crucial role in the phase distribution of Soltrol. The affects of partitioning, contact angles, and wettability must be addressed at some point by future researchers. At this time, the affect on the mechanical properties of the porous medium are unknown.

CHAPTER 10

CONCLUSIONS AND RECOMMENDATIONS

10.1 - Introduction

The experimental program was designed to evaluate the use of the centrifuge in modeling flow processes related to environmental problems. The experiments covered saturated and unsaturated flow in several types and combinations of porous media using fluids of various viscosities and densities. From Chapter 1, the hypothesis was stated as

> The centrifuge is a valid tool for modeling one and two-dimensional flow problems and the scaling laws when properly applied will properly predict prototype performance (pg 1).

The results of the experimental program validate the hypothesis. There are *caveats*, however, and the centrifuge does have restrictions on the types of problems which can be examined. Using macroscopic parameters, model behavior reasonably matches prototype behavior, indicating that the scaling relationships relating the model to the prototype's performance are valid, at least in the qualitative sense. The quantitative relationships should always be taken with caution, since many factors are seen to adversely influence the accuracy of the results. The concept of small scale modeling breaks down when unstable configurations that cause fingering are used, as theoretically predicted by Peterson and Cooke (1994).

10.2 - Conclusions for saturated flow

The saturated flow experiments were designed to use a single phase fluid to explore the relationship between the imposed g-level N and the hydraulic conductivity, and to determine the maximum Reynolds number which defined the upper limit of laminar flow. Based on the results of the experiments it is concluded that:

1. Density and viscosity are gravity independent and can be used in conjunction with the viscosity ratio Equation (4.15) to compare different fluids with different properties. This implies that Metolose, a non-toxic water based fluid, can be substituted for Soltrol for many experiments without loss of model similarity.

2. The hydraulic conductivity of a porous media scales as

$$K_m = NK_p$$

3. For sands, the upper limit of the Reynolds number is between 1 and 10 as developed by Bear (1972). The Reynolds number of 3.11 for the #30 sand indicated laminar flow conditions and confirms the findings of Goodings (1994), and contradicts those of Goforth et al. (1991).

4. For fissures, the upper limit of the Reynolds number is fissure specific. For the uniform aperture, the upper Reynolds number could be as high as 2300. For the "S" pattern fissure, the largest Reynolds number obtained was only 1386.

5. The effective hydraulic conductivity of layered sands can be calculated using the theoretical equivalent system defined by Equation (4.14). The effective hydraulic conductivity scales as

$$K_m = NK_p$$

6. Flexible wall permeameters showed larger data scatter compared to rigid wall permeameters, but this does not imply that the flexible wall permeameter is not as reliable as the rigid wall permeameter. Saturation of the flexible samples was more difficult than for the rigid samples; consistent results required raining the sand through the fluid in the rigid permeameter, especially as the viscosity increased.

7. Head loss through the sand apparatus is controlled by the reservoir inlet and sand sample with minor head loss through other components of the system. Head loss through the fissure apparatus is controlled by the system components with minor head loss through the fissure.

10.3 - Conclusions for two-phase unsaturated flow

The experimental program for two-phase unsaturated flow was designed to evaluate the scaling relationship for the unsaturated hydraulic conductivity and time. Based on the results of the experiments, it is concluded that:

1. For one-dimensional homogenous sand columns undergoing gravity drainage of the wetting fluid, the scaling of the unsaturated hydraulic conductivity and time scale as

$$K_m = NK_p$$

$$t_p = N^a t_m$$

The scale factor N was found to be approximately 5% higher than the actual g-

269

level (calculated using the angular velocity and arm radius). The time exponent "a" was found to be approximately 1.87, rather than the theoretical exponent of 2.

2. The centrifuge models were tested in both the small and the large centrifuges to determine the effect of the arm radius on the modeling of models. The variation of the g-field due to the length of the arm does not appear to be significant; however, the larger arm radius does reduce data scatter and produces more consistent results.

3. The density, viscosity, and interfacial tension of the wetting fluid control the shape of the cumulative outflow curve for homogeneous sands. The exact role of each is unclear; Soltrol has a viscosity approximately seven times that of water but an interfacial tension of only one third that of water. If the viscosity controlled the cumulative outflow, the final drainage time would be approximately seven times longer compared to water. Clearly, the lower interfacial tension reduces the drag on the drainage front leading to shorter drainage times. It appears that the two effects are counteracting each other. It should be noted that the residual saturation and capillary fringe for both water and Soltrol in the #70 sand are virtually identical.

4. One dimensional layered sand columns undergoing gravity drainage can be scaled as

$$K_m = NK_p$$

decreases with increasing g-level. The initial hydraulic conductivity can be computed using the theoretical equivalent homogeneous system of Equation (4.14). The final fluid entrapment appears to duplicate prototype behavior; the change from residual saturation to full saturation in each layer is clearly visible to the naked eye and well defined. The pore pressure profiles clearly show the effect of the layering on the drainage rate.

5. Experiments for the sands used in the experimental program, indicate that the maximum suction at which the pore fluid is still continuous is approximately 50 cm, which corresponds to the point on the suction saturation curve where the sand approaches residual saturation.

6. Due to the extremely fast drainage rate and very small degree of entrapment at normal gravity levels, there does not appear to be any advantage to modeling unsaturated fissure flow in the centrifuge. The unsaturated fissure experiments validated the concept of critical velocity and ordered pairs of fluids such that sharp front behavior was always maintained, contrary to the analysis of Peterson and Cooke (1994). The aperture distribution was crucial in determining the capillary pressure across the fluid interface. The aperture distribution in a fissure can be compared to the pore space radius in a heterogeneous sand.

7. Numerical models are still unable to accurately predict prototype performance. Due to the very sensitive relationship of the hydraulic conductivity with degree of saturation, the form of the suction-saturation curve is very important. For the numerical model of Durnford and Marinelli (1995), the Brooks-Corey curve

271

saturation, the form of the suction-saturation curve is very important. For the numerical model of Durnford and Marinelli (1995), the Brooks-Corey curve parameters were used, which yielded a very smooth suction-saturation curve. However, the abrupt change at the entry pressure and the steep rise of the curve at values near residual saturation present numerical difficulties. It is fortunate that there is little total fluid volume change in the regions above 50 cm of suction; in this case there did not appear to be a need to accurately simulate the portion of the curve above 50 cm of suction.

10.4 - Conclusions for multiphase flow

Theoretically, modeling multiphase problems in the centrifuge is possible. However, only those problems in which the ordered pair of fluids are placed so that ganglia are prevented and sharp front behavior is induced can be modeled. The Druck miniature pore pressure transducers capture the essence of the global pressure distribution, but as soon as a new phase passes the porous stone, the transducers measure an organic phase with a water-saturated porous stone or vice versa. The pressure measurements are then affected by the interface of the porous stone and the pore space fluid and no longer represent the pressure within the porous medium.

10.5 - Geochemical observations

During many of the tests run in the centrifuge, several phenomena occurred which have not been previously documented but which likely have a significant impact on

modeling organic contaminant problems.

When sands were exposed to Soltrol, an instantaneous and irreversible color change took place. This color change occurred even when water was present, indicating that Soltrol may be acting as the wetting fluid. Attempts at quantifying this behavior met with limited success. Current methods are not capable of measuring contact angles of rough surface particles, or when more than one fluid is present.

The interfacial surface tension, density, and viscosity cause very different behaviors depending upon the structure and composition of the organic phase. Alcohols and ketones appeared to remain chemically neutral to the sands used for the experiments, while the alkanes and benzenes appeared to chemically react.

10.6 - Recommendations

The centrifuge is still in its infancy with regard to use in solving geoenvironmental problems. The advantage of the centrifuge is its capability to use the actual porous media pore fluid in an experimental configuration that is a reduced scale of the prototype, which experiences an acceleration of the time scale. Experiments in the centrifuge can be completed within hours to days, and duplicate prototype conditions of several years.

Accurately modeling the prototype performance conditions is not a trivial exercise. For example, as shown with the pore pressure measurements, maintaining consistent boundary conditions is very difficult, yet the prerequisite to properly modeling a problem is maintaining consistent boundary conditions.

Highly accurate and reliable instrumentation is required, and new measurement

273

techniques must be developed that can determine separate phase pore pressures as well as relevant porous media parameters. Currently, laboratory methods are not convenient and the degree of repeatability is uncertain. Few natural materials have the uniformity of the experimental test materials, yet even the uniform materials are difficult to characterize. Heterogeneous materials are even more difficult to characterize. The suction-saturation curve for a heterogeneous porous medium must be reexamined with regard to the wetting and drying scanning curves. Organic contaminants will certainly affect the shape of the curves, and if the Brooks-Corey parameters obtained using the suction-saturation curve is used to compute relative permeability curves, significant errors may be introduced. The relative permeability Brooks-Corey parameter is not necessarily the same as the suction-saturation.

The experimental procedures, sample preparation, and method of data analysis must be at least as accurate as the instrumentation. A high degree of accuracy in the instrumentation is useless if the ability to prepare a sample, perform a test, and analyze the data is only within an order of magnitude. For example, the centrifuge has been proposed as a method to analyze problems involving radioactive waste containment over a period of 10,000 years using g-levels as high as 100g's. As previously shown, if the scale factor N and the time exponent "a" vary only 10%, the prediction in prototype performance would be plus or minus 1000 years. Is this 10% deviation an acceptable error when dealing with regulatory agencies and the general public? In this case, the experimental procedure and degree of analysis may not be as sophisticated as the ability to measure the experimental parameters.

The next logical step would be to use water as the wetting fluid and Soltrol as the nonwetting fluid using a more elaborate system. For multiphase flow problems using water and Soltrol, new measurement techniques and instrumentation will have to be developed. Oil-water separators will be required to measure cumulative outflows of each phase. Pore pressure transducers must be developed which are capable of measuring a specific phase and the gamma ray system may be needed to measure phase saturations. Finally, a convenient and accurate method to determine the relative permeability for each phase must be developed.

Use of standard laboratory equipment and materials such as plexiglass and gypsum cement, do not display the same contact angles and wettability characteristics as natural porous media and may be providing misleading data. The use of Soltrol as the LNAPL of choice for experimental programs should be carefully scrutinized; if Soltrol is indeed behaving as the wetting fluid even in the presence of water, the common assumptions of phase partitioning are not valid. The impact or mechanical changes caused by the Soltrol chemically reacting with the porous media are unknown.

The research presented in this thesis covered a very wide array of topics and provided both quantitative and qualitative results of important processes in flow problems, but was only the first step in examining the fundamental processes involved. Before elaborate problems in two or three dimensions can be attempted, quite a bit of work has yet to be accomplished in one-dimensional flow.

BIBLIOGRAPHY

Abriola, L.M., Pinder, G.F., "A Multiphase Approach to the Modeling of Porous Media Contamination by Organic Compounds", Water Resources Research, Vol 21, No.1, Jan 1985, pp 11 -18.

Amadei, B., Illangasekare, T.H., "Analytical Solutions for Steady and Transient Flow in Non-homogeneous and Anisotropic Rock Joints", Int. J. Rock Mech. Min. Sci. & Geomech. Abstr., Vol. 29, No. 6, 1992, pp 561-572.

Armbruster, E.J., "Study of Transport and Distribution of Lighter than Water Organic Contaminants in Groundwater", MS Thesis, University of Colorado, Boulder, 1990.

Arulanandan,K., Thompson, P.Y., et al, "Centrifuge Modeling of Transport Processes for Pollutants in Soils", Journal of Geotechnical Engineering, pp 185 - 205, Vol. 114, No. 2, Feb, 1988.

Baviere, M.,ed, Basic Concepts in Enhanced Oil Recovery, Elsevier Science Publishing Co., Inc., New York, N.Y., 1991.

Bear, J., Dynamics of Fluids in Porous Media, American Elsevier Publishing Company, Inc. Amsterdam, The Netherlands, pp 125 - 184, 1972.

Brooks, R.H., Corey, A.T., "Properties of Porous Media Affecting Fluid Flow", J. Irrig. and Drain. Div., Proc. ASCE, IR2. Vol 92, 1966, pp 66-88.

Buckley, S.E., and Leverett, M.C., "Mechanism of Fluid Displacement in Sands", Trans. AIME, Vol 146, 1942, pp 107-116.

Campbell, J.A., "Nonaqueous Phase Liquid (NAPL) Flow Through Heterogeneous Porous Media: Experimental Study and Conceptual Sharp-Front Model Development", MS Thesis, University of Colorado, Boulder, 1992.

Cargill, K.W., and Ko, H.Y., "Centrifugal Modeling of Transient Water Flow", Journal of Geotechnical Engineering, ASCE, Vol.109, No 4, Apr 1983, pp 536-555.

Carpaneto, R., "Multiphase Flow Parameters Estimation Using Flow Pump Laboratory Technique", MS Thesis, University of Colorado, Boulder, 1989.

Chuoke, R.L., P. van Meurs, and C. van der Poel, "The Instability of Slow, Immiscible, Viscous Liquid-Liquid Displacements in Porous Media", Trans. Am. Inst. Min. Eng., 216, 8073, 1959.

Cooke, A.B., "Determination of soil hydraulic properties", <u>Centrifuge 94</u>, Leung, Lee, and Tan (ed), Balkema, Rotterdam, 1994, pp 411- 416.

Cooke, A.B., and Mitchell, R.J., "Evaluation of contaminant transport in partially saturated soils", <u>Centrifuge 91</u>, Ko (ed), Balkema, Rotterdam, 1991, pp 503-508.

Corey, A.T., <u>Mechanics of Immiscible Fluids in Porous Media</u>, Water Resources Publications, Littelton, Co., 1986.

Croce, P., Pane, V., Znidarcic, D., Ko, H., Olsen, H.W., Schiffman, R.L., "Evaluation of Consolidation Theories by Centrifuge Modelling", Paper for <u>Applications of Centrifuge Modelling to Geotechnical Design</u>, Craig (ed), Balkema, Rotterdam, 1984.

Durnford, D.S., Marinelli, F., "Distribution of Liquid Hydrocarbons in Layered Soils: Hysteresis in Capillary Pressure Saturation Relations", <u>Basic Research in Environmental Quality, AFOSR Research Task Summaries</u>, May 1995.

Engineering Data Handbook, The Hydraulic Institute, 1979.

Fairbanks, T.M., "Light Non-aqueous Phase Fluid Barriers in Initially Water Saturated Heterogeneous Porous Media", <u>MS Thesis</u>, University of Colorado, Boulder, 1993.

Faust, C.R., "Transport of Immiscible Fluids Within and Below the Unsaturated Zone: A Numerical Model", <u>Water Resources Research</u>, Vol. 21, No. 4, Apr 1985, pp 587-596.

Freeze, R.A., Cherry, J.A., <u>Groundwater</u>, Prentice-Hall, Inc., Englewood Cliffs, New Jersey, 1979.

Fryberger, R.M., "Transmissivity of Simulated Concrete Tensile Fractures under Laminar Flow Conditions", <u>MS Thesis</u>, University of Colorado, 1990.

Glass, R.J., Parlange, J.-Y. and Steenhuis, T., "Immiscible Displacement in Porous Media: Stability Analysis of Three-Dimensional, Axisymmetric Disturbances With Application to Gravity-Driven Wetting front Instability", <u>Water Resources Research</u>, Vol. 27, No. 8, Aug 1991, pp 1947-1956.

Goforth, G.F., Townsend, F.C., Bloomquist, D., "Saturated and Unsaturated Fluid Flow in a Centrifuge", <u>Centrifuges in Soil Mechanics</u>, Craig, Jaes, & Schofieled (eds), Balkema, Rotterdam, 1988.

Goodings, D.J., "Implications of changes in seepage flow regimes for centrifuge models", <u>Centrifuge 94</u>, Leung, Lee, and Tan (ed), Balkema, Rotterdam, 1994, pp 393-398.

Goodings, D.J., "Relationships for modelling water effects in geotechnical centrifuge models", Applications of Centrifuge Modelling to Geotechnical Design, Craig (ed), Balkema, Rotterdam, 1985, pp 1-22.

Goodman, R.E., Introduction to Rock Mechanics, John Wiley & Sons, N.Y., 1989.

Held, R.J., "Investigation of Fingering of Dense Nonaqueous Phase Liquids in Saturated Porous Media", MS Thesis, University of Colorado, Boulder, 1993.

Hellawell, E.E., and Savvidou, C., "A study of contaminant transport involving density driven flow and hydrodynamic clean up", Centrifuge 94, Leung, Lee, and Tan (ed), Balkema, Rotterdam, 1994, pp 357-362.

Ibrahim, I. "Centrifugal Modeling of Water Movement in Unsaturated Soils", PhD Thesis, University of Colorado, Boulder, 1990.

Illangasekare, T.H., Znidarcic, D., Al-Sheridda, M., "Multiphase Flow in Porous Media", Centrifuges in Soil Mechanics, Craig, Jaes, & Schofieled (eds), Balkema, Rotterdam, 1988.

Kia, S.F., "Modeling of the Retention of Organic Contaminants in Porous Media of Uniform Spherical Particles", Water Resources, Vol. 22, No. 10, 1988, pp 1301-1309.

Ko, H., "Summary of the State-of-the-art in Centrifuge Modeling", Centrifuges in Soil Mechanics, Craig, Jaes, & Schofieled (eds), Balkema, Rotterdam, 1988.

Larson, R.G., Davis, H.T., and Scriven, L.E., "Displacement of Residual Nonwetting Fluid from Porous Media", Chemical Engineering Science, Vol. 36, Pergamon Press Ltd, 1981, pp 75-85.

Laut, P., "Application of centrifugal model tests in connection with studies of flow patterns of contaminated water in soil structures", Geotechnique 25, 1975, pp 401 - 406.

Lomize, G.M., "Flow in Fractured Rocks" (in Russian), Gosenergoizdat, Moscow, 1951, pp 127.

Louis, C., "A Study of Groundwater flow in Jointed Rock and its Influence on the Stability of Rock Masses", Imperial College Rock Mechanics Research, Report No. 10, 1969.

Manna, M., "Suction-Saturation Measurements in Soils Using the Flow Pump Technique", MS Thesis, University of Colorado, 1991.

Mapa, R.B., User Manual, Permeability and pressure-saturation measurement, University of Colorado, June 1995.

Mitchell, R.J., Stratton, B.C., "LNAPL penetration into porous media", Centrifuge 94, Leung, Lee, and Tan (ed), Balkema, Rotterdam, 1994, pp 345- 349.

Moreno, L., Tsang, C., Tsang, Y., Neretnieks, I, "Some Anomalous Features of Flow and Solute Transport Arising From Fracture Aperture Variability", Water Resources Research, Vol. 26. No. 10, pp 2377-2391, 1990.

Morrow, N.R., Songkran, B., "Effect of Viscous and Buoyancy Forces on Nonwetting Phase Trapping in Porus Media", Surface Phenomena in Enhanced Oil Recovery, Plenum Press, New York, 1981.

Muskat, M., The flow of homogeneous fluids through porous media, New York, McGraw-Hill.B, 1937.

Petersen, S.E., and Cooke, B., "Scaling concerns for immiscible multiphase flow in porous media", Centrifuge 94, Leung, Lee, and Tan (ed), Balkema, Rotterdam, 1994, pp 387-392.

Reible, D.D., Illangasekare, T.H., "Subsurface Processes of Nonaqueous Phase Contaminants", Intermedia Pollutant Transport, Ed David T. Allen, Yoram Cohen, and Isaac R. Kaplan, Plenum Publishing Corporation, 1989, pp 237-254.

Szlag, D.C., "An Experimental Evaluation of Two Sharp Front Models for Vadose Zone Non-aqueous Phase Liquid transport", EPA/600/R-94/197, November, 1994.

Tan, T.S., and Scott, R.F., "Centrifuge scaling considerations for fluid-particle systems", Geotechnique 35, No. 4, 1986, pp 461 - 470.

Van Genuchten, M., "Calculating the Unsaturated Hydraulic Conductivity with a New Closed-Form Analytical Model", Research Report No. 78-WR-08, Princeton University, Princeton, N.J., 1980.

Villar, H.P., Merrifield, C.M., Craig, W.H.., "Experimental aspects of modelling of migration phenomena", Centrifuge 94, Leung, Lee, and Tan (ed), Balkema, Rotterdam, 1994, pp 363-368.

Villar, H.P., Merrifield, C.M.., "Studies on groundwater transport of radioactive waste", Centrifuge 94, Leung, Lee, and Tan (ed), Balkema, Rotterdam, 1994, pp 369-374.

Walser, G.S., "Retention of Liquid Contaminants in soils", PhD Thesis, University of Colorado, Boulder, 1994.

Weber Jr, W.J., McGinley, P.M., Katz, L.E., "Sorption Phenomena in Subsurface Systems: Concepts, Models and Effects on Contaminant Fate and Transport"t, Water Resources, Vol. 25, N0. 5, pp 449 - 528, 1991.

Zimmerman, R.W., Kumar, S., Bodvarsson, G.S., "Lubrication Theory Analysis of the Permeability of Rough-Walled Fractures", Int. J. Rock Mech. Min. Sci. & Geomech. Abstr., Vol. 28, No. 4, pp 325-331, 1991.